TECHNISCHE UNIVERSITÄT MÜNCHEN

Lehrstuhl für Technische Elektronik

Perpendicular Nanomagnetic Logic: Three-dimensional devices for non-volatile field-coupled computing

Irina Eichwald

Vollständiger Abdruck der von der Fakultät für Elektrotechnik und Informationstechnik der Technischen Universität München zur Erlangung des akademischen Grades eines

Doktor-Ingenieurs

genehmigten Dissertation.

Vorsitzender: Univ.-Prof. Dr. rer. nat. Marc Tornow

Prüfer der Dissertation:

1. Univ.-Prof. Dr. rer. nat. D. Schmitt-Landsiedel
2. Prof. György Csaba, Ph.D.
   University of Notre Dame, USA

Die Dissertation wurde am 28.09.2015 bei der Technischen Universität München eingereicht und durch die Fakultät für Elektrotechnik und Informationstechnik am 26.01.2016 angenommen.

Abstract

The pursuit of continuous scaling of transistor-based logic is pushing the CMOS industry towards ever-growing challenges. Reaching physical limits, it is getting more and more difficult to build reliable and at the same time profitable, manufacturable nanoscale transistors. Looking for solutions, the focus is turned on emerging beyond-CMOS technologies and three-dimensional (3D) integration. A promising beyond-CMOS candidate is perpendicular Nanomagnetic Logic (pNML). It provides an alternative way for the realization of digital circuits by applying field-coupled ferromagnets. The bistable magnetization state of the magnets is orientated perpendicular to the film plane and encodes the digital states '1' and '0'. Logic operations are processed by pure magnetic field-interaction between neighboring magnets. pNML is especially suited for ultra-low power applications with additional features of radiation hardness, high integration density, and inherent memory functionality. In terms of 3D integration, the CMOS industry expects better device scalability and increased packing densities by exploiting the third dimension. The purpose of this work is to combine both approaches and to demonstrate the feasibility of 3D integrated pNML.

A monolithic fabrication process is developed and optimized to enable the successive stacking of functional layers. A special alignment technique is presented to enable accurate positioning of top to bottom layer. Critical fabrication parameters are investigated in detail by simulation and experiments to prevent negative consequences on the performance of vertically stacked nanomagnets.

A 'magnetic via' is fabricated proving directed vertical signal transfer between functional layers. A multilayer-crossing is presented, which enables the crossing of magnetic signals. The feasibility of 3D magnetic computing is proven on the basis of a 3D majority gate performing NAND/NOR operation. All the above mentioned elements are characterized by magnetic force and magneto-optical measurements. Design optimization and analysis is supported by micromagnetic simulations. Based on the 3D fabrication technique a magnetoresistance sensor is developed capable of translating signals from the magnetic- into the electrical charge-based domain. The sensor structure is integrable and compatible with the current pNML system design and provides an output interface to CMOS circuitry.

The presented work proves the feasibility of 3D integration of pNML by demonstrating all essential 3D elements required to build 3D pNML circuits. Employing the presented interface sensor, features of pNML and CMOS technology can be combined.

Contents

List of Figures

List of Tables

1 Introduction

In 1965 Gordon Moore predicted to the *Electronics* magazine, that the number of transistors on a chip would roughly double every year [1]. At this moment his prediction gained few attention. But the continual progress in the development of integrated circuits (ICs) of the microelectronic industry proved him right. Since then, Moore's law has been the driving force for down-scaling of device dimensions and interconnecting wires, bringing along the positive impacts of higher integration densities, lower power consumption and increased performance. Exploiting the properties of semiconductors and production processes this trend has been preserved for decades by the CMOS technology. However, nowadays it is getting more and more difficult to maintain the scaling trend with regard to both, physical and material limitations as well as economic profitability [2, 3]. Looking for solutions to delay the "end of the road", two main approaches are pursued: the investigation of new technologies and three-dimensional (3D) integration.
The first approach contains a new requirement on information processing technologies. Not only continual miniaturization should be enabled, but a new form of computational architecture must be accomplished, where logic and memory are combined in a single device [4]. Magnetic materials can provide both features: a remanent magnetization state serving as memory and a stray field, which can be exploited for interaction between magnetic, ultra small-scaled unities to perform logic operation. In the last 60 years, magnetic devices already approved in terms of data storage applications and gain an outstanding position in the microelectronic world. In terms of logic operation, research intensified investigations on magnetic materials, in the last decade. Here, perpendicular Nanomagnetic logic (pNML) proves as a very promising candidate for beyond-CMOS technology [5]. Basic logic operations using field-coupled nanomagnets were already demonstrated successfully. At the same time the inherent, non-volatile magnetization state of magnets can be used to store data. Hence, pNML fulfills the requirement of logic and memory in a single device.
The second approach focuses on the 3D integration of CMOS circuits. The full use of the third dimension may provide the longed for solutions due to better device scalability and improved packing density [2]. Furthermore, in 2007 the ITRS roadmap [6] predicted 3D integration as a key technique to overcome the so-called "wiring crisis". The latter involves with the complex wiring of shrinking transistors and the increasing transistor number on chip. First fabrication techniques and proposals for implementation of 3D CMOS devices and ICs appeared

in the literature in the 1980s [7, 8]. A crucial step forward in the development of 3D integration has been done by the invention of Through Silicon Vias (TSVs) [9, 10]. They enable an electrical connection passing through a silicon wafer or die and therefore provide the possibility to stack wafer or dies in the z-direction. Quoting the ITRS roadmap: "The changing marketplace by consumerization of electronic products presents the tremendous opportunity for the packaging industry in implementing 3D integration technologies to fill the gap created by physical limit of Moore's law scaling" [6], underlines the importance of this approach.
This work shows, that it is possible to combine both approaches and to realize 3D integrated pNML as envisioned in [BBK+13b, BKB+13]. As magnetic stray fields act in all three dimensions, this attribute can be exploited to propagate magnetic signals not only in the horizontal- but also in the z-direction. Furthermore, no wiring is needed, because signal propagation and computing are done by magnetic fields. The prospect of 3D integration of pNML offers new design possibilities for information processing and data storage, combined with high integration densities and low power consumption, while avoiding the "wiring crisis".

1.1 From the concept of 2D to 3D pNML

In general, the concept of Nanomagnetic logic (NML) can be traced back to the quantum cellular automaton (QCA). Here, an elementary cell possesses two stable states, representing the Boolean logic states '0' and '1'. The state of the cell is toggled by fields emanating from neighboring cells [11]. In NML, the elementary cells are nano-scaled, single-domain magnets with a bistable magnetization state. The emanated fields are magnetic stray fields enabling information processing between neighboring magnets. The magnetization vector of the cell itself can be orientated in the plane, referring to in-plane NML or perpendicular to the plane, referring to pNML. Materials with an in-plane magnetization are dominated by the shape anisotropy. The shape of the magnets rules its switching properties and therefore comprises a constraint in the design freedom of NML circuits. Furthermore, thermal fluctuations of in-plane magnets lead to reliability issues. Magnets of materials with a strong perpendicular magnetic anisotropy (PMA) are not as much restricted to any shape and proved to be more reliable. Therefore, this work focuses on the investigation of magnets composed of perpendicular magnetic media, as cobalt/platinum (Co/Pt) [12] or cobalt/nickel (Co/Ni) [13].
The history of pNML started at Technische Universität München in 2006. Csaba and Becherer investigated Co/Pt multilayer film characteristics and proposed basic logic blocks composed of magnets with PMA. Based on their findings, first magnetic logic devices in pNML could be realized. Bit by bit, all important components of a logic computing unity in two-dimensional (2D) pNML were demonstrated experimentally:

- chains of magnets for information transport in the horizontal direction [EBK+12, KBE+13a],

- majority gates to perform logic functionality [BKE+12],

- fanouts to deliver the signal of an output magnet to subsequent gate inputs [14],

- input and output sensors for magnetic/electrical interface and vice versa [15–17].

In Fig. 1.1 a a 2D pNML system is illustrated. An upwards pointing magnetization vector represents logic '1' and a downwards one, a logic '0'. A current carrying wire I produces a magnetic stray field applied to set the magnetization state of magnet A. Exploiting dipole field ($\mathbf{H_{Dip}}$) interaction, the magnetic signal is transmitted from A to magnet I_1. As magnetic field coupling is reciprocal, unidirectional signal flow between the magnets must be created artificially. Most commonly, focused ion beam (FIB) irradiation is used. FIB irradiation provides the possibility to create a sensitive spot in the magnet, which only reacts on the dipole field of its nearest neighbor magnet [18]. By placing this spot on one destined side of the magnet, one can determine on which neighbor the magnet has to react, leading to directed signal flow.
Input magnets I_1, I_2 and I_3 impose a majority decision on magnet D. The latter aligns itself in the direction of the dipole field emanated from the majority of the three inputs. Depending on the magnetization state of I_3 either NAND (I_3 permanently down) or NOR (I_3 permanently up) operation can be performed. Obviously, I_3 occupies a programming task, which enables to switch the gate's functionality between NAND/NOR during runtime. Combining such majority gates, a full-adder circuit can be implemented [BKE+13] or even more any arbitrary logic circuit can be realized.
A fanout is attained by a fork like structure of magnet F. Electrical read-out is realized exploiting the Extraordinary Hall Effect. A change in the magnetization state of O is detected by a change in the Hall voltage using a split current geometry [16] for measuring.
In order to build up 3D circuits, further device layers must be introduced and vertical signal transfer between layers must be guaranteed. In Fig. 1.1 b a 3D circuit is schematically depicted. Signal transmission between functional layers is realized by so called 'magnetic vias' [EKB+13]. In a magnetic via (see C_1-C_2 or C_2-C_3), two magnets are placed above each other, whereas one of the magnets is sensitized by FIB irradiation to the dipole field of its top or bottom neighbor. Furthermore, the placement of magnets in different functional layers enables new 3D architectures of pNML devices. In comparison to the 2D NAND/NOR gate, the programmable input I_3 can now be placed in an extra layer, beneath (or

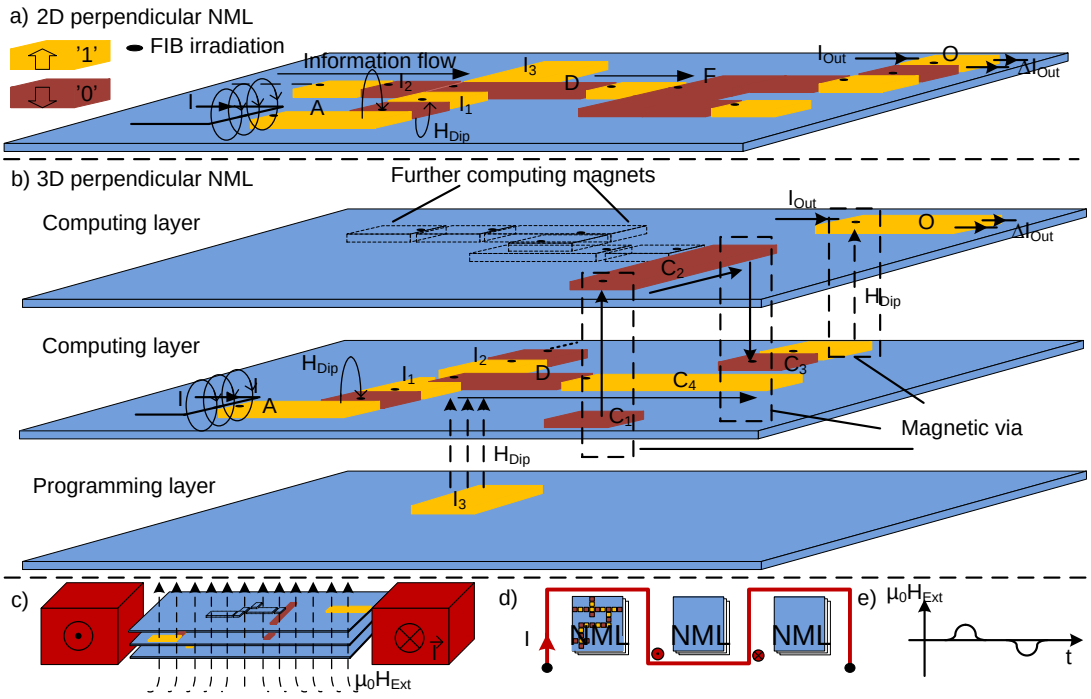

Figure 1.1: (a) Schematic depiction of a 2D pNML circuitry. (b) A comparative 3D architecture of a pNML circuitry including 'magnetic vias' for vertical signal transfer and a new device architecture of the majority gate. (c) Cross section: NML system embedded in between the current carrying arms of an on-chip inductor. (d) Top view: meander-shaped on-chip inductor, with parallel integrated 3D pNML systems. (e) Alternating external global field pulses generated by the on-chip inductor.

above) magnet D. D aligns itself in the direction of the majority acting dipole field emanated from the three inputs. The 3D NAND/NOR architecture enables a more compact design of the gate and promise higher reliability as the influence of the coupling field can be exploited in a better way than for 2D architectures [EBZ+14]. As a beneficial side effect, programming and computing operations can be distributed on different functional layers.

In addition, the 3D architecture simplifies magnetic signal crossings. Therefore, one of the crossing signals can be easily detoured through a further functional layer and transmitted back to its original layer by a magnetic via (see Fig. 1.1b, signal of C_1 crosses signal of C_4 by being first routed up to C_2 and back down to C_3 by magnetic vias) [EBK+14]. In a 2D architecture, the realization of magnetic signal crossings would be very complex and not practicable.

In general, NML systems require an additional energy source to proceed information. In our pNML system, it is an alternating global field (see Fig. 1.1 e). The

generation of the global clocking field is done via an on-chip inductor in form of a meander [BBK+13a, BKB+14], as depicted in Fig. 1.1 d. The NML system is embedded in between the meander (see Fig. 1.1 c).

1.2 Progressive characteristics and advantages of 3D pNML

In general NML claims the benefits of being a low power technology [19][BKB+12] (typically 100 k_BT per switching process of a magnet, where k_B is the Boltzmann constant and T is the actual operating temperature). It combines memory and logic in every single device, operates at room temperature and is resistant against electromagnetic radiation. But one of the most important advantages is, that no wiring between the magnets is required, as they communicate with each other by magnetic field coupling. Furthermore the fabrication of NML devices is compatible with the standard silicon back-end processing, making NML a very promising and appealing technology to complement CMOS-based circuitry. The 3D integration provides further progressive characteristics of pNML compared to 2D implementation:

High packing density
The possibility to fabricate magnets on multiple functional layers and connect them by magnetic vias, enables to stack magnetic logic circuits in the z-direction and therefore reduce the areal extent, while increasing packing density. Furthermore it enables to design logic devices that are more compact. Placing the magnets above instead of next to each other saves area, whereas the functionality of the device is retained.

Integration of many functions on a single chip
Circuits with different functionality requirements can be decoupled by putting them on separated layers, e.g. programming, storage and computing operations.

Higher reliability
The improved exploitation of the spatial geometry for the placement of magnets to each other enables to increase magnetic field interaction. This again guarantees more reliable signal transmitting and computing operations leading to less error-prone pNML circuits.

More design flexibility
The exploitation of both, horizontal and vertical field coupling provides more design freedom of logic devices and circuits as magnets can be arranged in an additional dimension to each other.

Shorter signal paths
Stacking magnetic circuits above each other shortens signal paths between logic computing elements. This improves system performance, as shorter signal routing times are required to propagate information.

1.3 Contribution and outline of this work

The nature of magnetic stray fields of acting in three dimensions can be seen as the basic motivation for this work: demonstrating the feasibility of 3D integration for pNML. A further partial aspect of this work deals with the investigation of a new sensor structure based on magnetoresistance effect to create a magnetic/electrical interface between pNML and CMOS enabling pNML integration in CMOS systems. The common basis of these two issues (3D integration and new sensor type) is the newly developed alignment technique of top to bottom layer required to realize the two issues.
Chapter two summarizes the state-of-the-art of NML, thereby giving an overview, starting with the roots of NML, which lie in the QCA approach over in-plane NML right up to the approach of pNML. Additionally, 3D devices developed in this work are presented. At the end, this chapter comprises the 3D integration techniques applied in CMOS, thereby focusing on the TSVs.
Chapter three is a theory chapter, summarizing the basic magnetic field quantities, magnetic spin distribution in the different types of magnetism and the term 'magnetic anisotropy'. Magnetization dynamics are derived starting with a phenomenological model for the magnetic moment and leading to the Landau-Lifshitz equation, which describes the motion of a magnetization distribution. Finally, a note on micromagnetic simulations, which determine the dynamics of a magnetization distribution by solving the Landau-Lifshitz equation is given.
Chapter four presents the measurement instruments and setups applied in this work.
Chapter five summarizes the fabrication steps for 3D integration. Additionally, critical fabrication steps are discussed and solutions provided to prevent negative consequences.
In **chapter six**, the most vital device for 3D integration, namely the 'magnetic via' is presented. A theory section introducing the aspects for correct functioning of the via is given. Important design parameters to attend and the experimental demonstration of the magnetic via itself are provided.

Chapter seven explains how magnetic vias can be exploited for the realization of magnetic signal crossings. A theoretical background is derived explaining why the magnetic signal crossing is possible despite field interactions between two crossing wires. The experimental demonstration finally proves the concept. Furthermore alternative approaches for signal crossings in 2D and 3D are provided.
Chapter eight presents the first 3D logic device, namely the 3D majority gate. Beside the theoretical background, the experimental demonstration of the device is discussed in detail. Error rates are calculated and possibilities to improve the reliability of the device are provided. All results are supported by micromagnetic simulations.
Chapter nine presents the magnetoresistance sensor, the physical principle behind it and the applied measurement setup. Correct functioning of the device is proven on the basis of different measurement techniques. Furthermore a concept is given, how to integrate the proposed sensor type in pNML circuits. Choosing a different material composition, it is tested, whether the magnetoresistive effect can be enhanced or not.
Chapter ten concludes this thesis and announces challenges in 3D magnetic integrated circuits.

2 State-of-the-art

Magnetic devices are widely known for data-storage applications. Thereby, information is stored in the magnetization state of ferromagnetic materials. The most famous application for fully integrated ferromagnetic solid-state memories is MRAM. It is the result of longtime research and takes an important position in the market of data storage today. Of course, in the past there have always been attempts to exploit ferromagnetism also for the realization of logic functionality e.g. magnetic core circuits in the 1940s [20, 21] and magnetic bubble logic in the 1970s [22, 23]. However, at this point of time, the development of electrical charge-based switches was so advanced, that they outperformed the proposed magnetic logic devices. Until the 21st century, when magnetic logic devices became again into focus of intensive research and a very promising candidate to maintain Moore's predicted scaling trend. Further driving aspects are built-in non-volatility, radiation hardness and low power operation. In the last decade various implementations have been proposed. Beneath others the propagation of domain walls in soft-magnetic materials (magnetic domain wall logic) [24] and spin wave devices, where collective spin oscillations are exploited for signal transmission and processing [19]. All the above mentioned technologies have been intensively discussed in [25, 26], wherefore detailed description is omitted here. This work focuses on a different magnetic logic approach, exploiting magnetic field coupling for processing, namely pNML. The pNML technology gained high attraction in the last five years. It has been included in the ITRS roadmap under the category *Emerging Research Devices* in 2013 [5]. This reveals its significance. A further aspect of this work is 3D integration. There are no recorded 3D integration techniques for magnetic logic devices yet. Therefore, it is worthwhile to mention already known 3D fabrication techniques in CMOS technology, which can be leading the way. Thus, this chapter is used to comment on both subject matter: state-of-the-art in pNML and fabrication techniques for 3D integration.
This chapter is organized as follows: the first section 2.1 covers all aspects of NML, namely, where it comes from, historical evolution, current experimental implementations of pNML in 2D, terminating with the 3D basic building blocks of pNML. The second section 2.2 covers 3D integration techniques in CMOS including historical evolution and currently applied fabrication techniques.

2.1 Nanomagnetic Logic

The history of NML can be traced back to the introduction of the QCA approach. QCA exploits field interaction between quantum cells to transmit and perform logic operation. The quantum cells are cells with two discrete stable states encoding the binary states '0' and '1'. Computation is achieved by bringing such cells together in the immediate vicinity to enable electrostatic (electrical QCA) or magnetostatic (magnetic QCA) interactions. The interacting cell system arranges itself in the energetically lowest state bringing forth a predictable outcome for each cell, given controlled inputs. Consequently signal transmission and computation depend on neither metallic wiring, nor electric currents [27]. This results in simpler processing without need for metallic wiring, and in improvement of energy efficiency. The notation quantum is due to the fact, that interactions are based on the quantum effect of (an) electron(s). A detailed description is given in the subsequent paragraph.

2.1.1 Quantum Cellular Automata approach

In the basic QCA, the cell consists of four quantum dots arranged in a square. Each cell comprises two electrons, which align in diagonal due to their Coulomb repulsion (energetically lowest state). This leads to two about 90° displaced diagonal states representing the logic states '1' and '0' (see Fig. 2.1 a). If the cells are isolated from fields acting from the exterior, the occupation probability of the two states is equally distributed and therefore 50%. Joining cells in the immediate vicinity, the energetically most favorable state of the cell is determined by fields emanated from next-neighbor cells. Logic states can be transmitted from A to B by a wire, where QCA cells are aligned in series (Fig. 2.1 b). Changing the cell's state at one side of the wire, the subsequent cells toggle in the same direction in order to minimize the electrostatic energy. An areal displacement of the cells results in the inverted signal (Fig. 2.1 c). A T-shape arrangement enables to branch the transmitting signal and form a fanout structure (Fig. 2.1 d). Logic computation is offered by a cross-shaped arrangement of cells (Fig. 2.1 e), called majority gate. The majority gate consists of three input magnets I_1, I_2, I_3 being the next-neighbors of a middle cell D. The majority of the inputs forces D to align in the same direction. With one of the inputs (here I_3) tied permanently to a '1' or '0' state, while the remaining two inputs are toggled, either AND or OR operation is performed. Thus logic operation of the majority gate is programmed by the third input. All logic functionality can be realized with the proposed basic elements.

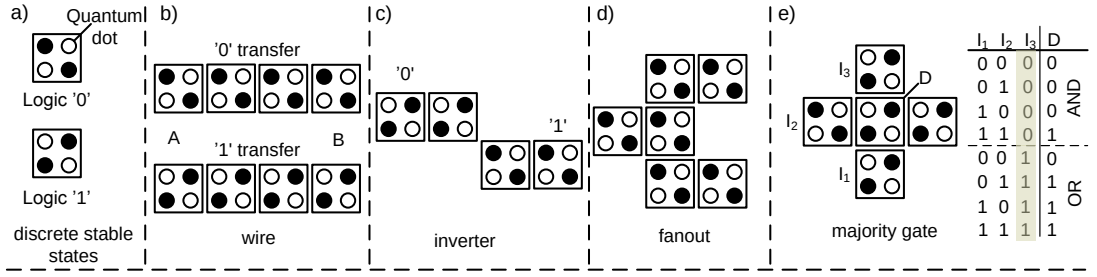

Figure 2.1: (a) Quantum cell, (b) wire, (c) inverter, (d) fanout, (e) majority gate after [27].

2.1.2 From the Quantum Cellular Automata approach to Nanomagnetic Logic

First experimental QCA implementations can be traced back to the late 90ies. Orlov *et al.* built the first QCA cell from four aluminium (Al) islands separated by tunnel barriers, composed of aluminium-oxide (AlO_x) [28]. The polarization of the cell was taken as the discrete two stable-states variable. Polarization change and therefore change in the logic state of the cell could be achieved by electron transmission through the tunnel barrier from one Al island to another. Amlani *et al.* [29] and Snider *et al.* [30] utilized the proposed quantum cell, connected multiple of them to a network and implemented logic functions, like the inverter and a majority gate. The basic cell network architectures depicted in Fig. 2.1 c,e were thereby replicated. The mentioned devices proved the feasibility of QCA but operated only in the mK-regime.

In the year 2000, Cowburn and Welland [31] developed a magnetic QCA, which enabled room temperature operation. Instead of using electrons as information carrier, as done in the above mentioned QCA, Cowburn and Welland utilized the magnetization direction of nanoscaled ferromagnetic islands as two stable-states variable. The circular-shaped islands, composed of Permalloy (Py), emanated strong magnetic fringing fields that were strong enough to influence the magnetization state of the next neighbor cell (distance between the magnets $< 30\,\mathrm{nm}$). An oscillating magnetic field supplied energy to the system and served as a clock. Cowburn and Welland built a chain of field coupled nanomagnets, in which magnetic excitations, called solitons were successfully propagated from the first to the last magnet of the chain. In their experiment, they proved, that propagation was due to field interaction between neighboring ferromagnetic islands. The feasibility of magnetic QCA was hereby verified. Furthermore, Cowburn and Welland announced the idea of 3D integration of magnetic logic devices. Fabrication on multiple functional layers was suggested.

Based on the findings of Cowburn and Welland, Csaba *et al.* firstly proposed nanomagnetic field-coupled logic devices and envisioned the idea of a whole nanomagnetic computing system in 2002 [32]. Therefore, Csaba *et al.* developed a macromodel to simulate the behavior of large field-coupled arrays of nanomagnets [32, 33]. The simulations helped to find out constraints on shape and the placement of the nanomagnets to achieve the desired logic functionality. Csaba *et al.* proposed pillar-shaped Py-magnets, with the easy axis of the magnetization vector orientated perpendicular to the film plane. The simulations confirmed, that the same cross-shaped arrangement of the magnets as proposed in the basic QCA approach (compare Fig. 2.1 e and Fig. 2.2 a) enables majority decision and therefore logic operation. The dipole field emanated from the three inputs I_1, I_2, I_3 forces the central magnet D to align in the opposed direction to the input majority. Also here, an external clocking field is applied for power supply. A clocking example is manifested on the basis of a magnetic chain, depicted in Fig. 2.2 d. In the initial state all magnets are aligned in the same easy-axis direction. Then, the magnets are first aligned to their hard-axis (parallel to the film plane) by a high external field amplitude $|\mu_0 \mathbf{H_{Max}}|$. In the second step only the input magnet is set to a certain state ('1' or '0') by a field $\mu_0 \mathbf{H_{Current}}$ generated by a current carrying wire located in the immediate vicinity to the input. During this process, the non-input magnets are still held along the hard-axis by $\mu_0 \mathbf{H_{Max}}$. In the third clocking phase, the clock field is continuously lowered to zero field. While removing the external field, the input's next-neighbor magnet relaxes in the direction of the input's coupling field $\mathbf{k}$*. The same happens to all subsequent magnets in the chain, which are all influenced by $\mathbf{k}$ of their direct preceding neighbor. To sum up, signal propagation is achieved by the anti-parallel ordering of field-interacting magnets, controlled by the input magnet. Although Csaba's *et al.* perpendicular approach with pillar-shaped Py-magnets turned out to be hard to fabricate, it laid down the basic concept for pNML later on.

A year later, Parish and Forshaw [34] offered an alternative approach to Csaba *et al.*. They proposed to use planar ellipsoidal Py-magnets with their magnetization vector orientated in the film-plane. The elongated form of the magnets provided also bistability and at the same time seemed easier to fabricate. This approach allowed the realization of the logic structures proposed by Csaba *et al.* but only with in-plane magnets (see majority logic gate with elongated Py-magnets in Fig. 2.2 b). First experimental proof of logic functionality performed by interacting elongated Py-magnets succeeded by Imre *et al.* in 2003. Signal propagation through a 64-magnet long chain [35] was demonstrated successfully. In the following years, a magnetic majority gate [36, 37], further basic blocks like

*$\mathbf{k}$ is equal to $\mu_0 \mathbf{H_{Dip}}$ in amount and direction. In the following, the dipole field is always denoted as the coupling field $\mathbf{k}$.

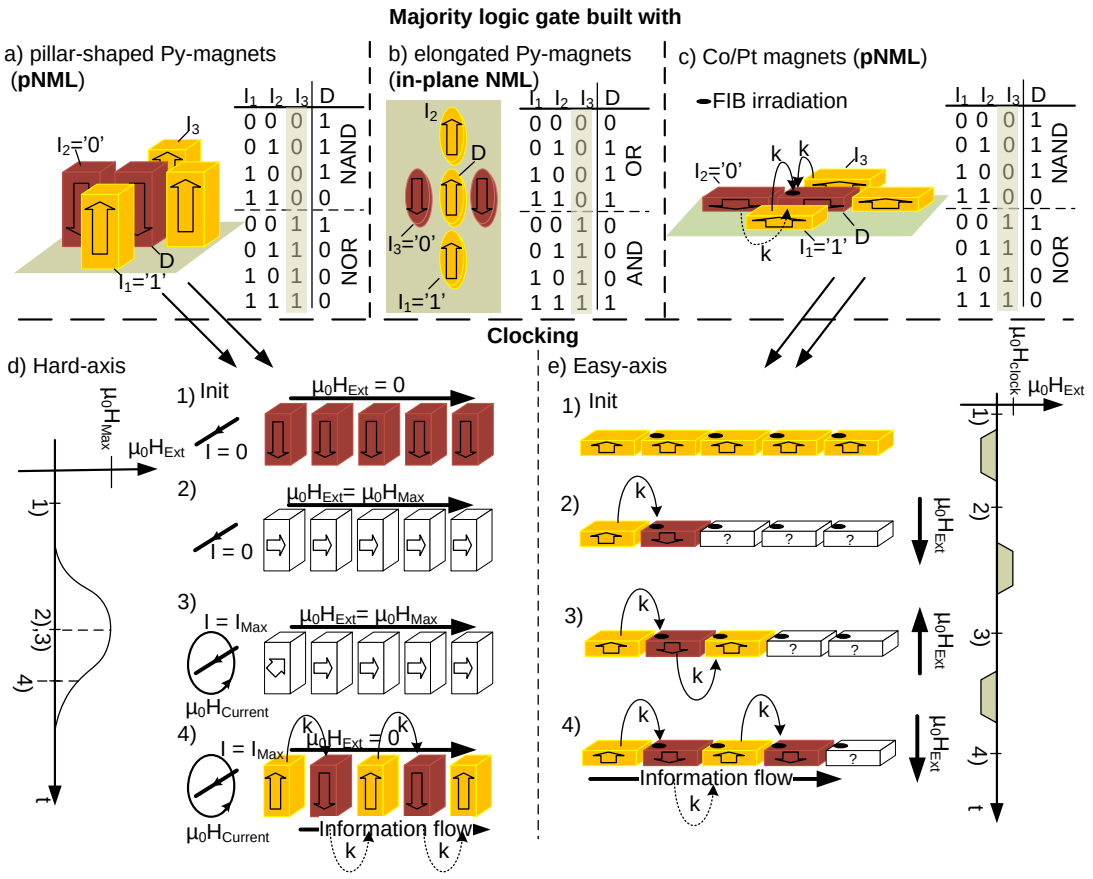

Figure 2.2: Majority logic gate implementations with different technologies: (a) NAND/NOR-gate with pillar-shaped Py-magnets (pNML), (b) AND/OR-gate with elongated Py-magnets (in-plane NML), (c) FIB irradiated Co/Pt-magnets arranged to a NAND/NOR-gate (pNML). Clocking concepts: (d) along the hard-axis as taken from [33] (e) along the easy axis as taken from [EBK+12].

a fanout [38] and a magnetic full adder circuit [39, 40] were implemented and their functionality experimentally proven. The same hard-axis clocking scheme, as already described for Csaba's *et al.* perpendicular approach was utilized.

It is undoubted, that the fabrication of in-plane NML prototypes has been a significant milestone in the history of NML. Still, the experiments revealed imperfections and constraints of this technology, which encouraged to look for more attractive approaches. A more promising approach in terms of reliability and design freedom offers pNML with Co/Pt magnets. Experimental realization and advantages are presented in the subsequent paragraph.

2.1.3 Perpendicular Nanomagnetic Logic

As already mentioned in the preceding paragraph, the idea of pNML was developed by Csaba *et al.* [32]. The main challenge of the proposed technology constituted the realization of the pillar shaped Py-magnets possessing perpendicular magnetization. Due to the high aspect ratio of the magnets compared to the very short distances between the magnets, their fabrication is not trivial and no experimental realization has been recorded until the beginning of this thesis. Therefore, a different approach was pursued. Ultrathin magnetic multilayer films composed of Co/Pt [12], Co/Ni [13], palladium-cobalt (Pd/Co) [41], cobalt-gold (Co/Au) [42] or cobalt-chrome (Co/Cr) [43] are known to possess a special crystalline structure, that induces a magnetization vector perpendicular to the film plane. In such films, PMA induction is independent from the magnet's shape but is due to the crystalline structure of the material stack. Therefore, no high aspect-ratio is required to achieve PMA and the fabrication is much easier.
In 2007, Becherer *et al.* firstly investigated FIB structured Co/Pt films for field-coupled magnetic computing in pNML [44]. Becherer *et al.* sputtered a Co/Pt film and afterwards patterned a grid by FIB irradiation through a lithographic mask into the film as proposed by [12, 45]. The results of the investigations were, that the grid structure divided the Co/Pt film into small single-domain magnets (200x200 nm^2). Several hundred magnets aligned anti-parallel to each other (without frustration) due to the strong ferromagnetic coupling phenomena between next neighbor magnets. This phenomena inspired Csaba and co-workers in 2008, to apply Co/Pt magnets for the realization of pNML [46]. First, micromagnetic simulations were used to reproduce the switching behavior of the magnets from the patterned Co/Pt film, fabricated and characterized by Becherer *et al.* in 2007. Second, the determined parameters were again fed into the micromagnetic simulator to simulate the interaction of magnets in wires and majority logic gate arrangements [46]. The simulation results confirmed the potential to build large-scale computing magnetic devices.
Logic operation in pNML with Co/Pt magnets is exemplary demonstrated on the basis of a majority gate, schematically shown in Fig. 2.2c. It is the same concept as already mentioned before. The input majority forces the output into the anti-parallel state. To guarantee that only the input magnets I_1, I_2, I_3 influence the output magnet D and not vice versa (non-reciprocal signal flow), FIB irradiation is used. Therefore a small area in D is irradiated by Ga^+ ions. The irradiation destroys the crystalline structure, leading to a highly reduced anisotropy in the irradiated spot [12, 45, 47]. This spot constitutes an easy nucleation region for a domain wall. Once a domain wall is nucleated, it propagates through the magnet, completely reversing its magnetization. Placing the irradiated spot in the immediate vicinity to surrounding magnets, domain wall nucleation can be prohibited or will be evoked by the coupling fields from the surrounding magnets. This way,

magnetization reversal of D is controlled by the coupling fields from the surrounding input magnets [14, 18].
Of course magnets of a pNML system do not flip on their own, meaning without an external energy source. Due to the strong crystalline anisotropy, the magnets possess a switching threshold, which must be overcome by an external magnetic clocking field. This clocking field provides the required basic energy, to lift the pNML system up on an energy level, from which magnetic ordering is solely governed by the energy coming from the coupling fields of neighbor magnets. The clocking concept of pNML systems with Co/Pt magnets differs from that one proposed for Py-magnets (compare Fig. 2.2 d and e). Here, an alternating clocking field is applied along the easy-axis of the magnets instead of the hard-axis. The clocking concept is explained on the basis of a magnetic chain, depicted in Fig. 2.2 e. In the initial state all magnets are aligned in the 'up' state. All magnets in the chain, except the input magnet, are left-side irradiated and therefore governed by the dipole field of their left neighbor. Applying a clocking pulse $\mu_0 H_{clock}$ in the down direction, $\mathbf{k}$ of the input magnet forces the second magnet in the anti-parallel state (down state). The magnetization state of all subsequent magnets is unpredictable. As the input magnet is not irradiated, it possesses a high inherent switching field and is therefore unaffected by the clocking pulse. Afterwards a positive clocking pulse is applied. Now, the coupling field of the second magnet forces the third magnet to switch in the 'up' state. In the meantime the second magnet cannot switch back. The coupling field of the input magnet counteracts the external field and prohibits the switching of the second magnet. To sum up, after every clocking pulse the correct ordering of one subsequent magnet can be guaranteed [EBK+12]. This is the main difference of the easy-axis clocking concept compared to the hard-axis clocking concept. Hard-axis clocking orders the whole chain within one clocking pulse. But tighter investigations have revealed that hard-axis clocking combined with pure uniaxial anisotropy leads to instabilities for a high number of magnets and therefore faulty information propagation [48]. The easy-axis clocking concept is regarded as the more promising approach in terms of reliability. Furthermore easy-axis clocking allows for information pipelining (after every second field pulse new information can be fed in) and propagation in all three spatial directions. Hard-axis clocking is restricted to one direction.

Becherer did the pioneering experiments in pNML with Co/Pt magnets [25]. He investigated different compositions of the multilayer stack [49] and introduced electrical input and output-sensors [50–53], which should serve as an interface between the electrical and magnetic domain on a chip. Kiermaier optimized the design of the proposed input and output sensors and performed further investigations in terms of temperature dependency [16, 17].
In the following years, the fabrication technique has been extended to FIB lithography, followed by hard mask evaporation, lift-off and ion beam etching. This

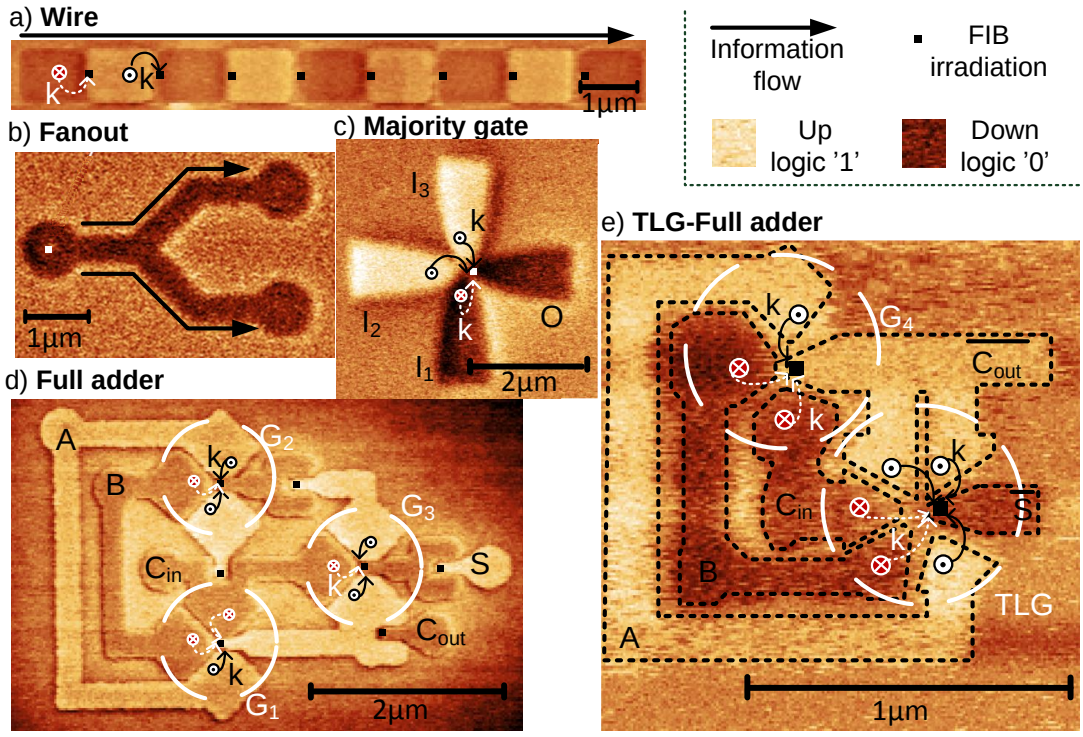

Figure 2.3: Magnetic force microscopy images of ordered final states. (a) Magnetic wire [EBK+12]. (b) Fanout: signal is split in two branches [14]. (c) Majority gate: NAND/NOR functionality [BKE+12]. (d) Full adder: consisting of three interconnected majority gates G_1, G_2, G_3 [BKE+13]. (e) Alternative layout of the full adder: consisting of one majority gate G_4 and one TLG. Acting $\mathbf{k}$ of $\overline{C_{out}}$ on $\overline{S}$ is two times higher than that one of each input A, B, C_{in} [BEK+14].

technique enabled to fabricate free standing magnetic islands and to realize all basic elements of a Boolean computing system: directed signal flow [18], inverter chain [EBK+12], [26] (see Fig. 2.3 a), fanout [14](see Fig. 2.3 b) and majority logic gate [BKE+12] (see Fig. 2.3 c). Wires, inverters and majority gates have been combined to form a full adder circuit [BKE+13] (see Fig. 2.3 d). Basically, from wires and majority gates any arbitrary function can be realized.
Recently it has been shown, that pNML is suitable for threshold based logic [PNC+14, BEK+14]. In general, in threshold logic gates (TLG), each single input is weighted and the weighted sum of the inputs is compared to a threshold. Depending on the geometry and shape of a magnet, one can achieve a certain weight of a magnet. This property has been applied for a further layout of the full adder circuit, shown in Fig. 2.3 e. Magnet $\overline{C_{out}}$ has double influence on magnet $\overline{S}$ compared to the remaining three inputs A, B, C_{in} (2/5 of the magnetic material

surrounding $\overline{S}$ belong to $\overline{C_{out}}$). So majority decision here, is a weighted sum of the four input magnets $A, B, C_{in}, \overline{C_{out}}$, whereas $\overline{C_{out}}$ counts twice. This kind of full adder layout compared to that one in Fig. 2.3 d, spares one majority gate and two inverters, thereby reduces circuit footprint and error-proneness. Compared to transistor based logic, pNML requires much fewer elements for realization of the same logic functionality.
All logic devices and circuits mentioned so far were built on a single functional layer. In the following, 3D building blocks are presented, that were developed in this work.

Comparative illustration of building blocks in 2D vs. 3D pNML

This section summarizes all 3D basic building blocks and compares them to 2D implementations. Differences are outlined to clarify the function. Note, the presented 3D building blocks will be discussed in detail in later chapters of this thesis. So the reader is referred to subsequent paragraphs for detailed information. The building blocks are schematically presented in Fig. 2.4 b, with the applied symbols explained in 2.4 a. The functioning is the following:

Signal transfer
To achieve horizontal signal transfer (x-y direction) from a certain point of the chip to another, magnets can be aligned in chains [EBK+12] or elongated magnets (magnetic wires) can be used. Depending on the placement of the FIB irradiation spot, one can evoke signal transfer from left to right (left-edge irradiation of the magnets) and vice versa (right-edge irradiation of the magnets). Signal transfer in the vertical direction is achieved by placing magnets above each other in different functional layers [EKB+13]. If the edges of the overlaying magnets overlap, parallel ordering occurs (stray field in the same direction as the magnetization). In case the edges of the overlaying magnets are slightly displaced (no overlay) the inverted signal is transmitted and anti-parallel ordering occurs (stray field in opposed direction to the magnetization). For an up-via, the top magnet is sensitized to the coupling field of the bottom magnet by FIB irradiation. For a down-via the bottom magnet is adequately irradiated.
Note, magnets layed out as neighbors in the plane always order in the anti-parallel direction.

Magnetic signal crossing
There is no experimental implementation of magnetic signal crossings in 2D for pNML recorded to date. The 3D approach is similar to electrical signal crossings, where wires are simply overlayed. Here, the magnetic signal is detoured through a further functional layer [EBK+14]. Exploiting the magnetic via, the magnetic

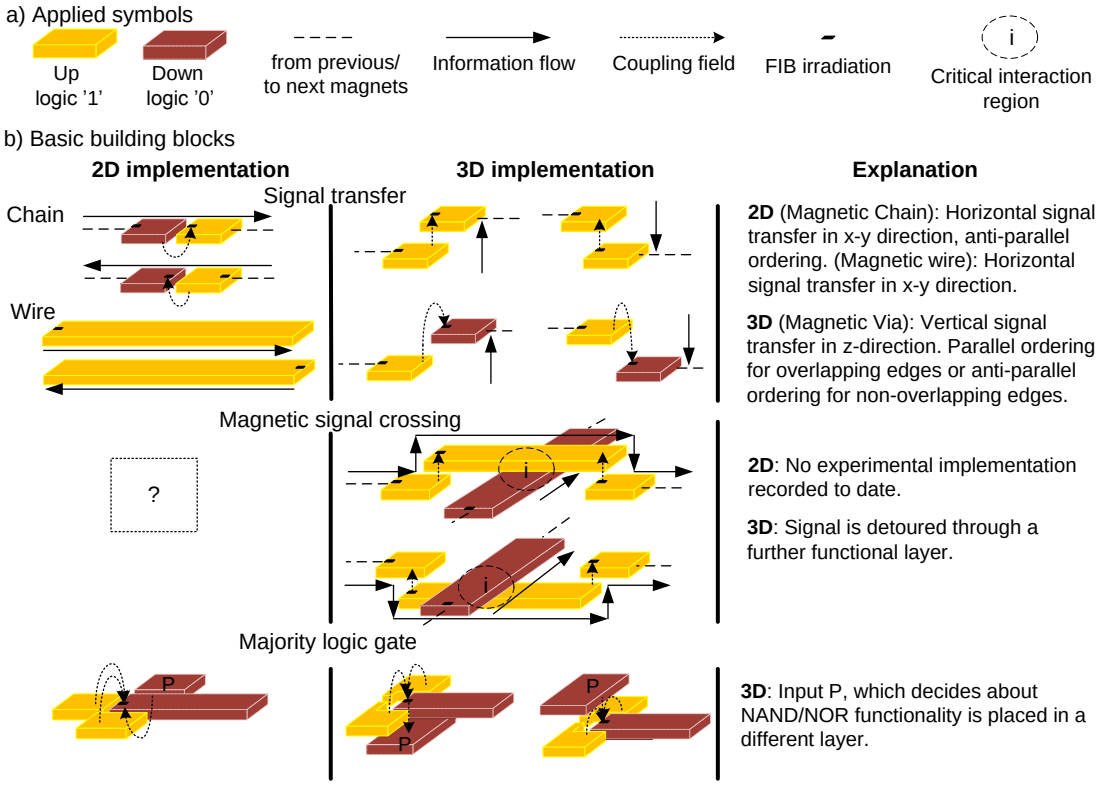

Figure 2.4: (a) Explanation of the applied symbols. (b) Comparison between 2D and 3D basic building block implementations.

signal can be first routed to a further functional layer and then lead back again to the original one. A critical interaction is given in the direct crossover region between two magnetic wires (marked by the encircled i in the figure), which may block a propagating domain wall. However, there are design parameters to keep this interaction as small as possible. Those design parameters guarantee unimpeded signal flow and will be discussed in detail in chapter 7.

Majority gate

The 3D implementation of the majority gate differs from the 2D implementation, by the location of the programmable input P. The 3D majority gate has P located in a different layer. The output aligns in the direction of the predominant coupling field emanated from the three inputs.

The following section describes the evolution of 3D integration in CMOS technology and summarizes different 3D fabrication techniques, which are common today. As an additional information, the proposed 3D pNML devices discussed above are monolithically fabricated. This fabrication technique will be discussed in detail in

chapter 5.

2.2 3D integration in CMOS

Super large integration, high speed, parallel signal processing and integration of multiple functions on a single chip are the drivers for the prolonged promotion of the fabrication techniques of 3D devices and circuits. Looking back on the historical evolution, first attempts can be traced back to the 1980s.
The first step towards 3D integration has been undertaken by General Electrics (GE) in 1981 by an order of NASA [7]. GE searched for possibilities to form electrical interconnects through semiconductor wafers. Here, different techniques have been investigated to form conductors in laser-drilled holes of silicon-on-sapphire wafers. One of the methods, that turned out to be the best, was to sputter a metal film on both faces of the wafer carrying the laser-drilled holes, followed by through-hole electroplating. A major advantage of this technique was, that the wafer surface remained flat and smooth enabling the subsequent wafer processing with conventional semiconductor processing techniques [7].
In 1984, Yasumoto [54] presented a 2-layer, bulk/CMOS ring oscillator fabricated by attaching two chips face-to-face by thermal compression. Therefore, the p-channel driver MOSFETs and the n-channel driver MOSFETs were separately fabricated on different chips and afterwards connected with each other by vertical gold interconnects.
Akasaka [8] summarized concepts providing basic guidelines for the monolithic integration of 3D structures in 1986, for both on device and circuit level. He claimed stacked 3D devices, where single components of the device itself are localized in different active layers, e.g. "load transistors of a CMOS inverter of a CMOS static RAM cell fabricated in an upper layer" [8] as implemented by Malhi *et al.* [55]. These active layers are vertically stacked on a single substrate without stacking wafers or dies above each other. Furthermore he expanded his idea to the circuit level and proposed fully integrated 3D monolithic IC structures.
Later on, Takahashi [56] proposed a new fabrication technique for wafer stacking. His idea was, to fabricate different devices on different wafers. Then the wafers are thinned and front and back leads are provided. At the end the thinned dies are connected to each other, forming a multi chip module. The wafer thinning process, which Takahashi performed by mechano-chemical polishing, has been an important step forward. The thinned wafers facilitated the fabrication of via-holes used for the vertical signal transfer. Here, a simple dry-etching process could now be used to penetrate through the very thin SiO_2 to form the via-holes. Takahashi fabricated successfully a two active layer device using this technique. Based on Takahashi's technique first applications with a two-chip memory combination (SRAM and flash, or flash and flash) appeared [57].

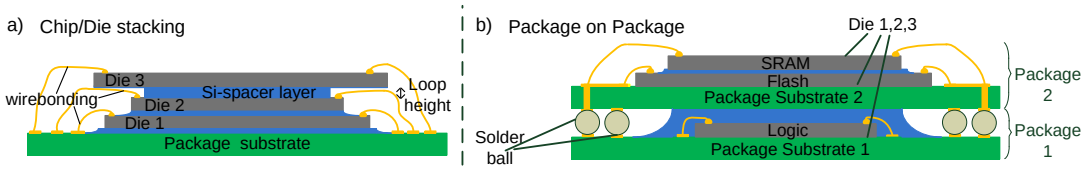

Figure 2.5: (a) 3D packaging: dies are stacked on top of each other and wirebonded to a common substrate. (b) PoP: different packages are stacked allowing the integration of otherwise incompatible technologies and offering multifunctionality.

The following sections summarize some of the numerous 3D integration techniques developed in CMOS.

2.2.1 3D packaging

One possible 3D packaging technique is called chip (or die) stacking. It enables to place multiple chips or dies above each other in a single package. Here, the chips do not communicate internally with each other, but they are mounted and wirebonded to a common substrate (see Fig. 2.5 a). Wirebonding requires a certain height to form the loop (under 100 µm [57]). Thus a chip lying on top of the other must be lifted high enough from the bottom chip to guarantee the required loop height and therefore allow wirebonding. The space between two chips can be added by a spacer layer of silicon. Chips of the same or different sizes, smaller to bigger or vice versa can be placed on top of each other. Furthermore arbitrary ICs can be stacked, memory, logic or analog ICs to form a package. The number of dies that can be stacked depends on the thickness of each layer in relation to the required size of the final package. Of course it is also possible to stack multiple packages above each other, also known as Package on Package (PoP) integration. Therefore, the substrates of the single packages are bumped on so called solder balls. These balls are reheated and consequently merge themselves with the contact pads of the adjacent substrates providing an interconnection (see Fig. 2.5 b). Today, applications of stacked packages with different functions (memory and logic) can be found in cell phones and digital cameras [57].

2.2.2 3D integration with Through Silicon Vias

An alternative to 3D packaging, is an integration technique, where components of vertically stacked dies or wafers do communicate internally with each other by vertical interconnects (no wirebonding to a common substrate). Such interconnects going through the silicon and enabling vertical signal transmission between multiple device layers are called Through Silicon Vias (TSVs). There exist dif-

ferent process approaches for TSV fabrication depending on which point in time they were fabricated, before, in between or after IC fabrication [58]:

Via First
In the Via First approach, the vias are made before IC processing (see Fig. 2.6 a)). The fabrication of the active device layers requires high temperatures. Therefore the conducting material of the via must be doped poly-Si to meet the material and thermal requirements (must be resistant against temperatures of 1000°C) for subsequent device processing. The high resistance of poly-Si compared to metal is a major matter why it is not viable for manufacturing.

Via Middle
In the Via Middle approach, the TSV fabrication takes place after the fabrication of active device layers and before fabrication of interconnect wiring layers (see Fig. 2.6 b)). The vias are formed blind on the wafer and afterwards made visible to the backside by wafer thinning. The wafer thinning process lays the TSVs free for further backside processing, including forming interconnects and routing. The interconnects and routing wires can be easily aligned on the revealed TSVs. Major advantage of this technique is that the critical heating, needed for device processing, takes place before TSV formation. This allows for using metals like tungsten (W) or copper (Cu) as conducting material of TSVs.

Via Last
In the Via Last approach, the TSV formation takes place after the fabrication of the complete IC wafer (see Fig. 2.6 c)). Therefore the wafer is thinned and the vias are etched from the backside into the substrate to the front-side metal. This technique requires a high alignment accuracy of the back-to-front lithography, to position the etched vias accurately above the metal contacts of the IC layer. After the TSV holes are freely etched, the sidewalls of the holes are insulated by the deposition of a dielectric. During this process, the dielectric covers not only the sidewalls but also the metal contacts of the interconnect/wiring layer. These metal contacts must be reopened by a further so called "bottom-clear etch" step. This step is challenging, as not only the metal contacts are reopened but also the sidewall insulator can be etched away. Furthermore the reopened metal surface can be negatively influenced by the utilized various etching plasmas. The contacting metal surface is hard to restore. Due to the high aspect ratio of the via, it is difficult to reach the bottom of a deep via by the standard sputtering etching techniques. Therefore this process technique is not widespread in the industry.

Summarizing all three TSVs fabrication techniques, the Via Middle approach seems to be the most viable in terms of TSV process requirements and manufacturability. Nevertheless, it depends on the application itself, what kind of

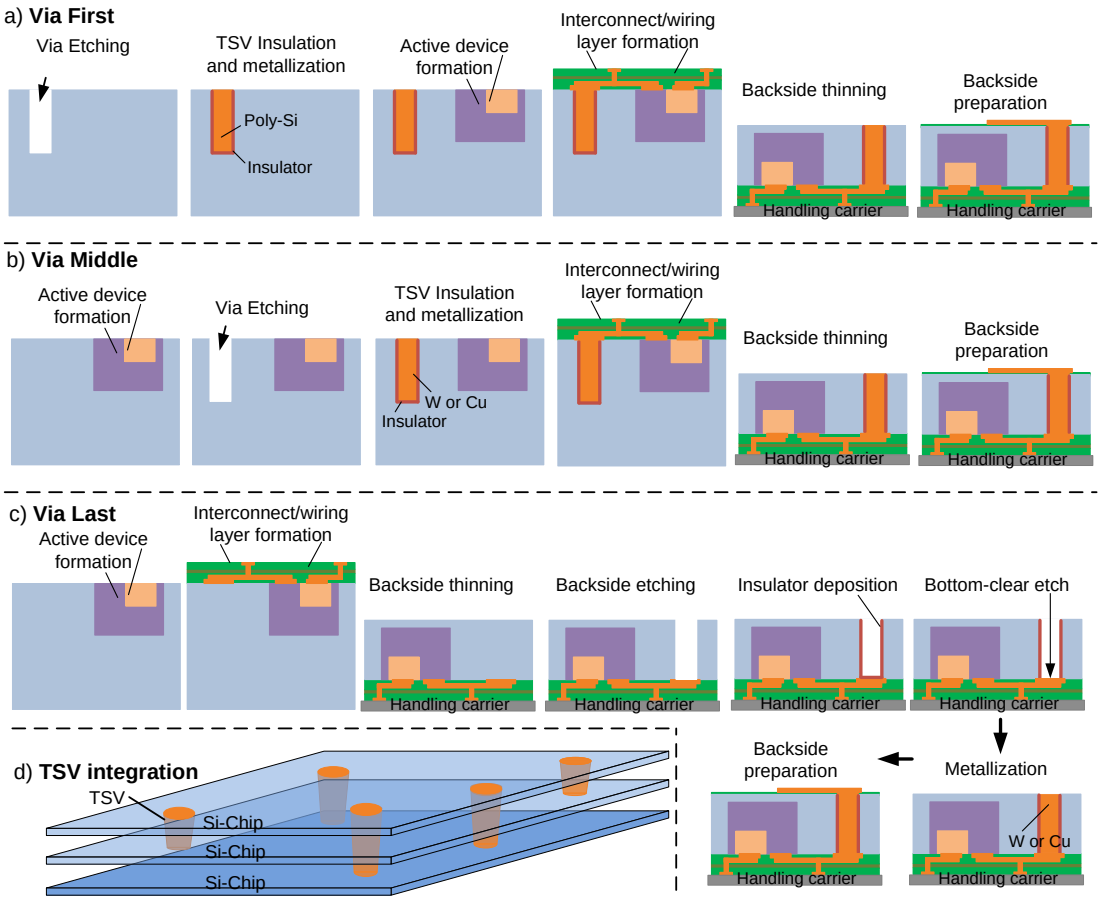

Figure 2.6: (a) Via First, (b) Via Middle, (c) Via Last approach [58]. (d) Schematic of TSV-connected chips.

process is allowed and which one is the most compatible with the required IC fabrication technique. In some cases the Via First or the Via Last approach may offer better solutions. A schematic of a 3D integrated system with TSVs is depicted in Fig.2.6 d. The diameter of the TSV is in the micrometer range, three orders of magnitude higher than the today's nanoscaled CMOS devices. These dimensions of the TSVs diminish the integration density benefits provided by 3D integration. A solution to this can be given by monolithic fabrication techniques.

2.2.3 Monolithic 3D integration

Monolithic 3D integration is a technology, that does not require TSVs. Here, all IC components are built in layers on a single substrate (no wafer/die stacking). This technique requires no alignment, wafer thinning or bonding. Although this technique offers many advantages, it faces a significant challenge. Up to now de-

vice processing requires high temperatures. By fabricating devices subsequently in different layers, devices and interconnects of the underlying layers are longterm exposed to the high temperatures, leading to performance losses and destruction. Therefore a fundamental breakthrough in low-temperature processing technologies is required [59]. In the last few years enforced research has been undertaken in this area but market maturity solutions have been not yet provided.

In contrast, in this work exactly this fabrication technique is applied. As pNML exploits magnetostatic field interaction between overlaying magnets to transmit information in different functional layers, the distance between the layers must be sufficiently small ($<$100 nm). Therefore, the only reasonable fabrication technique allowing for such small distances between the functional layers is the monolithic one.

3 Theoretical background of magnetism

3.1 Basic magnetic field quantities

For the description of the magnetic phenomena two important field quantities are required: the magnetic field $\mathbf{H}^*$ (unit : $[\mathrm{Am}^{-1}]$) and the magnetic flux density $\mathbf{B}$ (unit : $[\mathrm{T\,or\,Vsm}^{-2}]$). The relation between $\mathbf{H}$ and $\mathbf{B}$ in vacuum is [60]:

$$\mathbf{B} = \mu_0 \mathbf{H}. \tag{3.1}$$

The permeability μ_0 amounts to $4\pi \cdot 10^{-7}\mathrm{VsA}^{-1}\mathrm{m}^{-1}$.
In the literature, there are numerous explanations given to understand the difference between $\mathbf{H}$ and $\mathbf{B}$, as outside a magnetic material they can be used equivalently to describe the field and μ_0 is only a linear approximation of a phenomenological quantity. To understand why both quantities are needed, one has to go back to Maxwell's equations. $\mathbf{B}$ is a fundamental field in Maxwell's equation, which is created by currents or time-varying electric fields. $\mathbf{H}$ is an auxiliary field in Maxwell's equation, which is created by magnetic dipoles, where the poles of the dipole themselves are the sources of field. So in general, if everything would be describable by current distribution, field quantity $\mathbf{B}$ would be sufficient to describe magnetic fields. However, as spin distributions are hard to relate to currents in magnetostatics, $\mathbf{H}$ is quite fundamental to describe the magnetic phenomena inside magnetic materials.
Inside the magnetic material, the relation between $\mathbf{B}$ and $\mathbf{H}$ changes:

$$\mathbf{B} = \mu_0(\mathbf{H} + \mathbf{M}), \tag{3.2}$$

whereas $\mathbf{H}$ represents the inherent magnetic field, also known as the 'demagnetizing field'. $\mathbf{M}$ stands for the magnetic dipole moment per unit volume of the magnetic material and enhances the magnetic flux density.
Dia- and paramagnetic materials possess no inherent magnetic moment, but a magnetization $\mathbf{M}$ can still be evoked by the excitation with the field $\mathbf{H}$. For these kind of materials, the relation between $\mathbf{M}$ and $\mathbf{H}$ is linear:

$$\mathbf{M} = \chi_m \mathbf{H} \tag{3.3}$$

*Boldface type indicates a vector quantity.

where χ_m is the magnetic susceptibility, describing the magnetizability in an external magnetic field. The parameter χ_m is without unit. Substituting $\mathbf{M}$ in eq. 3.2 with the expression defined in eq. 3.3 gives:

$$\mathbf{B} = \mu_0(1 + \chi_m)\mathbf{H} = \mu_0\mu_r\mathbf{H} \tag{3.4}$$

whereas μ_r is called the relative permeability and depends on the investigated material. In ferromagnetic materials like Co or Ni, the relation between $\mathbf{M}$ and $\mathbf{H}$ is non-linear, showing a hysteretic behavior. This behavior is discussed in the subsequent section.

3.2 Types of magnetism

In the classical view of Bohr [61, 62], the origin of a dipole moment can be traced back to moving charges. Thereby matter always consists of atoms composed of a nucleus and electrons circling around it. The electron itself possesses a magnetic moment, called 'spin' arising from an intrinsic angular momentum. Additionally, the movement of the electron around the nucleus causes a magnetic force to be exerted. The magnetic moments of an atom often compensate each other completely or partially. So there remains either no magnetic moment or a net magnetic moment of just a few electrons, which are the source of magnetism. The ordering of the spins to each other and their behavior in an external field leads to different types of magnetism. In the following dia-, para- and ferromagnetism are discussed [60–62]:

Diamagnetism
Naturally, magnetic dipole moments align opposed to each other to minimize the overall energy. Atoms in diamagnetic materials have an even number of electrons. Hence the dipole moments cancel out each other, so there remains no *permanent* magnetic moment. In the presence of an external magnetic field, an interaction between the moments and the external field is given. Thereby, the impact of the external magnetic field is different for dipole moments aligned parallel relatively to the external field than for dipole moments aligned anti-parallel to the external field. Consequently the imbalance results in a weak net magnetic moment pointing opposed to the external field. However, in most cases this net magnetic moment is overlayed by other effects, so no permanent magnetization is observed. Diamagnetism occurs in all substances, since all matter consists of atoms with moving electrons around their nucleus.

Paramagnetism
Paramagnetic materials, like Pt or Ti consist of atoms with an uneven number of

electrons. Consequently, the magnetic dipole moments cannot compensate each other, leading to a natural *permanent* dipole moment. However, due to thermal motion and in the absence of an external field, these dipole moments are statistically distributed in all kind of directions, resulting in a net moment that is zero. Applying an external field, the dipoles align in the direction of the field. Removing the external field, the alignment is lost again.

Ferromagnetism
In ferromagnetic materials, the dipole moments of atoms/molecules are not independent from each other as it is in paramagnetic materials. In small entities (crystallites), the dipole moments align parallel to each other resulting in a *spontaneous* magnetization. These regions are called Weiss' domains. The coupling force (exchange coupling) between the moments responsible for their parallel alignment can be traced back to a quantum mechanical effect. Naturally, the magnetic moments of each domain are statistically distributed striving to minimize the overall energy. Thereby, the size of domains varies with different parameters, e.g. grain size, crystal growth, impurities in the crystal and so on. Above a critical temperature T_C, called the ferromagnetic Curie temperature, the magnetization vanishes and the specimen gets paramagnetic. For Co and Ni for example the critical temperature is: $\mathrm{T_{Co}} = 1388\,\mathrm{K}$ and $\mathrm{T_{Ni}} = 627\,\mathrm{K}$.

The overall magnetization of the entire ferromagnetic specimen is a vector sum of the magnetic moments of each domain. Therefore the absolute value of the magnetization can have values between zero (for special domain configurations, the magnetic moments may cancel each other out, called demagnetized state) and a maximum value, called saturation magnetization M_S (magnetic moments of each domain aligned in one direction forming a single domain). To achieve saturation magnetization an external field has to be applied. In the presence of an external field, some domains align in its direction and others, who are already aligned enlarge. This process is strongly nonlinear. The relation between the magnetization and the applied field is described by the hysteresis loop, shown in Fig. 3.1.
Assuming, that the material is initially demagnetized, the curve starts at point O. By applying a magnetic field the magnetization grows until all magnetic moments align in the direction of $\mathbf{H_{ext}}$ and the maximum magnetization (M_S) is reached (see Fig. 3.1, process is indicated by the 'Magnetization curve'). Reducing the field again to zero, the magnetization adopts higher values than in the initial state. This effect can be traced back to the irreversibility of the domain formation process. In a high magnetized state of the material, domains cannot return easily in their initial state due to tensions or lattice disturbances. At zero field a reminder of the magnetization remains, called remanence M_R. To achieve zero magnetization again, the external field has to be further reduced to the value $-H_C$. The field, where $M = 0$, is called coercive field. A further reduction leads

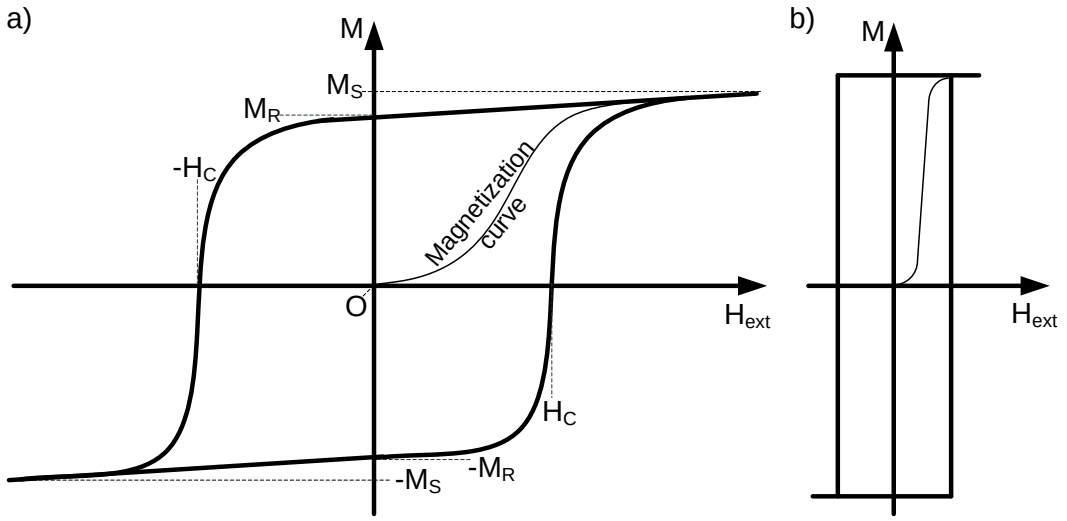

Figure 3.1: (a) Hysteresis loop, revealing the nonlinear behaviour between the magnetization $\mathbf{M}$ and the applied field $\mathbf{H_{ext}}$. (b) Hysteresis loop of a film used for pNML.

to the negative saturation of the specimen. Increasing the external field to positive values again, gives an at the origin mirrored curve.
The shape of the hysteresis curve may vary. The higher the energy required to change the magnetization direction, the higher is H_C. Furthermore the direction of the applied field in relation to the inherent magnetization direction of the investigated specimen modifies the form of the hysteresis. In pNML the magnets are composed of a Co/Pt or Co/Ni multilayer. These materials can exhibit very small coercivities. Furthermore $\mathbf{H_{ext}}$ is applied parallel to the inherent magnetization direction i.e. perpendicular to the film plane, to achieve abrupt switching.
All in all, the hysteresis loop of a magnet used in pNML exhibits a:
- sharp switching $\mathrm{d}\mathbf{M}/\mathrm{d}\mathbf{H} \rightarrow \infty$
- the maximum magnetization is almost retained even if the field is removed $M_R \approx M_S$
- with a low coercivity H_C for a low energy consumption during switching.

For the functioning of pNML, it is a prerequisite that the magnets possess a magnetization vector perpendicular to the film plane. However, the inherent magnetization direction (meaning in the absence of an external field) of a ferromagnetic specimen can be different and depends on different parameters. This phenomena is discussed in the subsequent section.

3.3 Magnetic Anisotropy

In the absence of an external field, the inherent magnetization of a magnetic specimen always aligns in the direction of minimum energy, called the 'easy axis'. The energetically most unfavorable direction is called the 'hard axis'. The observance, that the free magnetic energy of a magnetic system depends on the direction of the magnetization is called the magnetic anisotropy. It can be considered as a 'free energy function', whereas the magnetization direction targets the most favorable direction in the specimen. The origin of the magnetic anisotropy can be traced back to dipole-dipole interactions or spin-orbit coupling. It is distinguished between three different anisotropy contributions, namely the crystalline anisotropy, the shape anisotropy and the magnetoelastic anisotropy, forming the sum of the magnetic anisotropy. These three anisotropy types consider different causes of the magnetization direction dependent energy.

Shape anisotropy
The shape anisotropy has its origin in the long-range dipole-dipole interaction. On the surface of a magnetic specimen, this interaction generates a magnetic field, called the magnetic stray field $\mathbf{H_S}$. $\mathbf{H_S}$ strongly depends on the geometry of the considered specimen and is opposed to its magnetization $\mathbf{M}$ [11]:

$$\mathbf{H_S} = -\mathbf{NM}. \tag{3.5}$$

$\mathbf{N}$ is called the demagnetizing tensor containing the shape dependency. The corresponding stray field energy is given by [11]:

$$K_{Shape} = \frac{\mu_0}{2} V \mathbf{MNM}. \tag{3.6}$$

V constitutes the volume of the sample. Thin magnetic layers, in which the lateral extent is much larger than the film thickness, can be simply considered as a spheroid. In this case every component of $\mathbf{N}$ becomes zero except the one, normal to the film plane, which becomes one. Taking this fact and the relation, that $\mathbf{M}$ includes the angle θ with the film normal, eq. 3.6 is reformed to [11]:

$$K_{Shape} = \frac{\mu_0}{2} V M^2 \cos^2(\theta). \tag{3.7}$$

From this equation, it is obvious that the energy minimum is reached for $\theta = 90°$, meaning that the magnetization lies in the film-plane. Descriptively, this means, that the magnetic field lines cannot leave the magnetic film. Hence, magnetic stray fields and therefore the stray field energy are avoided. Taking this into account, it is obvious, that there must be other components, which ensure that the magnetic anisotropy can also be perpendicular to the film plane. These components are discussed in the following.

Magnetocrystalline anisotropy

The magnetocrystalline anisotropy originates from spin-orbit interaction. A rotation of the exchange coupled spins, and therefore of the magnetization evokes a torque on the orbital momentum, due to spin-orbit coupling. The torque leads to a rotation of the orbital momentum. However, the rotation of the orbitals is energy dependent. This can be traced back to the fact, that a rotation changes the overlap of the wave functions of d-electrons, which give rise to magnetism in ferromagnetic materials [63].

Briefly speaking, this means also here exist directions, in which the electronic orbitals and thereby the magnetization are aligned in order to minimize the overall energy. Indeed, the electronic orbitals are attached to the crystalline lattice and are ordered symmetrically. Consequently, the magnetic spins and thereby the magnetization prefer an alignment along the crystallographic axes.

Normally, in the limit of thin films, shape anisotropy prevails magnetocrystalline anisotropy [11], so that the magnetization still lies in the plane. But note, that each disturbance in the symmetry of the crystalline lattice influences spin-orbit coupling and therefore can change the anisotropy behavior in a way, that the crystalline anisotropy finally outweighs shape anisotropy, so that the effective magnetic anisotropy may be orientated perpendicular to the film plane. This effect is observed in multilayer films like Co/Pt and Co/Ni and is referred to the **interface anisotropy**.

The interface anisotropy is a special kind of the magnetocrystalline anisotropy. At the interface of two different film materials the crystalline lattice experiences a disturbance. Here, the symmetry of the crystalline lattice is broken, leading to a change of the orbitals and an additional angular dependence of the spin-orbit interaction. The interface anisotropy may prefer a magnetization direction perpendicular to the film plane. The interface anisotropy energy is given by [11]:

$$K_{interface} = K_S A_{film} \cos^2(\theta) \tag{3.8}$$

with K_S being a phenomenological surface anisotropy constant, θ the angle $\mathbf{M}$ includes with the film normal and A_{film} being the surface area of the considered film. For negative K_S, a minimum energy is given for the angles $\theta = 0°$ and $\theta = 180°$. It is obvious, that for these angles a magnetization perpendicular to the film plane is favored.

A negative K_S competes with shape anisotropy. To achieve perpendicular magnetic anisotropy, interface anisotropy has to be larger than shape anisotropy. Equalizing the amounts of equations 3.7 and 3.8 and replacing in eq. 3.7 the volume by the product $V = A_{film}d$ (d constitutes to the film thickness), a critical film thickness d_c can be deduced, where reorientation from in-plane to out-of-plane

takes place:

$$|K_{Shape}| = |K_{interface}| \tag{3.9}$$

$$\left|\frac{\mu_0}{2} A_{film} d M^2 \cos^2(\theta)\right| = \left|K_S A_{film} \cos^2(\theta)\right| \tag{3.10}$$

$$\Rightarrow d_c = \left|\frac{2K_S}{\mu_0 M^2}\right| \tag{3.11}$$

For a layer thickness below d_c, the interface anisotropy is predominant and perpendicular magnetic anisotropy is induced.

Magnetoelastic anisotropy
The magnetoelastic anisotropy also originates from spin-orbit coupling and is induced by strain. Strain leads also to a symmetry reduction in the crystalline lattice and therefore affects spin-orbit coupling leading again to an angular dependency of the magnetization. In the investigated thin films of this work the magnetoelastic anisotropy has negligible impact.

3.4 Magnetization dynamics

The following section deals with magnetization dynamics (motion) and explains the time-variant behavior of magnetic dipole moments.

Basically one can say, that every atom of a ferromagnetic material comprises one magnetic dipole moment. The magnetic dipole moment itself can be understood by phenomenological and atomic models. As already mentioned before, Bohr deduced the dipole moment $\mathbf{m_d}$ from the circular current, that an electron forms when circling around the nucleus of an atom. The circular current I_e embracing the area A results in a dipole moment amplitude of [61]:

$$m_d = I_e A = -\frac{e\omega_0}{2} r_e^2. \tag{3.12}$$

With the electron's orbit radius r_e, the embraced area A can be replaced by $\pi\, r_e^2$. When assuming, that the electron with the charge $-e$ is moving around the nucleus with a circular frequency ω_0, the resulting circular current I_e can be expressed by $-e\omega_0/2\pi$. Taking this into account, the derivation of the final expression given in eq. 3.12 [60] can be easily reconstructed.
Another elementary model describes the magnetic moment in terms of equivalent opposite magnetic charges separated by a predefined distance. The product of these two charges yields the magnetic dipole moment $\mathbf{m_d}$. (This model is analogous to the model of an electric dipole moment, where two opposite charges $+q$ and $-q$ are separated by a predefined distance.)

The nucleus exerts a force on the circling electron with the mass m_e, which yields in the angular momentum $\mathbf{L}$ (see Fig. 3.2a) with the amplitude :

$$L = \omega_0 m_e r_e^2. \tag{3.13}$$

As the energy levels of an atom are discrete, the angular momentum is quantized. Consequently, the magnetic dipole moment must also be quantized i.e. it can only adopt values, that are integer multiple of the Bohr magneton $\mu_B = \frac{e}{2m_e}\hbar$, with $\hbar$ being the Planck's constant:

$$m_d = -m_L \mu_B, \quad where\ m_L = 0, \pm 1, \pm 2, ... \tag{3.14}$$

The Bohr magneton represents the smallest indivisible dipole moment of an electron.
The quantity that links the orbital magnetic moment $\mathbf{m_d}$ and the mechanical angular momentum $\mathbf{L}$ together is called γ, the gyromagnetic ratio:

$$\mathbf{m_d} = \gamma \mathbf{L}, \tag{3.15}$$

whereas γ amounts to $-\frac{e}{2m_e}$ for a single electron moving in a circle. However, it must be considered, that the electron spin also gives rise to a magnetic moment. Taking this into account, a different ratio between the mechanical and the magnetic moment is given:

$$\mathbf{m_d} = g\gamma \mathbf{L} = -g\frac{e}{2m_e}\mathbf{L}. \tag{3.16}$$

The constant g is called the Lande gyromagnetic splitting factor. Depending on the value of g, only the orbital momentum (g=1), only the spin momentum (g=2), both and even more quantum electrodynamics (g=2.0023) are taken into account for calculation.
These have been the basic equations, describing the magnetic and mechanical properties of a moving electron. Now, the behavior of the magnetic moment in the presence of an external field is considered. Applying an external field in a certain angle to the magnetic moment, a torque $\mathbf{T}$ is imposed on the magnetic moment:

$$\mathbf{T} = \mu_0 \mathbf{m_d} \times \mathbf{H_{ext}}. \tag{3.17}$$

This torque is perpendicular to $\mathbf{m_d}$ and $\mathbf{H_{ext}}$. The torque gives rise to the precession motion of the magnetic moment around the direction of $\mathbf{H_{ext}}$. If $\mathbf{H_{ext}}$ and $\mathbf{m_d}$ point in the same direction, there will be no precession movement.
The torque is the gradient with respect to time of the angular momentum:

$$\mathbf{T} = \frac{d\mathbf{L}}{dt}. \tag{3.18}$$

Transposing eq. 3.16 after $\mathbf{L}$ and inserting it in eq. 3.18 gives:

$$\mathbf{T} = \frac{d}{dt}(\frac{1}{g\gamma}\mathbf{m_d}) = \frac{1}{g\gamma}\frac{d\mathbf{m_d}}{dt} = \mu_0 \mathbf{m_d} \times \mathbf{H_{ext}}. \tag{3.19}$$

It follows for the gradient of $\mathbf{m_d}$ with respect to time, which describes the motion of an undamped magnetic moment in a field:

$$\frac{d\mathbf{m_d}}{dt} = \mu_0 g\gamma \mathbf{m_d} \times \mathbf{H_{ext}} = -\mu_0 g \frac{e}{2m_e}\mathbf{m_d} \times \mathbf{H_{ext}}. \tag{3.20}$$

The value of the prefactor $-\gamma_{LLG} = -\mu_0 g\frac{e}{2m_e}$ amounts to $2.210 \cdot 10^5 \mathrm{m(As)}^{-1}$ (with g=2.0023) and is called the Landau-Lifshitz gyromagnetic ratio.
To achieve the equation of motion for a magnetization distribution $\mathbf{M}$, eq. 3.20 must be transformed to [64]:

$$\frac{d\mathbf{M}(\mathbf{r},t)}{dt} = -\gamma_{LLG}\left[\mathbf{M}(\mathbf{r},t) \times \mathbf{H_{eff}}(\mathbf{r},t)\right]. \tag{3.21}$$

Note, for the calculation here, an effective magnetic field $\mathbf{H_{eff}}$ is considered. The effective magnetic field comprises not only the component of the external magnetic field, but additionally exchange interactions, demagnetizing field, anisotropy distribution and thermal fluctuations [65]. This is convenient, as all these components are present in a magnetic material.
However for the given equation, still one important component has been neglected. Considering the given equation 3.21, the magnetization would never stop to precess as no dissipation is included. As this is not the case in reality, eq. 3.21 must be extended by an Ohmic type dissipation term:

$$(\frac{d\mathbf{M}(\mathbf{r},t)}{dt})|_{Diss} = \frac{\alpha}{M_S}\left[\mathbf{M}(\mathbf{r},t) \times \frac{d\mathbf{M}(\mathbf{r},t)}{dt}\right]. \tag{3.22}$$

Thereby, α is a phenomenological damping constant (Gilbert damping [66]) and M_S the saturation magnetization. Summing up eq. 3.22 to eq. 3.21 yields the Landau-Lifshitz equation (LLG) describing the changes of a magnetization distribution under the influence of an effective field:

$$\frac{d\mathbf{M}(\mathbf{r},t)}{dt} = -\gamma_{LLG}\left[\mathbf{M}(\mathbf{r},t) \times \mathbf{H_{eff}}(\mathbf{r},t)\right] - \frac{\alpha\gamma_{LLG}}{M_S}\left[\mathbf{M}(\mathbf{r},t) \times (\mathbf{M}(\mathbf{r},t) \times \mathbf{H_{eff}}(\mathbf{r},t))\right]. \tag{3.23}$$

The first term of the equation comprises the precession movement, while the second term takes dissipation into account. The dissipation term ensures, that the precession movement breaks and the magnetization is finally turned into the direction of $\mathbf{H_{eff}}$ (see Fig. 3.2 b). The dissipation itself constitutes to the transfer of energy from the motion of the magnetization to heat.

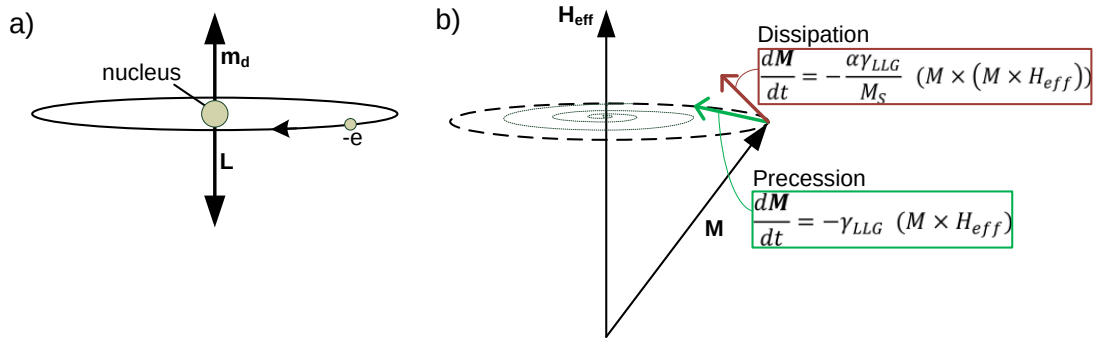

Figure 3.2: (a) Magnetic dipole moment $\mathbf{m_d}$ and corresponding angular momentum $\mathbf{L}$ of a circulating electron. (b) Interaction of the magnetization $\mathbf{M}$ with an effective field $\mathbf{H_{eff}}$. The torque forces $\mathbf{M}$ to a precession movement around $\mathbf{H_{eff}}$ while damping breaks the precession leading finally to the alignment of $\mathbf{M}$ into the direction of $\mathbf{H_{eff}}$.

The LLG equation specifies the magnetization distribution at time $t + dt$. It can be used to describe the motion of small magnetic moments in space and time, which are often a good approximation for single-domain nanomagnets. However, basically one can use the LLG equation for every magnetic material and body. Therefore the volume of the magnetic specimen is split into elementary volume elements, whose dynamics are calculated by the LLG. In doing so, every elementary volume element experiences a different $\mathbf{H_{eff}}$. Stationary solutions (i.e. $\frac{\mathrm{d}\mathbf{M}(\mathbf{r},\mathrm{t})}{\mathrm{dt}} = 0$) of the LLG representing the global or local energy minima of the ferromagnetic material yield stationary domain patterns.

3.4.1 A note on micromagnetic simulations

In this work, the object orientated micromagnetic simulation framework, called OOMMF [67] has been applied in order to study the behavior of nanomagnets in the presence of an external field and coupling fields. The OOMMF solver (OOMMF eXtensible Solver) is an extensible micromagnetic computation engine, which is capable of solving micromagnetic problems by relaxing the previously derived LLG equation. Therefore the considered magnetic volume is split up into small elementary volumes, defined on three-dimensional grids of rectangular cells (discretization in finite differences). Each cell comprises a 3D spin. The contribution of each cell is calculated and the minimum total energy state of the system derived by applying Fast Fourier transformation techniques.
As input parameters the simulator requires the material parameters i.e saturation

magnetization, the shape and geometry of the magnets, the initial magnetization state and anisotropy of each magnet, the applied external field and field steps. Furthermore, the size of the cells can be specified. The smaller the cells, the more calculation is required and the more simulation time is consumed, but the more precise it the solution.
In this work, the OOMMF simulation tool has been applied to determine coupling fields and to simulate the switching behavior of the magnets.

4 Metrology

There are several techniques available to characterize a magnetic specimen. Exploiting different (interaction) effects, information about the magnetization within and at the surface of a magnetic material can be gained. In the following, some of the various techniques are explained, which were utilized in this work to examine the magnetic features of magnetic films and nanoscaled magnets. Note, this chapter presents only measurement techniques. Detailed description on the settings of the applied measurement tools is given in the corresponding chapters, where the measurement results are presented.

4.1 Magneto-optical Kerr effect measurements

The following two measurement tools will be briefly discussed here, as their buildup has been intensive work of a diploma thesis [Bre09] and master thesis [Zie13]. For detailed information, the reader is referred to these two references.

Kerr microscopy is commonly used to study magnetic structure [68–71] exploiting the magneto-optical Kerr effect (MOKE). In this technique, plane-polarized light is used. Whenever, light hits the surface of the investigated magnetic material, the plane of polarization is rotated by the Kerr angle [72]. The sense of rotation hereby depends on the direction of magnetization. By passing the reflected beam through a polarizer, magnetic contrast is observed, so that domains get visible. It is also possible to record the switching behavior, meaning the hysteresis loop, of films and nanomagnets.
In our experiments, we use a home-made MOKE tool. Here, a pulsed, linearly polarized laser diode is used as light source. The laser beam is focused on the investigated specimen/magnet and experiences a change in the polarization in case of magnetization changes. The reflected beam is then analyzed by a polarizing beam-splitter and recorded by two photodiodes. Our MOKE system was extended by a closed-loop x-y stage with piezo actuators to enable accurate positioning of the laser beam on the magnets. The external magnetic field required to switch the magnetization is generated by an electromagnet, projecting a magnetic field vector perpendicular to the film-plane. The electro-magnet was integrated into the MOKE setup enabling characterization under influence of external magnetic fields.

MOKE microscopy enables fast contactless optical measurements without "destroying" or affecting the magnetic specimen. The resolution of the MOKE is limited by the wavelength of light. For our MOKE, it lies in the range of 635 nm. Detailed information on the x-y stage can be found in [Neu09].
A further analysis tool, which is also based on the magneto-optical Kerr effect and has been applied in this work, is the wide field magneto-optical Kerr effect microscope (W-MOKE). The above mentioned MOKE and the W-MOKE differ in the applied optical sensor system and the light source. The light source of the W-MOKE is a blue light emitting diode (LED) plus polarizer with a nominal wavelength of 470 nm. Thus, the W-MOKE has higher resolution. Furthermore, in comparison to the magneto-optical Kerr effect microscope (MOKE), where the sample surface is scanned point by point with the laser beam to establish an image, the W-MOKE possesses an imaging sensor. The sensor enables to observe the whole sample surface at once and is therefore suitable for pulse and probe experiments (investigation of domain wall motion in the presence of an external field). In order to magnetize or pulse the investigated magnetic specimen an external magnetic field source is required. There are three possibilities, in this case. First, an electromagnet, which is positioned right underneath the sample (similar to that one applied for the MOKE). Second, a micro-coil, also positioned right underneath the sample. Third, an on-chip coil, which is fabricated in an extra lithographic step directly on the sample surface. The three sources differ in the amplitude of the generated magnetic field and in the possible pulse length. The electromagnet handles the highest amplitudes with values of ± 150 mT. The micro-coil handles maximum values of ± 100 mT, whereas the on-chip coil handles ± 80 mT. With regard to the pulse length, the on-chip coil handles times in the range of [50 ns - 10 µs], the micro-coil [1 µs - 10 µs] and the electromagnet 100 ms. Depending on the requirements of the measurements it can be chosen between the three sources of magnetic field. For a detailed description of the W-MOKE and the sources of the external magnetic field, the reader is referred to [Zie13].

4.2 Magnetic force microscopy measurements

The magnetic force microscopy (MFM) is widely used for imaging magnetization patterns in a large number of technological and scientific applications: magnetic recording media [73–75], recording heads [76, 77], biomagnetics [78–80]. It is an extension of atomic force microscopy [81]. Here, the interaction between a ferromagnetic tip and the magnetic specimen is exploited to gain information about the magnetization. Therefore, the tip is mounted on a mechanical leaf spring, called cantilever and is immersed in the stray field of the magnetic specimen. Dipolar forces act on the tip and deflect the cantilever. The most common methods to detect the vertical cantilever deflections are based on optics [82–84]. But it can also

be done via a capacitance sensor [85]. Piezoelectric motors enable raster scanning of the surface with the tip.
To suppress the noise descending from the surface topography a so called 'interleave mode' can be used. Therefore a line scan in contact mode for surface topography information is interleaved with a scan, where the tip is lifted at a controlled hight (a few ten nanometers) above the surface of the investigated sample for long-range tip-sample interaction measurements. This technique enables to distinguish clearly between topography information and the magnetic signal. Furthermore the detection sensitivity can be increased by resonance detection techniques. Therefore, the tip is excited at the free-resonance frequency of the cantilever. Changes of the vibration amplitude, frequency, or phase are measured and information about tip-sample interaction is derived [86].
For the investigation of softmagnetic materials, tips coated with soft magnetic material are the most suitable ones. This ensures, that the magnetic moment of the tip does not change the magnetization state of the investigated specimen. Imaging can be done in ambient atmosphere, without any specific sample preparation. The achievable resolution of the MFM is much higher than that of the MOKE. In the best cases, resolutions down to 10 nm can be achieved [87].
The MFM tool has been extended by a 3D magnetic field module, developed in the work of Kiermaier [26, 88]. The module provides a magnetic field in all three spatial directions and can be integrated in the MFM tool. The integrated 3D magnetic field module enables the in-situ magnetization of the investigated specimen and therefore speeds up the analysis. Without the integrated field module, the sample would have to be magnetized in an external field and afterwards mounted in the magnetic force microscopy (MFM) again.

4.3 Scanning electron microscopy

In this work the scanning electron microscopy (SEM) is used to verify, if the lithographic mask has been transmitted correctly in the magnetic layers and to determine the distance between the magnets, as it is crucial for the coupling strength between the magnets. Therefore the sample is scanned by a beam of electrons of energies between 20 kV-30 kV. Information about the surface topography is achieved by the low-energy (secondary) electrons emitted from the surface. The secondary electrons have a broad energy distribution, where the maximum lies below 50 eV. Using a detector sensitive to these electron energies, spatial information is gained and is transformed to an image.
Note, there are several other processes that occur during scanning, e.g. the backscattering of high-energy (primary) electrons, which are sensitive to the atomic number. Therefrom information about the composition of the investigated specimen can be gained. However, this was not applied in this work.

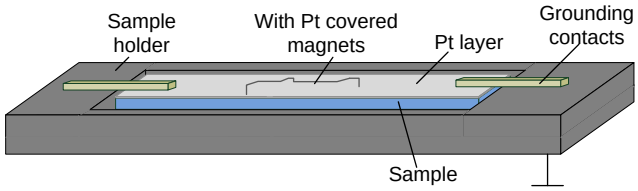

Figure 4.1: Sample holder applied for sample grounding in the SEM. The sample lies embedded in the sample holder and is pressed by the metal contacts into the ground of the sample holder. The magnets are covered with a Pt layer to establish a conducting connection between the magnets and the grounding contacts.

Imaging is always done under high-vacuum conditions. Difficulties arise, when the sample becomes charged. This problem can be avoided by careful grounding. As our magnetic islands lie isolated on the SiO_x grounding is impossible. To circumvent this problem, the whole surface of the investigated sample is sputter coated with a thin platinum (Pt) layer (2 nm) and grounded by metallic tips, which are contacted to the edge of the sample as shown in Fig. 4.1.

4.4 Focused ion beam

The FIB is an instrument, that can be used for different applications: for lithographic processes, where the FIB provides the exposure-source or for surface-analysis and -treatment or sputtering. The FIB operates similar to a SEM. Also here, a focused beam, but this time a beam of ions is used as the working tool. The surface of the investigated specimen can be scanned by the beam. The intensity of secondary electrons produced at each raster position is displayed to create an image of the sample.
The ion beam is produced using a reservoir of Ga, which is brought in contact with a sharp W needle. The Ga is liquid as it has a melting point near room temperature [89]. It wets the W-needle and flows to the tip of the needle. A high extraction field ($> 10^8$ V/cm) pulls the Ga into a sharp cone. From this cone, the ions are emitted as a result of field-ionization and post-ionization. As soon as the ions are emitted, they are accelerated down the FIB column (acceleration voltage lies in the range of 5 kV to 50kV) and hit the surface of the investigated specimen. Electrostatic lenses and effective aperture size can be appropriately adjusted, to achieve the required probe current density, which may be altered from tens of pA to several nA [90]. The beam is controlled by computer through a position generator interface. This allows to write any computer-defined patterns.
In this work, the FIB tool was applied for lithography, irradiation and milling

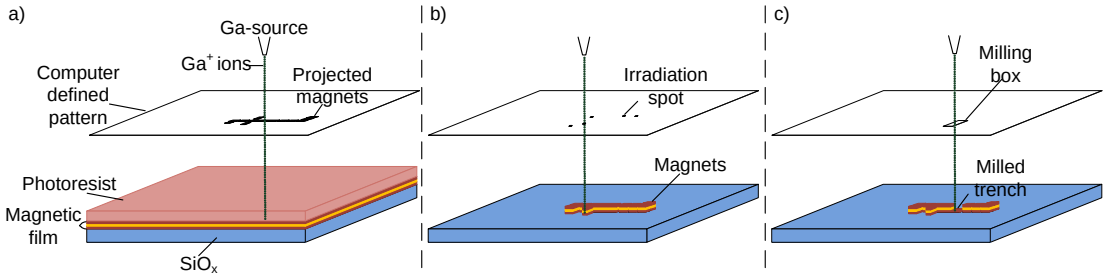

Figure 4.2: (a) FIB lithography: Exposure of the photoresist at the computer predefined areas. The magnetic film is protected by the photoresist.(b) FIB irradiation: Irradiation of the magnets in the computer predefined spots. (c) FIB Milling: Definition of the milling area for FIB milling.

(see Fig. 4.2). For FIB-lithography a computer-defined pattern is written on the sample, which is covered by a resist. The resist is then exposed by the ions in the predefined area.
The same is done during FIB irradiation. Here, also a computer-defined pattern is written on the sample, to define the spot of irradiation. The only difference is, that the sample is uncovered (no resist) and the ion dose per cm^2 is higher ($\approx$ factor 10) than for FIB lithography. Thereby it can be guaranteed, that the ions penetrate deep enough into the sample material and that the collisions of the ions with the sample material cause a damage to the crystalline structure and therefore weaken PMA. This is needed to achieve directed signal flow as will be explained in detail in chapter 6.

FIB milling for site-specific cross sectioning

If the ion beam is sufficiently energetic, the collisions of the ions with the surface under processing cause the ejection or sputtering of the atoms from the sample surface through a momentum transfer [91]. This process results in the removal or milling of the material. FIB milling occurs sequentially through each layer and after every scan of the sample surface, a thin layer is removed. The higher the current density, the more material is removed. Therefore continuous scanning enables the sequential removal of the surface material and the 'look-inside' the stack composition. In Fig. 4.3 a 3-dimensional NAND/NOR gate is shown, which was scanned seven times. The programmable input (I_3) lies in the topmost layer, while the other two inputs ($I_1$and I_2) and the output magnet (O) lie in the bottommost layer. It is obvious that with every scan a thin layer is removed and the magnets of the bottom layer get visible, while the magnet of the top layer is irretrievably milled away. FIB milling can also be applied for cross sectioning. Hereby, a rectangular trench is cut in the area of interest using a high Ga^+ beam current. After

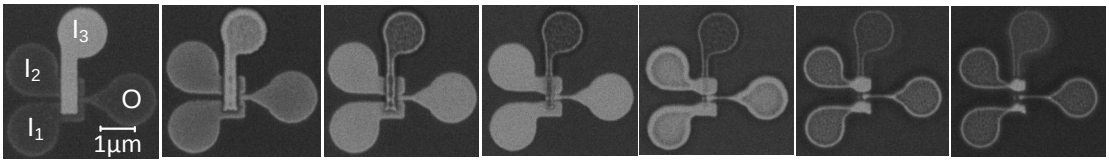

Figure 4.3: FIB surface scanning: after every scan, surface material is removed enabling the 'look-inside' the stack composition.

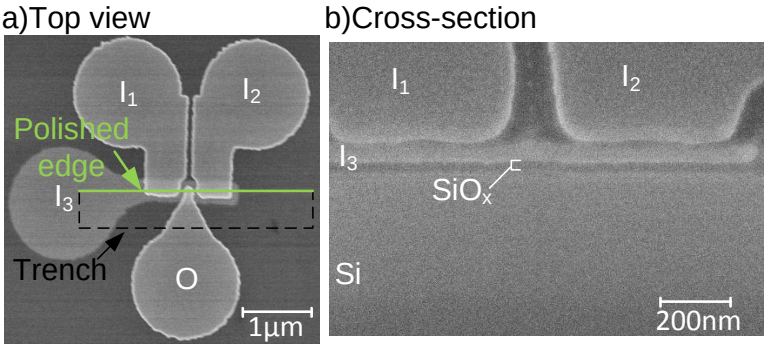

Figure 4.4: SEM images: (a) Top view. (b) Corresponding FIB milled cross-section. Image was taken with the SEM, by tilting the sample to 45°.

milling, the edge of the trench, where the cross-section should be investigated, is polished to achieve a smooth transition. The corresponding cross-section can be investigated in a conventional SEM by tilting the sample to 45°. In Fig. 4.4, a SEM image is shown of the 3D majority gate with top- and cross-sectional view. The milled trench is indicated by the dashed line and the polished edge by the green drawn through line. The cross-sectional view reveals the layer composition. Input I_3 lies on a SiO_x, whereas I_1 and I_2 are deposited in the layer above it. It is obvious that the layers are clearly separated. The great advantage of the FIB is, that it can be used to mill any computer defined pattern on the investigated specimen, directly without the need of resists or masks.
Nevertheless, for higher resolution images it must be switched to an alternative tool, the transmission electron microscopy (TEM). The TEM applies acceleration voltages up to a few 100kV, which results in the de Broglie wavelength of electrons in the range of a few pm. This enables a resolution below 1 nm. A further difference to a SEM tool, is that electrons must be transmitted through the specimen. Through the interaction of the transmitted electrons with the specimen, information for image generation is gained. Sample preparation for TEM analysis is costlier than for analysis with the scanning electron microscopy (SEM), as the sample must be thinned down a few 10 nm. For more details the reader is referred

to [26].
For this work, only a SEM tool was available, wherefore only the latter could be applied for cross section analysis.

4.5 Magnetoresistance measurement setup

The integration of pNML in CMOS-based circuitry can extend their functionality. Therefore integrated sensors are required, which translate the magnetic signal into an electrical one. So, a further part of this work is concerned with the electrical read-out of the magnetization state of the magnets. Commonly, sensors exploiting the magnetoresistive effect, like giant magnetoresistance (GMR) or magnetic tunnel junction (MTJ) are applied [92]. The commercialization of this technology is evidenced by product introductions in magnetic field sensors and read heads for hard drivers [93]. Such sensors consist of two magnets separated by a non-magnetic spacer layer. One magnet is the free magnet (FM) reacting on changes in the external field. The other magnet is the pinned magnet (PM) permanently retaining its magnetization, which serves as reference layer. Depending on their alignment to each other (parallel or antiparallel) the electrical resistivity of the sensor stack changes based on the magnetoresistive effect (see sec. 9). The change in resistivity provides information on the magnetization state of the FM and can be electrically detected.
In this work such sensors have been fabricated specified and designed for the electrical read-out ability of pNML magnets. The change in resistivity is measured with a Wheatstone-bridge circuitry, which will be discussed in detail in section 9. The bridge inclusive the measurement setup is shown in Fig. 4.5. The basic functioning of the bridge circuitry is that, whenever the resistance of the sensor changes from R_M (achieved for parallel alignment of FM to PM) to $(R_M + \Delta R)$(achieved for anti-parallel alignment of FM to PM), a diagonal voltage U_d, can be detected between the contacts a and b. Therefore, the investigated sensor must be built in the bridge circuitry as indicated in the figure. This could be done by evaporating Cu-contacts on the ends of the sensor. Afterwards the sample containing the test sensors is bonded on a chip carrier, where the signal contacts can be easily tapped and connected to the bridge circuitry. A sinusoidal voltage U_0 with a frequency of 1 kHz is converted to the AC-current I_0 by passing through a source resistance R_q. R_q is about a factor of 2000 times higher than the one of the magnetoresistance R_M and the remaining resistances of the bridge circuitry. This means, that in case of resistance change in the bridge circuitry, the change in the source resistance R_q is negligible small, so that a perfectly constant source current I_0 feeds the bridge circuitry. The amplitude of the applied current I_0 amounts to $5 \cdot 10^{-6}$ A. Applying this small current guarantees, that the sensors will not be destroyed during measurements.

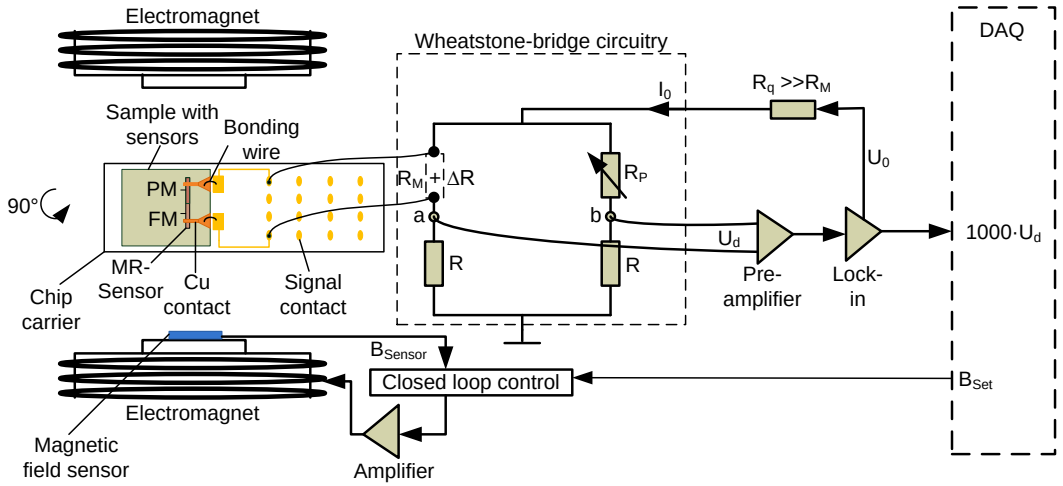

Figure 4.5: Magnetoresistance measurement setup.

The resulting voltage U_d is pre-amplified by a factor of 1000 and afterwards demodulated by the lock-in amplifier. The outcoming signal of the lock-in is recorded by the data acquisition (DAQ) hardware and processed by MATLAB. The applied pre-amplifier is based on the LT1167. It possesses a very good noise suppression and has been developed in a previous work by Kiermaier [26].
Of course, in order to detect any resistivity changes, the sensor must be exposed to an external magnetic field, where the different alignments of magnet FM to magnet PM could be enforced. The external field is generated by an electromagnet. The sample containing the sensors is placed in the air gap between the poles of the electromagnet, perpendicular to the generated external field. The applied magnetic field is measured with a magnetic field sensor and controlled in a closed loop. The required amplitude of the magnetic field is set in MATLAB and sent to the DAQ box. The output signal of the DAQ box passes the closed loop control and is amplified before it reaches the coils of the electromagnet.
The electromagnet generates a magnetic field with a maximum of $\pm 350\,\mathrm{mT}$ perpendicular to the sample plane.

5 Fabrication of 3D devices in pNML

In general, two ways for the fabrication of 3D devices and circuits exist: a 'bottom-up' or a 'top-down' approach. In a bottom-up approach, the devices are processed sequentially in each layer, starting with the bottom layer. Afterwards, the bottom layer is planarized and a second device layer is processed. This sequence is repeated until the number of desired layers is reached. The bottom-up approach enables the monolithic fabrication of 3D devices and circuits. In comparison in a top-down approach, there are multiple completed 2D devices/circuits fabricated by conventional processes on multiple substrates, which are then assembled to a 3D circuit.
For the top-down approach there is a main obstacle hindering its application for the 3D fabrication of pNML devices. The distance between the magnets of two overlying layers has to be $< 100\,\text{nm}$ to get a reliable signal transmission between the layers via field-coupling. As the stray field of a magnet declines with $1/r^n$ (r is the distance from the magnet's edge and n a form factor including the shape influence of the magnet [BBE+15]), the distance between two layers has to be kept small. From this context it is obvious, that the substrate, on which the magnets are situated has to be thinned down to a thickness below 100 nm to enable strong coupling between magnets of different layers. However, substrates of these thicknesses are very instable and cannot be easily assembled with other substrates. Furthermore, there are no known techniques, which would enable substrate-thinning down to this required thickness. Hence, the top-down approach is not suitable.
In the bottom-up approach this problem does not exist, as the bottom level magnets are planarized and the magnets of the subsequent layer are directly fabricated on the planarization substrate. Therefore this approach has been applied in this work.
In the following sections, the fabrication steps for a monolithic 3D integration of pNML devices/circuits are presented. Furthermore, critical fabrication steps are discussed in detail.

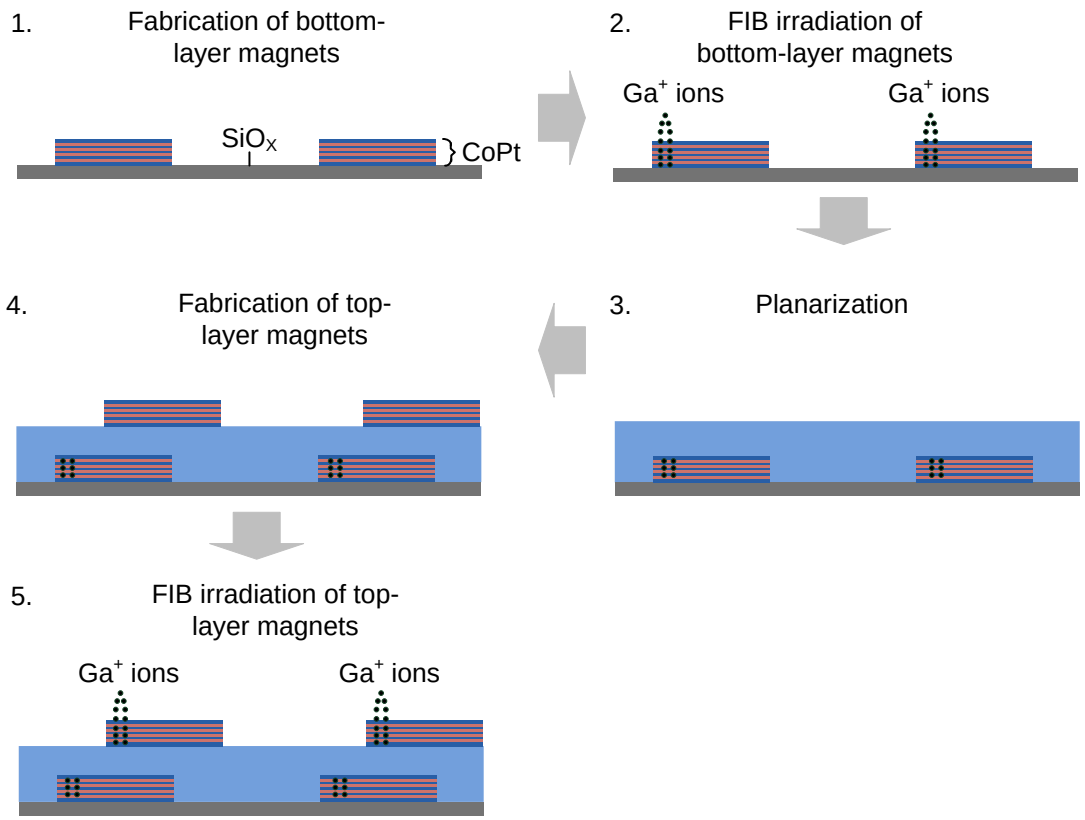

Figure 5.1: Main steps of the 3D fabrication process [EBvGZ+15].

5.1 Fabrication

The general fabrication process of 3D devices consists of five main steps, as depicted in Fig. 5.1 [EBvGZ+15]. In the first step, the magnets of the bottom layer are fabricated. In a second step the bottom-layer magnets are irradiated by the FIB in a predefined area to achieve directed signal flow in the magnets (as described in sec. 2.1.3). After irradiation, the bottom-layer magnets are planarized by a spin dielectric. In a forth step, the top-layer magnets are fabricated. In a last step the top layer magnets are irradiated by the FIB, also to guarantee directed signal flow in the second layer. Every fabrication step mentioned so far consists of several fabrication substeps, which are discussed in detail in the following subsections.

5.1.1 Fabrication of the bottom-layer magnets

Before starting with wafer cleaning and oxidation, the wafer must be sawed into small substrates of size $1\,\mathrm{x}\,1\,\mathrm{cm}^2$, as all measurement setups are designed for this

sample size. A photoresist serves as protection layer during the sawing and is afterwards removed with hot acetone (75° C). The residues of acetone again are removed by holding the sawed substrates into isopropanol, followed by a rinse in deionised (DI) water for three minutes.

Wafer cleaning and oxidation

The bottom-layer magnets are fabricated on a SiO_x-wafer, which must be prepared in the well-known Radio Corporation of America (RCA) cleaning and oxidation process, explained in the following.

To remove particles and organic molecules from the wafer, it is held in a RCA 1 solution for fifteen minutes. The RCA 1 solution is a mixture of ammonium hydroxide (NH_4OH), hydrogen peroxide (H_2O_2) and DI water. For a better efficacy of the RCA 1 clean, the solution is put in an ultrasonic bath. The H_2O_2 oxidizes the substrate's surface and the particles on it, leading to a weakening of the adhesion forces between the substrate and particles. The NH_4OH etches the substrate's surface and therefore undercuts the particles. The hydroxide-ions cause a negative charging of the substrate's surface and the particles and lead to a repulsion between the substrate and particles.

The occurred oxidation (plus already occured oxidation during stocking) by H_2O_2 is afterwards removed by a hydrofluoric acid (HF) dip.

In a second RCA clean, the substrate is delivered of all non-organic and metallic particles and molecules. The RCA 2 clean is a mixture of hydrochloric acid (HCl) and H_2O_2. With the HCl, the metals are transformed into their soluble metalchloride compounds. The H_2O_2 again oxidizes the substrate's surface and the particles.

After the cleaning process, the substrate is oxidized. Therefore the substrate is heated up to 1000° C in an oxidation oven. As soon as the temperature is reached, oxygen gas is passed into the oven and the Si is oxidized, forming an insulating layer of very good quality between the Si-substrate and the magnets.

Multilayer sputtering

The fabrication of the nanomagnets on the SiO_x-wafer is achieved by sputtering a Co/Pt multilayer on the substrate and afterwards patterning the multilayer in a special lithography process, followed by physical ion etching.

Sputtering is a deposition technique, where high energy ions (here argon (Ar) ions) are accelerated in an electric field towards a target material. The collision causes small particles of the target material to be ejected, which then condense onto the substrate forming a thin layer. If more than one target is used a multilayer can be sputtered. Indeed, for the sputtering of the Co/Pt multilayer applied in this work, three target materials were used. First, a thin titan (Ti) or tantalum (Ta) layer (usually 2 nm) is sputtered on the prepared substrate. It serves as an adhesion promoter for the following Co/Pt stack. The Co/Pt stack itself arises by the al-

ternating sputtering of Co- and Pt-layers, whereas it is always started and ended with a Pt-layer. The Pt-seedlayer has usually a thickness of 5 nm. The seedlayer has a sharp (111) texture providing strong PMA in the Co. The topmost Pt-layer serves as protection layer for the Co against oxidation. Perpendicular anisotropy is only achieved by the alteration of the layers, leading to a high magnetocrystalline and interface anisotropy governing over the shape anisotropy (for detail see sec. 3). It is important to know that a maximum Co-layer thickness of 0.8 nm is permitted and a minimum Pt-layer thickness of 1 nm is required. If these borders are exceeded, the shape anisotropy is predominant and the magnetization flips into the plane. Of course, the number of alterations is restricted. It has been manifested, that a maximum amount of Co is restricted to a total Co-thickness of 3.2 nm in the whole multilayer stack. So the total amount of Co governs the number of multilayer. A higher total Co-thickness than 3.2 nm leads to a higher surface roughness and a higher demagnetization energy and therefore lowers or even eliminates PMA.
The partial sputtering pressure for Pt can be varied between 2 µbar and 11 µbar and for Co between 5 µbar and 13 µbar. But note, the chosen partial sputtering pressure influences the crystallography of the films and thereby PMA. The applied pressures in this work, will be mentioned in the individual sections of the fabricated devices.
After film deposition, the multilayer is structured to achieve the desired magnetic islands. A lithography process combined with etching enables to define the desired pattern and to remove unwanted regions.

Particle beam lithography for hard mask pattern definition
Particle beam lithography is the central process enabling the fabrication of nanostructures. Thereby the particle beam can either be an electron- or an ion beam. Both, focused ion beam- and electron beam lithography are established techniques in todays nanofabrication [94–97]. Here, the beam is used to expose a sensitive resist. Both techniques have pros and cons and can only be fairly evaluated in terms of their application. On the one hand, the very small wavelength of electrons enables very small line-widths. On the other hand, due to the low mass of electrons, they scatter easily in the resist and therefore activate adjacent areas of the resist (Proximity-effect). This effect limits the minimum reachable line-width and leads to a higher edge roughness. Applying ions instead of electrons the effect can be mitigated. Due to a higher mass of the ions in comparison to electrons, the scattering is less than for electrons, leading to sharper edges and therefore a higher resolution.
In this work FIB lithography has been applied. Therefore, the magnetic film is first spin-coated with a photoresist, called polymethylmethacrilate (PMMA). PMMA is a high resolution positive resist, often used in particle beam lithography. The rotation velocity of the spin-coater is chosen to be 3000 *rpm* (revolutions per

minute), resulting in a resist thickness of 40 nm. Resist thicknesses below 40 nm may result in a damage of the beneath lying multilayer film. Therefore this minimum resist thickness is required. After the resist has been spun on for 30 seconds, the coated sample is baked out for 90 seconds on a hotplate at 100° C. The soft bake is necessary to remove the resist's solvent and promote adhesion.
Afterwards, the sample is mounted into the FIB on a special sample holder. The resist is exposed by gallium $(Ga)^+$ ions, applying a predefined computer pattern mask. The applied ion dose varies in the range of $[2.5 \cdot 10^{12}\text{-}3.75 \cdot 10^{12}]\text{ions/cm}^2$. The acceleration voltage is chosen to be 50 kV. As the PMMA is a positive resist, it is exposed in those areas, where afterwards the hard mask should protect the beneath lying multilayer.
After exposure, the resist is developed in a special developer called AR600-55 for fifteen seconds. The development process has to be inactivated afterwards by rinsing the sample in the a special resist stopper called AR600-60 for thirty seconds. The development process peels off the resist in the exposed regions. Evaporating a hard mask material on the sample in the next step, the uncovered parts of the film can be made imperishable for the following etching process.

Hard mask e-beam evaporation and lift-off
The hard mask evaporation is done via electron beam physical vapor deposition. Hereby, the hard mask material is heated up by a focused electron beam. The incipient thermal evaporation leads the outgoing atoms to condense on the magnetic film, and therefore to a deposition of the hard mask material on the sample. In this work, Ti serves as hard mask material. A minimum thickness of 3 nm of Ti ensures the protection of the beneath lying layers during consecutive etching. After deposition, the remained resist is lifted off by holding the sample in N-Methyl-2-pyrrolidon (NMP) and an ultrasonic bath for 15 minutes. By removing the resist, the removal of the above lying Ti layer is involved. Only the FIB defined regions remain covered by the Ti hard mask.

Physical etching with ions
Now, the Co/Pt multilayer can be structured by transferring the pattern of the hard mask into the multilayer stack by etching. Basically, there exist two ways of etching: wet- and dry etching. In the wet etching process, the material is dissolved by chemical or electrochemical processes. This process is intrinsically isotropic and causes sloped pattern edges. However, anisotropic etching may be achieved in oriented crystalline materials [98]. In comparison, a dry etching process can produce straight and sharp pattern edges, thus a better resolution. In this work a dry etching, physical process, such as ion beam etching has been applied. Hereby, Ar^+ ions, which are accelerated in an electric field, bombard the sample surface and cause the unwanted material (not protected by hard mask) to be removed. The fabrication of the bottom-layer magnets is hereby completed.

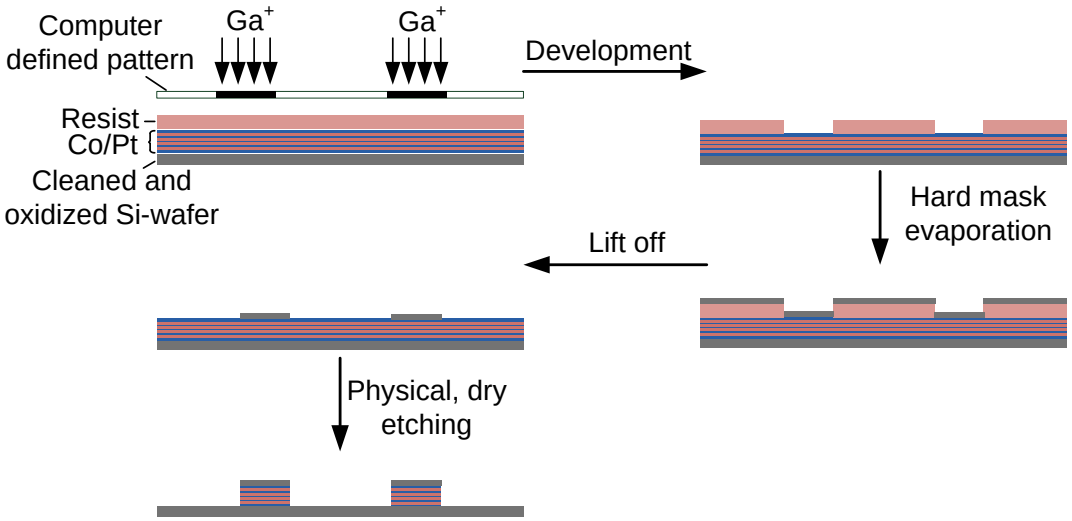

Figure 5.2: Fabrication process of the bottom-layer magnets.

The whole fabrication process of the bottom-layer magnets is summarized in Fig. 5.2.

5.1.2 Irradiation of the bottom-layer magnets

The irradiation of the magnets is an essential fabrication step to achieve directed signal flow in the magnets. The irradiation destroys the crystalline structure, leading to a lowered anisotropy in the irradiated spot [99]. In [100] reasons are discussed in detail for the anisotropy decrease. It is stated that through the ion bombardment, Co and Pt atoms are displaced, intermix together resulting in an asymmetric interfacial roughening and therefore leading to an anisotropy decrease.
Due to the lowered anisotropy, a domain wall can be easier nucleated in this irradiated spot than in the rest of the magnet. The domain wall nucleation process initiates the reversal process of the magnet. The reversal starts in the irradiated spot and by the propagation of the domain wall through the magnet, it is entirely reversed.
The generation of the irradiation spots is again done with the FIB. Therefore the irradiation pattern is locked in on specified orientation marks on the chip. The magnets cannot be located directly by scanning the sample surface, as every scan is associated with ion irradiation. By locking in on the orientation marks (these ones have been made visible by scanning before), the magnets can be located blindly as the location of the magnets starting from the orientation marks is known. In

many experiments, performed by our group, it has been manifested that ion doses in the range of $[5 \cdot 10^{12}\text{-}5 \cdot 10^{14}]$ions/cm^2 and irradiation spot sizes of $40\,\text{x}\,40\,\text{nm}^2$ up to $80\,\text{x}\,80\,\text{nm}^2$ [101] are sufficient to create a sensitive spot in the magnet, that evokes directed signal flow. Also here the same acceleration voltage of 50 kV as for FIB lithography is applied.

5.1.3 Planarization of the bottom-layer magnets

In order to place a second layer of magnets, the bottom-layer magnets have to be planarized. Therefore hydrogen silsesquioxane (HSQ), a spin-on dielectric is applied. HSQ is also applied in advanced technologies as intermetallic dielectrics [102]. As it has a low dielectric constant, it is very attractive to reduce RC delays. HSQ is known to have good planarization properties and as it is liquid at room temperature, it can be easily spun on the sample without the need of oxide precipitation. For the experiments applied in this work, it has a further important benefit. Due to its transparency, it is very suitable for MOKE microscopy analysis.
The HSQ is spin-coated like a normal resist on the sample surface. The rotation velocity is chosen to be 3000 *rpm*, resulting in a layer thickness of $\approx$60 nm. The liquid HSQ is spun-on for 30 seconds. Afterwards the sample is baked on a hot plate at 100° C for 5 minutes to remove the solvents. A further bake at 225° C for 5 minutes is required to harden the HSQ. Alternatively a O_2-, N_2-, or H_2- plasma treatment can be applied to harden the HSQ [103]. However, in experiments, where a O_2-plasma has been applied, negative effect on PMA could be detected. Therefore the bake on the hotplate was applied.
For the coating process it must be considered that the coating material thickness must exceed the height of the device features to ensure complete planarization (here $\approx$20 nm). This is the lower bound for the HSQ layer thickness. The upper bound for the HSQ layer thickness, is the required minimum strength of the coupling field from a bottom to top magnet and vice versa. As the coupling field decreases with increasing distance, an inter-layer thickness above 100 nm is not suitable for NML applications. The thickness of the HSQ layer can be adopted by different parameters, e.g. spin speed or different ratios of the HSQ diluent, called methylisobutylketon (MIBK). The higher the velocity or the diluent ratio, the thinner is the resulting HSQ layer. To investigate the planarization capability of HSQ two profiles were extracted of topography images of an unplanarized magnet shown in Fig. 5.3 a and a magnet planarized by HSQ shown in Fig. 5.3 b. In (a) a bottom-layer magnet is shown. The profile plotted along the yellow line indicates a total hight of the magnet of $\approx$35 nm. It is higher than the expected 20 nm (when only counting the film composition of the magnet), because the ion beam etching process also etches some parts of the SiO_2 substrate, the bottom magnet is situated on. The profile given in (b) is plotted along a magnet of the top layer, also

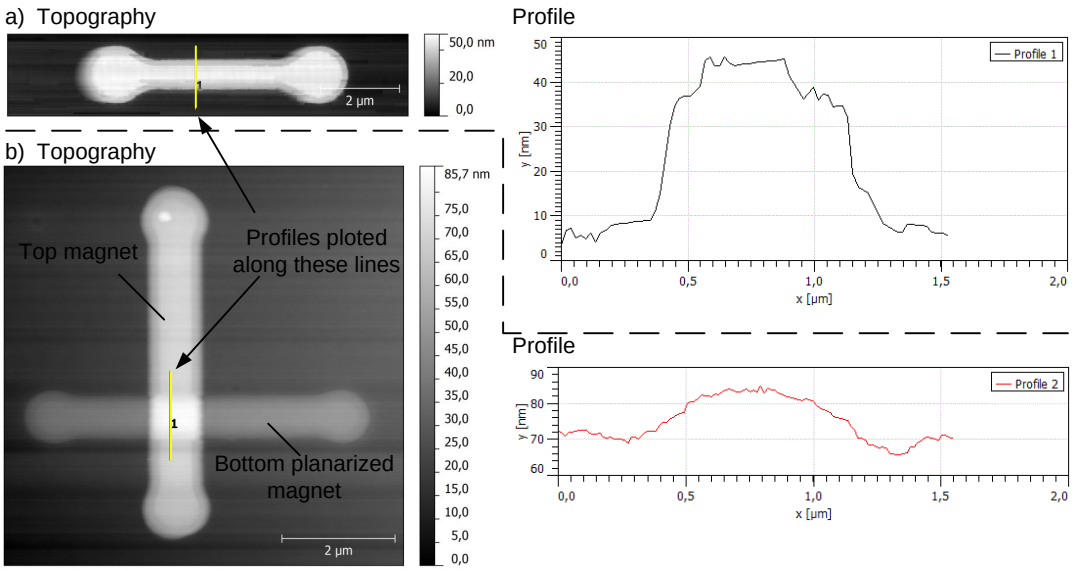

Figure 5.3: Topography and profile images of (a) unplanarized magnet and (b) planarized magnet by HSQ. The profiles are measured and plotted along the yellow indicated lines.

indicated by the yellow line. The top-layer magnet including the HSQ beneath it, covers the bottom magnet, whose profile has been given in (a). It is justified, to investigate the profile along the top magnet and not besides, because parts of the HSQ layer, that covers the bottom magnet are etched away during the etching process required to pattern the top magnetic layer. Thereby the measurement results can be distorted. From the profile given in (b), it can be clearly seen, that the height of the bottom magnet has been reduced from the 35 nm before to $\approx$ 15 nm. Furthermore, it is obvious, that the gradient of the profile in (b) is much smaller than the one of (a). The rise in (b) is very smooth with $\approx 3°$ compared to the one in (a) which is almost perpendicular. These measurements reveal the good planarization capability of HSQ.
In [102], it is stated, that the device density has also a great impact on the planarization capability. With higher densities, the planarization improves drastically. Note, the combination of HSQ planarization with polishing, e.g by chemical mechanical polishing (CMP), may lead to the best planarization results but difficult to accomplish on cut wafer samples.

5.1.4 Fabrication of subsequent layer magnets

After the planarization, the top layer magnets are fabricated in the same way as the bottom layer magnets. First, sputtering, second FIB lithography, followed

by hard mask evaporation and lift off, and ending with physical etching. After structuring, the magnets are again irradiated with the FIB.

5.2 Critical parameters and challenges

The monolithic 3D fabrication process has challenges in terms of alignment of top to bottom layer, thermal processing and FIB penetration depth during irradiation [EBvGZ+15]. The greatest challenge hereby is to preserve the bottom magnets performance during the fabrication of the top magnets. In the following subparagraphs these challenges are discussed in detail.

5.2.1 FIB irradiation of top layer magnets

During the irradiation of the top layer magnets, the ion penetration depth is the crucial factor that can destroy or create undesired domain wall nucleation centers in the bottom layer magnets. Consequently, in vertically coupled magnets, signal directionality is lost. Hence, it is important to preserve the bottom layer magnets performance during top magnet irradiation. It is mandatory to control of the ion penetration depth. There are several parameters, that have impact on the penetration depth:

- acceleration voltage of the ions,
- HSQ-interlayer thickness,
- layer thickness of the hard mask,
- ion dose.

These parameters were investigated with the aid of a specified simulation tool, named SRIM [104], 'The Stopping and Range of Ions in Matter'. SRIM enables quick calculations on stopping powers, range and straggling distributions for any ion type at any energy in any elemental target. The stopping calculations are based in great part on theory, as experimental measurements of stopping powers is a difficult task. The applied models go back to 400 years knowledge [104]. In first approximation, the tool gives a good estimation of the trajectories, coils and recoils of ions in matter.
In the following performed simulations, the investigated layer stack is composed of the two magnets, each covered by a hard mask and the HSQ-interlayer, separating the top and bottom magnet: **(hard mask/top magnet/HSQ-interlayer/hard mask/bottom magnet)**. The layer composition of the magnet itself remains always the same (for top and bottom magnet), namely:
$[Pt_{3nm}/Co_{0.6nm}3x(Pt_{1nm}/Co_{0.6nm})/Pt_{3nm}/Ta_{2nm}]$
whereas the hard mask layer and HSQ-interlayer thicknesses may vary, depending on the investigated parameter. The simulations are performed with Ga^+ ions. The ions are always injected at one point of the stack surface.

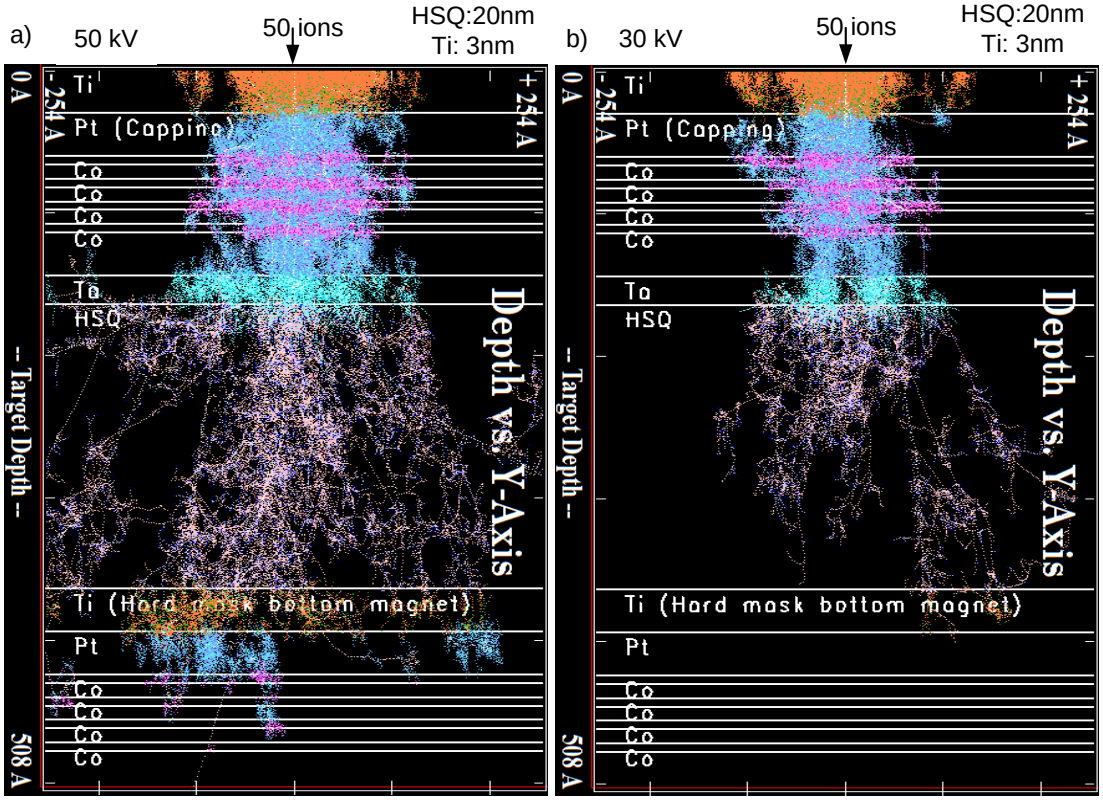

Figure 5.4: Influence of acceleration voltage for identical stack compositions: (a) Penetration depth at 50 kV. (b) Penetration depth at 30 kV .

Influence of acceleration voltage

In a first simulation, the impact of two different acceleration voltages is investigated, namely 50 kV and 30 kV. The hard mask is a 3 nm Ti layer. The HSQ-interlayer has a thickness of 20 nm. The ion injection dose amounts to 50 ions per scanning point of the FIB. The results containing the trajectories, coils and recoils are shown in Fig. 5.4. It can be easily seen, that for an acceleration voltage of 50 kV, the ions even penetrate into the bottom magnet, while for 30 kV the ions are already stopped in the hard mask layer of the bottom magnet. Considering the 50 kV, the damage of the bottom magnet is less than the one of the top magnet. However it must be considered, that the simulation is done only for one scanning point of the FIB. Indeed, the real irradiation spot itself consists of several scanning points. This means, that the destruction might be indeed stronger.
Nevertheless, in this work, an acceleration voltage of 50 kV has been applied, as the utilized FIB tool is better calibrated for this voltage. Therefore, other parameters have been optimized to still enable FIB irradiation of the top-layer magnets.

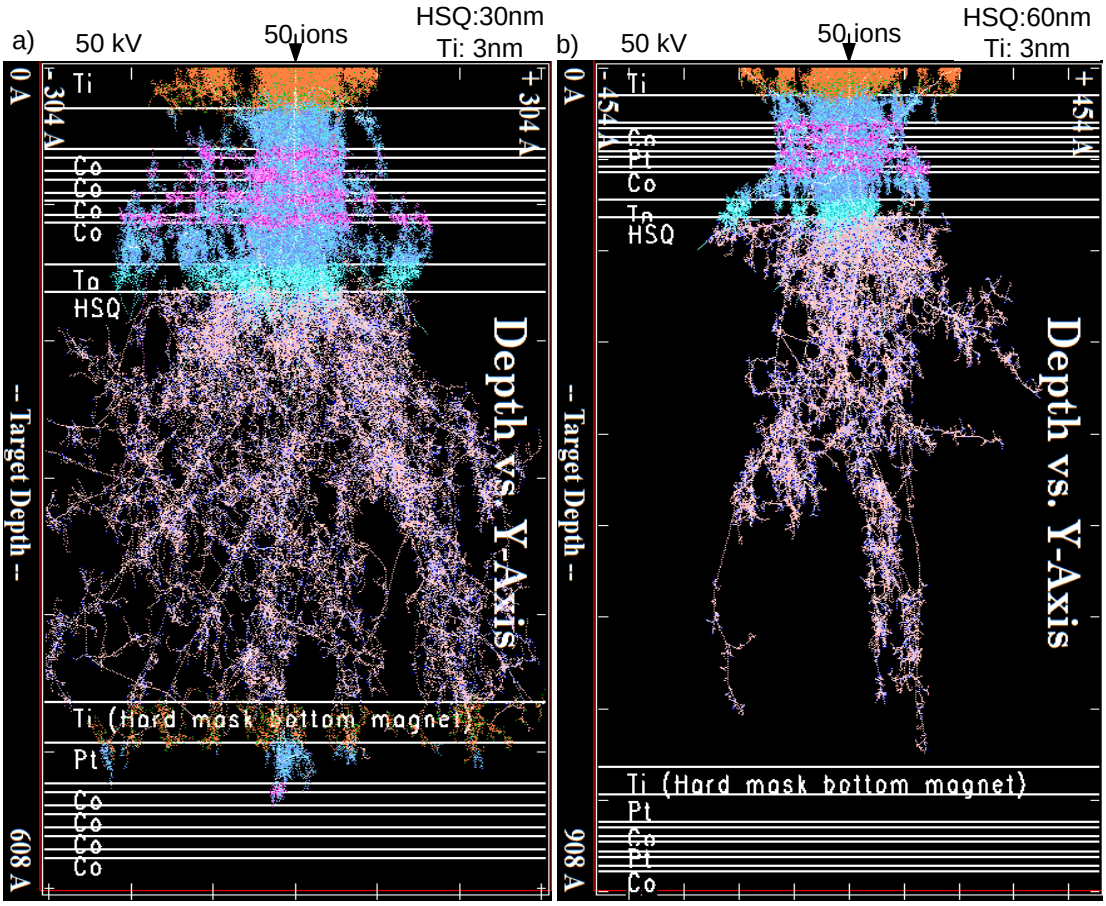

Figure 5.5: Influence of interlayer thickness (despite the interlayer thickness, the stack compositions are identical): (a) Penetration for 30 nm HSQ-interlayer thickness. (b) Penetration for 60 nm HSQ-interlayer thickness.

All further simulations have been done at 50 kV.

Influence of HSQ-interlayer thickness

To evaluate the influence of the interlayer thickness, two identical stack compositions, up to the interlayer thickness (30 nm vs. 60 nm) are considered. A Ti hard mask layer thickness of 3 nm and an acceleration voltage of 50 kV are applied. The simulation results are depicted in Fig. 5.5. An interlayer thickness of 30 nm is not sufficient to protect the bottom layer magnets (see 5.5 (a)). The ions already penetrate into the first magnetic multilayer. Simulations have also been evaluated for interlayer thicknesses of 40 nm and 50 nm. However, it turns out, that only a minimum interlayer thickness of 60 nm provides full protection of the underlying magnets as can be clearly seen in (b).

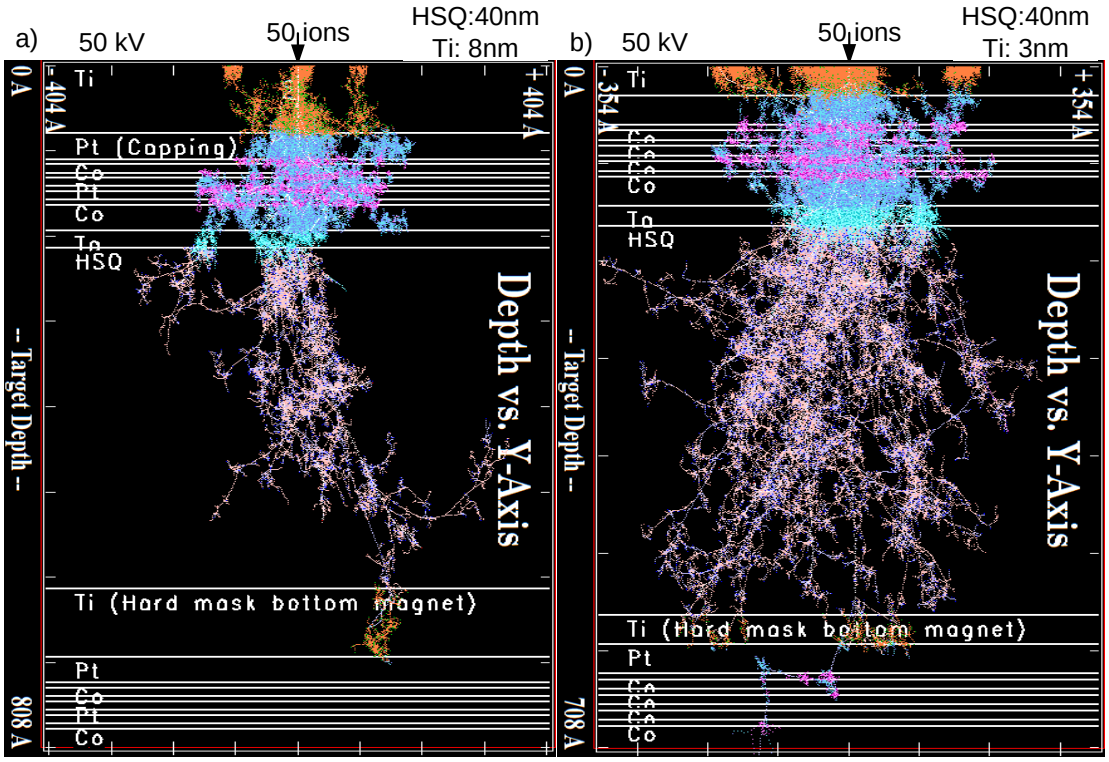

Figure 5.6: Influence of hard mask layer thickness (despite the hard mask layer thickness, the stack compositions are identical): (a) Penetration for 8 nm hard mask layer thickness. (b) Penetration for 3 nm hard mask layer thickness.

Influence of hard mask layer thickness

The influence of the hard mask layer thickness is considered for different thicknesses between 3 nm and 8 nm, at an interval of 1 nm. Hereby the Ti hard mask layer thicknesses of the top and bottom magnet are similarly changed. The rest of the stack composition is kept equal for all simulations. The acceleration voltage is again 50 kV. The HSQ-interlayer is chosen to be 40 nm, as for this thickness, the influence of the hard mask layer can be investigated best. At 30 nm, 50 nm and 60 nm, the influence of the HSQ-interlayer thicknesses is too strong, to observe any changes evoked by the hard mask layer thickness. At 40 nm HSQ-interlayer thickness, the penetration depth of the ions can be significantly influenced by the hard mask layer thickness. The results for 3 nm and 8 nm hard mask layer thicknesses are shown in Fig. 5.6. From the simulation results, it can be easily extracted, that a hard mask layer of 3 nm is not sufficient. A certain amount of ions still penetrate into the bottom magnet and even goes through the whole magnet. At 8 nm layer

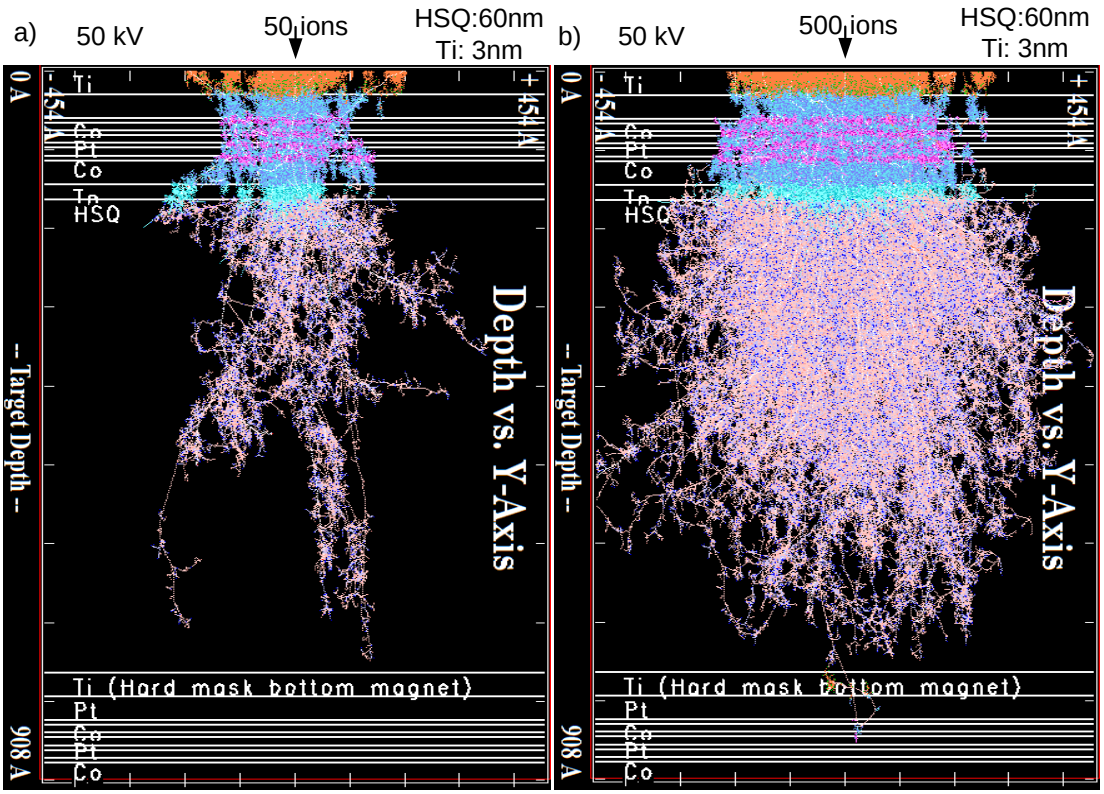

Figure 5.7: Influence of ion dose: (a) Penetration for 50 ions per FIB scattering point. (b) Penetration for 500 ions per FIB scattering point.

thickness, the ions only reach the Pt capping layer of the bottom magnet and do not affect the magnetic stack. Furthermore it can be observed, that the scattering radius of the ions is much smaller than the one for the 3 nm Ti layer. The most ions are intercepted in the top magnet.

Influence of ion dose

To investigate the influence of the ion dose, different numbers of ions, 50 vs. 500 ions per scattering point are applied. The stack compositions are identical for both experiments. A Ti hard mask of 3 nm layer thickness and a HSQ-interlayer thickness of 60 nm is chosen. Again for these parameters, the impact of the ion dose can be investigated the best. An ion number of 50 ions per scattering point corresponds to an ion dose of $5 \cdot 10^{13}$ ions/cm^2 and an ion number of 500 ions corresponds to an ion dose of $5 \cdot 10^{14}$ ions/cm^2. The results are shown in Fig. 5.7. For 500 ions per scattering point, a small number of ions reaches the bottom magnet, whereas for 50 ions per scattering point all ions stop in the HSQ-interlayer. Furthermore it can be observed, that for a high ion dose, the scattering radius is much larger than for the low dose.

Summary
All simulation results reveal the impact of the four above mentioned parameters. Acceleration voltage and HSQ-interlayer thickness seem to have the most impact on the penetration depth. Furthermore it is obvious, that the top magnet is more influenced by the ions than the bottom layer magnet. The amount of ions stopped in the top magnet is much larger than the one in the bottom magnets. Of course, from simulation it is hard to quantify, whether the consequences in the bottom layer magnet are the same as in the top layer magnet (generation of a domain wall nucleation region) but qualitatively, the impact on the bottom layer magnet is much less. But note, the simulations are performed for one scattering point of the FIB. In real, the irradiation area is defined by several scattering points of the FIB, which may cause a stronger impact of the ions in the bottom layer magnets. Furthermore, in experiments performed with a 3 nm Ti hard mask, a HSQ-interlayer thickness below 50 nm and ion doses above 500 ions per scattering point, a malfunction of the bottom layer magnets was detected. A HSQ-interlayer thickness of 60 nm combined with a Ti hard mask layer thickness of 8 nm and an ion dose of 50 ions per scattering point always resulted in the correct function.

5.2.2 Alignment of top to bottom layer

The precise alignment of the top magnets to the bottom layer magnets has a great impact on the correct device functioning. As NML technology bases on signal processing by field-coupling, variations of the vertical and horizontal distances can lead to an asymmetrical coupling or rather insufficient coupling between the magnets. So the wrong positioning of the top to bottom magnets may lead to fatal errors in magnetic signal processing. In the following the alignment process is explained.
To position the FIB on a certain point on the sample, first a point of origin is defined (normally one corner of the sample). Starting from this point of origin, the x-axis of the FIB is aligned along one edge of the sample. These two steps are essential to define the coordinate system on the sample. This coordinate system constitutes the basis, from which all further placements of the magnets take place. If more than one magnetic device layer is fabricated, the coordinate system must be anew located for every new lithography process. As the location of the coordinate system is done by eye inspection, a mismatch between the preceding layer and the succeeding layer is very probable. A mismatch in the location of the points of origin or an angle dependent mismatch between the layers can be the consequence. A direct alignment on the magnets themselves is not possible. For a direct alignment, the sample surface must be scanned. This would involve an ion bombardment and thereby the destruction of the magnets.
A possible and more precise solution is to introduce alignment marks on every

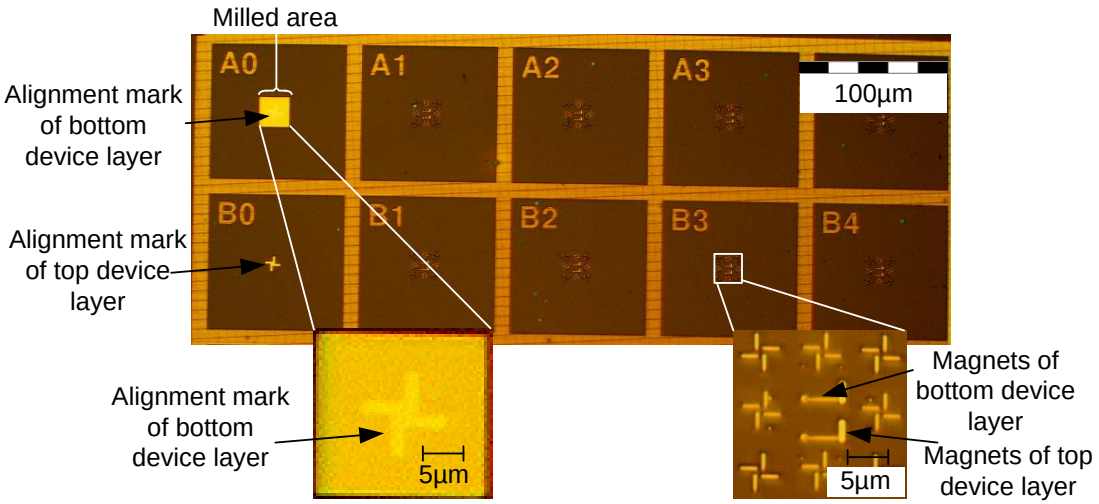

Figure 5.8: Optical microscopy image, including alignment marks and two device layers.

layer, that is fabricated. In Fig. 5.8, the introduced alignment marks are shown. The field columns with index '0', e.g. 'A0', 'B0', are used to write alignment marks during FIB lithography of each device layer. In 'A0' the alignment mark of the first device layer is located, whereas in 'B0' the alignment mark of the second device layer is located. In the remaining fields 'A1, A2,..B1, B2' the magnets are located. To align the top device layer on the bottom device layer, the alignment mark in 'A0' is used. Of course, when the top device layer is fabricated, the alignment mark of the bottom device layer is covered by the planarization substrate, the magnetic multilayer and the resist. Therefore the alignment mark of the bottom layer is not visible and must be initially milled free. Then the FIB coordinates can be locked in. The more alignment marks are applied and locked in, the smaller is the misalignment error, as it is averaged over a greater amount of locking points. Nevertheless, a total correction of the misalignment is not possible. In the vertical and horizontal direction, there may still remain a misalignment of up to 200 nm maximum. In the best cases a misalignment below 50 nm was observed.

5.2.3 Thermal treatment

A further important process parameter, that may have a negative effect on the magnets performance, is longterm thermal treatment. In magnetic multilayer films and nanoparticles, it is often observed, that annealing changes H_C, M_S and M_R [105–109]. Hereby, the impact strongly depends on the annealing temperature and time. In [107], the influence of air and vacuum annealing on Co/Pt multilayer films for different temperatures $[100° - 500°]$C was investigated. An increase in

H_C and M_R and a decrease in M_S could be detected for air annealing. As a possible reason, the oxidation of Co is noted. Thereby, the oxidation of Co proceeds through the column boundaries of the film, forming Co oxides. The oxidized parts in the film increase and a diffusion of atoms proceeds. These oxidized parts act as a domain wall binder. In [108], the domain structures in Co films grown on Au under the influence of annealing were studied. As a result it is stated, that the heat treatment causes the morphology and the magnetic microstructure to change drastically.
As in pNML 3D fabrication, 225° C for the hardening of **each** HSQ-planarization layer are required, the investigation of the impact of longterm heat treatment on the fabricated 3D structures is important. Imagine, the fabrication of several device layers above each other involves a longterm heat treatment of the magnets in order to harden each HSQ planarization layer.
In the applied experiment, a two device layer stack, with bottom and top magnets both equally fabricated and situated on a HSQ-layer (whereas the bottom layer was planarized by HSQ) is annealed at 225° C for overall 3 hours under air atmosphere on a hotplate. In between this time period, the annealing process is several times interrupted (first 15min interval, then 30min, at last 1h) and hysteresis curves measured with the MOKE. The results are shown in Fig. 5.9.
Considering the hysteresis curves of the top magnet, it can be detected, that the value of $\mu_0 H_C$ obviously decreases after the first 15min of annealing. Afterwards, $\mu_0 H_C$ slightly increases again (see additionally Fig. 5.10). Nevertheless, during the whole process of annealing, the hysteresis curve retains its rectangular shape, indicating instantaneously switching of the magnets. The drop in the value of $\mu_0 H_C$ after the first 15min may be traced back to an entrance of the oxygen atoms to the interior of the magnet and thereby creating a new domain wall nucleation spot.
In contrast, the bottom magnets' behavior is different. The value of $\mu_0 H_C$ increases (see Fig. 5.10). Furthermore, the shape of the hysteresis changes from rectangular to a slope, indicating domain wall pinning. The bottom magnet is completely encapsulated in HSQ, so no oxygen atoms can enter the bottom magnet. Nevertheless, the encapsulating HSQ may change its crystallography thereby affecting the magnet's edges, which may act as a domain wall pinning center. Note, this is only an assumption as investigation is hard.
To sum up, the consequences of longterm air annealing on the top and bottom magnet are different. The most important conclusion however is, that temperature

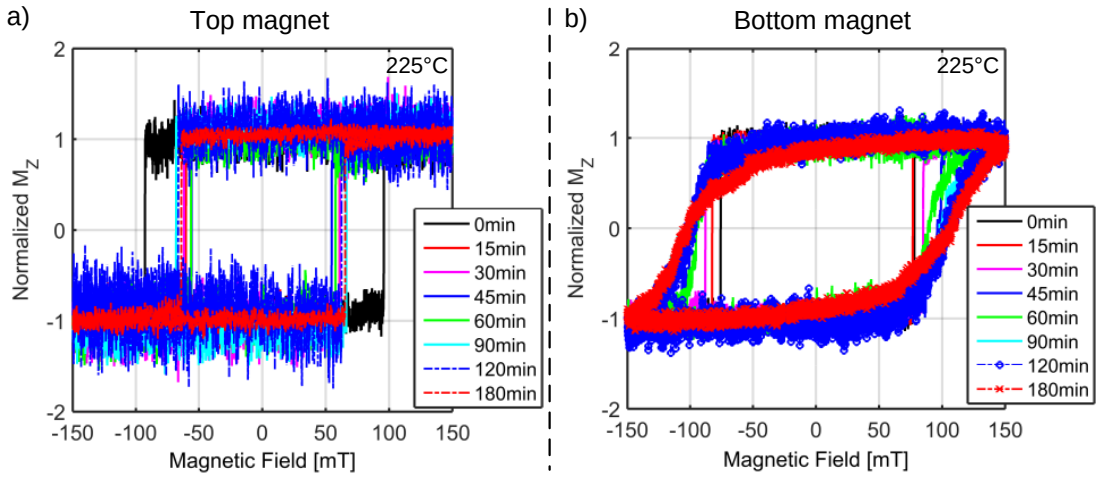

Figure 5.9: Hysteresis curves measured after different annealing times at 225° C for (a) top magnet and (b) bottom magnet.

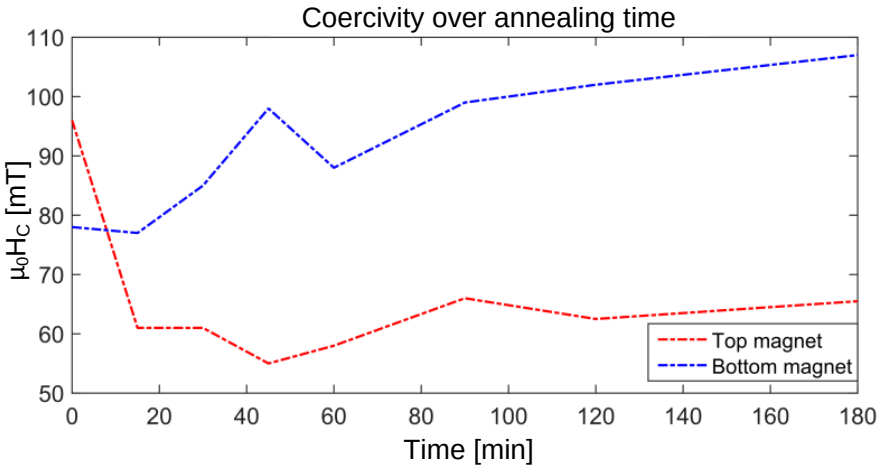

Figure 5.10: Coercivity over annealing time (T = 225°C) for top and bottom magnet.

does change the value of $\mu_0 H_C$ and it changes them in a different way for top and bottom magnet. This behavior is undesirable, as the fabrication dependent switching field distributions are hereby increased. As a consequence, the magnetic circuit gets more error-prone.
Note, this is the first time the impact of air annealing on multilayered 3D nanostructures is investigated. Further investigations are required on this topic. Furthermore, solutions (alternative fabrication methods) must be found to circumvent the change in coercivity. Annealing under vacuum atmosphere may be an expe-

dient alternative.

5.3 Conclusion

This paragraph concludes the investigations on the fabrication process for 3D integration in pNML. The proposed and applied fabrication process is a monolithic one. This enables to keep the distance between functional layers small enough ($< 100\,\mathrm{nm}$) to enable reliable signal transmission in the z-direction exploiting pure magnetic field-interaction.
A detailed description on the fabrication steps for every single functional layer and the applied planarization technique has been provided. Measurements of the profile of planarized magnets confirm the good planarization capability of the HSQ-interlayer.
Critical fabrication steps, like ion irradiation of top layer magnets, alignment of top to bottom layer and annealing have been investigated in detail. From simulations on the ion penetration depth during FIB irradiation it could be extracted, that acceleration voltage and HSQ-interlayer thickness have the most impact. However experiments revealed that the thickness of the hard mask, the chosen hard mask material and also the ion dose have a great impact on the ion penetration depth. Within the scope of this work suitable values for HSQ-interlayer thickness, ion dose, hard mask material and thickness have been determined experimentally, which guarantee to preserve the bottom magnets performance during ion irradiation of the top magnets.
A special alignment technique applying orientation marks on every functional layer enables the precise alignment (without scanning the surface of the sample, which would destroy the magnets) of top to bottom layer.
Experiments on the longterm thermal treatment of the magnets at 225° C (temperature is required to harden the HSQ-interlayer) showed that the influence on the top and bottom magnets is different. While the top magnets preserve their sharp switching behavior during the whole annealing process (180 min), the bottom magnets show step wise propagation of the domain wall indicating domain wall pinning. Furthermore the coercivity of the magnets from both functional layers changes over annealing time. These results require further, more detailed investigations.

6 Magnetic via

This chapter presents one of the most vital 3D pNML devices, but also one of the most important ones, the magnetic via. The magnetic via has a similar functionality as the via in CMOS, namely the vertical signal transfer between functional layers. In comparison to CMOS, where an enormous fabrication effort must be undertaken to fabricate a vertical wire between the functional layers (see sec. 2.2), in magnetic circuits, the 3 dimensional character of the magnetic field can be exploited for vertical signal transfer. No extra fabrication steps in the layer separating the stacked pNML layers are required. Only the physical magnetic interaction between vertically stacked magnets are decisive for signal transfer in the z-direction. In the following sections, signal transfer in a magnetic via [EKB+13], composed of two vertically stacked magnets is investigated. Important design criteria are studied. The fundamental experimental findings establish the theory of magnetic signal transport in the vertical direction.

6.1 Theory of field coupled nanomagnets

In pNML, information is transmitted and computed by the field interaction of single-domain nanomagnets possessing perpendicular magnetic anisotropy. The nanomagnet itself constitutes the basic element of pNML. Each nanomagnet has a fringing field . The field lines exit and enter the magnet perpendicular to its film plane and encircle the whole magnet (see Fig. 6.1 a). Bringing two magnets in close vicinity to each other, they interact through their field lines (see Fig. 6.1 b). Hereby, the field lines always force the neighbor magnet in their direction in order to reduce the magnetostatic energy of the system (see Fig. 6.1 c, global minimum). Consequently neighbor magnets in the horizontal arrangement prefer to align in the anti-parallel direction, whereas vertically overlayed and overlapping magnets arrange in the parallel direction. For the opposed configurations, the field lines of neighbor magnets counteract each other resulting in a higher total energy of the magnetic system. These states are also stable states but constitute only a local minimum (see Fig. 6.1 c, local minimum).

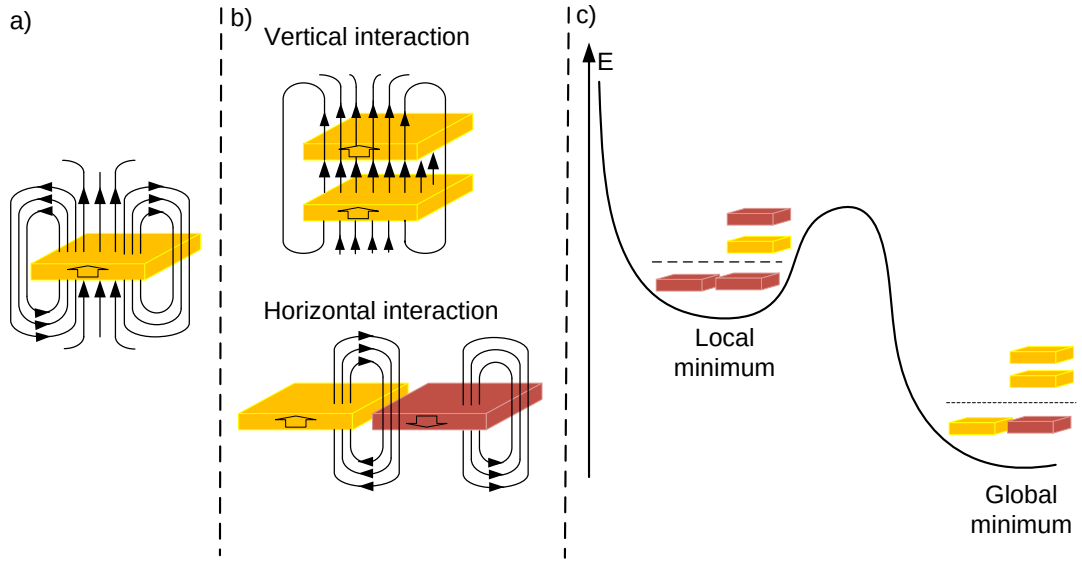

Figure 6.1: (a) Single nanomagnet and corresponding stray field lines. (b) Most favorable ordering of vertically and horizontally interacting neighbor magnets. (c) Magnetostatic energy landscape for different magnet configurations. Global minimum for anti-parallel aligned neighbor magnets in the horizontal and parallel aligned neighbor magnets in the vertical direction.

6.1.1 Achieving signal directionality

The ordering of the interacting magnets in the energetically lowest state constitutes the essential signal transmitting/computing operation. However, field coupling is reciprocal, i.e. it cannot be guaranteed that the ordering takes place from left to right or from top to bottom magnet or vice versa. To achieve directionality in the signal flow, it must be somehow restricted on which stray field, i.e. from which neighbor magnet the subsequent magnet has to react. Therefore the switching behavior of the magnet has to be tuned artificially, e.g. by FIB irradiation [14]. As the irradiation decreases or even destroys the anisotropy, domain wall nucleation can be the easiest evoked in the irradiated spot than in the rest of the magnet. To get a predefined signal flow direction, it must be ensured, that the irradiation spot is as close as possible to the one neighbor magnet from which the signal must be received and transmitted. For better understanding consider the case example shown in Fig. 6.2. Directed signal transmission in the horizontal and in the vertical direction is depicted for different time steps during one clocking pulse. The middle magnet M_2 is irradiated at one edge. Furthermore M_2 is surrounded by two neighbor magnets. Placing the irradiation spot as close as possible to neighbor M_1 guarantees that domain wall nucleation in M_2 is ruled

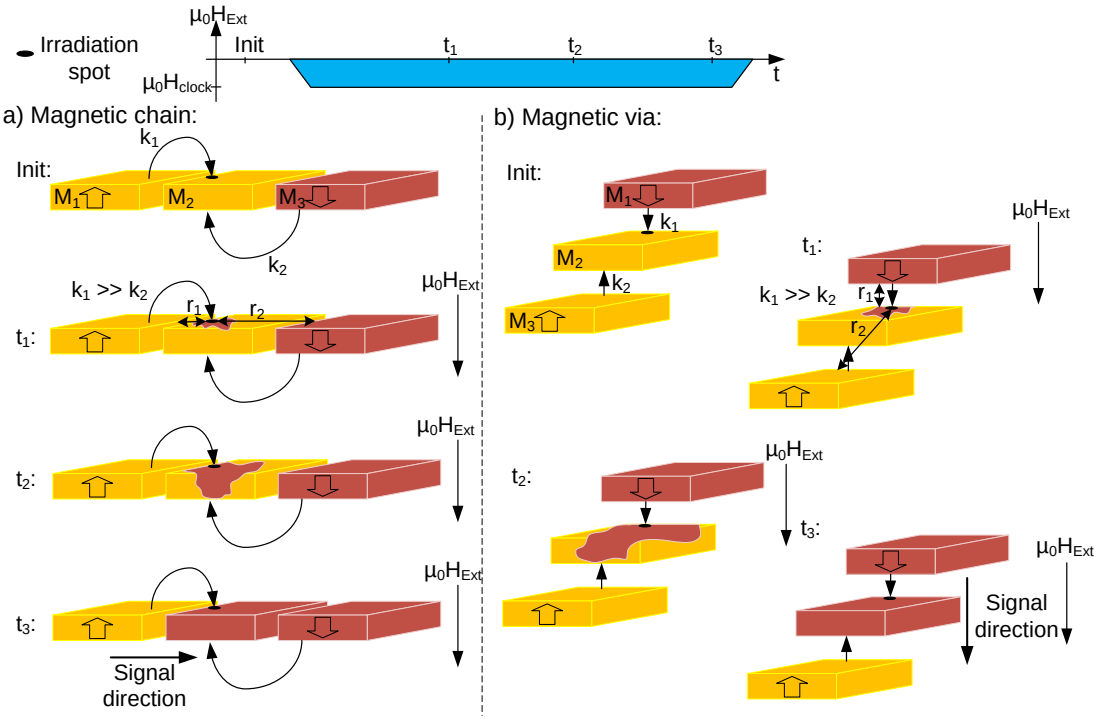

Figure 6.2: Controlled reversal during one clocking pulse. (a) Horizontally and (b) vertically coupled magnets. M_2 is controlled by the stray field of its left neighbor magnet and its top neighbor magnet respectively, ensuring non-reciprocal signal flow.

by the coupling field of neighbor M_1 [18]. The influence of the neighbor magnet M_3 on M_2 is negligible, as the irradiated spot is too far away from M_3. The coupling field decreases with increasing distances r from the magnet's edge with $1/r^{\mathrm{n}}$. Consequently, the coupling field $|\mathbf{k_2}|$ is negligibly small compared to $|\mathbf{k_1}|$. Applying a global clocking field with the amplitude $\mu_0 H_{clock}$, the superposition of of the clocking field with $\mathbf{k_1}$ provides enough energy to force M_2 in the desired direction, namely the direction of the $\mathbf{k_1}$. During the clocking pulse, the domain wall nucleates in the irradiated spot and propagates to the non-irradiated edge by totally reversing the whole magnet. Even if the stray field of M_3 forces M_2 in the opposite direction, the coupling field of M_1 dominates and thereby controls the domain wall nucleation process in M_2. Note, field-coupled magnets in the horizontal always transmit the inverted signal (anti-parallel alignment), whereas vertically overlapping field-coupled magnets transmit the original signal (parallel alignment). Without FIB irradiation, the location where domain wall nucleation takes place in the magnet is fabrication-dependent and therefore random. It starts in those regions where defects in the crystalline lattice of the magnet's film com-

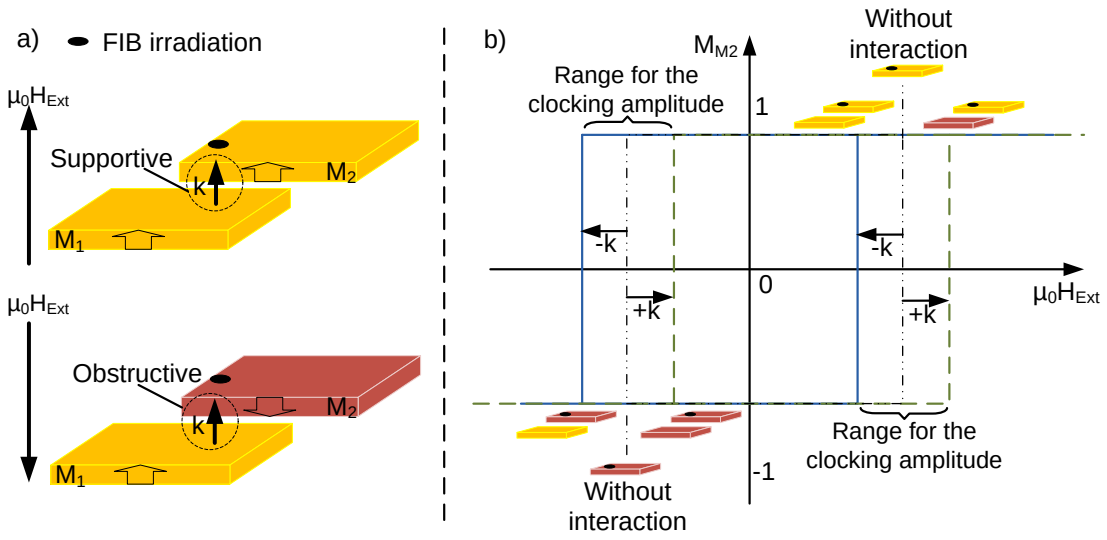

Figure 6.3: (a) Principle of measuring field-interaction in a magnetic via. M_2 is switched alternatively in the parallel and anti-parallel configuration to M_1. (b) Hysteresis curves indicating the switching behavior of M_2. The influence of $\mathbf{k}$ either decreases or increases the value of the required external field amplitude. For the parallel alignment, $\mathbf{k}$ is supportive and therefore lowers the amplitude of $\mu_0\mathbf{H_{Ext}}$. For the anti-parallel alignment, $\mathbf{k}$ is obstructive and therefore enhances the amplitude of $\mu_0\mathbf{H_{Ext}}$.

position are located [12]. This position is not controllable. On the contrary, FIB irradiation creates a predominant nucleation spot (anisotropy reduction is the highest by FIB) in a predefined position, which can be afterwards controlled by $\mathbf{k}$.

6.1.2 Determination of the coupling strength

The coupling strength between two magnets is a key parameter in terms of correct signal transfer. If the coupling strength is not high enough, the signal may not be transferred to the next neighbor magnet. A possible method to determine the coupling strength between two magnets is to analyze the switching behavior of one magnet for both configurations, parallel and anti-parallel alignment to each other.

In the following, the determination of the coupling strength for a magnetic via is explained. Consider two magnets placed above each other (see Fig. 6.3 a). M_1 is an unirradiated, as-grown magnet with an inherent high switching field compared to M_2, whose switching field is strongly reduced due to FIB irradiation [18]. The

magnetization state of magnet M_1 is fixed to a certain state (here 'up'), while M_2, which is irradiated and hereby sensitized to $\mathbf{k}$ of M_1 is switched alternately up and down. The amplitude required to switch M_2 in the different states is too low to affect the magnetization state of M_1. Thereby it can be guaranteed that M_1 retains its magnetization during the switching of M_2.

To switch M_2 in the anti-parallel state to M_1, a higher external field amplitude is required than for the parallel alignment. The reason is that $\mathbf{k}$ stabilizes the parallel alignment of M_2 by counteracting to the field lines of the external field. The influence of $\mathbf{k}$ can only be overcome by an external field amplitude which is enhanced by the amount of $|\mathbf{k}|$.
For the opposite case i.e. the switching of M_2 in the parallel state to M_1, the field lines of the external field and $\mathbf{k}$ coincide. Thereby, a part of the energy required for switching is already provided by $\mathbf{k}$. Consequently a lower external field amplitude is required. More precisely, the external field amplitude is lowered by the amount of $|\mathbf{k}|$ (see straight line for negative field in Fig. 6.3 b). The difference in the switching fields of M_2 depending on the parallel or anti-parallel alignment amounts to two times $|\mathbf{k}|$. So the interaction between two coupled magnets can be proven and measured by the shift in the hysteresis curves as depicted in Fig. 6.3 b. The higher $|\mathbf{k}|$ the wider is the shift. Without the interaction with a neighbor magnet, the switching field amplitude of M_2 remains the same for 'up' and 'down' switching (also indicated in Fig. 6.3 b).

6.1.3 Constraints on the clocking amplitude

As already mentioned in section 2.1.3, signal propagation and computation in pNML is done by alternating global external field pulses applied perpendicular to the film plane. The alteration of the field direction ensures that magnets can align in the direction of the acting coupling field from surrounding input neighbor magnets (which can be 'up' or 'down'), when they are forced to. Nevertheless, the amplitude of the clocking field must be chosen adequately. If the amplitude is chosen too high, all magnets align in one direction and computation performed by field coupling cannot take place. The same is, if the amplitude is chosen too low, the influence of the coupling fields is not sufficient to evoke magnetization reversal, if it is requested. Hence, the clocking amplitude must be in the range in which the coupling fields can rule the switching of the respective neighbor magnet. Considering the hysteresis curves for obstructive and supported switching (presented in Fig. 6.3 b), it is obvious, that the range must be in between the two shifted hysteresis curves. A possible clocking scenario of four magnets with two alternating pulses is depicted in Fig. 6.4.
In the initial state, the input M_1 is aligned in the down state. Note, the coupling field of each magnet is assumed to be the same, i.e. $|\mathbf{k_1}| = |\mathbf{k_2}| = |\mathbf{k_3}|$. However for

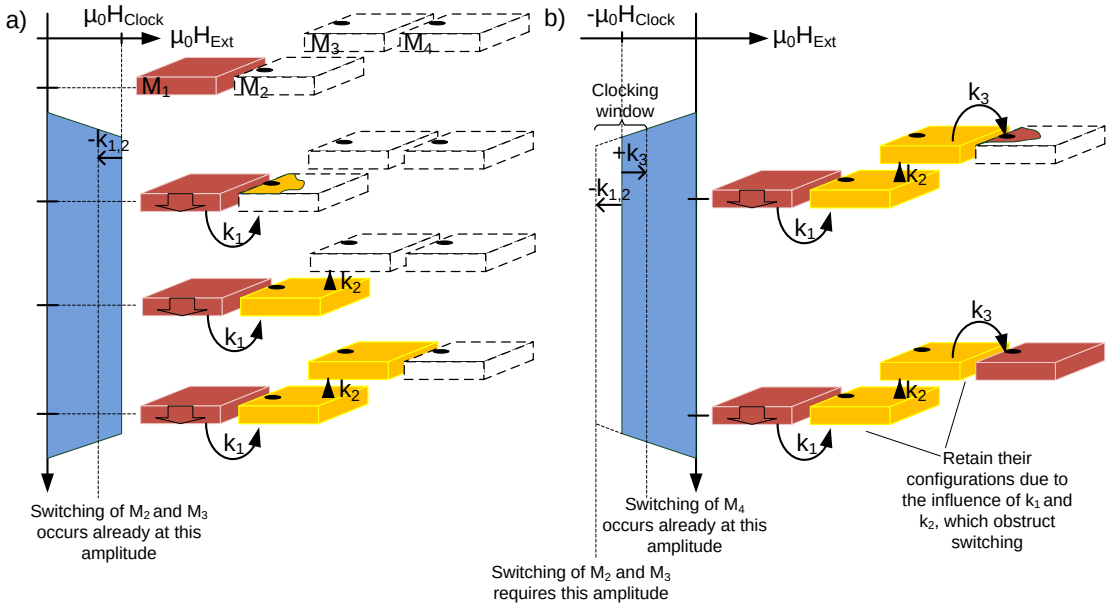

Figure 6.4: (a) Signal propagation during a positive field pulse. Switching of M_2 and M_3 already occur at the field values of $(\mu_0 H_{Clock} - \mathbf{k_1})$ and $(\mu_0 H_{Clock} - \mathbf{k_2})$ respectively. (b) Signal propagation during a negative field pulse. Switching of M_4 already occurs at the field value $(-\mu_0 H_{Clock} + |\mathbf{k_3}|)$. The magnets M_2 and M_3 set during the previous positive field pulse retain their configuration as $\mathbf{k_1}$ and $\mathbf{k_2}$ prevent their switching.

clarification, from which magnet the coupling field is emanated, the indices 1, 2, 3 are introduced here. First, a positive clocking field pulse perpendicular to the film plane is required to propagate the signal to M_2 and M_3 respectively. The coupling field $\mathbf{k_1}$ coincides with the external field. It acts supportive to the external field and forces M_2 in the antiparallel state. Due to the influence of $\mathbf{k_1}$ the switching of M_2 already takes place at $(\mu_0 H_{Clock} - |\mathbf{k_1}|)$. As soon as M_2 is reversed, its coupling field supports the switching of M_3. Within the same clocking pulse, M_3 switches at the amplitude $(\mu_0 H_{Clock} - |\mathbf{k_2}|)$ in the parallel state to M_2.
Now, to transmit the signal to M_4 a negative field pulse is required (see Fig. 6.4 b). The coupling field of M_3 together with the clocking field forces M_4 in the anti-parallel state. Thereby, switching of M_4 already occurs at the field value of $(-\mu_0 H_{Clock} + |\mathbf{k_3}|)$. Applying a negative field pulse it must be guaranteed, that M_2 and M_3 are unaffected and are not switched back by the field pulse. However, this is ensured by the given direction of $\mathbf{k_1}$ and $\mathbf{k_2}$. As $\mathbf{k_1}$ and $\mathbf{k_2}$ are counteracting to the external field, a clocking amplitude of $(|-\mu_0 H_{Clock} - |\mathbf{k_{1,2}}||)$ would be required for switching, which is not the case. Consequently, M_2 and

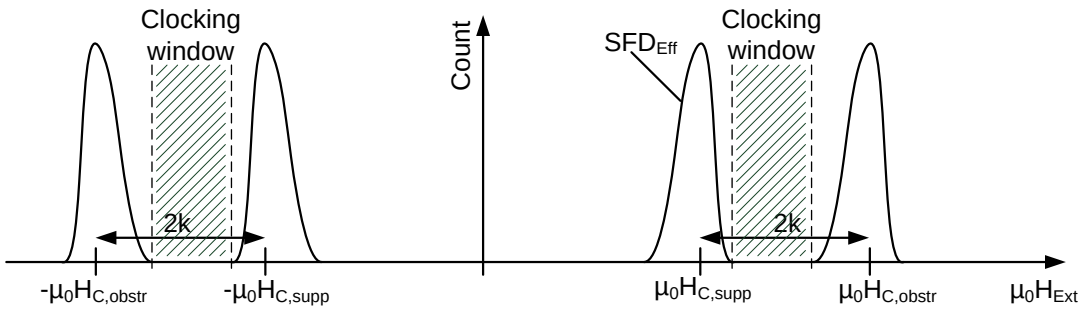

Figure 6.5: Effective SFDs for supported and obstructed switching in positive and negative field direction. Clocking window lies in between the SFD_{Eff} for supported and obstructive switching.

M_3 retain their configurations as the influence of $\mathbf{k_1}$ and $\mathbf{k_2}$ prevents switching. If the external field amplitude would have been high enough, i.e. $|\mu_0\mathbf{H_{Ext}}| \geq (|-\mu_0 H_{Clock} - |\mathbf{k_{1,2}}||)$, the influence of $\mathbf{k_1}$ and $\mathbf{k_2}$ would have been overcome and M_2 and M_3 would have been switched in the wrong configuration resulting in a signal loss.
On the basis of the presented clocking scenario, it is obvious, why the clocking amplitude must be chosen adequately and controlled precisely i.e. in between the switching field values for supportive and obstructive switching (see clocking window in Fig. 6.4 b). Note, in a pNML system there are devices (e.g. three input majority gate) that must be designed in the way, that the coupling strength between all neighbor magnets is equal to ensure same influence. However, this is not always trivial to achieve due to lithographic imperfections and inaccurate positioning of the FIB irradiation spot and further reasons mentioned in the next section.

6.1.4 Factors diminishing the clocking window

Derived from the previous subsection, the coupling strength defines the width of the clocking window. This fact is only valid, if it is assumed, that all magnets do switch identically and always at exactly the same field amplitude. However, switching field variations of a single magnet due to thermal fluctuations can be observed [110]. Furthermore, in large nanomagnetic arrays it is commonly seen, that there is a large difference in the switching fields between nanomagnets [110, 111]. As possible reasons for this behavior, differences in the switching volume or switching mechanism of the magnets are mentioned. These differences may occur from variations in the direction of the intrinsic anisotropy brought about by etch damage or redeposition during the etching of the magnets [110, 112, BBK+13a].
For the magnets fabricated and applied in this work, these thermally and fabri-

cation induced switching field variations could also be detected [EBK+12]. Considering the fabrication techniques applied in this work, the FIB irradiation may cause variations in the intrinsic anisotropy. The number of ions, the penetration radius and depth respectively are hard to control. So distribution of the Ga^+ ions during FIB irradiation varies from magnet to magnet resulting in switching field variations of the magnets.
Considering the reliability of NML, thermally induced switching field distribution (SFD_T) and fabrication induced switching field distribution (SFD_{Fab}) have to be taken into account. Both effects result in an effective switching field distribution (SFD_{Eff}, being the convolution of the SFD_T and SFD_{Fab}) of the magnets, which narrows the clocking window (see Fig. 6.5). Now the clocking window is not defined by two times the amount of $|\mathbf{k}|$, but by the separation of the SFD_{Eff} for supported and obstructive switching. Thereby $\pm\mu_0 H_{C,supp}$ and $\pm\mu_0 H_{C,obstr}$ represent the mean switching field values of the distributions respectively.
An error occurs, if the distributions overlap and no clocking window is left. Fabrication variations cause the largest distributions and further investigations have to be undertaken to minimize them. An enhanced coupling field shifts the distributions further apart from each other and is therefore a decisive factor for reliability. Parameters influencing the coupling field are discussed in the following section.

6.2 Important design parameters

The easiest way to increase the clocking window is to increase the coupling field, as the SFD_{Fab} is hard to control. Enhancing the total amount of the ferromagnetic material in the stack, reducing the inter-magnet distance or optimizing the magnet's shape help to achieve this. 3D micromagnetic simulations with OOMMF on these factors have been performed, to investigate this influence.

Influence of the total amount of the ferromagnetic material

To evaluate the influence of the total amount of the ferromagnetic material in the film composition on the coupling field, simulations on two different film compositions are performed. The first magnet is composed of a Co/Pt multilayer stack, which is modeled as a 10 nm thick homogeneous layer with $M_S = 4.2 \cdot 10^5$ A/m. The second magnet is composed of a Co/Pt multilayer, with the half magnetization amount $M_S = 2.1 \cdot 10^5$ A/m compared to the first magnet. The simulations of the coupling fields are evaluated in the plane, where the second magnet of the via is supposed to be, here z = 40 nm above the simulated magnet. The magnet's shape is a structure with flat round edges. The resulting magnetic flux densities in z-direction B_Z are shown in Fig. 6.6 a and b. As expected the magnet with the half amount of $M_S = 2.1 \cdot 10^5$ A/m (Fig. 6.6 b) yields only in the half

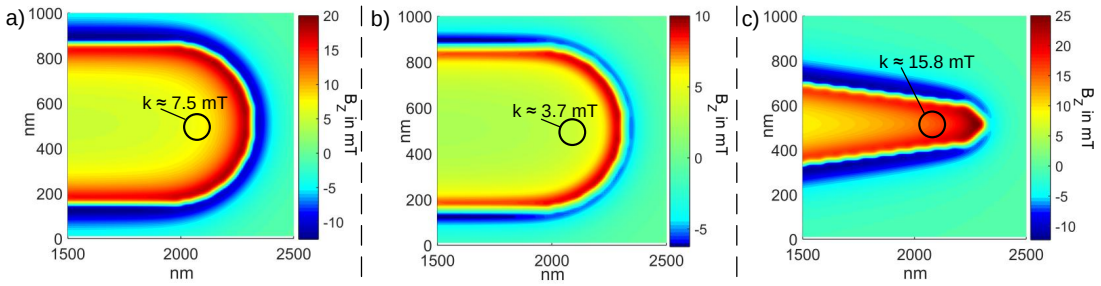

Figure 6.6: OOMMF simulation results of the coupling field generated by a Co/Pt magnet in a vertical distance of z = 40 nm above the magnet itself. The encircled region indicates the positioning of the irradiation spot and the resulting coupling field in this region. (a) Resulting B_Z for $M_S = 4.2 \cdot 10^5$ A/m. (b) Resulting B_Z for $M_S = 2.1 \cdot 10^5$ A/m. (c) Resulting B_Z for $M_S = 4.2 \cdot 10^5$ A/m and a pointy end.

amount of the coupling field compared to the magnet with the double M_S. The encircled region indicates the positioning of the irradiation area of a possible top or bottom neighbor magnet. The **k** acting in this region is decisive for the coupling strength between two overlying magnets and hence for the separation of the SFD_{Eff}s. Therefore, for reliability requirements, the magnet with high M_S is more suitable. High M_S can be achieved by enhancing the number of Co layers or Co-layer thickness. However, these parameters are limited by the resulting perpendicular magnetic anisotropy, which can be affected negatively by a too high number of multilayer or a too thick Co-layer [106].

Influence of inter-magnet distance

To evaluate the influence of the vertical distance between the magnets on the coupling field, again OOMMF simulations of a Co/Pt magnet with $M_S = 4.2 \cdot 10^5$ A/m and on the same magnetic structure as shown in Fig. 6.6 a are performed. This structure is chosen later on for experimental demonstration.
The resulting B_Z at different heights ($z \in \{20\,\text{nm}, 40\,\text{nm}, 60\,\text{nm}, 80\,\text{nm}, 100\,\text{nm}\}$) above the magnet is extracted from the simulations. Hereby, the focus of interest is the behavior of B_Z in the position of the irradiation area of a second placed above magnet. It is assumed that the irradiation center is supposed to be at position x = 2100 nm, y = 500 nm and z-coordinate is variable at the above mentioned positions (see Fig. 6.7 a).
The simulation results in Fig. 6.7 b and c show the resulting B_Z once in y-direction for a fixed x-coordinate x = 2100 nm (center of the irradiation spot) and once in x-direction for a fixed y-coordinate y = 500 nm (center of the irradiation spot). It is obvious, that $|\mathbf{k}|$ is the highest for the smallest inter-magnet distance. The

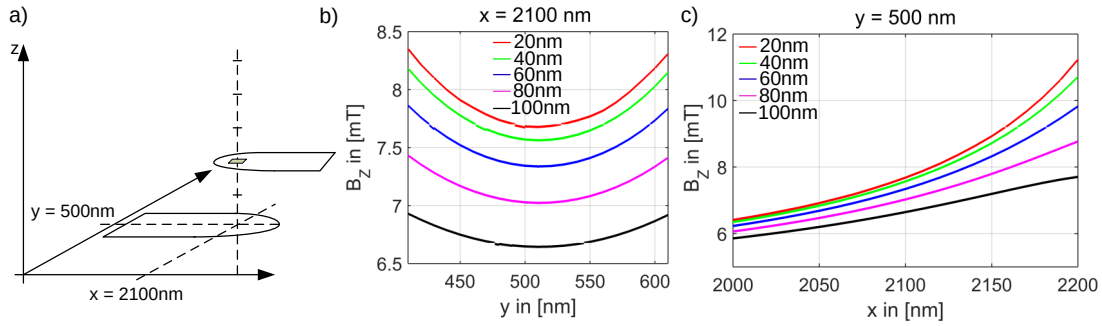

Figure 6.7: (a) Schematic depiction describing, that B_Z is evaluated in the irradiation center of a supposed placed above neighbor magnet at different heights. (b) and (c): OOMMF simulation results of B_Z generated by a Co/Pt magnet with $M_S = 4.2 \cdot 10^5$ A/m at different vertical distances above the magnet at a fixed position x = 2100 nm along the y-axis (b) and at a fixed position y = 500 nm along the x-axis (c).

deviation between the minimum and maximum value is ≈ 1 mT for the different z-heights. Considering the behavior of B_Z along the y-direction, it can be detected, that to the left and to the right side of the irradiation center, B_Z increases. The highest values are reached, the further apart from the irradiation center it goes. This is due to the fact, that the further apart from the irradiation center, the closer are the edges of the magnet, where the stray field concentration is the highest. However, the increase in B_Z is still below 1 mT. This behavior is symmetrical.
It is different, when considering the behavior along the x-direction. B_Z increases, the closer it goes to the edge of the magnet (right side). Going to the left side of the irradiation center, B_Z decreases. Here, the difference between the minimum and maximum value along the x-axis is significant for z = 20 nm and z = 40 nm distances (> 4 mT). Assuming inaccuracies in the positioning of the irradiation spot from magnet to magnet, this behavior of B_Z results in high variations of the coupling field from magnet to magnet. However, these variations shrink for higher vertical distances (see progression for z = 100nm).
For reliability demands of devices with more than one input e.g. three input majority gate, one would place the irradiation center further apart from the edges to diminish variations in the coupling field (due to inaccurate alignment of top to bottom layer), which involves a decrease of $|\mathbf{k}|$ at the same time. However a trade-off must be made, as high coupling fields are worthwhile but at the same time low variations are required.

Influence of magnet's shape

To investigate the influence of the magnet's shape on the coupling field, different geometries of the magnet have been considered and the resulting B_Z again determined by OOMMF simulations. Therefore, the shape shown in Fig. 6.6 a has been changed to a structure with a pointy end as shown in Fig. 6.6 c.
It is observed, that structures with a small width and a pointy end reach a higher B_Z compared to a simple strip-like geometry with flat rounded ends. This observance can be traced back to the fact that the smaller the surface of the magnet, the less demagnetizing energy is situated in the magnet itself as less field lines counteracting to the magnetization do penetrate the magnet's surface. Furthermore is observed that the highest coupling field is reached at the edges. For broad structures the stray field energy is distributed on a quite long edge, while for narrow structures, this stray field energy is distributed on a quite short edge and therefore concentrates at pointy ends. So to achieve high coupling fields, the structure shown in Fig. 6.6 c is more suitable than the one shown in a) and b).
However, due to the reduced geometry, the accurate positioning of top to bottom level magnets is aggravated.

Comment on the realization of a displaced via

Displaced magnetic via means that the top and bottom magnet do not overlap but are slightly displaced to each other. A displaced magnetic via as indicated in chapter 2 in Fig. 2.4 b would transmit the inverted signal, which would extend the functionality of the magnetic via. However, from the simulation results presented in Fig. 6.6 it is not advisable to fabricate a displaced via, as the coupling field drops rapidly when diverging from the magnets edge.

6.3 Information transport - Experimental demonstration

6.3.1 Device design and fabrication

The magnetic via is fabricated in a two-step process as described in sec. 5. A magnetic multilayer film namely $Ta_{2nm}Pt_{3nm}Co_{0.6nm}4x(Pt_{1nm}/Co_{0.6nm})Pt_{5nm}$ is sputtered. The partial sputtering pressure of Ta was chosen to be 2µbar and the one of Pt and Co to be 6µbar. After sputtering, the first device layer is structured by FIB lithography. Depending on the directionality the via should provide, the next step is either planarization or FIB irradiation for the generation of artificial domain wall nucleation centers. For a down-via, the magnet of the bottom layer must be first irradiated followed by planarization with HSQ. The applied

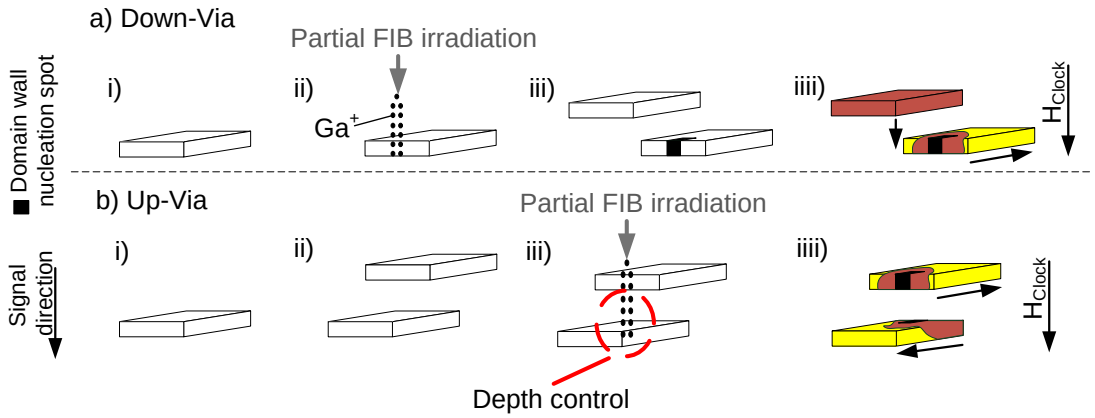

Figure 6.8: Sequential fabrication steps for a down-via (a) and up-via (b). For the up-via, FIB irradiation takes place after fabrication of both magnets. Ion penetration depth control is evident to preserve the bottom layer magnet from irradiation.

ion dose is chosen to be $5 \cdot 10^{13}$Ions/cm^2 and the size of the irradiation spot to be [80 nm $\times$ 80 nm]. The thickness of the HSQ interlayer is set to 40 nm. Afterwards, the same film composition is sputtered on the planarization layer and is again patterned by FIB lithography.
The fabrication of the down-via is less critical than the one of the up-via due to the chronology of FIB irradiation (see Fig. 6.8). For a down-via, FIB irradiation takes place before fabrication of the top magnet. On the contrary, for an up-via, the top magnet is irradiated after both, top and bottom magnet were fabricated. Hereby, the penetration depth of the FIB must be well controlled. Otherwise two domain wall nucleation centers are created right below each other. As a consequence, sensitivity of top to bottom magnet is lost and thereby signal directionality. This means that during clocking, both magnets are switched by the external field pulse and domain wall propagation in top and bottom magnet proceeds in opposed directions (see Fig.6.8 b). Constraints to prevent deep ion irradiation were described in sec. 5.2.
The most important thing during the fabrication of a magnetic via is, that the irradiation area of the magnet overlaps with the edge of it's top or bottom neighbor respectively. Otherwise signal transmission by field coupling can not take place.

6.3.2 Determination of the coupling field

In the past, there have been experiments on the field interaction between the pole of an in-plane magnet composed of Py and a vertically placed Co/Pt magnet, with perpendicular magnetic anisotropy [26]. In the following experiments, field

interaction between two vertically coupled magnets with perpendicular anisotropy is proven and measured, for the first time.
To measure this field interaction, one of the magnets must be fixed to a certain state, while the other magnet is switched into the parallel and anti-parallel state in relation to it. In a first experiment a magnetic down-via is realized (see Fig. 6.9 a) to exclude possible errors from too deep ion irradiation. Therefore the bottom layer magnet is irradiated and sensitized to the stray field of its top neighbor. Due to FIB irradiation, the switching field of the bottom magnet is significantly reduced compared to its non-irradiated top neighbor. The switching field of the top magnet amounts to $\mu_0 H_{C,meanTop} = 376\,\mathrm{mT}$. Applying a saturation field pulse with the amplitude of 400 mT in the positive direction, both magnets align in the up state. Now, an alternating field with maximum amplitude of 100 mT is applied and hysteresis curves of the bottom magnet are recorded with the MOKE. The maximum amplitude of the external field is lower than the switching field of the top magnet. Hence, the top magnet is unaffected by the applied external field and retains its magnetization during the whole measurement. At the same time, this amplitude is high enough to switch the bottom magnet. During the measurement, the bottom magnet is switched a hundred times in the up and down state. Hereby, the field is ramped with a rate of 100 mT/s with a field resolution of 1 mT. Afterwards, the hysteresis measurements of the bottom magnet are repeated for an initial down configuration of both magnets. This is achieved by applying a saturation field pulse of -400 mT. Finally, switching field distributions are extracted from the recorded hysteresis measurements (see Fig. 6.9 b).
The bottom magnet switches at $\pm\mu_0 H_{Cmean,p} = \pm 55\,\mathrm{mT}$ in the parallel state and at $\pm\mu_0 H_{Cmean,a-p} = \pm 70\,\mathrm{mT}$ in the anti-parallel state. The resulting $|\mathbf{k}|$ amounts hereby to 7.5 mT. The switching behavior of the bottom magnet is as expected and theoretically derived. The SFDs for parallel and anti-parallel alignment are clearly separated enabling an error-free signal transfer from top to bottom magnet. A further discovery of this measurement is that the SFDs for the parallel alignment are broader distributed than the SFDs for the anti-parallel configuration. It seems that the coupling field which is counteracting to the external field during switching in the anti-parallel state, suppresses thermal noise. However, this behavior has to be intensively investigated by additional simulations.
Comparing the measured results to the determined coupling field from the OOMMF simulation results for the same magnet's geometry (see Fig. 6.6 a) it can be seen that they are in very good agreement confirming the correctness of the Finite Element calculations. Note, measurements on a later on fabricated magnetic up-via show the same switching behavior as the down-via. This is derived in the next chapter 7. This chapter is dedicated to the magnetic signal crossing device, which requires also the up-via for its functionality.

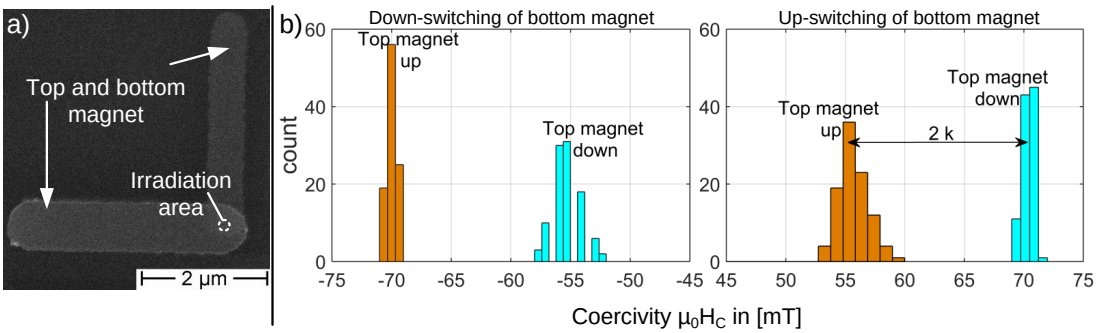

Figure 6.9: (a) SEM image of the fabricated down-via. (b) SFDs of bottom magnet. SFDs are shifted to higher field amounts for anti-parallel alignment and to lower field amounts for parallel alignment to the top magnet.

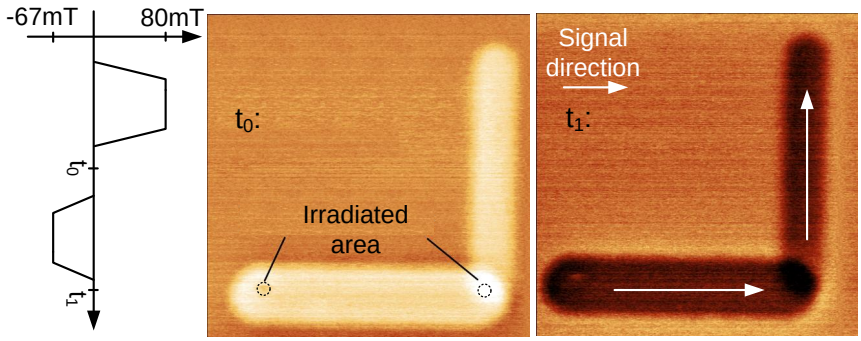

Figure 6.10: MFM images revealing the magnetization states of the via magnets before and after clocking.

6.3.3 Signal propagation during clocking

To integrate the magnetic via in a pNML system, further constraints have to be fulfilled. Both magnets must switch within one clocking pulse. Furthermore both magnets must be irradiated as they both would receive the signal from a neighbor magnet (see Fig. 6.4b). Therefore, further experiments are performed on the same pair of magnets presented in the preceding section.
First the top magnet is also irradiated with the same ion dose as the bottom magnet on its left edge. Afterward the switching field of the top magnet is determined. As long as its switching field lies within in the clocking window (which is defined by the separation of the SFD_{Eff}s for parallel and anti-parallel alignment of the bottom magnet), both magnets do switch within one clocking pulse and signal transmission is guaranteed due to field coupling between the magnets. The switching field of the top magnet is again determined with the MOKE by mea-

suring the hysteresis curves. The irradiated magnet has a mean switching field at 65 mT. A field amplitude of -67 mT guarantees switching of both magnets within one clocking pulse. To visualize the magnetization state of both magnets after applying a clocking pulse, MFM measurements are performed (see Fig. 6.10). An initial field pulse of 80 mT aligns both magnets in the up state (point of time t_0 in the figure). After a further field pulse of -67 mT both magnets are switched in the down state as expected (point of time t_1 in the figure). This experiment manifests that signal transmission takes place within one clocking pulse, starting in the top magnet and propagating to the bottom magnet. Nucleation in the bottom magnet first can be excluded as in the beginning the coupling field of the top magnet is opposed to the external field thereby prohibiting switching of the bottom magnet. Only, as soon as the top magnet is fully reversed, **k** flips its direction and supports switching of the bottom magnet from there on. Performing this experiment proves the applicability of the magnetic via for pNML system integration.

6.4 Conclusion

This paragraph concludes investigations on the magnetic via representing the most important element required for 3D integration. It enables signal transmission in the vertical direction by exploiting coupling field interaction between overlying magnets of two superposed functional layers. The measurement technique to determine the coupling strength and the clocking window has been explained. In this context, the influence of thermal and fabrication dependent switching field variations on the width of the clocking window has been outlined. Both, thermal and fabrication dependent switching field variations narrow the clocking window leading to a higher error-proneness of the device/circuitry. The strength of the coupling field has been discussed as the key parameter to enlarge the clocking window and thereby diminish the error-rate. From micromagnetic simulations of the coupling field, parameters like the magnet's shape, inter-magnet distance and amount of the ferromagnetic material in the film stack the magnets are composed of, have been determined to have a strong impact on the resulting coupling strength. The more ferromagnetic material, the smaller the shape and the vertical distance, the higher becomes the emanated coupling field.
Hysteresis curves measured with the MOKE proved the vertical field interaction between the magnets of the fabricated magnetic via. Additional investigations with the MFM confirmed signal transmission through the via within one clocking pulse.

7 Magnetic Signal Crossing

The ability to transmit magnetic signals in the vertical direction between different functional layers, brings this work to the realization of a further building block, namely the crossing of signals, which is essential in every circuitry. Even in the most rudimentary designs of pNML circuits, like the presented full-adder (see Fig. 2.3 d) or TLG-full adder (see Fig. 2.3 e) it is obvious, that signal crossings are indispensable, if the isolated inputs B and C_{in} of the full adders should be connected to previous logic elements of the pNML circuitry. The previously presented magnetic via enables to route a magnetic signal through a further functional layer, thereby realizing a multi-layer crossing. However, there are still some challenges to manage, which are among others focus of this chapter. Furthermore different approaches for signal crossing in different QCA-based technologies are discussed. Theoretical background for multi-layer signal crossing in pNML is provided and its functionality is experimentally proven.

7.1 Approaches for signal crossings

In the past, there have been several ideas presented to enable signal crossing for technologies based on QCA-like architectures. As already mentioned, such technologies exploit field interaction (electrostatic or magnetostatic) between nearest neighbor cells to process signals. However, exactly this special character of QCA-based technologies puts a certain challenge on signal crossings and makes them more difficult to physically implement than in a CMOS equivalent, as the given field interaction has to be circumvented to enable unimpeded signal flow.

Signal crossing in QCA

In QCA, there have been two essential approaches. One with signal crossing wires on one plane referred to as coplanar crossover [113, 114] and one with signal crossing wires on multiple layers referred to as multi-layer crossover [115]. The coplanar approach focuses on one plane to enable completely planar circuits. Hereby regular cells (quantum dots positioned at the corners of a square) are placed adjacent to rotated cells (orientation of quantum dots rotated by 45°) as shown in Fig. 7.1. Due to the rotation of the dot's geometry there is very little mutual interaction given between the regular and the rotated cells enabling signal crossing. However

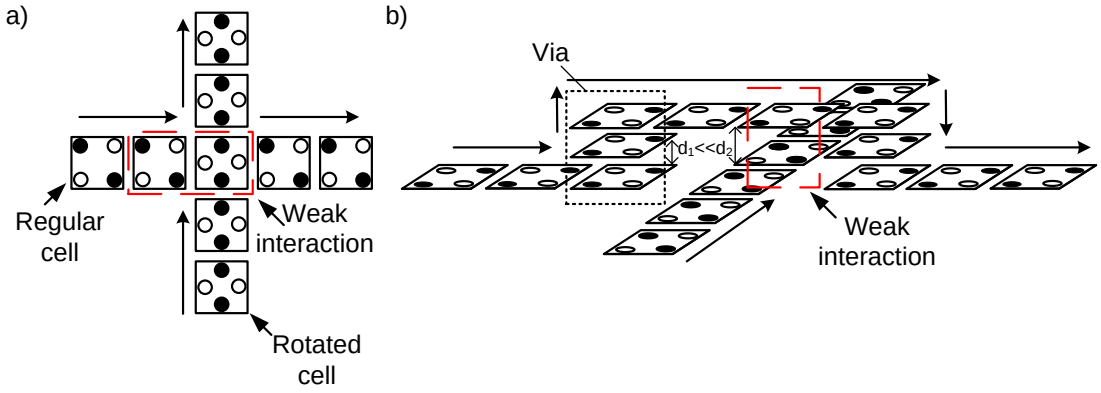

Figure 7.1: Coplanar vs. multi-layer crossing as taken from [115]. (a) Independent signal transmission along two cell wires containing different cell types. The interaction between the regular and the rotated cell is weak enough to enable signal crossing. (b) Multi-layer crossing. Routing the signal to a further functional layer, interaction in the crossing region can be kept weak enough to enable signal crossing.

it is claimed, that such a cell symmetry is hard to fabricate. Even small fabrication variations in the position of cells or dots introduce crosstalk between the interconnects, which leads to a dominant behavior of one cell type and thereby a malfunction of the signal crossing. Due to this fact, complex circuits using coplanar crossovers are very likely to fail.
Therefore an alternative approach is envisioned exploiting multiple layers, but under the maintenance of one cell type [115]. It is stated that by stacking cells on top of each other, the signal can be transmitted to another functional layer, where from there on, the signal can further be horizontally transmitted and crossed (see Fig. 7.1 b). The vertical interaction between overlying cells must be matched to that one of the horizontally cells to guarantee error-free vertical signal transmission. If the signal is transmitted over several vertical cells in the via, from one to another functional layer only weak interaction in the direct crossover region is given, due to a larger vertical distance between the cells here. As indicated in Fig. 7.1 b, the vertical distance d_2 between the cells in the direct crossover region is twice the vertical distance d_1 of the cells in the via, which serves to route the signal up or down. This leads to insufficient interaction and therefore guarantees unimpeded signal flow in the crossover region.

Signal crossing in in-plane NML

Niemier and co-workers firstly envisioned coplanar signal crossings in in-plane NML in 2007 [116]. It is proposed to adopt the magnet's shape in such a way that

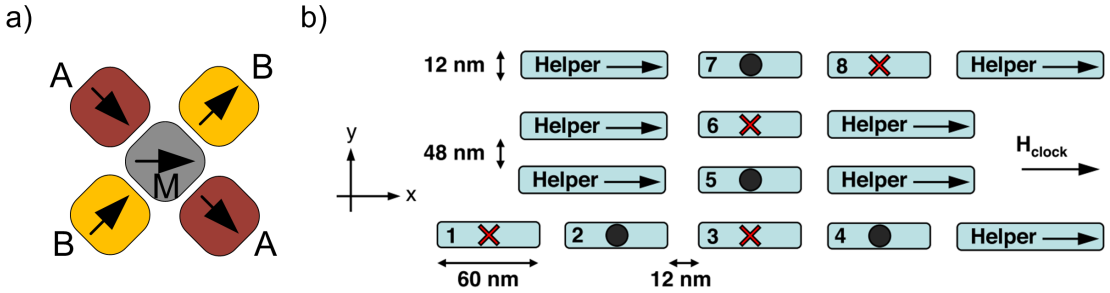

Figure 7.2: Coplanar vs. multi-layer crossing in in-plane NML [117]. (a) Top view: The middle magnet M is capable of representing two bits of information simultaneously, i.e. the orientation of M comprises the information of both input magnets at the same time thereby enabling signal crossing. (b) Cross section of multi-layer crossing.

a single magnetic island can represent two bits of information simultaneously. In Fig. 7.2 a a schematic of such a shape-based coplanar wire crossing is shown. The middle nanomagnet M has a component to both inputs A and B and transfers the magnetization of both inputs to both outputs. Micromagnetic simulations were performed on the proposed structure confirming the correct functionality at room temperature for all possible input configurations [117]. However, the fabrication of such nanomagnets is challenging.
Therefore, Niemier and co-workers introduced a further concept of multi-layer crossing for in-plane NML [117]. It is claimed, that magnetic islands could be placed in different layers separated by an oxide. Magnetic field interaction in the out-of-plane direction guarantees for vertical signal transfer. The layout of the proposed crossing structure is shown in Fig. 7.2 b. The 'x' and 'o' indicate the magnetization direction of the magnets. Large helper magnets are required to promote hard axis stability of the anti-ferromagnetically ordered wires in vertical as well as in horizontal direction. Clocking in the hard axis direction with a magnetic field that slowly decreases in magnitude, relaxes the system into the desired state. Also, here micromagnetic simulations were performed confirming the correct functionality of the device.

Summary

Signal crossings are absolutely essential in every circuit design. Of course, there is the possibility to realize a signal crossing without any special architecture of cells, but by a special serial connection of the 'standard' logic elements, namely four NAND gates [117]. However, such a realization consumes a lot of space and is highly error-prone due to the high number of cells required. The above mentioned approaches present alternative approaches involving coplanar as well

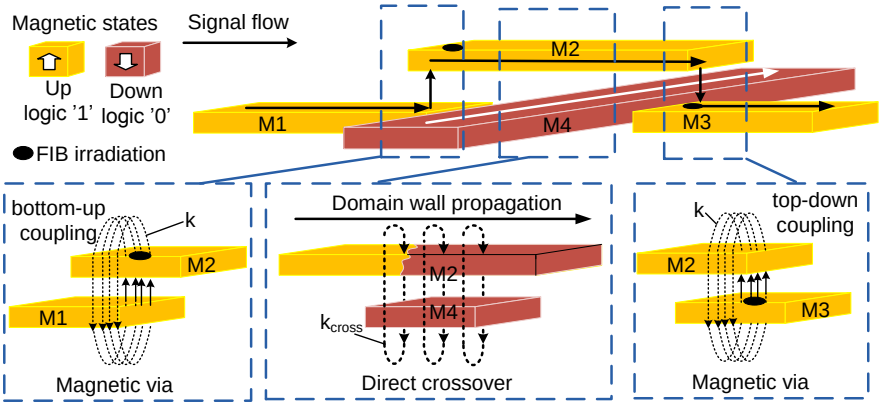

Figure 7.3: Multi-layer signal crossing in pNML [EBK+14].

as multi-layer crossing architectures. Multi-layer crossings have the benefit of being non-restricted to a local signal crossing, but they can transmit the signal to every place on the chip and not only to the next neighbor cell. Furthermore multi-layer crossings permit to cross more than one wire at the same time. For that reasons multi-layer crossings are more favorable. This work focuses on the easiest, most efficient and most robust solution for signal crossings in pNML. Hereby, the concept of multi-layer crossing is most promising, to achieve these aims.

7.2 Theory of magnetic signal crossing in pNML

The approach of a multi-layer crossing in pNML is similar to the one in QCA, where the signal is routed through a further functional layer. The concept is schematically shown in Fig. 7.3. Magnetic vias, whose functioning has been proven in the previous chapter 6 are exploited to vertically transmit the magnetic signal to another layer, where the actual crossover takes place. After crossing, the signal is transmitted back to its original layer, again exploiting vertical field-coupling ($\mathbf{k}$). The directionality of the via is defined by the position of the irradiation spot. In the direct crossover region, where also stray field interaction between the magnets is given (see Fig. 7.3 $\mathbf{k_{cross}}$ between M_2 and M_4), unimpeded domain wall propagation must be guaranteed constituting the most challenging part of the proposed realization. In contrast to the QCA approach, where the signal is not crossed in the direct next layer but in layers further apart (see Fig. 7.1 b, vertical signal transmission takes place over several cells and thereby over several layers guaranteeing for insufficient interaction in the direct crossover region), in our approach only a one layer signal routing is applied. This simplifies the fabrication process crucially. Hereby, for correct functioning, the field energy provided by the clocking field must always be high enough to propagate a domain wall in

the crossover region despite a hindering stray field ($\mathbf{k_{cross}}$) from M_4.
This condition is explained in detail in the following: Consider the reversal process of a single magnet. It can be split up in two main processes, namely a nucleation and a propagation process. First a domain wall must be nucleated at the amplitude $\mu_0 H_{Nuc}$. As soon as the domain wall was nucleated, it must be propagated by the amplitude $\mu_0 H_{Prop}$. By appropriate tuning the irradiation dose and multilayer film composition one can achieve that $\mu_0 H_{Nuc}$ is higher than $\mu_0 H_{Prop}$. By the way, this is the prerequisite for the correct functioning of all pNML devices. Hence, to achieve the total reversal of a magnet, the applied clocking amplitude $\mu_0 H_{Clock}$ must be equal to the nucleation field of a domain wall and after nucleation, $\mu_0 H_{Clock}$ must remain higher than the propagation field [EKB+13]:

$$\mu_0 H_{Clock} = \mu_0 H_{Nuc} > \mu_0 H_{Prop}. \tag{7.1}$$

In the case of two crossing magnets, the impact of $\mathbf{k_{cross}}$ has to be considered additionally (see Fig. 7.4 a). In the worst case, the direction of $\mathbf{k_{cross}}$ is opposed to the direction of the clocking field i.e. the effective acting field $\mu_0 \mathbf{H_{Eff}}$ in the direct crossover region is lowered [EKB+13]:

$$\mu_0 H_{Eff} = (\mu_0 H_{Clock} - |\mathbf{k_{cross}}|). \tag{7.2}$$

Whenever the reduction of the clocking field is higher than the required propagation field, the domain wall gets stucked. So a tighter condition for domain wall propagation in the crossover region is given [EKB+13]:

$$\mu_0 H_{Eff} = (\mu_0 H_{Clock} - |\mathbf{k_{cross}}|) > \mu_0 H_{Prop}. \tag{7.3}$$

As long as this condition is fulfilled, the domain wall propagates unimpeded. So in general, there are three parameters, which influence the functioning of the proposed signal crossing device, whereas $|\mathbf{k_{cross}}|$ is the one with the most impact. $\mu_0 H_{Nuc}$ can be tuned by the irradiation dose and $\mu_0 H_{Prop}$ by the film composition and the edge roughness. Both, $\mu_0 H_{Nuc}$ and $\mu_0 H_{Prop}$ are always tuned in the way to minimize the clocking energy. The parameter $|\mathbf{k_{cross}}|$ depends on the distance of the two functional layers, the overall magnetization of the magnets and the dimensions of the wires. As in pNML high coupling fields are favored in order to minimize the error-rate, a trade-off between high coupling fields and low clocking fields must be met to satisfy the condition given in eq. 7.3 (not to fall below $\mu_0 H_{Prop}$).
Note, coplanar crossings in pNML would result in errors. This case is illustrated in Fig. 7.4 b. As the coupling fields $\mathbf{k}$ of $I1$ and $I2$ act in opposed directions on the crossing magnet C, C is forced simultaneously in two different directions. Hence, during clocking, C follows the direction of the clocking field instead of aligning in the direction predefined by the coupling fields of $I1$ and $I2$. Thereby the information to be processed gets lost.

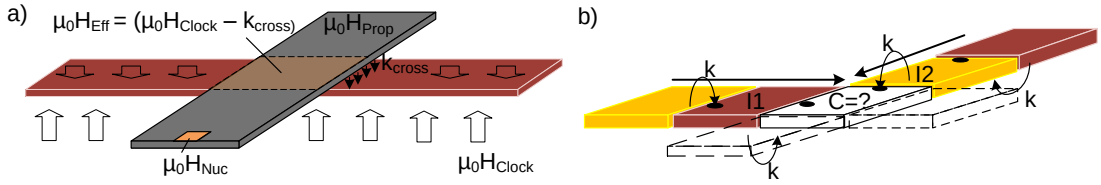

Figure 7.4: Multi-layer a) vs. coplanar crossing b) in pNML. (a) Illustration of the different field distributions in a clocked crossing structure. The scenario is depicted for a domain wall, that should be propagated in the top magnet, when the bottom magnet's magnetization is opposed to the clocking field direction. In the irradiation spot, $\mu_0 H_{Nuc}$ is required to nucleate the domain wall. In the remaining volume, $\mu_0 H_{Prop}$ must be satisfied. In the direct crossover region $\mu_0 H_{Clock}$ is reduced by the stray field $|\mathbf{k_{cross}}|$ of the bottom magnet. However, the amount of $\mu_0 H_{Eff}$ must remain higher than the one of $\mu_0 H_{Prop}$ to be able to propagate the domain wall in the crossover region. (b) Due to the symmetric coupling of $I1$ and $I2$ on C, C is forced simultaneously in two different directions resulting in erroneous signal processing [EBK+14].

7.3 Experimental demonstration

The experimental proof of the proposed signal crossing device is divided in two experimental setups. In a first setup only the two crossing wires on different functional layers are considered (M_2 and M_4 in Fig. 7.3) without the component of magnetic vias for vertical signal transmission. This setup shortens the fabrication process and makes it less error-prone at the same time. It serves to investigate, whether the condition of eq. 7.3 can be satisfied or not.
The second setup considers the whole crossing building block including signal routing from top to bottom layer and vice versa through the magnetic vias. The feasibility of signal transmission over the whole crossing structure within on clocking pulse is investigated here. More, it is investigated, whether fabrication variations can be kept small enough to define a clocking window for the fabricated signal crossing device.

7.3.1 Wire crossover - First setup

Fabrication

In the first setup, the following film composition for the two wires has been chosen: $Ti_{2nm}Pt_{4nm}Co_{0.4nm}4x(Pt_{1nm}/Co_{0.4nm})Pt_{5nm}$. The wires are fabricated by the process described in chapter 5. The two functional layers are separated by 30 nm of HSQ. This HSQ thickness is not critical here in terms of ion penetration depth

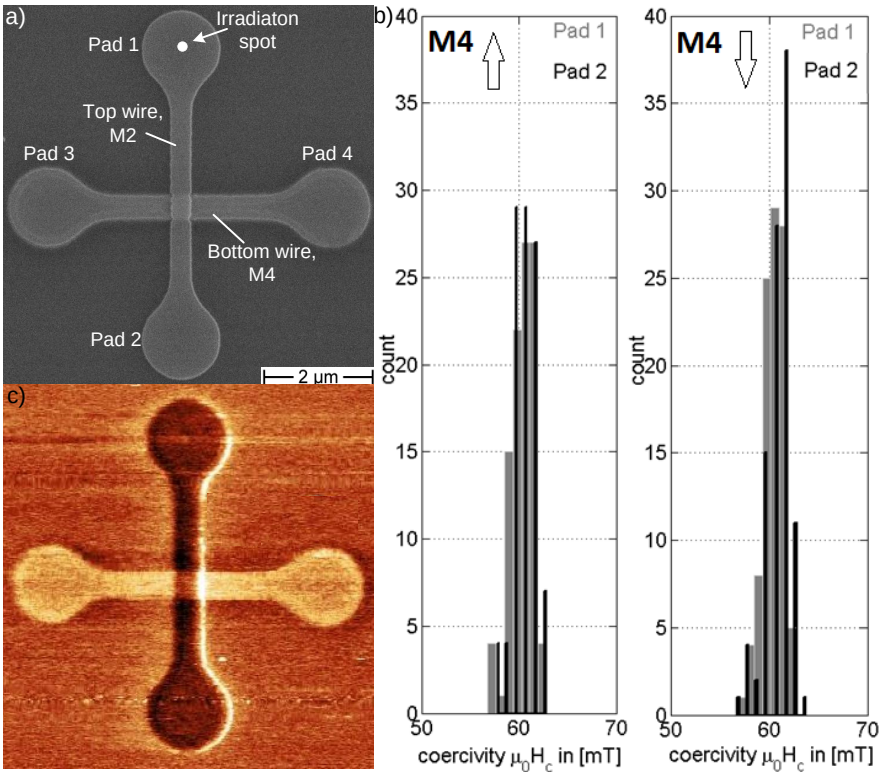

Figure 7.5: Analyses on the crossing wires [EKB+13]. (a) SEM image of the fabricated structure. (b) Overlapped SFD_Ts measured on Pad 1 and Pad 2 of top wire $M2$. The total overlap reveals, that in both cases, independent whether obstructive $\mathbf{k_{cross}}$ ($M4$ down) or supportive $\mathbf{k_{cross}}$ ($M4$ up), the domain propagates unimpeded. (c) MFM image taken after the nucleation field pulse.

because there is no irradiation needed in the direct crossover region. So damage of the bottom layer magnet can be excluded. However, this thin thickness of the HSQ layer is good to test the behavior of the crossing wires for high $|\mathbf{k_{cross}}|$.
The wires of both layers are identical in their dimensions. However, different wire sizes have been considered. The lengths of the wires have been chosen to be constant at 7 µm while the wire width varied between 300 nm, 500 nm and 750 nm.
The top wire $M2$ is irradiated at one end by a dose of 1×10^{14}Ions/cm^2 and a spot size of 80×80 nm^2 to control the domain wall nucleation site. The wires have rounded pads on their ends, with dimensions much larger than the wire width, to facilitate MOKE measurements. One of the fabricated structures is shown in Fig. 7.5 a.

Measurement results

To show correct functioning of the fabricated device, a domain wall in the irradiated region of the top magnet $M2$ must be nucleated and unimpeded domain wall propagation over the crossover region must be demonstrated, independently, which magnetization state the bottom magnet, $M4$ occupies.
In the initial state, both wires are magnetized in an either 'up' or 'down' state by a high saturation field pulse.
Here, an amplitude of 400 mT is sufficient to align both wires in one direction, as the mean switching field of all considered bottom wires has been determined to be below 160 mT and the one of all top irradiated wires to be below 90 mT. After saturation, $M2$ is switched alternately in the up and down state, while $M4$ maintains its magnetization state. The alternate switching of $M2$ guarantees that both cases, obstructive as well as supportive $\mathbf{k_{cross}}$ are given to test domain wall propagation. Therefore, the external field is swept with a rate of 100 mT/s, starting at zero field and ramping up to the amplitude of 100 mT in both directions. One hundred curves with a field resolution of 0.1 mT are recorded. The field amplitude is chosen to be above the switching field of the top wires but below the switching field of the bottom wires to not disturb their magnetization.
During measurement, hysteresis curves on measuring Pad 1 and 2 of $M2$ are recorded with the MOKE. Afterwards, the resulting $\mathrm{SFD_T}$s are derived from the measured hysteresis curves. To confirm unimpeded domain wall propagation, the $\mathrm{SFD_T}$ of Pad 1 has to overlap completely with the $\mathrm{SFD_T}$ of Pad 2. It means that the domain wall is nucleated on Pad 1 and arrives at Pad 2 at the same applied field amplitude, proving unimpeded signal flow.
A stopped domain wall would result in a significant deviation of the $\mathrm{SFD_T}$s of Pad 1 and Pad 2. If $|\mathbf{k_{cross}}|$ is too large, so that $\mu_0 H_{Eff}$ drops below $\mu_0 H_{Prop}$, further domain wall propagation can only be achieved by applying higher fields. In that case, the $\mathrm{SFD_T}$ of Pad 2 would be shifted to higher field values. Hence, from the shift of the SFDs of Pad 1 and Pad 2 it can be derived, whether the domain wall has propagated without hindrance or not.
The hysteresis curves have been measured for all possible configurations and for all given wire widths. The measurement results are summarized in Tab. 7.1 [Wu12]. The table contains the positive mean coercivities $\mu_0 H_{C,Mean}$ of hundred hysteresis curves measured on Pad 1 and Pad 2 of wire $M2$, while $M4$ kept either an 'up' or 'down' state. An 'up' state of $M4$ hereby means supportive $\mathbf{k_{cross}}$ (best case, lowest energy barrier potential). A 'down' state of $M4$ means obstructive $\mathbf{k_{cross}}$ (worst case, highest energy barrier potential). Furthermore, the corresponding standard deviations (σ) are determined. Both values, $\mu_0 H_{C,Mean}$ and σ characterize the resulting $\mathrm{SFD_T}$. Comparing the differences between the mean coercivities of Pad 1 and Pad 2, it can be seen, that the lowest difference amounts to 0 mT (cells marked in gray in the table) and the highest difference amounts to 0.8 mT

Table 7.1: Switching field analysis

Wire width [nm]	State $M4$	Pad of $M2$	Mean coercivity $\mu_0 H_{C,Mean}$ [mT]	Standard deviation σ [mT]
300	up	Pad 1	79.4	1.4
		Pad 2	79.4	1.3
	down	Pad 1	79.7	1.8
		Pad 2	79.6	2.8
500	up	Pad 1	60.6	1.4
		Pad 2	60.8	1.6
	down	Pad 1	60.7	1.6
		Pad 2	61.2	1.6
750	up	Pad 1	81.0	1.7
		Pad 2	79.2	2.1
	down	Pad 1	80.6	1.3
		Pad 2	79.9	1.7

(cells marked in green in the table), whereas this deviation is within the range of the standard deviation values. This fact confirms, that it is justified to say, that domain wall nucleation at Pad 1 and arrival at Pad 2 takes place at the same field amplitude revealing unimpeded domain wall propagation. These experiments prove, that even in the worst case, when $\mathbf{k_{cross}}$ is opposed to the external field, the amount of $\mu_0 H_{eff}$ in the crossover region remains high enough to propagate the domain wall through $M2$. Exemplary, the resulting SFD_Ts measured on Pad 1 and Pad 2 of a 500 nm wide crossing structure (the one shown in Fig. 7.5 a) are shown in Fig. 7.5 b. During measurement, $M4$ is once aligned in the 'up' and once in the 'down' direction.
Furthermore, these experiments reveal, that the wire width has no noticeable impact on the domain wall propagation. Those different widths were investigated to exclude domain wall pinning due to edge roughness. It is assumed that edge roughness giving the potential for domain wall pinning has a higher impact in narrowed than in wider structures. Albert et al. investigated the impact of edge roughness on domain wall motion. It is stated, that edge roughness introduces an additional depinning field $\mu_0 H_{depin}$ in the nanostructure [118]. The depinning field increases with decreasing wire widths [119]. For the investigated structures here, this means that, when a critical width is reached, the depinning field may

get higher than the provided external field and domain wall pinning occurs:

$$\mu_0 H_{Eff} = (\mu_0 H_{Clock} - |\mathbf{k_{cross}}|) < \mu_0 H_{depin} = \mu_0 H_{Prop}. \tag{7.4}$$

For narrowed structures, the edge roughness creates a significant decrease in the wire width, so that the critical width is reached more probably than in wider structures. However, the observance of domain wall pinning in the narrowest structures of this work (300 nm) has not been made. But note, even smaller widths and different lithography methods may lead to other results.
Further parameters like $|\mathbf{k_{cross}}|$ and $\mu_0 H_{Prop}$ are determined in the experiment. $|\mathbf{k_{cross}}|$ is determined with the aid of OOMMF simulations, as measuring $|\mathbf{k_{cross}}|$ directly on the fabricated structure is not possible. The simulations consider $|\mathbf{k_{cross}}|$ of different wire widths acting in the hight of 30 nm (distance between the two functional layers). Hereby, the magnetic wires are modeled as a 10 nm thick homogeneous layer with $M_S = 2.8 \cdot 10^5$ A/m. Those M_S value corresponds to the overall magnetization of the five layers of 0.4 nm Co, the wires are composed of. In the simulations, the middle part of the wire segment is evaluated, where the direct crossover takes place. Different wire widths have different impact on the magnitude of $\mathbf{k_{cross}}$. OOMMF simulations show, that for all wire widths, the maximum $|\mathbf{k_{cross,max}}|$ is reached at the edges of the wire, whereas the narrowest structure (300 nm) produces the highest stray field. Here a maximum $|\mathbf{k_{cross,max}}|$ of 9.3 mT is determined. The lowest stray field is produced by the 750 nm wide structure ($|\mathbf{k_{cross,max}}|$ amounts here to 8.1 mT at the edges).
The last parameter to be determined is $\mu_0 H_{Prop}$ of the domain wall. Measuring $\mu_0 H_{Prop}$ directly on the fabricated wires is not possible. However to have a first approximation of $\mu_0 H_{Prop}$ for the considered film composition, a demagnetized film is used. Demagnetization ensures a multi-domain state of the film. Consequently a demagnetized film possesses already domain walls. Applying an external field, $\mu_0 H_{Prop}$ is determined by the initial curve of the hysteresis. For the considered multilayer the propagation field amounts to 45 mT. Note, measuring $\mu_0 H_{Prop}$ on a continuous film does not consider the impact of edge roughness but gives a first estimation of the domain wall propagation field.
Adding $\mu_0 H_{Prop}$ and $|\mathbf{k_{cross,max}}|$ together, a minimum clocking field of 54.3 mT is required to guarantee unimpeded signal flow through the crossover region in the worst case. However, the nucleation field for the domain wall lies above 60 mT for the considered structures and thereby the required amplitude of the clocking field. This way it can be guaranteed, that the condition in eq. 7.3 is always satisfied and unimpeded domain wall propagation is ensured for all considered wire structures in this work.
In a last experiment, MFM measurements on the 500 nm wide crossing wires are performed (the one shown in Fig. 7.5 a). In the initial state, both wires are downwards magnetized applying a high field pulse of 400 mT in the down direction. Afterwards, a nucleation field pulse of 65 mT is applied for 500 ms. The resulting

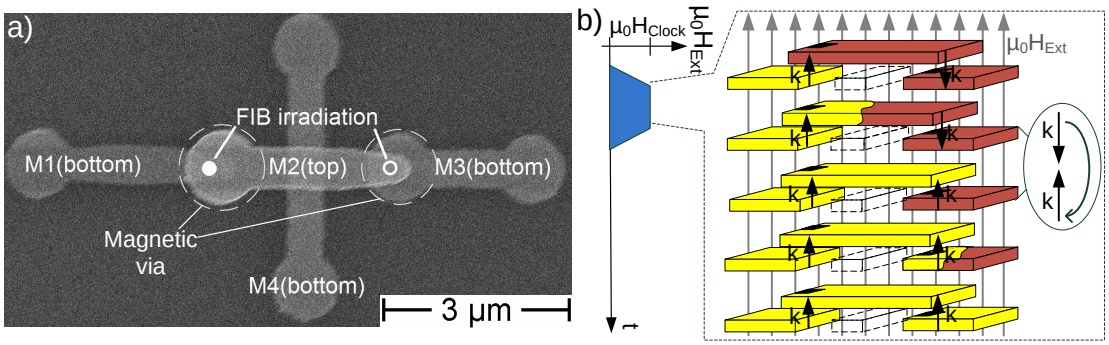

Figure 7.6: Crossing building block. (a) SEM image of the fabricated structure. (b) Corresponding signal transmission scenario within one clocking pulse. Signal is first transmitted from $M1$ to $M2$. As soon as $M2$ is completely reversed, its coupling field supports switching of $M3$.

magnetization states of both wires are shown in Fig. 7.5 c. The image shows two successfully crossed magnetic signals. The top wire possesses a single domain state proving, that the domain wall was not stopped in the crossover region.

7.3.2 Clocked multi-layer crossing - Second setup

Fabrication

The second setup considers the whole multi-layer crossing device, including the magnetic vias for vertical signal transfer (see Fig. 7.6 a). The aim is to show, that signal propagation over the whole crossing device is possible within one clocking pulse (see Fig. 7.6 b). Precondition for correct functioning is the existence of a clocking window. As already mentioned in sec. 6.1.4, thermally induced and fabrication dependent switching field variations narrow the clocking window and are hard to control. A parameter, which counteracts to this, is a high coupling field. Therefore the shape of the magnets and the layer composition of the new crossing device are accordingly adapted to meet this requirement. This time, the magnets are composed of a $Ti_{2nm}Pt_{4nm}Co_{0.6nm}4x(Pt_{1nm}/Co_{0.6nm})Pt_{5nm}$ film stack. The amount of Co constitutes 150% the amount of the previously discussed crossing structure. Furthermore the magnetic vias have pointy narrowed ends to achieve high concentrated fields at the ends. These two provisions enhance the coupling field.
$M2$ is sensitized to the bottom magnet $M1$ (forming an 'up via') and $M3$ to the stray field of $M2$ (forming a 'down via') by irradiating an area of $60\,\mathrm{x}\,60\,\mathrm{nm}^2$ with an ion dose of $1\,\mathrm{x}\,10^{13}\mathrm{Ions/cm}^2$. $M1$ and $M4$ are not irradiated and thereby possess high inherent switching fields. $M1$ serves as stable input, which is not affected by the external field during switching of $M2$ and $M3$.

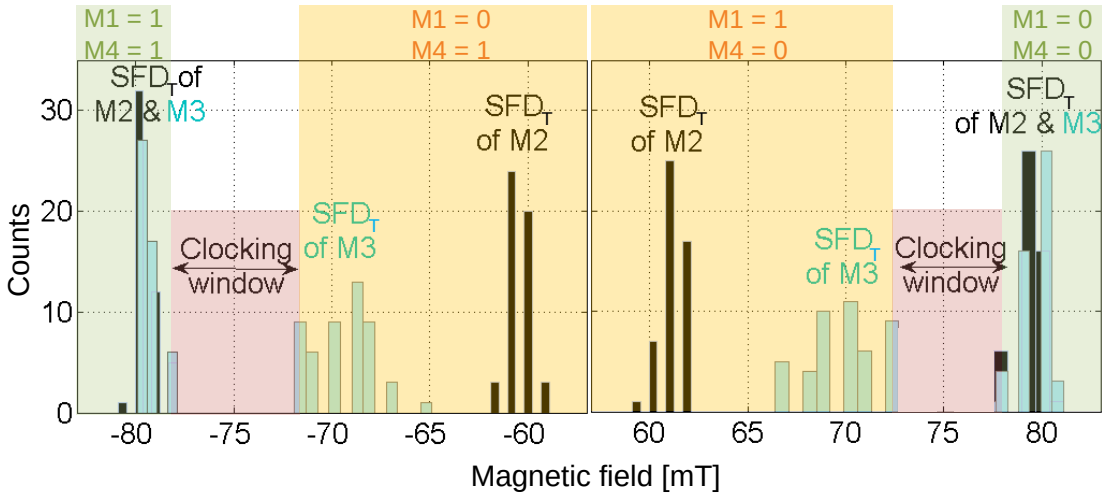

Figure 7.7: SFD_Ts of $M2$ and $M3$ for different alignments respectively to $M1$ and $M4$. Note, the magnetization state of $M4$ has always been chosen to be hindering for domain wall propagation in $M2$.

The separation between the first and second functional layer amounts to 30 nm. An additional change has been done in the fabrication process compared to the one applied for the previously discussed crossing structure. The partial Ar^+ pressure of Co has been reduced from 13 µbar to 11 µbar, in order to reduce $\mu_0 H_{Prop}$ [120]. In [120] it is claimed, that higher sputtering gas pressure leads to a mixture of the Co/Pt layers. This causes a magnetorestriction and thereby an additional contribution to the interface anisotropy. Consequently PMA is enhanced and thereby the coercivity of the magnetic film. Also we could observe in numerous experiments, that reducing the Ar^+ sputtering pressure also reduced the propagation- and the inherent switching field.

Measurement results

Hysteresis curve analysis of $M2$ and $M3$ help to define the clocking window. Thereby, the switching field values of $M2$ and $M3$ depending on their alignment respectively to $M1$ and $M4$ must be determined. Hereby, $M1$ and $M4$ are first set to a fixed state by a high external field pulse of 400 mT, as their mean switching field values have been determined to be below 380 mT. Note, the magnetization state of $M4$ is always chosen to be worst case, i.e. obstructive $\mathbf{k_{cross}}$ for domain wall propagation. Subsequently, $M2$ is switched alternately in the 'up' and 'down' state, thereby once aligning in the parallel and once in the anti-parallel state to $M1$. Therefore, the external field is swept with a rate of 100 mT/s, starting at zero field and ramping up to the amplitude of 100 mT in both directions. The field amplitude is chosen to be below the switching field of $M1$ and $M4$ to not disturb

their magnetization. Fifty hysteresis curves for every possible configuration of $M1$ and $M4$ are hereby recorded. The same measurements are repeated afterwards for $M3$. The results of the SFD_Ts derived from the hysteresis measurements are shown in Fig. 7.7. In the orange marked area lie the SFD_Ts of $M2$ and $M3$ whenever they aligned in the parallel state to $M1$. In the green marked area lie the SFD_Ts of $M2$ and $M3$ whenever they aligned in the anti-parallel state to $M1$. It can be clearly seen that parallel (supportive $\mathbf{k}$) ordering takes place at lower field values than anti-parallel ordering (obstructive $\mathbf{k}$), as expected. The switching field values for parallel and anti-parallel alignment are clearly separated, thereby leaving a clocking window. Furthermore it is obvious, that $M2$ switches in parallel to $M1$ before $M3$ does it ($\mu_0 H_{C,M2} < \mu_0 H_{C,M3}$). This confirms that signal transmission first takes place from $M1$ to $M2$ and afterwards from $M2$ to $M3$ when applying a clocking amplitude in the range of the clocking window.
A theoretical clocking scenario explaining the measured curves is shown in Fig. 7.6 b. $M1$ serves as stable input. In the initial state $M2$ and $M3$ possess an opposed magnetization state to $M1$. As soon as the clocking field is applied, the stray field ($\mathbf{k}$) of $M1$ transmits the signal to $M2$. Once, $M2$ is completely reversed, its stray field flips in the direction of the applied external field and now enables signal transmission to $M3$.
MFM measurements allow to visualize unimpeded signal flow during clocking. Applying field amplitudes of the mean coercivities of $M2$ and $M3$, determined with the aid of the hysteresis measurements, signal flow from $M1$ over $M2$ to $M3$ can be visualized. The MFM results are summarized in Fig. 7.8. In the initial state, $M2$ and $M3$ always occupy the opposed magnetization state to $M1$, while $M4$ is once aligned in the 'up' and once in the 'down' state. Thereby the four initial configurations are tested: $\{M_1 M_2 M_3 M_4\} \in \{0110, 0111, 1000, 1001\}$. After the first pulse with $\mu_0 H_{C,M2}$ the magnetization state of $M1$ is first transmitted to $M2$ and $M2$ remains single domain independent which magnetization state $M4$ occupies (supportive or obstructive $\mathbf{k_{cross}}$). This fact proves, that the domain wall propagated unimpeded through $M2$. After the second pulse, with $\mu_0 H_{C,M3}$ the magnetization state of $M2$ is transmitted to $M3$ and thereby to the original layer of the incoming signal $M1$. Note, the amplitude of $\mu_0 H_{C,M3}$ slightly differs (1 mT) in the experiment due to thermally induced switching field variations.
When applying the determined clocking amplitude in the range [73 mT − 78 mT], signal transmission within one clocking pulse from $M1$ to $M3$ over the crossing magnet $M2$ is observed.
Further experiments on the coupling strength in the magnetic vias and on the propagation field confirm an increase of $|\mathbf{k}|$ up to = 10 mT and a decrease of $\mu_0 H_{Prop}$ down to 18 mT. As expected $\mathbf{k}$ could be increased due to a higher amount of Co and an improved shape of the via ends (pointy ends compared to flat round ends). As expected the propagation field drops due to the reduced sputtering pressure.

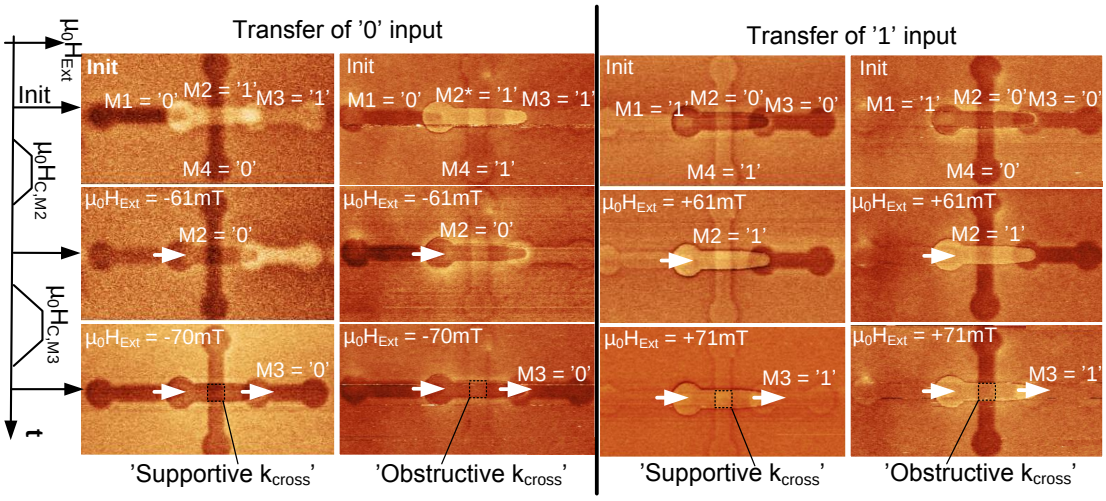

Figure 7.8: MFM measurements for all possible input configurations. After the first pulse, $M2$ adopts the magnetization state of $M1$ proving correct signal transmission through the 'up' via to the second layer. $M2$ always remains in the single domain state demonstrating unimpeded domain wall propagation without any hindrance by $\mathbf{k_{cross}}$ from $M4$. After the second field pulse, $M3$ adopts the magnetization state of $M2$, also proving correct signal transmission through the 'down' via.

The parameter $|\mathbf{k_{cross}}|$ is again determined with the aid of OOMMF simulations. $M4$ is modeled as a 10 nm thick homogeneous layer with $M_S = 4.2 \cdot 10^5$ A/m. This M_S value corresponds to the magnetization of the five layers of 0.6 nm Co the wires are composed of. To determine the amount of $\mathbf{k_{cross}}$, again the middle part of the wire segment is evaluated, where the direct crossover takes place. Hereby, a maximum $|\mathbf{k_{cross}}|$ of 15 mT was determined.
Adding $|\mathbf{k_{cross}}|$ and $\mu_0 H_{Prop}$ together gives 32 mT, whereas the applied clocking amplitude is in the range of [73 mT − 78 mT] proving that condition 7.3 can be always satisfied.

7.4 Conclusion

This chapter concludes the idea and the theoretical background of multi-layer signal crossing in pNML. Additionally other signal crossing approaches in QCA-based technologies are presented and compared. It is explained why multi-layer crossings are more favorable than coplanar crossings. The functionality of the proposed magnetic multi-layer crossing device is proven by means of two measurement setups. The first measurement setup investigates the direct crossover of

two magnetic wires, while the second setup considers the whole crossing structure including magnetic vias for signal routing in different functional layers. Both setups confirm correct functionality in terms of unimpeded signal flow. Furthermore the second setup guarantees signal transmission within one clocking pulse for all possible input configurations. However, it must be taken into account, that the duration of the clocking pulse must be long enough to ensure domain wall nucleation and propagation [BEZ+14] in all three magnets, which reduces the clocking frequency. Further parameters like $|\mathbf{k}|$ and $\mu_0 H_{Prop}$ are optimized to reduce the error-proneness of the device. The presented signal crossing device is the first experimentally proven in pNML. It consists of a minimum number of magnets, which makes it robust against fabrication dependent switching field variations. The shown multi-layer crossover enables flexible magnetic signal crossing on the chip, which is not locally restricted.

8 3D Majority Logic Gate in pNML

The 3D devices presented in the preceding chapters (magnetic via, multi-layer crossover) perform only transmitting operations, but no computing ones. The most basic element performing logic computing operations is the majority gate. A 3D implementation of the majority gate demonstrates the feasibility of 3D magnetic logic computing [EBZ+14], thereby representing a decisive progress of pNML in terms of integration density, error-proneness and design flexibility. In this chapter, the theoretical background, progressive characteristics, important design criteria and the proof of concept of a 3D majority gate are provided. All experimental results are propped by OOMMF simulations.

8.1 Theoretical background

The name majority gate descends from the majority decision, that an uneven number (>1) of input magnets perform on an output magnet. Every input produces a stray field, whereas the majority stray field direction controls the magnetization state of the output magnet. The most primitive majority gate consists of three input magnets and one output magnet (see Fig. 8.1). The magnetic stray fields $\mathbf{k_1}$, $\mathbf{k_2}$, $\mathbf{k_3}$ emanating from the three inputs I_1, I_2, I_3 superpose and force the output magnet O to align itself with the resulting net magnetic stray field $\mathbf{k_{Net}}$. One of the inputs (here I_3) programs the functionality of the gate to either NOR or NAND by tying its magnetization state permanently to either an 'up' or 'down' state. The remaining two inputs correspond to the alternating logic inputs. The 2D implementation has all four magnets located on one plane, while the 3D configuration has the third input located in a different functional layer. A comparison between the two concepts is depicted in Fig. 8.1. Note, the output is irradiated in order to be sensitive to the stray fields of the input magnets.

Switching behavior of the output O

The three input magnets influence the switching behavior of the output magnet O by their emanating stray fields. This influence becomes apparent in the switching field values of O (see Fig. 8.2 a-b). It is obvious, that without any influence of

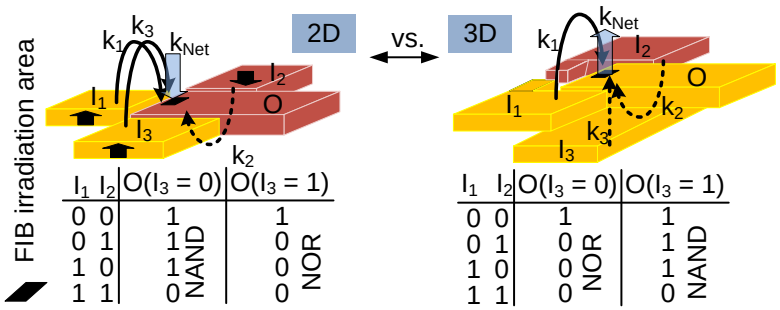

Figure 8.1: Comparative illustration of 2D and 3D implementation of the majority gate. The output O always aligns in the direction of resulting net stray field $\mathbf{k_{Net}}$ being the sum of stray fields $\sum_{\mathbf{i=1}}^{\mathbf{3}} \mathbf{k_i}$ emanated from the three inputs I_1, I_2, I_3. I_3 serves as stable input, which programs the functionality of the gate to either a NOR or NAND.

the input magnets, switching in the 'up' and 'down' state is similar resulting in the same coercivities $\pm\mu_0 H_C$ of O (indicated in (a)). However, in the presence of surrounding input magnets, the coercivity of O is shifted. In (b), the shift is exemplary indicated for the input configuration $\{I_1 I_2 I_3\} \in \{011\}$. It is assumed that the stray field of every input magnet has the same strength to ensure same influence on the output. The stray fields of I_1 and I_2 cancel each other out, so that only the stray field of I_3 remains that produces a $\mathbf{k_{Net}}$ in the 'up' direction. Applying an external field in the 'up' direction, $\mathbf{k_{Net}}$ superposes with the external field and in sum the amplitude $\mu_0 H_{Ext}$ required to switch O in the 'up' state is reduced by the amount of $|\mathbf{k_{Net}}|$. The switching of O in the opposed direction to the resulting $\mathbf{k_{Net}}$ is at the same time aggravated and requires an external field amplitude that is increased by the amount of $|\mathbf{k_{Net}}|$ to overcome its influence.
In summary, the configurations $\{I_1 I_2 I_3\} \in \{000, 001, 011, 101\}$ shift the hysteresis curve of O to the left, as they produce a $\mathbf{k_{Net}}$ pointing in the 'up' direction. Hereby switching of O in the 'up' state is facilitated by $\mathbf{k_{Net}}$ resulting in reduced switching field amplitudes. Switching in the 'down' state is inhibited by $\mathbf{k_{Net}}$ resulting in enhanced switching field amplitudes. For input configurations $\{I_1 I_2 I_3\} \in \{010, 100, 110, 111\}$ the hysteresis curves are shifted to the right, as a $\mathbf{k_{Net}}$ pointing in the 'down' direction is produced. Furthermore the shift is the highest for the input configurations $\{I_1 I_2 I_3\} \in \{001, 110\}$ as the sum of the input stray fields is maximal here and therefore the amount of $|\mathbf{k_{Net,max}}| = 3|\mathbf{k}|$. For all other configurations $\mathbf{k_{Net}}$ amounts to $|\mathbf{k_{Net,min}}| = |\mathbf{k}|$.

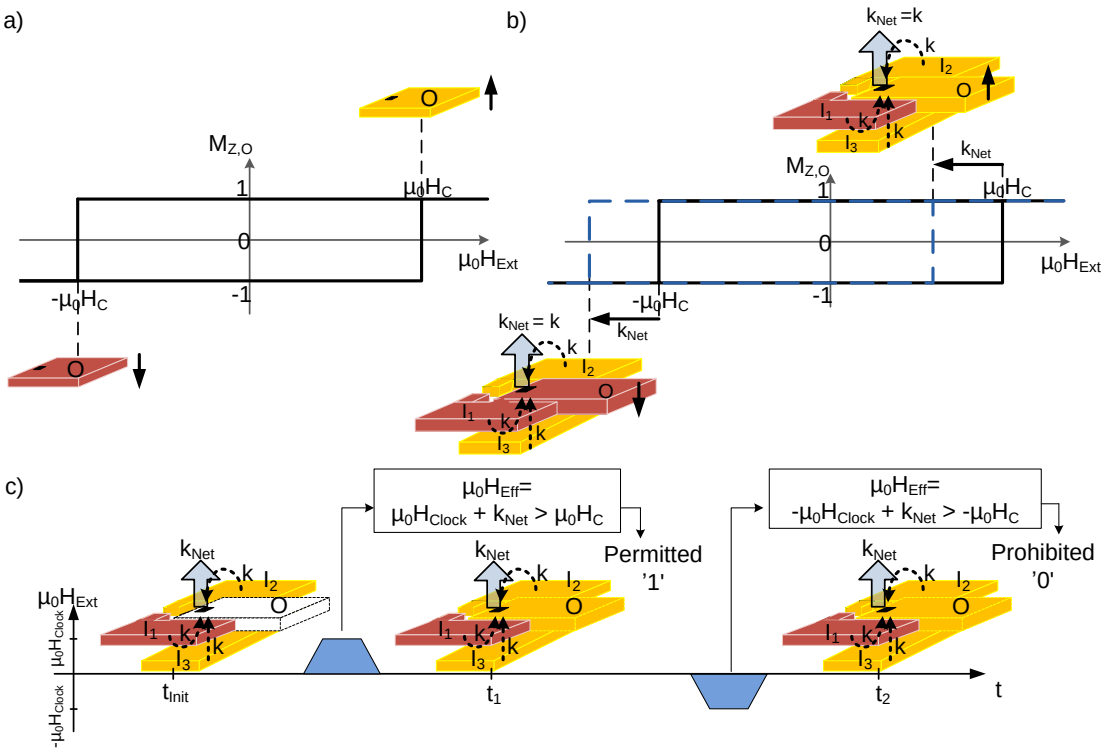

Figure 8.2: Schematic of switching behavior of O without influence of surrounding neighbor magnet (a) and under influence of three input magnets (b). (c) Gate clocking scenario. Whenever $\mathbf{k_{Net}}$ coincides with the clocking field, O is switched otherwise $\mathbf{k_{Net}}$ reduces the amplitude $\mu_0 H_{Clock}$ so that not enough field energy for switching of O is provided and incorrect switching cannot occur.

Gate clocking

The correct result of the output is always controlled and computed by the resulting $\mathbf{k_{Net}}$ that forces O in its direction, while the opposed direction is prohibited. During clocking exactly this behavior is exploited. The clocking amplitude $\mu_0 H_{Clock}$ lies thereby at the inherent switching field amplitude $\mu_0 H_C$ of O plus/minus supportive/obstructive $\mathbf{k_{Net}}$:

$$(\mu_0 H_C - |\mathbf{k_{Net}}|) < \mu_0 H_{Clock} < (\mu_0 H_C + |\mathbf{k_{Net}}|) \tag{8.1}$$

A possible clocking scenario is shown in Fig. 8.2 c. When applying the clocking amplitude, the amount $\mu_0 H_{Clock}$ is once enhanced by $\mathbf{k_{Net}}$ (clocking field and $\mathbf{k_{Net}}$ point in same direction), so that the inherent switching amplitude of $\mu_0 H_C$ of O is reached for sure and the desired switching of O occurs. In the next half clocking cycle $\mu_0 H_{Clock}$ is reduced by $\mathbf{k_{Net}}$ (clocking field and $\mathbf{k_{Net}}$ point

in opposed direction), so that $\mu_0 H_C$ of O is not reached and therefore incorrect switching cannot occur.

8.2 Experimental demonstration

8.2.1 Design criteria and fabrication

The most important design criterium is to achieve equivalent coupling fields of all three input magnets on the output magnet to guarantee similar influence of the inputs. If the coupling field of one input overweights the sum of the coupling fields produced by the two other inputs, the majority decision is no more valid and it comes to an erroneous function of the gate. Furthermore, variations in the coupling fields influence the width of the clocking window.
The realization of similar amount of $\mathbf{k}$ is especially challenging for the programming input lying in an additional functional layer. As already mentioned in chapter 6, the strength of the coupling field depends on the distance of the input magnet to the irradiation spot of the output magnet and on the magnet's shape. When considering the structure of the proposed 3D majority gate (Fig. 8.1), it is obvious that the inputs I_1 and I_2 have identical shapes and same distance to the irradiation spot of O. This way, similar $|\mathbf{k}|$ of I_1 and I_2 can be easily guaranteed. However, the stray field lines and their pathway differ in horizontal and vertical direction. Consequently, the coupling field produced by I_3 is acting differently. Thus, the shape, the magnetization of I_3 and the vertical distance between I_3 and O have to be adequately adapted to achieve the same coupling field as produced by $I_1|I_2$.
A possible layout of the majority gate is shown in Fig. 8.3 a. The big rounded pads of the magnets are required for MOKE measurements to satisfy its limited resolution. The best design for I_1 and I_2 (highest $|\mathbf{k}|$) would be a shape, where both inputs enclose the irradiated area of O as much as possible. The more material surrounds the irradiated area, the higher is $|\mathbf{k}|$ acting in the irradiated area. To have a first estimate of the produced $|\mathbf{k}|$ by $I_1|I_2$, OOMMF simulations are performed. The magnets are modeled as a 10 nm thick homogeneous layer with $M_{S,High} = 4.2 \cdot 10^5$ A/m. This value corresponds to a $5 \times \mathrm{Co}_{0.6\,\mathrm{nm}}$ amount in the Co/Pt multilayer stack the magnets are supposed to be composed of. The simulation results show, that the stray field acting in the irradiation area is approximately $|\mathbf{k}| = [5 - 6]$ mT as shown in Fig. 8.3 b.
To achieve the same $|\mathbf{k}|$ for I_3, simulations have been performed, considering different shapes (indicated by the yellow line in Fig. 8.3 a), film compositions (different M_S) and vertical distances between I_3 and O. The results are summarized in Fig. 8.3 c) - e) in contour diagrams that envision the areas with the corresponding $|\mathbf{k}|$ in mT, acting in a certain height z above the actual input I_3 (note, the irradiated

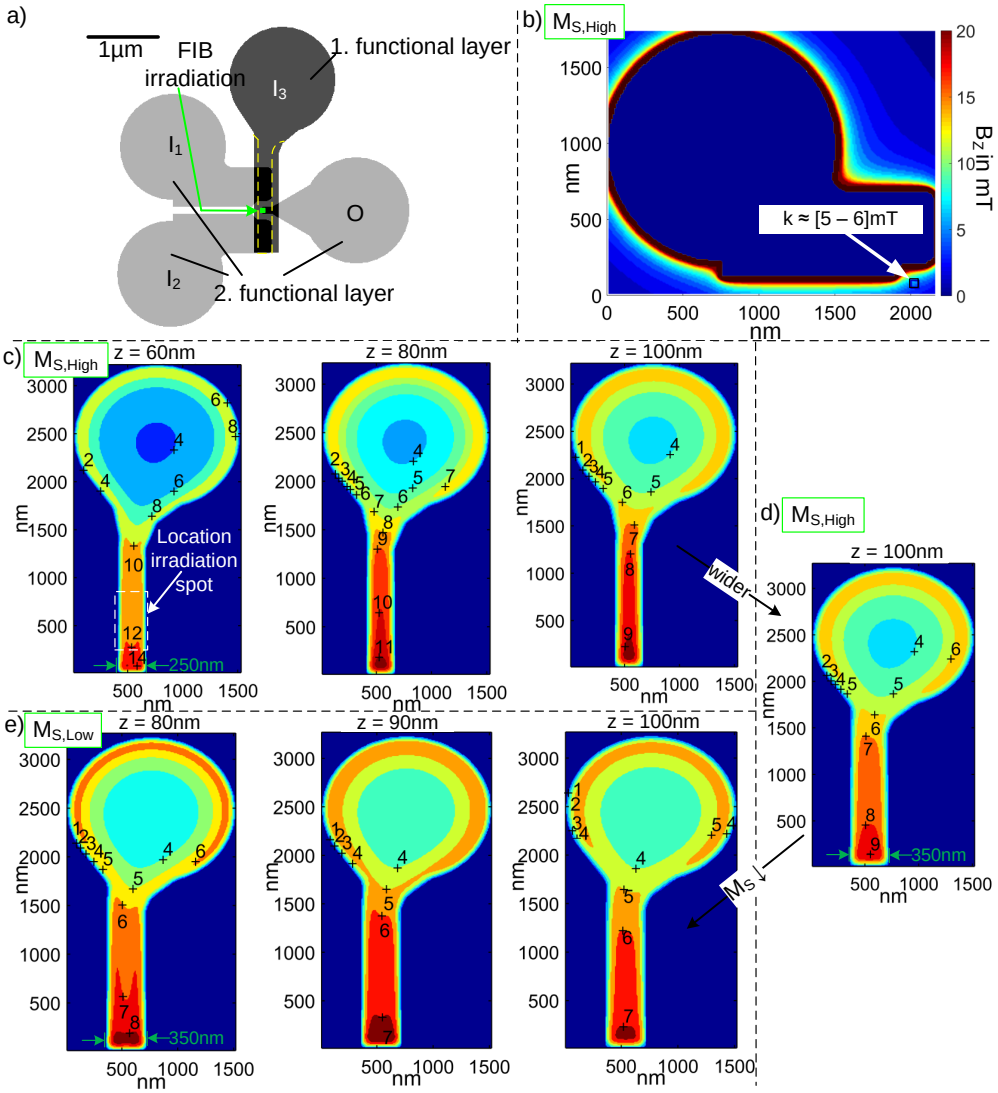

Figure 8.3: Proposed layout and simulation results of the emanated coupling fields. (a) 3D majority gate layout. The yellow dashed line indicates different widths of I_3. (b) Simulated $|\mathbf{k}|$ produced by $I_1|I_2$. At the position of the irradiation spot of O, $\mathbf{k}$ amounts to $[5-6]$ mT. (c)-(e) Contour diagrams of the produced $|\mathbf{k}|$ by I_3 in different heights z above I_3, for different M_S, and different width of I_3. The structure shown in e) has been applied for the experiment.

O is positioned in a certain height z above I_3). As the position of the irradiation spot of O respectively to I_3 in the plane strongly depends on the precision of the alignment of top to bottom layer a larger area of I_3 is evaluated for the resulting $|\mathbf{k}|$ that may act in the irradiation spot of O. The area is indicated in c) and is

valid for all investigated contour diagrams including c)-e).
Simulations results shown in c) and d) relate to the same $M_{S,High}$ as chosen for $I_1|I_2$. It is tested, whether all three input magnets can be composed of the same film stack. In c) a 250 nm wide line constitutes the input I_3. It is obvious, that the height $z = 60$ nm is not suitable. Here, the resulting $|\mathbf{k}|$ amounts twice the calculated one for $I_1|I_2$. Even if the height is increased from 60 nm up to 100 nm, the resulting $|\mathbf{k}|$ is too strong (8 mT). However, when the width of I_3 is increased up to 350 nm (see d), $|\mathbf{k}|$ can be further reduced to 7 mT but still remains to high. The reduction is due to the improved distribution of the high edge amount compared to the magnet's surface. Simulation results presented in e) relate to the same shape as shown in d) (350 nm width) but with a lower $M_{S,Low} = 3.36 \cdot 10^5$ A/m corresponding to 4 $\times$ $Co_{0.6\,nm}$ amount in the Co/Pt multilayer stack. Also here, different heights have been investigated. It is obvious, that a reduction of M_S further reduces $|\mathbf{k}|$ to 6 mT, which corresponds to the searched for $|\mathbf{k}|$, also produced by $I_1|I_2$.
These simulations demonstrate the influence of different parameters, more precisely the shape, magnetization and height on the amount of $\mathbf{k}$. Hereby, the simulations performed in e) show the most suitable results for I_3 to match the $|\mathbf{k}|$ produced by $I_1|I_2$. Furthermore, parameters chosen in e) are robust against variations in height. All simulated heights (80 nm,90 nm,100 nm) lead to low variations in $|\mathbf{k}|$.
Consequently, for the fabrication of the gate, the parameters figured out in e) were applied. Hereby, the most-bottom layer comprising the programmable input I_3 is composed of a $Ti_{1\,nm}Pt_{5\,nm}Co_{0.6\,nm}3x(Pt_{1\,nm}/Co_{0.6\,nm})Pt_{3\,nm}$. The magnets of the first functional layer are planarized by HSQ, which result in a total HSQ separation layer thickness of 60 nm. The second functional layer comprising $I_1|I_2$ and O has one more Co-layer: $Ti_{1\,nm}Pt_{5\,nm}Co_{0.6\,nm}4x(Pt_{1\,nm}/Co_{0.6\,nn})Pt_{3\,nm}$. To sensitize O to the inputs, a small area of (40 nm x 40 nm) is irradiated by a dose of $1 \cdot 10^{14}$Ions/cm^2.
A SEM image of the fabricated gate is shown in Fig. 8.4. The size of the magnets is in the µm regime to enable MOKE measurements. However, the actual computing area of the gate accounts to $\approx 700\,\text{nm} \cdot 550\,\text{nm}$, as will be shown in a subsequent section 8.2.4.

8.2.2 Measurement results

The functionality of the fabricated gate is verified via measurements with the MOKE and the MFM. The hysteresis curve measurements performed with the MOKE serve to determine the clocking window and the coupling field of every single input. The MFM measurements manifest the final magnetization state of all four magnets after the gate has been clocked with the determined clocking amplitude.

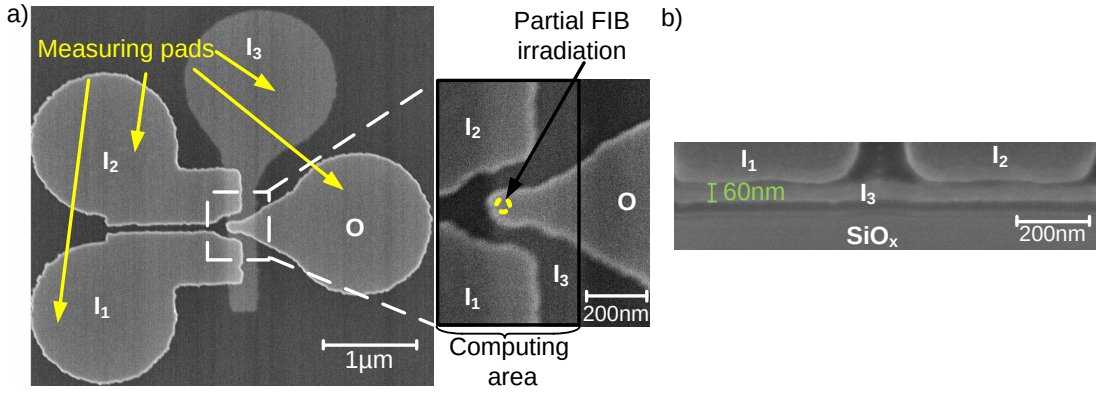

Figure 8.4: SEM images of the fabricated majority gate [EBZ+14]. (a) Top view including an enlarged extract of the computing area. I_3 is located in the bottom functional layer.(b) Cross section making obvious the distance between first and second functional layer. To take this image, the sample was rotated to 45° respectively to the beam path.

MOKE measurements

Hysteresis curve measurements are performed to analyze the switching behavior of O and to determine the resulting net stray field $|\mathbf{k_{Net}}|$ for every possible input configuration. Thereout, the $\mathrm{SFD_T}$s are determined and the remaining clocking window derived.
At first the three inputs are set to one of the eight possible input configurations by appropriate external field pulses. Due to variations in the fabrication process, all three input magnets possess different switching fields. The mean switching fields have been determined to: $\mu_0 H_{C,I_1} = 153\,\mathrm{mT}$, $\mu_0 H_{C,I_2} = 122\,\mathrm{mT}$ and $\mu_0 H_{C,I_3} = 105\,\mathrm{mT}$. These variations allow for setting the inputs by applying external field pulses with different amplitudes, starting with the input having the highest coercive field followed by the inputs with decreasing coercivities. Hereby, the amplitude of the external field was appropriately lowered to not overwrite or disturb the magnetization state of the previously set magnet. For example, to achieve a $\{\mathrm{I_1 I_2 I_3}\} \in \{101\}$ configuration, first a pulse of $+160\,\mathrm{mT}$ is applied, setting I_1 in the 'up' state. Second, a pulse of -130 mT is applied, setting I_2 in the 'down' state without disturbing the magnetization state of I_1, as the field amplitude required to reverse I_1 amounts to $|153\,\mathrm{mT}|$. At last a pulse of $+110\,\mathrm{mT}$ is applied to set I_3 in the 'up' state without overwriting the magnetization states of I_2 and I_3. The pulse length was 1s thereby guaranteeing that the whole magnet is reversed within one pulse.
After the input configuration is set, O is switched in turns in the parallel and antiparallel state to the resulting $\mathbf{k_{Net}}$ and the hysteresis curves are recorded by the

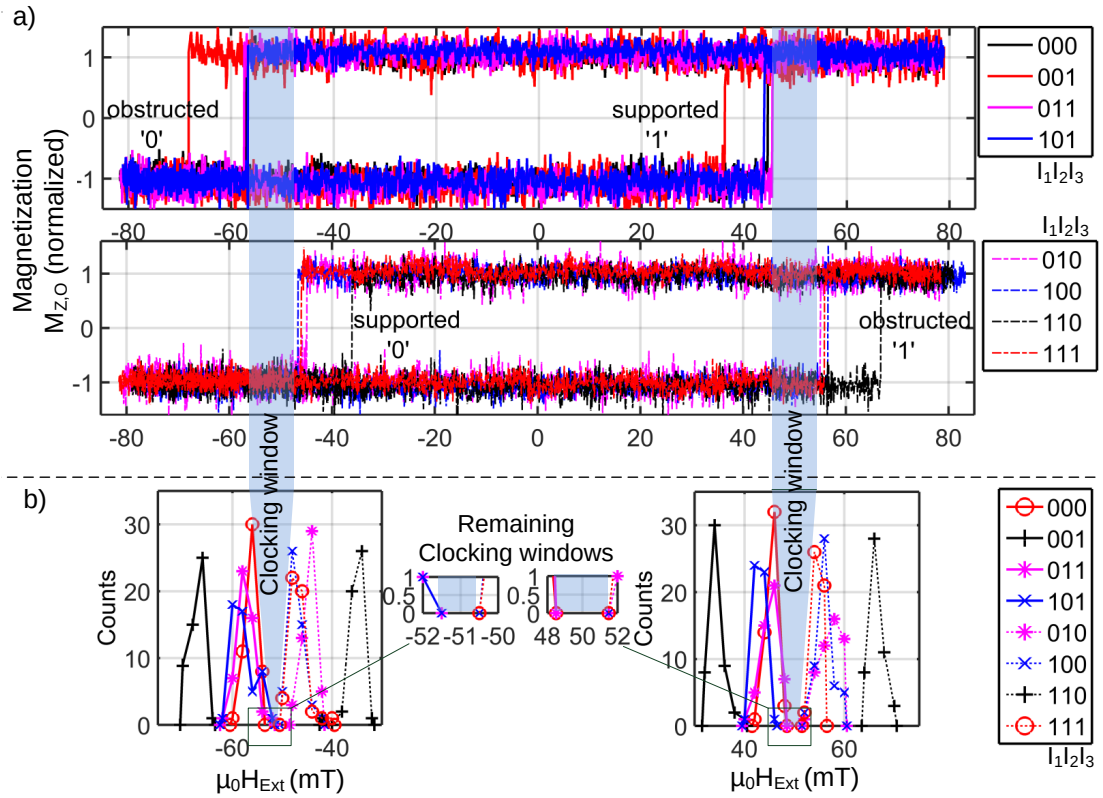

Figure 8.5: MOKE measurement results [EBZ+14]. (a) Eight hysteresis curves of O, measured for each possible input configuration $\{I_1I_2I_3\}$. (b) SFD_Ts of O derived from fifty switching cycles per each possible input configuration. The clocking window lies in between the SFD_Ts for 'supported' and 'obstructed' switching.

MOKE measurement setup. Due to irradiation of O, its switching field value is highly reduced in comparison to the input magnets. This provides the possibility to investigate its switching behavior without overwriting the inputs. To switch O in the 'up' and 'down' state, the external field is ramped up from 0 mT to 80 mT in 0.1 mT steps in the positive and negative direction at a sweep-rate of 100 mT/s. The maximum field amplitude of 80 mT enables to record the hysteresis curves of the output magnet for all possible input configurations without disturbing the magnetization states of the input magnets. The measurement results are summarized in Fig. 8.5 a.

Considering the eight hysteresis curves shown in Fig. 8.5 a their asymmetric behavior is obvious. As expected, configurations $\{I_1I_2I_3\} \in \{000, 001, 011, 101\}$ shift the hysteresis curves to the left. The required external field amplitudes to switch O in the 'up' state are reduced by the corresponding $\mathbf{k_{Net}}$, while 'down' switching

Table 8.1: Mean switching field values of O

Input			Output		
I_1	I_2	I_3	$\mu_0 H_{C,mean}$ $(O \mapsto 0)$	$\mu_0 H_{C,mean}$ $(O \mapsto 1)$	Clocked O
0	0	0	-57 mT	45 mT	1
0	0	1	-67 mT	36 mT	1
0	1	1	-57 mT	44 mT	1
1	0	1	-57 mT	43 mT	1
0	1	0	-45 mT	56 mT	0
1	0	0	-46 mT	56 mT	0
1	1	0	-37 mT	67 mT	0
1	1	1	-45 mT	54 mT	0

(opposed to the resulting $\mathbf{k_{Net}}$) is obstructed and requires higher amplitudes.
As expected, the input configurations $\{I_1 I_2 I_3\} \in \{010, 100, 110, 111\}$ shift the hysteresis curves to the right. Here, switching in the 'down' state (parallel to the resulting $\mathbf{k_{Net}}$) is supported and requires lower field amplitudes than for the 'up' switching.
Furthermore, the curves confirm that the shift is the highest for the input configurations $\{I_1 I_2 I_3\} \in \{001, 110\}$, as the resulting $\mathbf{k_{Net}}$ is the highest here. These first measurements demonstrate that 'supported' and 'obstructed' states of O are clearly separated leaving a wide clocking window.
However, as already mentioned in chapter 6, the switching field of a magnet is distributed over time due to thermal noise [110, 111]. For a high number of switching cycles, the switching field values of O vary in a certain range, thereby narrowing the clocking window. Hence, for error rate analysis and to guarantee the correct functionality of the gate even in the presence of thermal noise, the experiments were repeated for a high number of clocking cycles. In sum, for each possible input configuration, fifty hysteresis curves of O were recorded. Thereout, the $\mathrm{SFD_T}$s were derived, presented in Fig. 8.5 b. The corresponding mean switching field values are summarized in Table 8.1.
As expected, the clocking window is significantly narrowed. Nevertheless, the $\mathrm{SFD_T}$s obtained for the configurations $\{000, 001, 011, 101\}$ and $\{010, 100, 110, 111\}$ are still separated from each other proving the correct functionality of the gate. In case of overlap, it cannot be clearly distinguished between 'supported' and 'obstructed' states and therefore between logic '1' and '0'.
The mean switching field values can be exploited to calculate $|\mathbf{k}|$ emanated from every single input I_x, with x $\in (1, 2, 3)$. The influence of every single input shifts the hysteresis curve by $\pm|\mathbf{k}|$ to the left and right respectively. Hence, $|\mathbf{k}|$ can be determined from the difference of the mean switching field values of O, where $I_x = 1$ and $I_x = 0$ divided by two. As eight values of $\mu_0 H_{C,mean}$, where $I_x = 1$ and

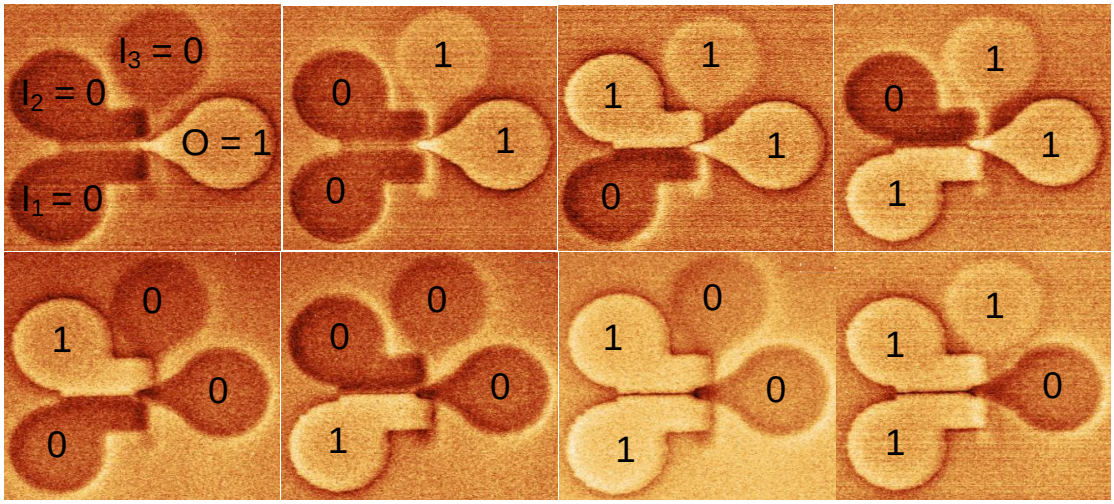

Figure 8.6: MFM images revealing the magnetization states of all four magnets temporally acquired after one clocking cycle. The input configurations $\{I_1 I_2 I_3\} \in \{000, 001, 011, 101\}$ computed the '1' state of O correctly. The input configurations $\{I_1 I_2 I_3\} \in \{010, 100, 110, 111\}$ computed the '0' state of O correctly.

$I_x = 0$ each are given, the whole expression has to be additionally divided by eight:

$$|\mathbf{k_{I_x}}| = \mu_0 \frac{(\sum_{i=1}^{8} H_{C,mean}(I_x = 1) - \sum_{i=1}^{8} H_{C,mean}(I_x = 0))}{2 \cdot 8}. \tag{8.2}$$

Resolving eq. 8.2 with the values of $\mu_0 H_{C,mean}$ given in Table 8.1 yields: $|\mathbf{k_{I_1}}| = 5\,\mathrm{mT}$, $|\mathbf{k_{I_2}}| = 5.25\,\mathrm{mT}$ and $|\mathbf{k_{I_3}}| = 5\,\mathrm{mT}$.
The values reveal, that the influence of each input varies by 5%. Depending on the input configuration, the maximum value of $|\mathbf{k_{Net}}|$ can reach up to 15.25 mT and the minimum $|\mathbf{k_{Net}}|$ is 4.75 mT.

MFM measurements

High-resolution images acquired by MFM reveal the final magnetization states of all four magnets after gate clocking (see Fig. 8.6). Therefore the inputs were set to one of the possible eight input configurations by applying the required external field amplitudes (same procedure as done for MOKE). Afterwards the gate is clocked, applying one alternating field pulse with the amplitude of 51 mT (determined from the clocking window). Evaluating the resulting MFM images, it is obvious, that for every input configuration after one clocking cycle at the latest the magnetization state of O was ordered correctly by the resulting $\mathbf{k_{Net}}$.

8.2.3 Error rates and critical parameters

The error rate of the considered gate can be calculated determining the probability for an overlap between the SFD_Ts resulting from configurations $\{000, 001, 011, 101\}$ and $\{010, 100, 110, 111\}$. It is assumed that the switching field values of O are randomly distributed [111]. The normal distribution is therefore suitable for the calculation of the searched for probability. In the following, it is first summarized, how a certain probability for a normally distributed stochastic variable can be calculated. In a second step, the derived formulas are applied to calculate the searched for 'overlap probability' $P_{Overlap}$ of the gate.

Determination of probability for normally distributed stochastic variables

All following explanations are additionally graphically illustrated in Fig. 8.7a for better understanding. As already mentioned, the switching field value $\mu_0 H_C$ of O is a stochastic variable with a expectancy value μ_H and the standard deviation σ_H. The corresponding probability density function $f(x)$, which is an expedient to describe the probability distribution of $\mu_0 H_C$ is defined as:

$$f(x) = \frac{1}{\sqrt{2\pi}\sigma_H} e^{-\frac{1}{2}(\frac{x-\mu_H}{\sigma_H})^2}. \tag{8.3}$$

The integration over $f(x)$ within an interval $[a; b]$ gives the probability P, that O switches within this interval:

$$P(a \leq \mu_0 H_C \leq b) = \int_a^b f(x)dx. \tag{8.4}$$

The value of P constitutes to the area the graph $f(x)$ encloses with the x-axis within the given interval. When the area is enclosed within the boarders $[-\infty; +\infty]$, P amounts to 1. Consequently, the probability $\bar{P}$, that O does not switch within the given integral $[a; b]$ can be calculated by:

$$\bar{P} = 1 - P. \tag{8.5}$$

To determine the value for the integral of $f(x)$, it is common to utilize the normal distribution, which defines the value of the integral from $-\infty$ to a random boarder c:

$$F(c) = \int_{-\infty}^{c} f(x)dx = \int_{-\infty}^{c} \frac{1}{\sqrt{2\pi}\sigma_H} e^{-\frac{1}{2}(\frac{x-\mu_H}{\sigma_H})^2} dx. \tag{8.6}$$

The normal distribution can then be normalized to the standard normal distribution ϕ, whose values can be easily extracted from a look-up table. The required substitution therefore is: $z = \frac{x-\mu_H}{\sigma_H}$ and $dz = \frac{dx}{\sigma_H}$. Inserting this in eq. 8.6 gives:

$$\phi(\frac{c-\mu_H}{\sigma_H}) = \int_{-\infty}^{\frac{c-\mu_H}{\sigma_H}} \frac{1}{\sqrt{2\pi}} e^{-\frac{1}{2}z^2} dz. \tag{8.7}$$

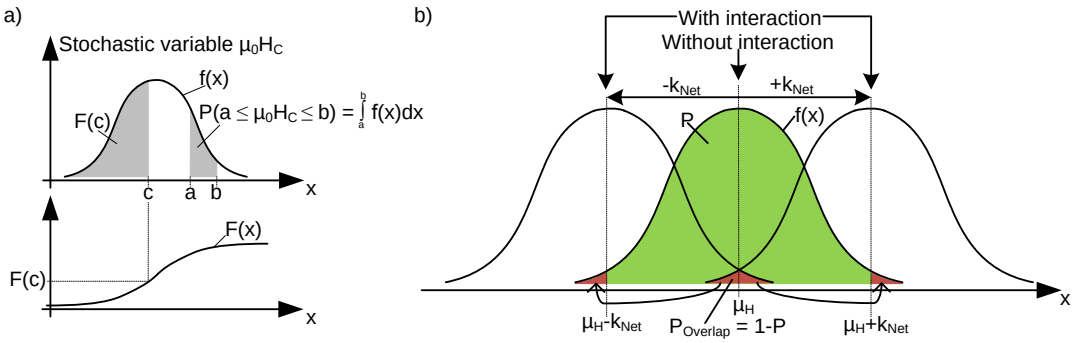

Figure 8.7: Normal distribution and probability calculation. (a) The probability for $\mu_0 H_C$ being within $[a; b]$ can be calculated by integrating over the probability density function $f(x)$. The integral can be solved with the aid of the normal distribution function F(x). (b) Tagging of the overlap area between two shifted $f(x)$ graphs representing two shifted $\mathrm{SFD_T}$s of O. The shift occurs due to interaction of O with the input magnets by $\mathbf{k_{Net}}$. Simplified, $P_{Overlap}$ can be found in the area outside the interval $[(\mu_H - |\mathbf{k_{Net}}|); (\mu_H + |\mathbf{k_{Net}}|)]$, that $f(x)$ encloses with the x-axis. This simplification enables the calculation of $P_{Overlap}$.

Applying eq. 8.6 and eq. 8.7 to eq. 8.4, the expression for P can be replaced by:

$$\begin{aligned} P(a \leq \mu_0 H_C \leq b) &= \int_{-\infty}^{b} f(x)dx - \int_{-\infty}^{a} f(x)dx \\ &= F(b) - F(a) \\ &= \phi(\frac{b-\mu_H}{\sigma_H}) - \phi(\frac{a-\mu_H}{\sigma_H}). \end{aligned} \tag{8.8}$$

Determination of $P_{Overlap}$

All following explanations are additionally graphically illustrated in Fig. 8.7 b for better understanding. As already mentioned, to determine the error-rate of the considered gate, the overlap probabilities $P_{Overlap}$ between the $\mathrm{SFD_T}$s resulting from the configurations $\{000, 001, 011, 101\}$ and $\{010, 100, 110, 111\}$ must be calculated. The way to calculate this is explained by the following consideration.
The $\mathrm{SFD_T}$ of O can be expressed by f(x) given in eq. 8.3 with μ_H being the expectancy value of the switching field of O and σ_H being the standard deviation of the switching field. If interaction between the inputs and O is given, the $\mathrm{SFD_T}$ of O is shifted by the resulting $|\mathbf{k_{Net}}|$ to the left and to the right respectively and so is $f(x)$ (see Fig. 8.7 b). $P_{Overlap}$ between the two shifted graphs of f(x), however

can be easily calculated, when considering that the overlap area constitutes to the same area that lies outside the interval $[(\mu_H - |\mathbf{k_{Net}}|); (\mu_H + |\mathbf{k_{Net}}|)]$, that $f(x)$ encloses with the x-axis (see Fig. 8.7 b). Consequently, $P_{Overlap}$ is:

$$P_{Overlap} = 1 - P((\mu_H - |\mathbf{k_{Net}}|) \leq \mu_0 H_C \leq (\mu_H + |\mathbf{k_{Net}}|)), \tag{8.9}$$

whereas P represents, the probability that O does switch within the interval $[(\mu_H - k_{Net}); (\mu_H + k_{Net})]$. P can be calculated with the aid of the standard normal distribution and the expression derived in eq. 8.8:

$$P((\mu_H - |\mathbf{k_{Net}}|) \leq \mu_0 H_C \leq (\mu_H + |\mathbf{k_{Net}}|)) = \phi(\frac{+|\mathbf{k_{Net}}|}{\sigma_H}) - \phi(\frac{-|\mathbf{k_{Net}}|}{\sigma_H}). \tag{8.10}$$

As $f(x)$ is symmetrical to the straight line at $x = \mu_H$, the expression is valid:

$$\phi(\frac{-|\mathbf{k_{Net}}|}{\sigma_H}) = 1 - \phi(\frac{+|\mathbf{k_{Net}}|}{\sigma_H}). \tag{8.11}$$

Inserting eq. 8.11 in eq. 8.10 results in:

$$P((\mu_H - |\mathbf{k_{Net}}|) \leq \mu_0 H_C \leq (\mu_H + |\mathbf{k_{Net}}|)) = 2\phi(\frac{+|\mathbf{k_{Net}}|}{\sigma_H}) - 1. \tag{8.12}$$

The searched for overlap probability is then:

$$P_{Overlap} = 1 - P((\mu_H - |\mathbf{k_{Net}}|) \leq \mu_0 H_C \leq (\mu_H + |\mathbf{k_{Net}}|)) = 2 - 2\phi(\frac{+|\mathbf{k_{Net}}|}{\sigma_H}). \tag{8.13}$$

For the considered gate, a worst case approximation has been undertaken to calculate the error-rate. This means, that the highest σ_H and the smallest $|\mathbf{k_{Net}}|$ have been applied to calculate $P_{Overlap}$. The smallest possible $|\mathbf{k_{Net}}|$ amounts to 4.75 mT as determined in the previous subsection 8.2.2. σ_H was determined for every measured $\mathrm{SFD_T}$ of O. Therefore, each $\mathrm{SFD_T}$ was fitted by a Gaussian curve using the MATLAB Curve Fitting tool [121] (least square fit) and the resulting σ_H determined by a comparison of the coefficients. The highest σ_H was determined to be 2.3 mT. The resulting value of ϕ for the boarder $\frac{+|\mathbf{k_{Net}}|}{\sigma_H} = 2.06522$ amounts to 0.980, as taken from the look-up table [122]. The searched for overlap probability $P_{Overlap}$ as derived in eq. 8.13 amounts thereby to 4% representing the maximum error rate of the gate.

The amount of $\mathbf{k_{Net}}$ is crucial for the correct functionality of the gate. It defines the width of the clocking window and thereby the area of overlap between the $\mathrm{SFD_T}$s of the gate's output O. There are several parameters that influence

the strength of $\mathbf{k_{Net}}$. The influence of the total ferromagnetic amount and inter-magnet distance have already been discussed in sec. 6.2. The more ferromagnetic amount and the closer the input magnet is situated to the irradiation spot of the output magnet, the higher is the coupling field.
The fabricated 3D gate structure also contributes to a higher $|\mathbf{k_{Net}}|$ compared to the 2D architecture. The location of the third input in an extra functional layer enables to enhance the amount of ferromagnetic material surrounding the output magnet by 1/3. Thereby the influence of each input magnet is increased by 1/6 and the same is $|\mathbf{k_{Net}}|$.
An enhancement of $|\mathbf{k_{Net}}|$ up to 8.5 mT would already result in an error rate $\leq 0.01\%$.

8.2.4 Simulating the computing area

Coupling field simulations

For the proposed gate and its given physical dimensions, the actual 'computing area' of the gate is of great interest (see Fig. 8.4 a). The original size of the gate is in the µm regime to enable MOKE measurements. However, there is a great overhead in the size of the inputs, which is actually not necessary to guarantee correct functionality of the gate. The computing area considers only the magnetic area of the inputs required to produce the measured stray field values. Hence, the computing area of the gate has a reduced footprint at the same time maintaining the gate's functionality. In this context, in numerous OOMMF simulations different input sizes were considered and the resulting coupling fields compared. The aim was to determine the required surface contribution, which matches the most with the stray field produced by the original input size. For the simulations, the shape of each input was extracted from the SEM image given in Fig. 8.4 a. This guarantees the most accurate replica of the input's shape. The chosen M_S corresponds to the ferromagnetic amount each input of the real 3D majority gate is composed of.
Fig. 8.8 summarizes the results of the simulations. Note, the color data of the applied color bar, which represents the coupling field values has been restricted to $[0 - 15]$ mT, as this is the range of interest. The coupling field values emanated by the reduced size of the inputs match those produced by the original size of the inputs (compare Fig. 8.3 with Fig. 8.8). The overhead in the original size of the inputs due to the required measuring pads and beyond that is negligible for the correct functionality of the gate. Only the magnetic material, which is close to the irradiation area of O delivers the main contribution to the resulting net stray field. The gate's inputs can be reduced to the size shown in the simulation images (see Fig. 8.8) resulting in a $\approx 700\,\text{nm} \cdot 550\,\text{nm}$ computing area footprint of the gate.

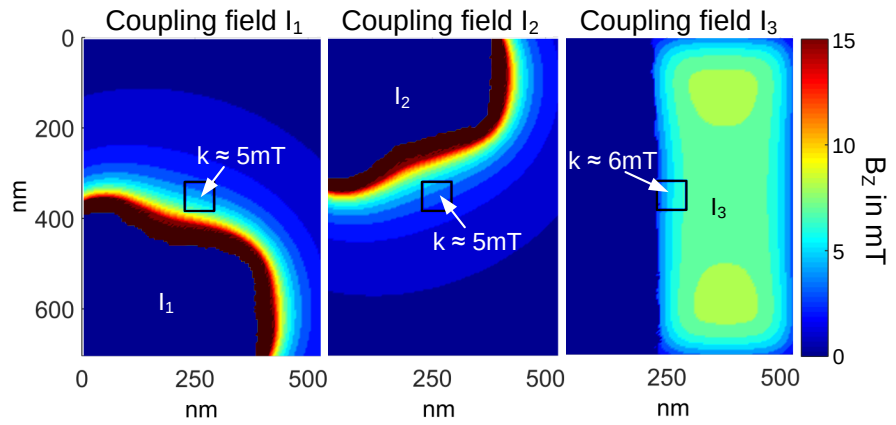

Figure 8.8: OOMMF simulation results of the coupling fields emanated by the gate's inputs, which are reduced in size.

Hysteresis and magnetization reversal

Additionally, to the stray field simulations, further simulations analyzing the switching behavior of O for the reduced gate size were performed. The simulations should confirm the same influence of the reduced inputs on O as the original ones. Therefore, in the initial state, the inputs were set to one of the possible eight input configurations and O was switched from the 'down' in the 'up' state by enhancing the applied external field in 1 mT steps from 0 mT up to 200 mT. The corresponding simulation results are shown in Fig. 8.9 and 8.10.
Hysteresis curves as well as magnetization reversal of O are analyzed by the simulations. Note, influence of thermal fluctuations is not considered here, as it is very time consuming and does not contribute any additional important information about the basic gate functionality. Due to the negligence of thermal fluctuations, the inherent switching field of O is enhanced compared to the measured ones as can be easily seen in the hysteresis curves in Fig. 8.9 and 8.10. However, the most important thing for analysis is the shift of the switching field values of O representing the influence of the input magnets.
In the simulations, O shows the same behavior as during measurements. The input configurations $\{I_1 I_2 I_3\} \in \{000, 001, 011, 101\}$ emanate a net stray field pointing in the 'up' direction. For these configurations, O is easier to switch in the 'up' state (obvious by the lower switching fields) than for the input configurations $\{010, 100, 110, 111\}$ (obvious by the higher switching fields), which produce a net stray field pointing into the 'down' direction. So here, the shift in the hysteresis curves depending on the input configurations is similar to the shift manifested by the MOKE measurements.

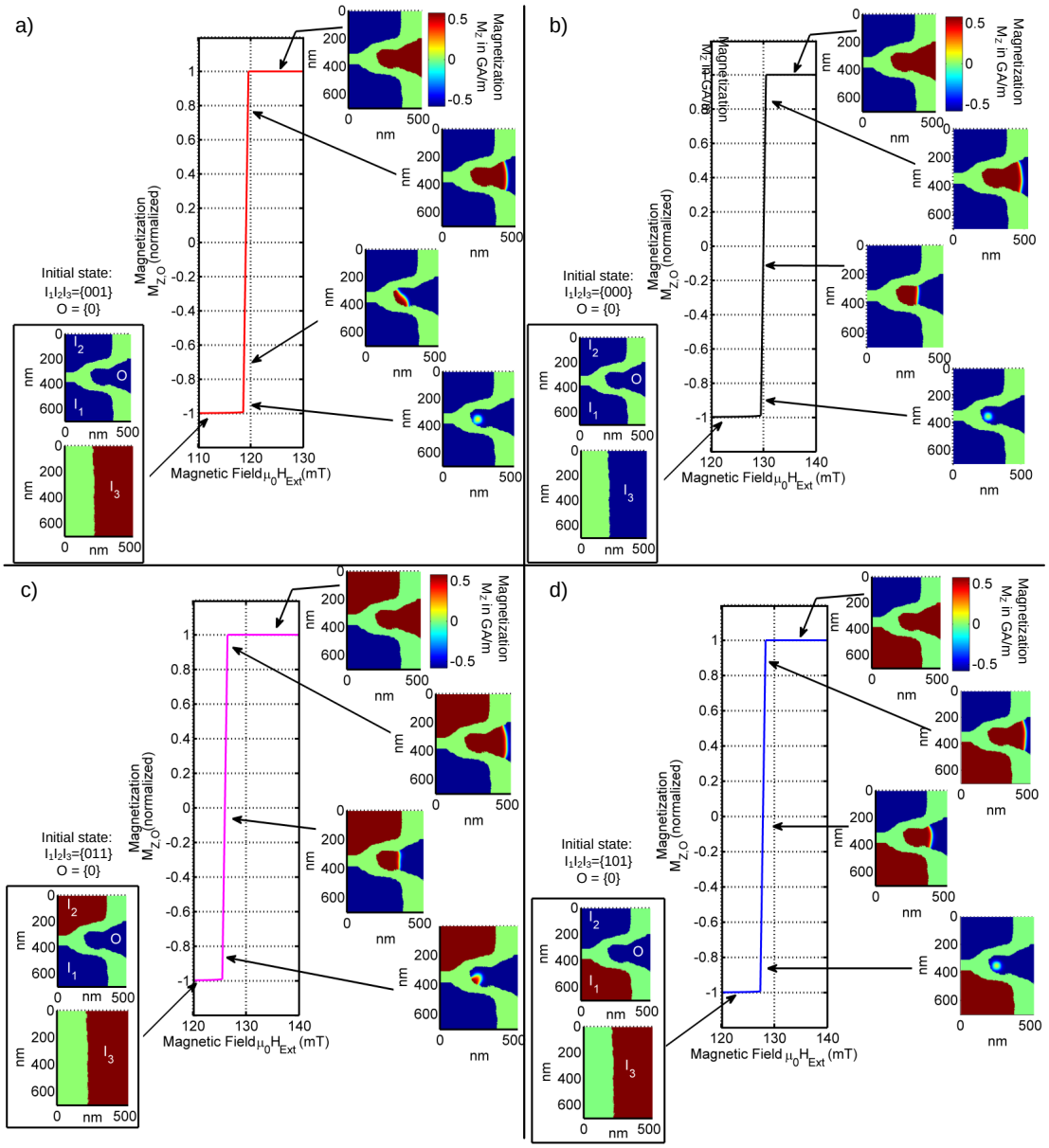

Figure 8.9: OOMMF simulation results for the configurations $\{I_1I_2I_3\} \in \{001\}$ (a), $\{000\}$ (b), $\{011\}$ (c) and $\{101\}$ (d). Configuration $\{001\}$ results in the largest shift of the hysteresis curve due to the highest sum of the input stray fields. Configurations $\{000, 011, 101\}$ result in smaller but similar hysteresis shifts as expected.

The influence of each configuration $\{I_1I_2I_3\} \in \{000, 011, 101\}$ on O is nearly the same as expected. For these configurations, the stray fields of two inputs always cancel each other out and only the stray field of the third input remains active.

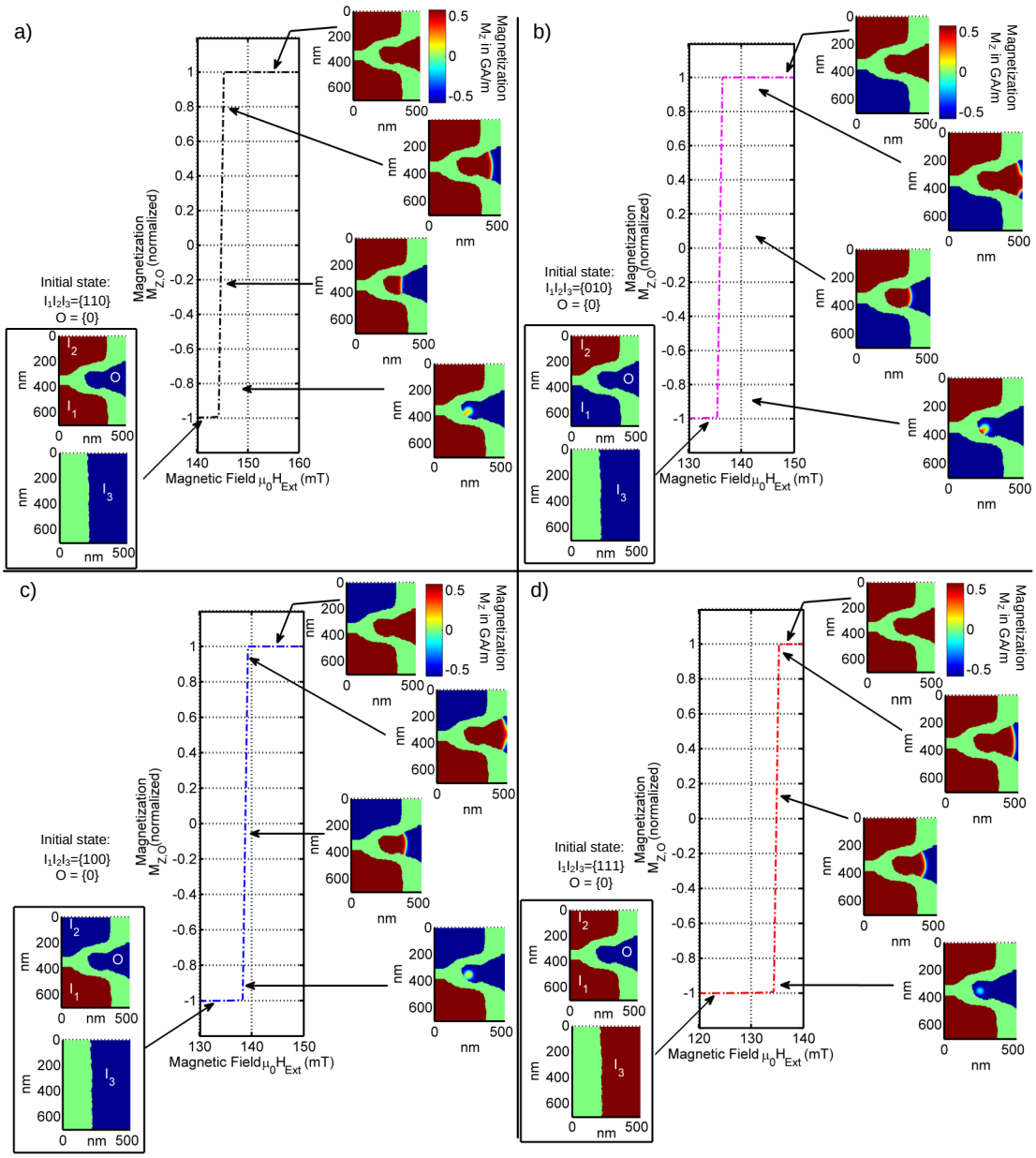

Figure 8.10: OOMMF simulation results for the configurations $\{I_1 I_2 I_3\} \in \{110\}$ (a), $\{010\}$ (b), $\{100\}$ (c) and $\{111\}$ (d). Configuration $\{110\}$ results in the largest shift of the hysteresis curve due to the highest sum of the input stray fields. Configurations $\{010, 100, 111\}$ result in smaller but similar hysteresis shifts as expected.

When considering the corresponding switching field values of O for these configurations, it is obvious, that they vary only in a small range [126 mT − 129 mT] (see

Fig. 8.9 b, c, d). The same is observed for the configurations $\{010, 100, 111\}$. The obtained switching field values of O differ only in a small range [135 mT − 138 mT] (see Fig. 8.10 b, c, d). This indicates same influence on O by the before mentioned configurations. However, the small deviations can be traced to non-accurate positioning of the irradiation spot (discussed in the next paragraph) and the non-identical shape of the inputs. The latter is already conditioned by the layout (compare I_1, I_2 vs. I_3) and by imperfections of the applied lithography process (compare I_1 vs. I_2).
Furthermore, the simulations confirm, that the influence of the configurations $\{001, 110\}$ on O is the highest, as expected. This is obvious by the lowest and highest switching field values of O obtained for these configurations ($\{001\} \rightarrow \{118\,\text{mT}\}$ and $\{110\} \rightarrow \{145\,\text{mT}\}$) (see Fig. 8.9 a and Fig. 8.10 a).
The simulations confirmed for all input configurations, that domain wall nucleation starts in the irradiated area and thereby the reversal process of the output magnet (compare magnetization images given in Fig. 8.9 and 8.10). This manifests the irradiated spot as the most sensitive part of the output magnet, again proving the concept of irradiation for unidirectional signal flow.

Influence of irradiation spot placement

The choice of the irradiation spot location in the output magnet has a decisive impact on the resulting switching field value of O and its magnetization reversal process. In the simulations, the placement of the irradiation spot can only be estimated as it was not visible neither in the MFM nor in the SEM images. During processing, the placement of the irradiation spot has been done blindly only by the orientation on special alignment marks sidewards the 3D gate. Therefore, the spot, where the real ion beam irradiation took place could only be estimated.
To investigate this influence in detail, two different irradiation spot locations and sizes have been tested in the simulations (see Fig. 8.11). The first location has been selected to be right in the middle of O. The total size of the irradiation spot amounted to 80 nm x 80 nm. The second location has been chosen to be located right in the middle between I_1 and I_2 and closer in distance to both inputs. A reduced size of the irradiation spot of 60 nm x 60 nm has been applied to make sure, that the irradiation area still lies inside the volume of O. Note, the irradiation area chosen in the simulations was always bigger than the one chosen in the mask (here 40 nm x 40 nm). This assumption is justified as the ion beam diameter has a certain extent.
When simulating the hysteresis behavior for the location shown in Fig. 8.11 a, the switching of O was asymmetrical and it could be detected, that the influence of I_3 overweighted the influence of I_1 and I_2. Due to this behavior, the functioning of the gate was incorrect. Therefore the second location of the irradiation spot (shown in Fig. 8.11 b) has been tested. The second location resulted in the desired

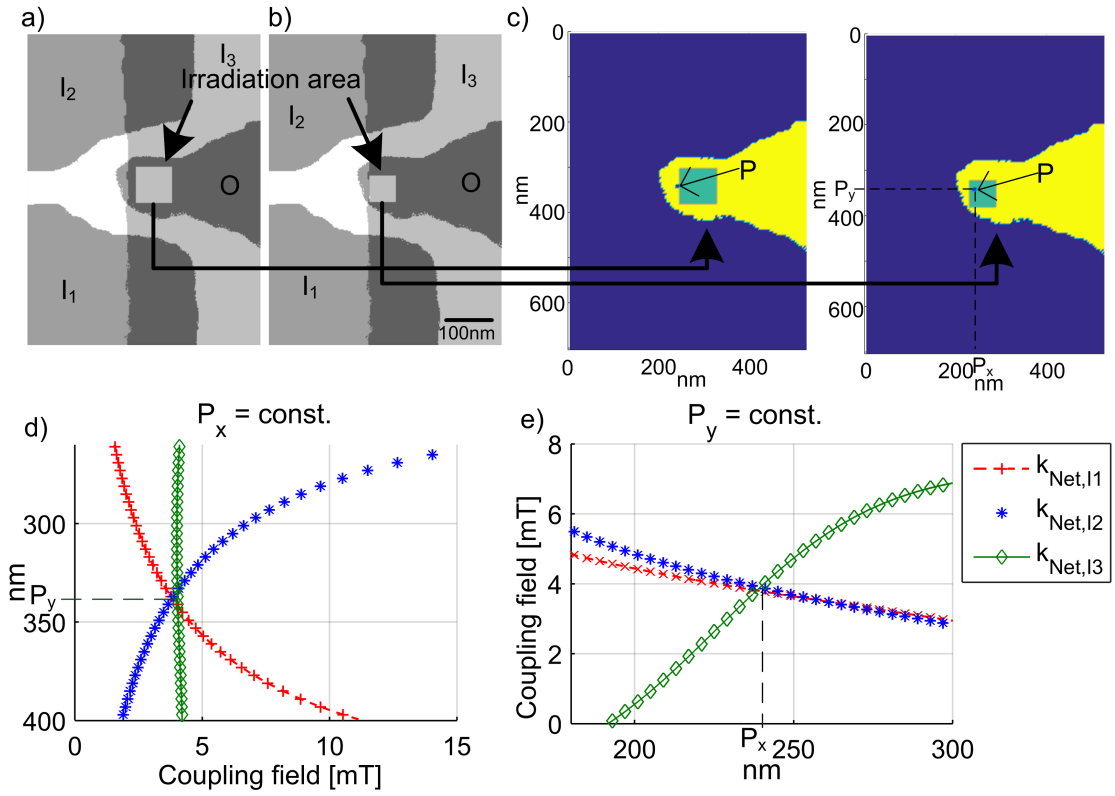

Figure 8.11: Irradiation spot positions in O (a-b). (c) Determined point P of equal coupling field influence and the corresponding position of the irradiation spot. (d-e) Progression of the net coupling fields versus y-axis (for P_x const.) and x-axis (for P_y const.

results (presented in Fig. 8.9 and 8.10), which are in very good agreement with the measured ones.

To understand why positioning a) does not work out and b) does, the progression of the coupling field lines, when entering O have been investigated. The goal was to find out, at which position in O all three coupling fields $\mathbf{k_{I1}}, \mathbf{k_{I2}}, \mathbf{k_{I3}}$ have the same strength and thereby same influence on O and how the coupling fields look like in close environment of this position.

The following basis of computation has been applied to determine this. At first the mean net stray field $\left|\overline{\mathbf{k_{Net,I1}}}\right|$ resulting from the configurations $\{I_1I_2I_3\} \in \{000, 100, 011, 111\}$ is determined. These configurations enable to calculate the influence of input I_1 as the coupling fields emanated from I_2 and I_3 are opposed to each other for these configurations, thereby canceling each other out. Same has been done for the inputs I_2 and I_3. Thereby the configurations $\{I_1I_2I_3\} \in \{000, 010, 101, 111\}$ enable to calculate the mean $\left|\overline{\mathbf{k_{Net,I2}}}\right|$, and the mean $\left|\overline{\mathbf{k_{Net,I3}}}\right|$

can be calculated by the configurations $\{I_1 I_2 I_3\} \in \{100, 101, 010, 011\}$.
In further calculations $\left|\overline{\mathbf{k_{Net,I1}}}\right|$ has been subtracted from $\left|\overline{\mathbf{k_{Net,I2}}}\right|$ thereby determining the region where these two coupling fields cancel each other out. Afterwards $\left|\overline{\mathbf{k_{Net,I1}}}\right|$ has bee subtracted from $\left|\overline{\mathbf{k_{Net,I3}}}\right|$ and again the region determined, where the subtraction gets zero. Last, the region where the subtraction of $\left|\overline{\mathbf{k_{Net,I2}}}\right|$ and $\left|\overline{\mathbf{k_{Net,I3}}}\right|$ gives zero is determined. The overlap of all the three regions gives the point P, where the amounts of $\left|\overline{\mathbf{k_{Net,I1}}}\right|$, $\left|\overline{\mathbf{k_{Net,I2}}}\right|$ and $\left|\overline{\mathbf{k_{Net,I3}}}\right|$ are identical (see Fig. 8.11 c). The progressions of the coupling fields apart from P in the $x|y$ direction are summarized in Fig. 8.11 d)-e).
When comparing the determined position P with the selected position of the irradiation spot, it is obvious, that the position chosen in a) lies completely to the right hand side of P (see Fig. 8.11 c). The further apart from P in the positive x-direction, the coupling field of I_3 increases drastically, while the influence of $I_1|I_2$ decreases (compare Fig. 8.11 e). This confirms, the observed behavior during hysteresis simulations, that the influence of I_3 overweights the influence of I_1 and I_2 in such a way that correct functioning cannot be guaranteed.
In contrast, the position of the irradiation spot chosen in b) matches with P (see Fig. 8.11,c). Now, the smaller distance between the irradiation spot and I_1 respectively I_2 increases their influence on O and at the same time diminishes the influence of I_3. However, when considering the progression of the coupling field shown in d) and e), it is obvious that the progression is different for all three inputs. Therefore, the resulting $|\mathbf{k_{Net}}|$ is hard to predict and even more the position of domain wall nucleation in the irradiated spot. Nevertheless, the position of the irradiation spot chosen in b) provides the major accordance to the measured results.
The combination of a SEM and FIB tool is required to enable the correct positioning of the irradiation spot. Furthermore, the best results i.e. identical coupling of all three inputs would be achieved, when the irradiation spot could only be reduced to the point P itself. However, this is not possible in reality, as ions are always scattered in matter thereby affecting the region around the irradiated spot. Furthermore, former experiments on the influence of ion irradiation revealed, that a small pointy irradiation has not sufficient impact on PMA so that a sensitive spot could be created.

8.3 Conclusion

This paragraph concludes the investigations on the 3D majority gate. It is the elementary device, that proves the computing feasibility with nanomagnets in all three spatial dimensions. Theoretical background, provided at the beginning of this chapter, explained the majority operation and the behavior of the gate's output magnet during clocking. The necessary condition on the clocking amplitude is

derived and design criteria are outlined. To meet the condition of equal influence of each input magnet, OOMMF simulations were performed in advance predicting the coupling field of an input magnet depending on its shape, film composition and distance to the irradiation spot of the output magnet. The finally fabricated gate with the optimized shape and values extracted from the simulations was characterized by the MOKE and the MFM. Hysteresis curve measurements confirm the correct ordering of the output magnet for each possible input configuration even for a high number of switching events. The switching field distributions derived from the hysteresis measurements confirm the existence of a clocking window. When applying the clocking field, correct ordering of the output after at least one clocking cycle was observed by the MFM.
The error-rate of the gate was calculated using a worst-case approximation. Therefore, the overlap probability between the switching field distributions obtained for obstructed and supported switching of the output magnet was calculated. For the fabricated gate, the error-rate amounts to 4%. However, this rate can be further reduced by enhancing the coupling field, which can be achieved by e.g. reducing the inter-magnet distance or increasing the amount of the ferromagnetic material in the film stack.
Simulations performed on the computing area of the gate confirmed its correct operation even for an areal size of $700 \times 550\,\mathrm{nm}^2$, when neglecting the overhead in area produced by the measuring pads. Additional simulations on the switching behavior of the gate outlined the importance of correct positioning of the irradiation spot. Already small deviations from the optimal position (where the coupling field of each of the three inputs is equal) can evoke a dominant behavior of one input. This leads to a smaller clocking window or in the worst case to a complete disappearance of the clocking window.
The presented gate is the first 3D computing device built from nanomagnets. It enables NAND/NOR operation and the 3D implementation provides the possibility to place the third programming input in an additional functional layer and thereby decouple programming and computing functionality. Furthermore, instead of using a magnet with perpendicular magnetic anisotropy as the programming input, one can also use a magnet with in-plane anisotropy, that produces a stray field in the out-of plane direction at its poles [KBE+13b]. This way the programming input can be addressed separately by in-plane fields and it becomes possible to switch the logic functionality of the gate between NAND and NOR during runtime. By connecting multiples of such majority gates any arbitrary logic circuit can be realized. The fabricated gate envisions the 3D computing feasibility of pNML systems.

9 Electrical read-out sensor based on the magnetoresistive effect

The electrical read-in and read-out ability of NML devices is an important step towards CMOS integration. The combination of both technologies would extend state-of-the-art CMOS functionality and offers the possibility to exploit the advantages of both technologies. In a hybrid circuitry fast computing operations relying on speed are performed with CMOS, while energy consuming operations requiring a huge number of identical processing elements (as it is done in systolic architectures) are done by NML devices. To enable NML integration, a magneto-electrical interface must be given to translate the magnetic signal into the electrical domain and vice versa.
Possible electrical in- and output sensors for pNML devices based on the Oersted switching and the extraordinary Hall effect have already been proposed by Becherer [52] and Kiermaier [26]. However, the proposed structures consume a lot of space and the resulting effect must be enhanced for a reliable application. Alternative sensors based on the magnetoresistive effect like the GMR- or MTJ-sensor revolutionized the world of memory and storage applications like in magnetic hard disk drives or magnet random access memory [92]. They promise for higher effects and a more reliable operation. Therefore a GMR-based sensor type has been investigated as a possible read-out interface [EBvGK+15], in this work. In the following, the physics, the measurement principle, the fabrication and further parameters improving the effect are presented.

9.1 The physical principle of GMR-sensors

A typical GMR-structure consists of two ferromagnetic layers separated by a metallic, non-ferromagnetic layer (NM) (see Fig. 9.1a). Typically, one of the ferromagnetic layers has a high coercive field, which is pinned to a certain magnetization state (see Fig. 9.1c) and serves as reference layer. This layer is called the pinned layer (PM). The other ferromagnetic layer, called the free layer (FM) has a low coercive field, whereas the orientation of the magnetic moments in the layer is controlled via magnetic fields. Depending on the magnetization state of the two layers respectively to each other i.e. parallel or anti-parallel, the electrical resistivity of the stacked magnetic thin film system changes. Hereby, the anti-parallel

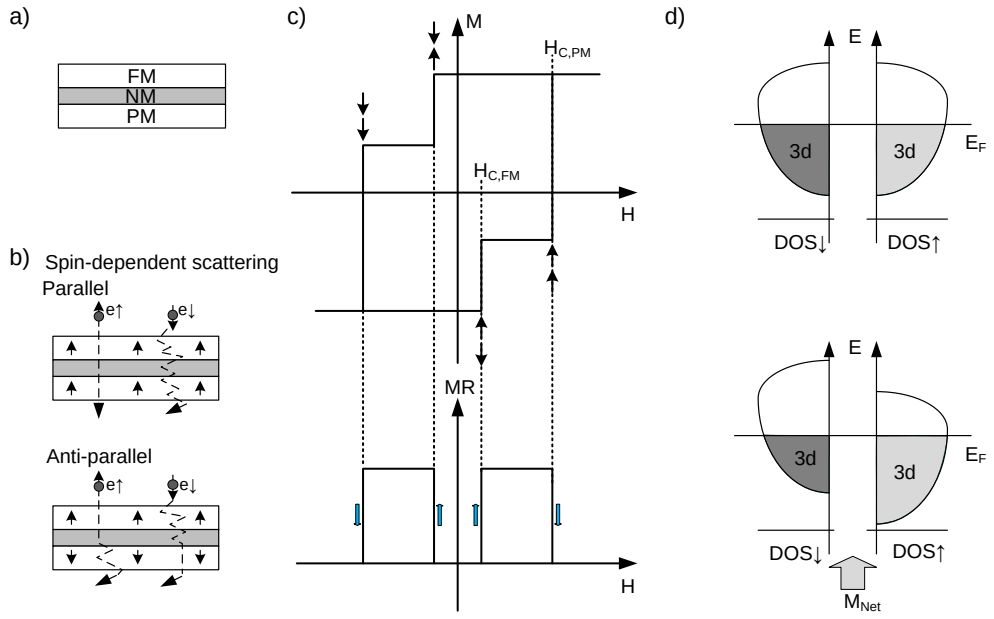

Figure 9.1: (a) Basic GMR multilayer structure composed of the two ferromagnets FM, PM and a non-magnetic metallic spacer layer (NM). (b) Mott's two-current model: for parallel alignment, electrons of only one channel are scattered, while in the opposed case, electrons of both channels are scattered. (c) Hysteresis curve of the two magnet system (top) with the corresponding MR graph (bottom). (d) DOS for ↑ and ↓ electrons for a material without (top) and with net magnetization upwards (bottom).

alignment results in high resistivity values R_{AP}, whereas the parallel alignment results in low resistivity values R_P. The intensity of the GMR effect is expressed by the magnetoresistance (MR) ratio, which is defined as following:

$$MR_{ratio} = (R_{AP} - R_P)/R_P \; = \; \Delta\, R/R_P. \tag{9.1}$$

The resistivity changes originate from the GMR effect, which can be traced back to the spin-dependent scattering of the current carrying electrons in inhomogeneous ferromagnetic/metallic systems. According to Mott's two-current [123] model, the current in 3d transition ferromagnetic metals is carried independently by spin-up (↑) and spin-down (↓) electrons in two separated channels. Electron scattering appears, when the spin-polarization of the electron is opposed to the polarization of the ferromagnetic layer [124]. Hence, in case both ferromagnetic layers (PM and FM) are aligned parallel to each other, electrons of only one channel are scattered

resulting in a low magnetoresistance of the stack as depicted in Fig.9.1 b and c. When, the ferromagnetic layers are aligned anti-parallel, electrons of both current carrying channels are scattered resulting in a high magnetoresistance.
To understand the different scattering rates and why electron scattering is possible, one has to look deeper into the theory of solids [125, 126] (see Fig. 9.1 d). The electron density of states (DOS) represents the number of electrons having the energy within an interval [E, E+dE]. In this special case, only the 3d electrons are considered, as they give rise to ferromagnetism. Each energy state can be occupied only by one electron independently whether it has an up- or down-spin. In the ground state, all the energy levels below the Fermi level E_F are occupied by electrons. The integral over the DOS beginning at the lowest possible energy state up to E_F gives the total number of valence electrons in the metal (see Fig. 9.1 d colored areas). If the net magnetization (M_{Net}) is zero, the DOS of $\uparrow$ and $\downarrow$ electrons are identical (see Fig. 9.1 d top). In case there is a net magnetization, the DOS of $\uparrow$ and $\downarrow$ at E_F are distinct (see Fig. 9.1 d bottom, magnetization is indicated by the big gray arrow). For an up magnetization, the most energy states below the Fermi level are occupied by $\uparrow$ electrons. The DOS of $\uparrow$ electrons is shifted below the Fermi level, corresponding to a larger integral and therefore a higher number of $\uparrow$ valence electrons. At the same time, the DOS of $\downarrow$ electrons is shifted above E_F i.e. the number of $\downarrow$ valence electrons is decreased. The difference of the DOSs at the Fermi level causes a significant difference in resistance for $\uparrow$ and $\downarrow$ electrons. Mott assumed, that the current is predominantly carried by the low-mass s and p electrons [123], while the heavier 3d electrons provide a spin-dependent reservoir of empty states into which these $s-p$ electrons can be scattered [92, 127]. Applying this statement to the theory of solids, this means that for a net magnetization upwards, where most states are occupied by 3d $\uparrow$ electrons, there is a reservoir of empty states left for $\downarrow$ electrons into which the $s-p$ electrons can be scattered. The difference in the DOSs for $\uparrow$ and $\downarrow$ electrons explains the spin-dependent scattering rates.

9.2 Measuring the magnetoresistance

Knowing the magnetization direction of the reference magnet PM, the magnetization direction of FM can be easily derived from the measured MR values. Low MR means parallel alignment of FM to PM. High MR means anti-parallel alignment of FM to PM. Different resistance values correspond to two different logic states of FM. This explains the basic functioning of a GMR sensor. The applied technique to measure the MR is a Wheatstone-bridge circuitry, explained in the following.

9.2.1 The Wheatstone-bridge: basic principle

In 1843 Wheatstone developed a bridge circuitry, with four resistances $[R_1, .., R_4]$ arranged as shown in Fig. 9.2 a. R_1 with R_2 and R_3 with R_4 form a potential divider. The bridge is fed with a constant voltage U_0. The diagonal voltage U_d between the two parallel branches (between the points **a** and **b**) is the difference between U_3 (voltage at the resistance R_3) and U_1 (voltage at the resistance R_1):

$$U_d = U_3 - U_1. \tag{9.2}$$

Substituting U_3 and U_1 by the known resistances and U_0, U_d can be reformed to:

$$U_d = U_0 \frac{R_3}{R_3 + R_4} - U_0 \frac{R_1}{R_1 + R_2} = U_0 \frac{R_2 R_3 - R_1 R_4}{(R_1 + R_2)(R_3 + R_4)}. \tag{9.3}$$

Whenever U_d is zero, the bridge is balanced and the correlation:

$$R_2 R_3 \; = \; R_1 R_4 \tag{9.4}$$

is valid. This way, any resistance can be determined, if three of them are known. The bridge can also be fed with current instead of voltage. In this case U_0 is expressed in dependency of the applied current I_0:

$$U_0 = I_0([(R_1 + R_2)||(R_3 + R_4)]) = I_0 \frac{(R_1 + R_2)(R_3 + R_4)}{(R_1 + R_2 + R_3 + R_4)}. \tag{9.5}$$

Applying eq. 9.5 to eq. 9.3, the expression for U_d for a current fed bridge changes to:

$$U_d = I_0 \frac{R_2 R_3 - R_1 R_4}{(R_1 + R_2 + R_3 + R_4)} \tag{9.6}$$

9.2.2 Detection and calculation of resistivity changes

This bridge circuitry can be applied to measure resistivity changes of the magnetic stack. Therefore the changing resistance is interconnected with three known resistances to a bridge. One of the three known resistances must be adjustable to enable the balancing of the bridge. In Fig. 9.2 b, the applied bridge circuit is depicted. The resistivity of the investigated magnet can change its value from R_M (parallel alignment of the magnets) to $(R_M + \Delta R)$ (anti-parallel alignment of the magnets). We put two identical fixed resistances R_F and one adjustable resistance, which is a series of the fixed resistance R_{FS} and the potentiometer resistance R_P. R_P provides the possibility, to adjust the series resistance to the value of R_M:

$$R_{FS} + R_P = R_M. \tag{9.7}$$

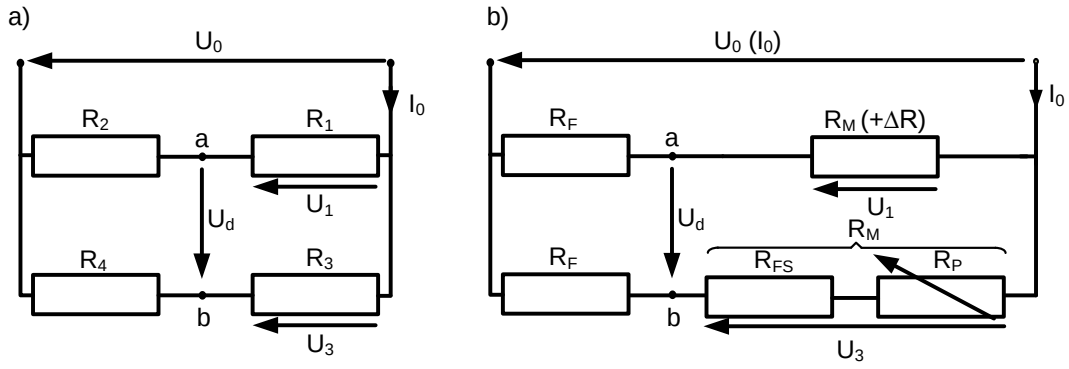

Figure 9.2: (a) Basic layout of the Wheatstone- bridge circuitry to determine an unknown resistance. (b) Layout of the applied Wheatstone-bridge circuitry to measure resistance changes in the magnetic stack ($(R_M + \Delta R)$). Hereby, two resistances are fixed (R_F) and one is adjustable being a series resistance of the fixed resistance R_{FS} and the potentiometer resistance R_P.

The combination of a fixed resistance with a potentiometer as adjustable resistance enables the precise balancing of the bridge circuitry. This is due to the fact, that the values of all fixed resistances R_F, R_{FS} already lie in the range of R_M and only a small part must be adjusted by the potentiometer.
In our experiments, the bridge is fed with current. In the ground state, the magnets are aligned in parallel to each other and the bridge is balanced ($U_d = 0$). In this case, the resistance of the magnetic stack amounts to R_M and eq. 9.7 is valid for the series resistance. When the magnets switch into the anti-parallel state, the resistivity of the stack is increased and the resistance changes to $(R_M + \Delta R)$. Thereby, U_d changes to:

$$U_d = I_0 \frac{R_F R_M - (R_M + \Delta R) R_F}{2R_M + 2R_F + \Delta R} \tag{9.8}$$

This equation is achieved by replacing $R_1 = (R_M + \Delta R)$, $R_2 = R_4 = R_F$ and $R_3 = (R_{FS} + R_P) = R_M$ in the derived eq. 9.6. Resolving the latter equation after ΔR, gives the expression for the resistivity change:

$$\Delta R = -\frac{2U_d(R_M + R_F)}{U_d + I_0 R_F}. \tag{9.9}$$

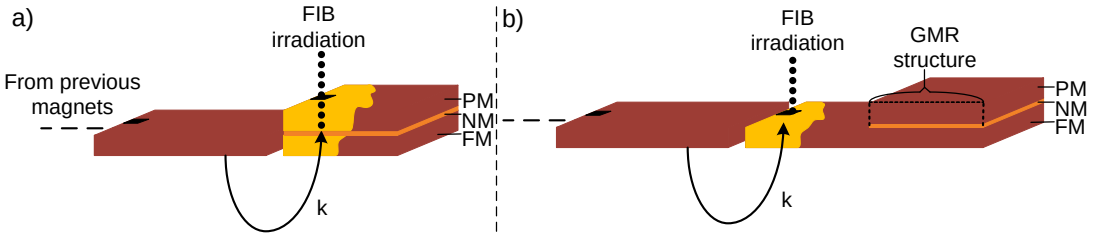

Figure 9.3: Scenarios of integrated GMR sensors in pNML systems. (a) The integration of a conventional GMR structure renders FIB irradiation of FM impossible, without affecting PM. (b) A special sensor structure enables the sensitization of FM by FIB irradiation to previous logic elements of the pNML circuitry [EBvGK+15].

9.3 Integration of GMR read-out sensor in pNML

The integration of a GMR sensor in pNML requires some further reflections. FM should be defined by the stray field of a previous neighbor magnet performing logic operations, while PM is fixed to a certain state. Hence, a possibility must be provided to irradiate FM, to sensitize it to the stray field of its neighbor magnet. In a conventional GMR-sandwich structure as it is shown in Fig. 9.3 a, an irradiation of FM results in a irradiation of both ferromagnets. As soon as both magnets are irradiated, the behavior of the GMR stack is unpredictable, as both magnets react on the stray field of their previous neighbor and behave as a single magnet. To enable irradiation of FM, a special geometry of the GMR sensor is required, specifically of the FM layer. FM must be fabricated in such a way, that a free standing part of the structure is created, which can be used for irradiation, while a further part of the structure is covered by NM and PM, constituting the GMR structure itself. In Fig. 9.3 b a possible integration scenario in pNML is depicted. The anterior part of the FM is uncovered and can be irradiated by the FIB. The irradiation creates a weak spot which is sensitive to the stray field $\mathbf{k}$ of its neighbor magnet. The posterior part of FM contains the sensing part, namely the GMR sandwich.
The most important thing to achieve the GMR effect is that the ferromagnetic layers must be in direct contact with the non-magnetic metallic spacer layer NM. Only then spin-dependent scattering can take place and a GMR effect arises. This requirement puts a certain challenge on the fabrication technique. As the ferromagnetic layers get easily oxidized, it is not possible to structure first the FM layer and afterwards the NM/PM layer. The reason is that, between sputtering the multilayer, layer patterning by FIB lithography and etching, the facilities must be changed, which is not possible to do in vacuum. An alternative fabrication process developed and presented in this work in the subsequent paragraph enables

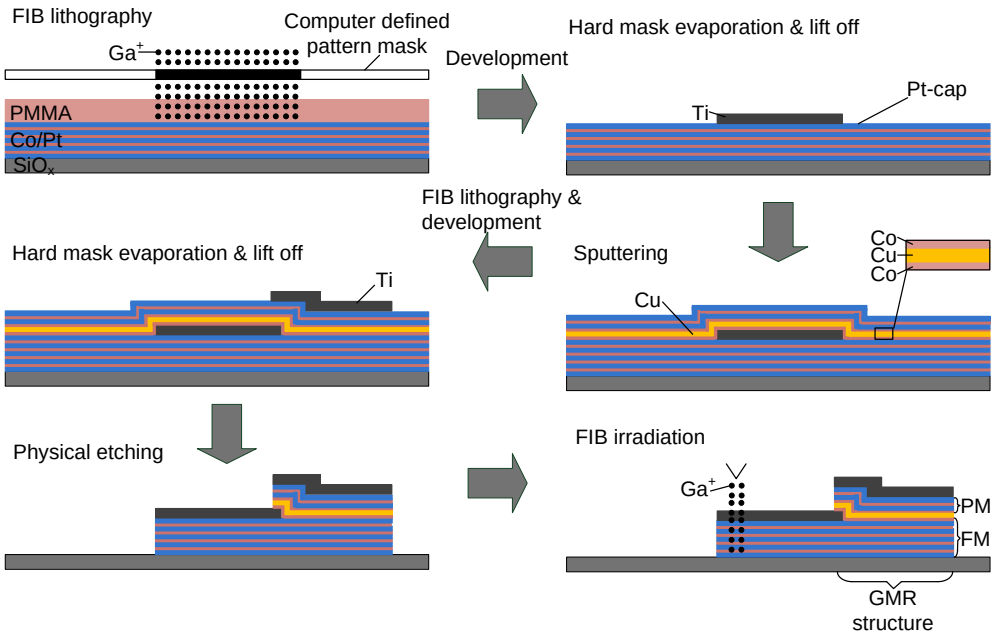

Figure 9.4: Two-step lithography process for GMR sensor fabrication. The structuring of the multilayer via physical etching takes place after both hard masks (for FM and PM) have been evaporated. This enables to fabricate the most sensitive part, namely the Co-Cu-Co interface, under vacuum condition [EBvGK+15].

to satisfy the strict vacuum condition for sputtering the critical interface layers to the NM layer, thereby rendering sensor fabrication for pNML possible.

9.4 Fabrication

The fabrication process of the proposed structure is a two-step lithography process depicted in Fig. 9.4. At first a magnetic multilayer composed of $4\text{x}(\text{Co}_{0.6\,\text{nm}}/\text{Pt}_{1\,\text{nm}})$ is sputtered on a $\text{Pt}_{3\,\text{nm}}$-seed layer. The final Co-layer is covered by 3 nm Pt as oxidation protection. The layers are RF-magnetron sputtered at a base pressure of $\approx 2 \times 10^{-7}$ mbar with an RF-power of 20 W. The partial pressure of Ar is chosen to be 6 µbar for all layers of the FM. The sputtering process is followed by FIB lithography for hard mask pattern definition as described in sec. 5.1.1. After resist development, 4 nm of Ti are evaporated as hard mask layer. Lifting off the remaining resist, the hard mask material remains only in regions defining the free standing part of FM. As already mentioned in the previous paragraph, to achieve a GMR effect, it must be guaranteed that a ferromagnetic Co-layer of the FM layer magnet is in direct contact with the NM. Therefore in a further sputtering

process, first a Co layer of 0.6 nm is sputtered again at 6 µbar Ar partial pressure before sputtering the NM layer. The extra Co layer is exchange coupled to the rest of the already given multilayer stack of FM, as the preceding 3 nm Pt-layer, which serves as oxidation protection is thin enough to not disturb exchange coupling between the ferromagnetic Co-layers. Subsequently, the NM layer, which is composed of Cu is directly sputtered on the Co layer. The 3 nm Cu-layer is deposited with a RF-power of 50 W at a partial Ar pressure of 7 µbar. The required Cu-thickness to weaken oscillatory interlayer exchange coupling between FM and PM, so that separate switching of the magnets can occur has been investigated in previous works by Lechner [Lec12] and Efinger [Efi14]. Following the Cu-layer, the magnetic multilayer stack of PM is sputtered, containing $2\text{x}\text{Co}_{0.4\,\text{nm}}$ and 1 nm Pt as interlayer. Also here, it is guaranteed that the first Co layer of PM is in direct contact to the NM-Cu layer. As capping layer 4 nm of Pt is sputtered again serving as oxidation barrier. Note, the total amount of Co in the PM stack is much less than in the FM multilayer stack. This has been done consciously to prevent high coupling fields of the PM on the FM magnets. Furthermore the Co-layers of the PM stack were sputtered at a higher partial Ar pressure, namely 11 µbar as the experience was made in former experiments, that a higher Ar pressure results in higher switching fields. This property of the PM layer is needed as PM is the magnet that is supposed to be the pinned one and is not switched by the external clocking field amplitude. Same influence of the sputtering gas pressure on the film coercivity was observed by [120, 128]. It is assumed that the higher coercivity values originate from the change in the film morphology and may be caused by domain wall pinning.
After the second sputtering step, the pattern definition for the hard mask is again done by FIB lithography. The precise alignment is hereby again vital. A small part of the top and bottom hard mask must overlap to guarantee a continuous connection between the FM and PM magnet. If there is no overlap, the structures can be separated during the physical etching process. Therefore, the alignment technique described in 5.2.2 is applied. After hard mask evaporation (again 4 nm of Ti) and lift-off, the undesired parts of the film are etched away by Ar^+ ion beam etching. In a last step the anterior part of the FM magnet is irradiated by an ion dose of $5 \cdot 10^{13}\,\text{Ions/cm}^2$.
The presented fabrication process enables the fabrication of the required sensor structure, with the free-standing part of FM being irradiated to receive the incoming signal from surrounding neighbor magnets and the posterior part of FM comprising the actual GMR sensor. With the proposed fabrication process, the most critical fabrication steps (sputtering deposition of the Co-Cu-Co interface) can take place under vacuum condition.
In summary, the first fabrication step serves to define the anterior geometry of FM. In a second lithography step, the Co-Cu-Co interface, together with the second ferromagnet is positioned at the posterior part of FM. The fabricated structures

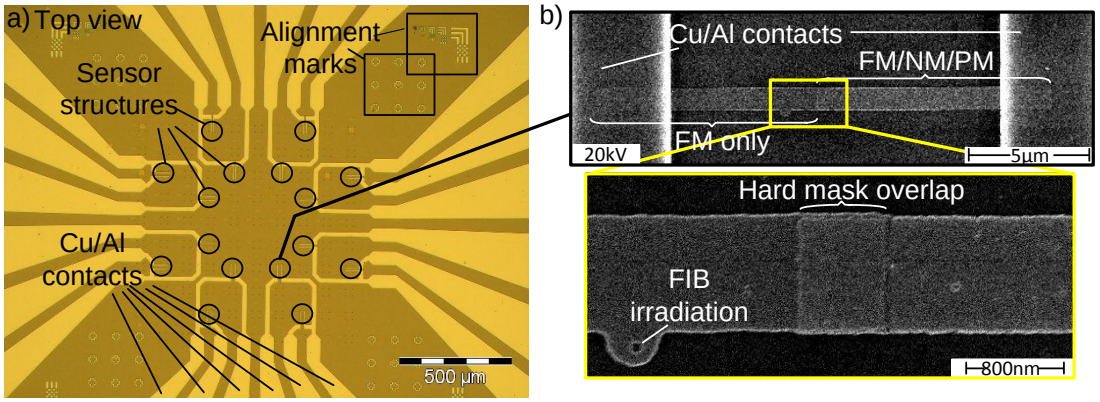

Figure 9.5: (a) Optical microscopy image: Top view on the SiO_x chip comprising the Cu/Al contacts, alignment marks for optical lithography and the corresponding contacted GMR sensors. (b) SEM image: Enlarged extract of the contacted GMR sensor. The contacts lie on top of FM and PM. The sensor itself consists of two parts: a FM only part which is FIB irradiated and a part that contains the actual sensing GMR structure, namely FM/NM/PM. Also visible is the precise alignment of the bottom to the top hard mask [EBvGK+15].

are 19 µm long and 1 µm wide. The overlap area between the two hard masks of FM and PM amounts to 500 nm × 1 µm (see Fig. 9.5 b yellow rectangle).
In a last step, the $Cu_{400\,nm}/Al_{150\,nm}$ metal contacts for electrical connection are deposited on the sensor structure applying an additional optical lithography and e-beam vapor deposition step. The sensor is contacted from the top on the left and right hand side (see Fig. 9.5 b) resulting in a current flow perpendicular to the film plane. The whole fabricated chip is shown in Fig. 9.5 a. It contains 24 Cu/Al contacts and 16 sensors (8 contacts are used twice). In the enlarged extract (see Fig. 9.5 b yellow rectangle), the precise alignment of top to bottom hard mask is clearly visible confirming the applied alignment technique. In case of misalignment, the whole structure would not look like a solid line but would be in form of a 'Z' or ante- and posterior of FM would even be separated. Note, the irradiation spot of FM has not been placed to its left edge (see Fig. 9.5 b) to exclude interaction with the left Cu/Al contact. At the same time, the irradiation spot has been placed sufficiently far apart from the edge of the overlying PM magnet to exclude any dipole-field interaction with the PM magnet.

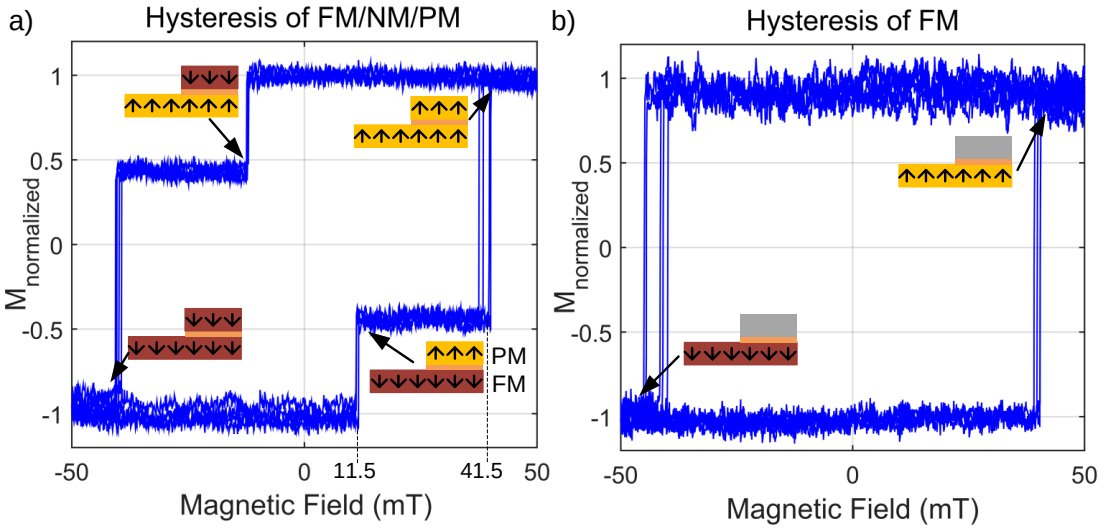

Figure 9.6: Hysteresis curve measurements of the GMR sandwich structure (a) and the FM layer magnet (b) [EBvGK+15].

9.5 Measurement results

The MRs of the fabricated sensors are measured with the Wheatstone-bridge measurement technique described in sec. 9.2 and the setup explained in sec. 4.5. Before measuring the MR, the structures are characterized with the MOKE and the wide-field MOKE first. The results are presented in the following.

9.5.1 Hysteresis curve measurements with the MOKE

Hysteresis curve measurements serve to analyze the switching behavior of the magnets. They are performed to confirm that the magnetic layers FM and PM are not exchange coupled and behave like individual magnets. Furthermore the switching field values of FM and PM can be extracted, which is important to know in order to find out which magnet is the soft and which is the hard magnetic one. In a first experiment, the laser beam of the MOKE is positioned on the posterior part of the sensor, containing the sandwich stack FM/NM/PM. Five hysteresis curves are recorded. During the measurement, the external magnetic field is swept with a rate of 50 mT/s, starting at zero field and ramping up to the amplitude of 50 mT. The field resolution amounts to 0.1 mT. The recorded curves are shown in Fig. 9.6. In a), the hysteresis curves show a double switching behavior. This confirms that FM and PM behaves like single magnets as they do switch separately. This experiment proves on the one hand that a Cu-layer thickness of 3 nm is sufficient to prohibit exchange coupling between FM and PM. On the other hand, the experiment confirms that all layers of FM are exchange

coupled to each other and behave like a single magnet, although the last Co-layer of the FM magnet is sputtered in an extra process step. In case the last Co-layer of FM would have switched on its own, three steps in the hysteresis curve would have been detected.
However from the hysteresis measurements performed in a) it is not possible to assign the resulting coercivities to the corresponding FM and PM. Further, hysteresis measurements are performed on the FM magnet. Therefore, the scanner is positioned on the free-standing part of the FM magnet and again five hysteresis curves are recorded. The analysis shows that the FM magnet is the one with the higher coercivity (see Fig. 9.6 b)), which is supposed to be the soft one. The mean coercivity of PM amounts to 11.5 mT and the one of FM to 41.5 mT. This experiment reveals, that enhancing the partial Ar sputtering pressure is not sufficient to evoke a hard magnetic switching of PM. The morphology of the Cu-layer may be a possible reason for the reduced coercivity of the PM layer. The texture of Cu may cause defects in the subsequent layers resulting in domain wall nucleation centers with weak anisotropy constant. If the Cu-layer possesses grains, they create strong defects in the crystalline structure of all subsequent sputtered layers leading to the low coercivity of PM. Compared to PM, the FM layer is sputtered on a Pt-seed layer, which possesses a distinct (111) texture resulting in high PMA and higher switching field values. Here, further experiments have to be performed on parameters like sputtering pressure, RF power and layer thickness of Cu as they have the most impact on the microstructure of the film. In [129] it is stated, that oxygen addition during high Ar pressure sputtering successfully increases the coercivity. So this may be a pathway, which demands further investigations.
A possible and common solution applied in the industry to pin the magnetization state of PM is to use an antiferromagnet (AF) in direct contact with the PM layer. First documented experiments on exchange biasing by applying an AF were performed in 1956 [130]. The AF possesses alternating spins compensating each other. However, at the interface PM/AF remain small uncompensated net moments in the direction of the PM layer. Due to the exchange coupling of the uncompensated moments in AF with the moments in PM, the magnetization of PM is fixed in one direction.
Anyhow, with the fabricated structure, parallel and anti-parallel alignment between PM and FM can be still achieved, which is sufficient to demonstrate the basic functioning of the fabricated sensor type and to ensure that the MR is increased for anti-parallel alignment and decreased for parallel alignment.
In a last experiment, hysteresis curves under the influence of current bias are recorded. This experiment is extremely important, as current heats up the sensor structure and may lead to a different domain wall behavior or switching behavior of the magnets or can even destroy the sensor. Therefore this experiment serves to verify that the current has no negative effects on the magnets. In the experiment itself, the same current amplitude, namely 5 µA is applied to the sensor as during

the MR measurements. This current is applied for half an hour to several sensor structures and hysteresis curves were reported several times during this period of time. During the experiments no modified switching behavior due to the current bias was observed. The magnets behave in the same way as for the non current bias case. This proves, that modifications due to current bias are excluded.

9.5.2 Wide-field MOKE measurements

The wide-field MOKE measurements serve to detect the domain wall nucleation spot and investigate domain wall propagation. Nucleation is supposed to take place in the irradiated region of the FM magnet and the propagation of the domain wall is supposed to be without any hindrance despite interaction with the PM layer. Therefore the sensor structure is first saturated in the down direction with an external field pulse of 200 mT. Afterwards a nucleation field pulse ($\mu_0 H_{Nuc}$) of +43 mT is applied for 1 µs to nucleate the domain wall. As soon as the domain wall is nucleated, the field amplitude is reduced to +35 mT, as less field is required to propagate the domain wall ($\mu_0 H_{Prop}$). The reduced amplitude is consciously applied in order to propagate the domain wall in small distances through the structure to get a high spatial resolution of the domain wall motion. As domain wall velocity is proportional to the field amplitude [BFK+15], higher amplitudes result in larger covered distances during pulse time and therefore in a lower resolution. In sum five pulses of 1 µs duration each, are needed to propagate the domain wall through the whole structure. The results are shown in Fig. 9.7. As expected, the domain wall is nucleated in the irradiated spot after the nucleation pulse have been applied. Nucleation at the border of 'FM only' and 'FM/NM/PM' can be excluded. If so, the domain wall must have been propagated to both sides uniformly during the nucleation pulse and a domain wall in the FM as well as in the FM/NM/PM layer would be observable, which is not the case. The domain wall enters the FM/NM/PM part firstly after the first propagation pulse has been applied. After five propagation pulses, the whole FM layer is reversed without detection of any hinderance despite interaction with the PM layer. Even the last Co-layer of FM, which has been sputtered in an extra fabrication step reverses simultaneously with the remaining Co-layers of FM. There is no separate nucleation center for a domain wall in the last Co-layer of the FM detected by these experiments.
However, it has to be mentioned that it was not possible in these experiments to evoke a hindering magnetization state of PM for domain wall propagation in the FM layer due to the low coercivity of the PM. PM always switches in the parallel state to FM before even domain wall nucleation in FM takes place. The industrial solution to shorten the stray field lines of PM and thereby prevent undesired interaction with the FM, is to introduce an artificial antiferromagnet (AAF). The AAF is strongly antiferromagnetically interlayer exchange coupled to PM. This

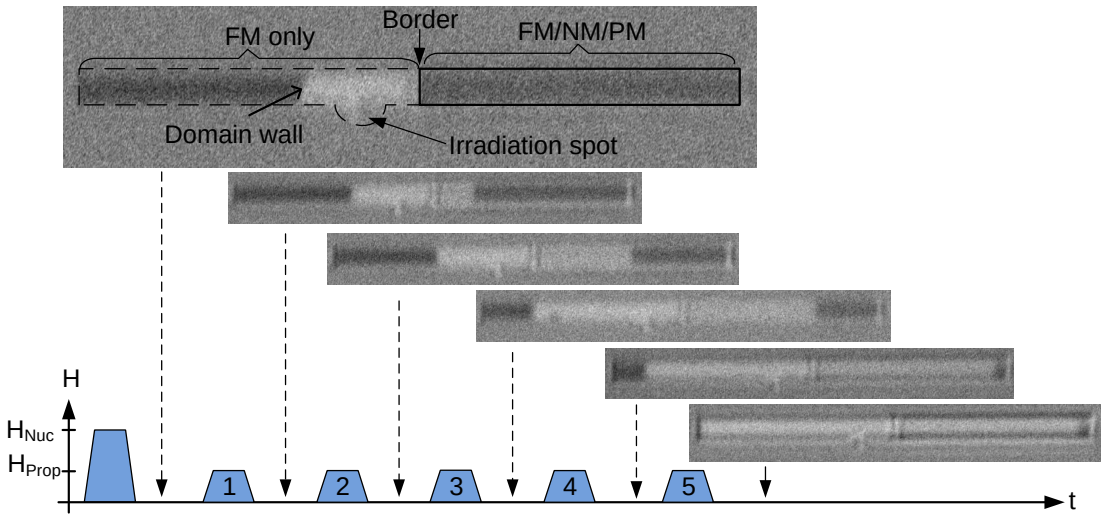

Figure 9.7: Wide-field MOKE measurements. The domain wall is nucleated in the irradiated spot of the FM and propagates by 5 propagation pulses to the left and right side of the sensor structure [EBvGK+15].

guarantees the compensation of the magnetic moment of the PM. For exemple rutanium (Ru) as interlayer results in antiferromagnetic exchange coupling [131]. In summary, the pinned layer of the sensor structure must consist of two ferromagnets separated by Ru to prevent stray field interaction to the free layer. Further a AF must be added to pin the PM magnet. This would be a solution, which guarantees that even in the opposed state of PM to FM, the domain wall can propagate unimpeded into the sensing/posterior part of the FM.

9.5.3 Magnetoresistance measurements

The MR measurements are performed with the setup shown in Fig. 4.5 and described in sec. 4.5. Before starting with the MR measurements, the resistance values of R_F, R_M, R_{FS} and R_P (compare Fig. 9.2 b) for the Wheatstone-bridge circuitry have to be determined in order to balance the bridge correctly. First, the initial resistance of the magnetic stack R_M is measured via four-point measurement, with four test probes applied in series. In the initial state FM and PM are aligned parallel to each other and the measured resistance amounts to 466 Ω. The magnitudes of all fixed resistances thereby orientate themselves towards this value. R_F is chosen to be 468 Ω and R_{FS} amounts to 396 Ω. The adjustable range of the potentiometer is chosen to be 100 Ω. Hereby it can be guaranteed that the series resistance of R_{FS} and R_P can be adjusted to the value of R_M to balance

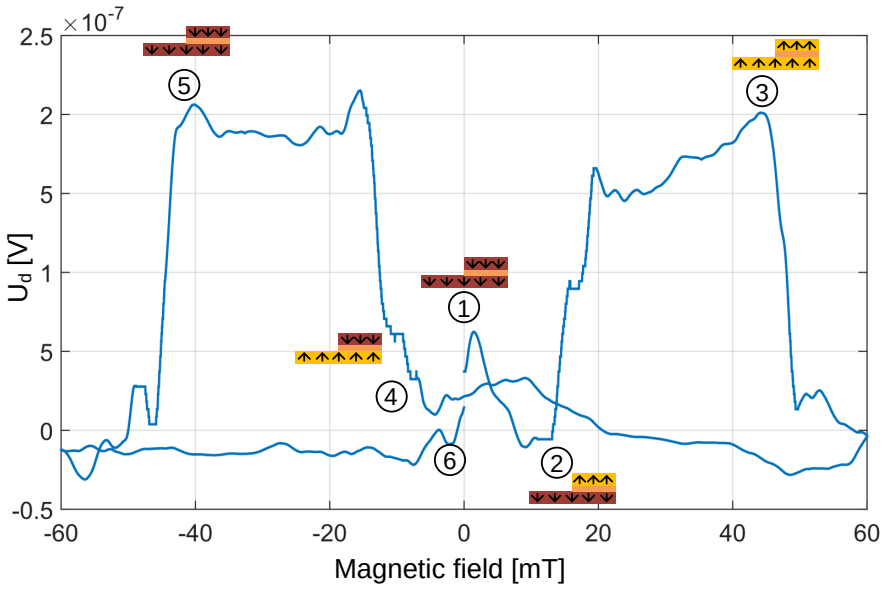

Figure 9.8: Measured diagonal voltage U_d versus applied external magnetic field [EBvGK+15].

the bridge.
To measure MR, the sample has to be exposed to the external field to enforce the two possible different alignments between FM and PM. While the field is ramped up and down in different directions, a current is biased ($I_0 = 5\,\mu A$) into the sensor structure and the resulting diagonal voltage U_d between the two resistance branches (between the points **a** and **b** of Fig. 9.2 b) is measured.
In the initial state, the magnets are aligned parallel to each other and the bridge is balanced by adjusting the potentiometer to the right value. Starting at zero field, the field amplitude is increased in 0.025 mT steps to the peak field of 60 mT. Afterwards, the field amplitude is decreased to the value of -60 mT in the same step size as before. At last, the field amplitude is again increased to the value of zero field. During field ramping four jumps in the diagonal voltage could be detected, as depicted in Fig. 9.8. At point '1' FM and PM are both downwards magnetized (initial condition at zero field). Then the field is increased and at point '2' the switching field of PM is reached. PM switches in the anti-parallel state at the same time MR is increased and thus U_d. U_d remains high until PM switches in the parallel state at point '3'. Between point '3' and '4', the diagonal voltage remains low as both magnets are parallel to each other (both up magnetization). At point '4' the negative switching field value of PM is reached and PM switches in the opposed direction to FM leading to an increase in the MR and therefore in U_d. Again U_d remains high until the negative switching field value of FM is reached (at point '5'). FM switches in the parallel state to PM, whereas

MR is decreased again and thus U_d . Reducing the external field again to zero field (point '6') no further switching events occur.
The resulting ΔR from eq. 9.9 is calculated from the amplitude of U_d. From the graph shown in Fig. 9.8, U_d is determined to be $2 \times 10^{-7}\,\mathrm{V}$, which results in $\Delta R = 160\,\mathrm{m\Omega}$. Inserting the value of ΔR in eq. 9.1, the MR_{ratio} amounts to $0.34\,‰$.

9.5.4 Summary

A two-step lithographic fabrication process was presented enabling the fabrication of a specific MR sensor structure for application for electrical read-out in pNML systems. The functioning of the fabricated sensor was verified by different measurement setups. Although the last Co-layer of the FM magnet is sputtered in a further process step, the experiments confirm that all layers of the FM are exchange coupled to each other and behave as a single magnet during switching. This behavior was proven by hysteresis and Wide-field MOKE measurements. Furthermore, the hysteresis curves showed a double switching behaviour attributed to switching of FM and PM. This proves, that the 3 nm Cu-layer is sufficient to prohibit exchange coupling between FM and PM and thereby enable individual switching of the FM and PM magnet. Wide-field MOKE measurements confirmed domain wall nucleation in the irradiated area of the FM. Measuring the MR, an increase could be proven for the anti-parallel orientation of PM to FM and a decrease for the parallel orientation respectively. However, the resulting effect is still small, there are nurmerous parameters discussed in the literature to enhance the effect, such as oxygen addition during sputtering [132], modification of the microstructure [133], choice of appropriate substrates [134], annealing treatment [135, 136] or choice of Co/Ni multilayers as ferromagnets [137]. These parameters require additional investigations.
In sum, the performed experiments approve the presented fabrication technique and even more the applicability of the proposed sensor structure for pNML read-out. This is the first fabricated integrable sensor structure in pNML offering an interface between CMOS and pNML. The same sensor structure could also be used to realize MTJ-based sensors as they promise for higher effects (as high as 50% or more) than GMR-based sensors ($\approx$ 24%) [92]. Hereby only the metallic Cu-layer must be replaced by an insulating tunnel barrier [138, 139]. A widely used material for the tunnel barrier is MgO_x.
With regards to the electrical contacts, in a pNML application, the bottom contact of the sensor would be an Au seedlayer, on which the whole NML system is situated, whereas the top electrode is contacted on the top of the FM/NM/PM layer resulting again in a current-flow perpendicular to the film plane. Electrical contacting in this way enables the highest integration densities of the proposed sensor structure.

9.6 Magnetoresistance in Co/Ni films

The pursuit for higher MR-effects led to the investigation of alternative multilayer systems. In [137] it is stated, that Co/Ni multilayer possess a higher spin polarization than Co/Pt layers corresponding to a higher GMR-effect. In this context, GMR sandwiches with the two ferromagnets both consisting of a Co/Ni multilayer were investigated. Hereby, the material of the spacer layer remained the same. Furthermore, a different fabrication technique including shadow masks for pattern definition has been applied to enable faster evaluation of the GMR sandwiches. In the following, the alternative fabrication technique and the measurement results are presented.

Achieving PMA in Co/Ni multilayers

Before starting with the fabrication of the Co/Ni GMR sandwiches, perpendicular magnetic anisotropy (PMA) must be guaranteed. Achieving PMA in Co/Ni films is not trivial and therefore different film compositions and parameters have been investigated in previous works, here at the Lehrstuhl für Technische Elektronik [Eic11, Ruf12, Kun14b]. The results are summarized in the following.
Co/Pt multilayer films possess a high PMA due to two main reasons: the sharp (111) texture of the Pt-layer, which is part of the crystalline anisotropy and the lack of symmetry in the crystalline order at the Co/Pt interface, which is part of the interface-anisotropy. Both factors lead to strong PMA sufficient to overcome shape anisotropy. In Co/Ni films, the sharp (111) texture can be introduced by an Au- [140, Kun14b], Au/Pt- [Eic11] or Ta/Pt-seedlayer [Ruf12]. The Co/Ni interface provides also a crucial impact to the interfacial anisotropy even if both materials differ only by one valence electron and have almost equal atomic size [141]. However due to the lack of the (111) texture in between the Co layers, PMA in Co/Ni films is lower than in Co/Pt films. An additional annealing step is required to increase the sharpness of the (111) texture of the seedlayer in order to achieve PMA in Co/Ni films. Annealing enables recrystallization processes. Hereby defects in the crystalline lattice are healed.
In all previous works done here at the Lehrstuhl [Eic11, Ruf12, Kun14b] the following parameters have been found crucial for PMA: choice of material for seedlayer, seedlayer thickness, thickness of Co and Ni layer, number of bilayer repetitions, annealing temperature and time.
Hereby an Au- or Au/Pt seedlayer shows the best results concerning magnetic domain size and perpendicular switching behaviour. With regard to the seedlayer thickness, it could be observed, that the thickness of Au has the most impact. With increasing Au thicknesses (up to 20 nm), the size of domains increased and the switching behaviour (rectangle shape of hysteresis curve) improved, whereas the best results were achieved for $t_{Au} = 10$ nm, if a combination of Au- and Pt-layer

is chosen, and for $t_{Au} = 20\,\text{nm}$ if solely an Au-layer is chosen as seedlayer. For a greater thickness the crystallinity improves due to bigger grain size and thereby the (111) texture of Au becomes more pronounced. When choosing the combination of Pt and Au, for an Au-thickness above 10 nm no further improvements could be observed.
In terms of Ni-layer thickness, it could be approved, that the thickness of Ni-layer has to be twice that of the Co-layer as predicted by [13]. The corresponding thickness of the Co-layer amounts to 0.2 nm. Thickness below 0.2 nm is not favorable because it causes a reduction of the PMA. Very small film thicknesses correspond no longer to continuous films but break up into islands resulting in a lower interface contribution and therefore in a reduction of the PMA. With Co-layer thicknesses above 0.2 nm, the domain size continuously decreases as more magnetic material leads to enhanced demagnetization energy and thereby to the introduction of further domain walls.
The maximum number of bilayer repetitions to achieve domains in the 1 µm range has been determined to be five. A higher bilayer number results in decreased domain sizes due to increased magnetization. The more magnetic material, the higher is the demagnetizing energy and from the energetically point of view it is more favorable to introduce new domain walls in the film. Another reason for decreased domain size could be a higher roughness induced by the multiple alteration of the layers and thereby the multiple change in crystallography [141, 142].
Annealing temperatures of 150°C - 200°C on a hotplate under air condition for 20min-1h induced PMA. Without annealing neither sharp switching behaviour, nor domains could be detected. Temperatures below 150°C showed no PMA induction. Temperatures above 200°C are not advisable as high coercivity values and losses in saturation magnetization due to the formation of paramagnetic islands [140] are induced. Annealing temperatures above 350°C can even destroy PMA due to interfacial alloying between Co and Ni. Furthermore the perpendicular switching behaviour is lost. Same behavior could be observed for annealing times over 1h. In summary, the above mentioned parameters have been optimized to achieve the highest possible overall magnetization (for high coupling fields) and at the same time to maintain domain size at the 500 nm - 1 µm regime to enable MOKE measurements (resolution is limited to $\approx 500\,\text{nm}$). However, depending on the technology, the required film properties can be adopted by varying the above mentioned parameters.

Alternative fabrication process

In order to have a fast characterization possibility for different GMR-film compositions a different fabrication process is proposed. Instead of doing nanostructuring, which requires FIB lithography, it was turned to bigger structures in the mm regime applying shadow mask patterning. The applied fabrication process is

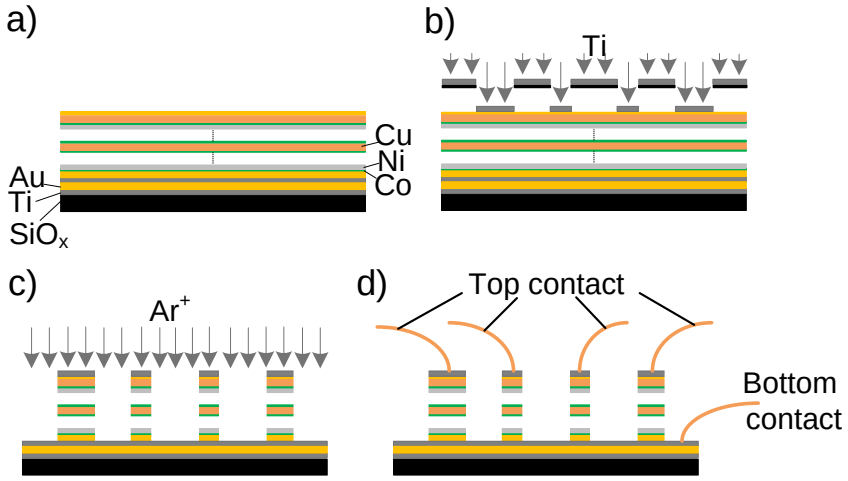

Figure 9.9: Fabrication process of Co/Ni dots. (a) Sputtering. (b) Hard mask e-beam evaporation. (c) Ion beam etching. (d) Direct bonding.

presented in Fig. 9.9. At first the multilayer stack is sputtered, beginning with a ($Ti_{1\,nm}/Au_{10\,nm}/Ti_{2\,nm}/Au_{20\,nm}$) bottom layer sputtered on the SiO_x wafer. The first Ti-layer serves as adhesion promoter for the first Au-layer, which is supposed to be the bottom electrode. The top Ti-layer serves as etch stop for the physical etching process required to structure Co/Ni multilayer stack. The second Au-layer serves as seedlayer for the following Co/Ni/Cu multilayer stack. However, before multilayer deposition, the seedlayer is pre-annealed at 150°C on a hot plate for 20 minutes. Afterwards the first ($Co_{0.2\,nm}/Ni_{0.4\,nm}$) multilayer with $N \in \{3, 5\}$ for Co and respectively $N-1$ times for Ni is sputtered defining the bottom magnet. The layer of the top magnet (above the Cu layer) is hereby identically composited. The thickness of the Cu-spacer layer has been varied by $t_{Cu} \in \{1.5\,nm, 4\,nm, 6\,nm, 8\,nm\}$. The cap layer is a ($Cu_{4\,nm}/Au_{2\,nm}$). The Cu-cap layer is not obligatory but had to be applied here as oxidation protection of the top-most Co-layer. The Au layer could not be deposited instead because number of targets of the sputtering machine is limited to three targets. As the Co/Ni/Cu multilayer deposition under the strict adherence of the vacuum condition is more important, those three targets were built in the sputtering machine. To deposit the Au-layer the sputtering machine had to be changed.
To pattern the magnetic film a 4 nm Ti-layer serving as etch stopper is evaporated through a shadow mask (see Fig. 9.9 b) containing rectangles of footprint $0.25\,mm^2$ and $0.5\,mm^2$. Afterwards, all unprotected parts are physically etched by Ar^+ ions (see Fig. 9.9 c). In a last step, the remaining dots are directly contacted by a bonding wire to the chip carrier (see Fig. 9.9 d).

Measurement results

The fabricated dots were characterized by hysteresis measurements and MR measurements with the same setup as described in sec. 4.5. The measurement approach of the MR equals the one described in the preceding subsections. However the applied current in the Wheatstone-bridge circuitry amounted to 5 mA. Due to a larger cross sectional area compared to the Co/Pt/Cu structures, higher current amplitudes are allowed whereas the critical current density is not exceeded.
In a first step, the resistances of the fabricated dots composed of the above mentioned films are determined. The values varied in the range from 4 Ω to 10 Ω, whereas the smaller dots always resulted in higher resistance values than the larger dots due to a reduced cross sectional area through which the current flows. All of the applied film compositions except the one with the 1.5 nm Cu-spacer layer resulted in exchange-decoupled magnetic layers, proven by the double switching behavior of the hysteresis loop (see Fig. 9.10 a). However, the sort of coupling was not ferromagnetic as it has been observed in the Co/Pt/Cu films, but antiferromagnetic. This could be detected by hysteresis measurements. Whenever the soft magnet was aligned parallel to the hard magnet, its coercivity was shifted to higher amplitudes. The reverse case was observed when the soft magnet was switched anti-parallel to the hard magnet. Hereby, lower coercivity values were measured.
In terms of MR measurements, the best results were achieved for the film composition with $N = 3$ and a Cu-spacer layer of 4 nm. Here, a MR_{ratio} of 1.3 ‰ was measured (corresponding curve of the diagonal voltage is shown in Fig. 9.10 b).
A correlation between the thickness of the Cu-spacer layer and the resulting MR_{ratio} was not observed. For the increased number of multilayer $N = 5$ no improvement in the MR_{ratio} was detected. Here, an increase of the MR_{ratio} was expected due to a higher ferromagnetic amount providing a higher probability for electron scattering. However, further experiments must be performed to permit final conclusions as the investigated parameters are extremely sensitive to variations in the fabrication process.
Compared to the Co/Pt/Cu film presented in the previous section, the MR_{ratio} could be increased by a factor of 3.8. To exclude the influence of the applied fabrication technique, Co/Pt/Cu dots have been fabricated with the same shadow mask technique. The resulting MR_{ratio} was in the range of 0.02 ‰ [Kun14a]. This fact indicates the better performance of the Co/Ni/Cu films.
Applying the fabrication technique proposed in 9.4 to enable the split sensor geometry (Fig. 9.3 b) also with Co/Ni/Cu films requires an additional Pt-cap layer to be sputtered on the first FM film stack (otherwise Co gets oxidized). This leads to a disruption of the Co/Ni/Cu multilayer structure, which may have a negative effect on the MR. So experiments have to be performed on that, to confirm the predicted better performance of Co/Ni films for the applied fabrication technique.

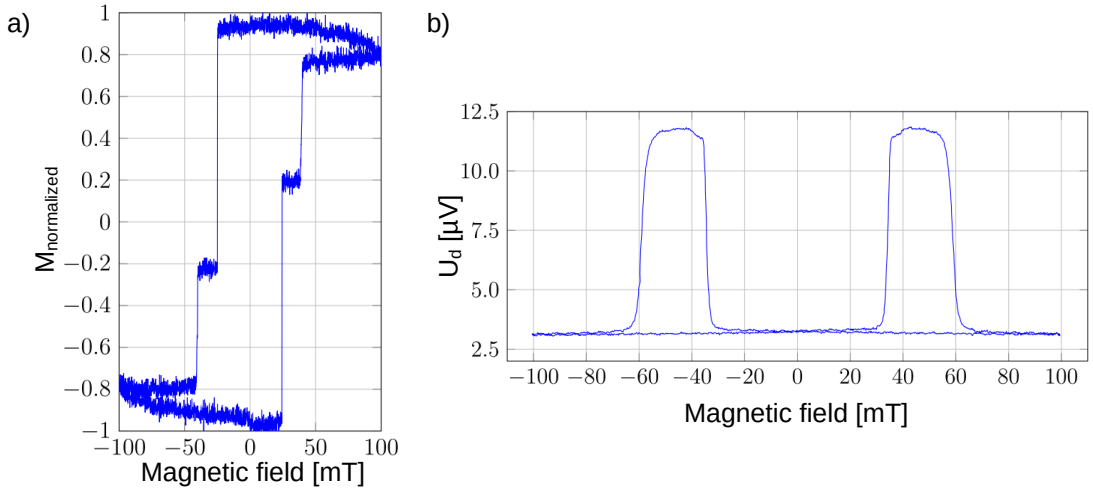

Figure 9.10: (a) Hysteresis curve of a Co/Ni magnetoresistance sensor with a Cu-spacer layer thickness of 4.0 nm and (b) the corresponding diagonal voltage versus applied magnetic field [Kun14a].

It is assumed, that the best results can be achieved, when the vacuum condition is maintained for all fabrication steps.

Summary

In this section an alternative material film composition i.e. Co/Ni multilayers for magnetoresistance sensors in pNML has been investigated and discussed, as these kind of materials promise for higher magnetoresistive effects. It turned out, that to achieve perpendicular magnetic anisotropy in Co/Ni multilayers, a special seedlayer (Au or Au/Pt) and an additional annealing step after sputtering is required. Furthermore, the annealing temperature and time must be well controlled to achieve the desired results. An alternative fast fabrication process including shadow masks for pattern definition and direct bonding was additionally presented. It requires neither FIB lithography for multilayer patterning, nor optical lithography to deposit electrical contacts on the sensor structures. By avoiding these two fabrication steps more than 50% of the fabrication time could be saved. Hysteresis curve measurements confirmed double switching behavior and thereby separated switching of the FM and PM composed of Co/Ni multilayers. Magnetoresistance measurements showed higher MR_{ratio} values for the sensors composed of Co/Ni multilayers compared to those composed of Co/Pt multilayers.

10 Conclusion

Nanomagnetic Logic (NML) is a novel beyond CMOS technology exploiting magnetic field interaction between nano-scaled magnetic islands for information processing. NML systems operate at room temperature and at ultra-low power, as the power is only provided by a magnetic clock with rather low amplitude. So no power supply network is needed. Furthermore, NML systems are radiation hard and free of leakage currents, as signal processing relies on pure magnetic field interaction. The inherent non-volatile magnetization state of the magnets provides the possibility to combine logic and memory functionality in every single device. Further benefits of NML are data pipelining, parallel signal processing by a global clocking field and high integration densities. It can be integrated in the back-end process of CMOS systems and extend their functionality or even partially substitute them.

Intense research in the last decade has revealed the basic feasibility of NML devices and circuits. It all started from multilayer sputtering, followed by patterning of small magnetic islands and arranging them in a magnetic network in 2D to enable logic computing operations. Single devices and circuits in 2D in in-plane as well as in perpendicular NML were built up successfully in the past. This work goes a step further and focuses on the 3D integration pNML.

A new fabrication process is developed enabling monolithic 3D integration of pNML by stacking multiple functional layers in the vertical direction above each other. The fabrication process is based on the planarization of functional layers by a transparent spin-on dielectric (HSQ) representing the simplest but also the most efficient way to create a planar substrate for the magnets of subsequent functional layers. The transparency of the planarization substrate allows for visibility of underlying functional layers, which is important for evaluation of the proper function. For precise alignment of top to bottom layer a special technique based on the log in on artificially introduced orientation marks is presented. Critical parameters influencing the bottom magnets performance during the fabrication of the top magnets are intensely studied by simulations and experiments. Limit values for the critical parameters to preserve the bottom magnets performance are determined and confirmed by experimental results.

For comparison, 3D integration techniques in CMOS are evaluated including 3D packaging, integration with Through Silicon Vias and monolithic integration. As vertical signal transfer in pNML is done by magnetic field-interaction, distances below 100 nm between functional layers are required for reliable operation. Hence,

the only suitable fabrication technique allowing for such thin substrates is the monolithic approach. At the same time this approach promises for highest integration densities.
For sample characterization different measurement techniques and setups like the SEM, MOKE, MFM, Wide-field MOKE and Wheatstone-bridge circuitry are applied. Micromagnetic simulations are extensively performed with the OOMMF, which enable the prediction of the coupling field and the switching behavior of the magnets.
The research and development of operating 3D pNML devices is the main focus of this work. In first experiments, field-coupling between two magnets lying in two different functional layers is investigated. One of the magnets is partially irradiated by the focused ion beam (FIB) to be sensitive to the stray field of its neighbor magnet (FIB irradiation is a well-known method in pNML that provides signal directionality by creating a weak spot in the magnet, where domain wall nucleation and thereby the reversal process of the magnet can be controlled by the stray field from surrounding neighbor magnets). Measurement results on such pair of magnets prove vertical field-interaction and the ability to transmit magnetic signals in the vertical direction. The so called 'magnetic via' is born paving the way for all further developed 3D pNML devices. Different parameters to enhance the coupling field and thereby reduce the error-proneness of the device are additionally investigated by simulations.
The ability to transmit magnetic signals in another functional layer provides the possibility for the realization of magnetic signal crossings. A multi-layer crossing is presented and implemented. Hereby, one of the crossing signals is detoured through a further functional layer and afterwards transmitted back to its original layer exploiting magnetic field interaction in the magnetic via. The functionality of the fabricated multi-layer crossing is successfully proven by experiments for the first time. The successive transmission of the signal from one to another layer and back to the original layer is additionally revealed by MFM measurements. To the best of our knowledge, this is the first magnetic signal crossing proven experimentally.
The feasibility of 3D magnetic computing in pNML is demonstrated on the basis of a majority gate, whose inputs are distributed on two different functional layers. The superposition of the stray fields emanated from the three inputs controls the magnetization state of the output magnet. The design criterion to achieve equal influence of each input on the output magnet is discussed in detail. Micromagnetic simulations capable to predict the coupling field emanated by each input magnet helped to find parameters to satisfy this design criterion. Experimental results show the correct operation of the fabricated gate over many clocking cycles for every possible input configuration. Simulations on the computing area of the gate confirm that a large part of the area of each input magnet (overhead from measuring pads) can be neglected without affecting the functionality of the gate.

The presented gate enables NAND/NOR functionality and is the first 3D device that proves magnetic logic computing by magnets interconnected over multiple functional layers. In comparison to the 2D implementation of the majority gate, the 3D majority gate has its third input, which programs its functionality to either a NAND or NOR gate, located in another functional layer. This provides the possibility to decouple programming and computing operations on chip.
A further aspect of this work deals with the integration of pNML in common CMOS technology to combine the features of both technologies in one system. Therefore an electrical interface converting the signal from the magnetic domain into the electrical charge-based domain is investigated. A special output interface is realized by a magnetoresistance sensor. The sensor possesses a special structure, which is integrable and compatible with the current pNML system design. The fabricated sensor is characterized by a Wheatstone-bridge circuitry measurement setup and shows the desired sensitivity. Further materials for the composition of the sensor are investigated and discussed in order to further improve the sensor's performance.
In summary, the presented work is the first exploring the feasibility of 3D integration in pNML. A monolithic fabrication process is presented, which enables the successive fabrication of multiple magnetic functional layers. All basic elements required for 3D integration are presented and experimentally demonstrated. The presented 3D elements are the basis to build up powerful, embedded, high density, complex, multifunctional 3D pNML systems combined with the 2D elements that already exist and that have been successfully demonstrated in the past by our research group in Munich. Furthermore the presented integrable magnetoresistance sensor provides the required interface between pNML and CMOS technology.
In terms of pNML systems it is important to mention, that investigations on the consequences of possible "cross-coupling" between large magnet arrays are required. The high integration densities particularly achieved by 3D integration, will lead to the problem, that the stray fields of far-away magnets will add up to the stray fields of nearest neighbor magnets and may cause errors in the field-interaction and therefore signal processing [143]. Dealing with these problems and providing solutions must be in the focus of the future work on 3D pNML.

Acronyms

AlO_x	aluminium-oxide
H_2O_2	hydrogen peroxide
H_2	hydrogen
MgO_x	magnesium-oxide
NH_4OH	ammonium hydroxide
N_2	nitrogen
O_2	oxygen
SFD_T	thermally induced switching field distribution
SFD_{Eff}	effective switching field distribution
SFD_{Fab}	fabrication induced switching field distribution
SiO_x	silicon-oxide
2D	two dimensional
3D	three dimensional
AAF	artificial antiferromagnet
AF	antiferromagnet
Al	aluminium
Ar	argon
AR600-55	resist developer for ion beam lithography
AR600-60	resist stopper for ion beam lithography
Au	aurum
CMOS	complementary metal-oxide semiconductor
CMP	chemical mechanical polishing
Co	cobalt
Co/Au	cobalt/aurum
Co/Cr	cobalt/chrome
Co/Ni	cobalt/nickel
Co/Pt	cobalt/platinum
Cu	copper

DAQ	data acquisition
DI	deionised
DOS	density of states
FIB	focused ion beam
FM	free magnet
Ga	gallium
GMR	giant magnetoresistance
HCl	hydrochloric acid
HF	hydrofluoric acid
HSQ	hydrogen silsesquioxane
ICs	integrated circuits
ITRS	International Technology Roadmap for Semiconductors
LED	light emitting diode
LLG	Landau-Lifshitz-Gilbert equation
MFM	magnetic force microscopy
MIBK	methylisobutylketon
MOKE	magneto-optical Kerr effect microscope
MR	magnetoresistance
MTJ	magnetic tunnel junction
Ni	nickel
NM	non-ferromagnetic, metallic layer
NML	Nanomagnetic logic
NMP	N-Methyl-2-pyrrolidon
OOMMF	object orientated micromagnetic framework
Pd/Co	palladium/cobalt
PM	pinned magnet
PMA	perpendicular magnetic anisotropy

PMMA	polymethylmethacrilate
pNML	perpendicular Nanomagnetic logic
Pt	platinum
Py	permalloy
QCA	quantum cellular automaton
RCA	Radio Corporation of America
Ru	rutanium
SEM	scanning electron microscopy
Si	silicon
SRIM	The stopping and range of Ions in matter simulation tool
Ta	tantalum
TEM	transmission electron microscopy
Ti	titan
TSV	through silicon vias
W	tungsten
W-MOKE	wide field magneto-optical Kerr effect microscope

List of Symbols

A	by the circular current I_e embraced area
A_{film}	magnetic film surface
$F(x)$	normal distribution
I_e	circular current produced by an electron
I_0	AC current of the Wheat-Stone bridge circuitry
K_S	phenomenological surface anisotropy constant
$K_{interface}$	interface anisotropy energy
K_{shape}	shape anisotropy energy
L	amplitude of the angular momentum produced by an electron
M_R	remanence magnetization
M_{Net}	net magnetization
M_S	saturation magnetization
P	switching probability of O of the majority gate
$P_{Overlap}$	overlap probability of the SFD_Ts of the majority gate
R_1	one of the four resistances of the Wheat-Stone bridge circuitry
R_2	one of the four resistances of the Wheat-Stone bridge circuitry
R_3	one of the four resistances of the Wheat-Stone bridge circuitry
R_4	one of the four resistances of the Wheat-Stone bridge circuitry
R_F	fixed resistance in the applied Wheat-Stone bridge circuitry of this work
R_P	potentiometer in the applied Wheat-Stone bridge circuitry of this work
R_{FS}	fixed series resistance to the potentiometer resistance R_P in the applied Wheat-Stone bridge circuitry of this work

R_M	magnetoresistance
R_q	source resistance of the Wheat-Stone bridge circuitry
T_C	Curie temperature
U_0	(sinusoidal) supply voltage of the Wheat-Stone bridge circuitry
U_d	diagonal voltage of the Wheat-Stone bridge circuitry
V	volume
ΔR	resistivity change
α	phenomenological damping constant
χ_m	magnetic susceptibility
γ	gyromagnetic ratio
γ_{LLG}	Landau-Lifshitz gyromagnetic ratio $-\gamma_{LLG} = 2.210 \cdot 10^5\,\mathrm{m/(As)}$
$\hbar$	reduced Planck constant $\hbar = 1.055 \cdot 10^{-34}\,\mathrm{Js}$
$\mathbf{B}$	magnetic flux density
$\mathbf{H_{Current}}$	magnetic field produced by a current wire
$\mathbf{H_{Dip}}$	magnetic dipole field
$\mathbf{H}$	magnetic field
$\mathbf{H}_{ext}$	external magnetic field
$\mathbf{L}$	angular momentum produced by an electron
$\mathbf{M}$	magnetization, magnetic dipole moment per unit volume
$\mathbf{N}$	demagnetizing tensor
$\mathbf{T}$	torque acting on a magnetic moment
$\mathbf{k_{Net}}$	net coupling field
$\mathbf{k_{cross}}$	coupling field in the direct crossover region of two crossing magnetic wires
$\mathbf{k}$	coupling field
$\mathbf{m_d}$	magnetic dipole moment
$\mu_0 H_{Clock}$	clocking field amplitude
$\mu_0 H_C$	coercive field amplitude
$\mu_0 H_{Eff}$	effective acting field amplitude
$\mu_0 H_{Nuc}$	nucleation field amplitude
$\mu_0 H_{Prop}$	propagation field amplitude
$\mu_0 H_{depin}$	depinning field amplitude

μ_H	expectancy value of the switching field of O
μ_0	vacuum permeability $\mu_0 = 4\pi \cdot 10^{-7}$ Vs/(Am)
μ_B	Bohr magneton $\mu_B = 9.274 \cdot 10^{-24}$ J/T
μ_r	relative permeability
ω_0	angular frequency
$\phi(x)$	standard normal distribution
σ_H	standard deviation of the switching field
θ	angle, $\mathbf{M}$ encloses with the film normal
d	magnetic film thickness
d_c	critical magnetic film thickness
e	charge of an electron $e = 1.602 \cdot 10^{-19}$ C
$f(x)$	probability density function
g	Lande gyromagnetic splitting factor
m_d	amount of a magnetic dipole moment
m_e	mass of an electron $m_e = 9.1094 \cdot 10^{-31}$ kg
n	form factor including the magnet's shape influence
q	charge
r_e	orbit radius of an electron
rpm	revolutions per minute

Related Publications of the Author

[BBE+15] M. Becherer, S. Breitkreutz, I. Eichwald, G. Ziemys, J. Kiermaier, G. Csaba, and D. Schmitt-Landsiedel, "Low-power 3D integrated ferromagnetic computing (invited)," in *Proceedings of Joint International EUROSOI Workshop and International Conference on Ultimate Integration on Silicon (EUROSOI-ULIS)*, 2015.

[BBK+13a] M. Becherer, S. Breitkreutz, J. Kiermaier, I. Eichwald, G. Csaba, and D. Schmitt-Landsiedel, "Nanomagnetic Logic Clocked in the MHz Regime," in *IEEE Proceedings of the 43rd European Solid-State Device Research Conference (ESSDERC)*, 2013, pp. 276–279.

[BBK+13b] M. Becherer, S. Breitkreutz, J. Kiermaier, I. Eichwald, and D. Schmitt-Landsiedel, "3D Integration of Nonvolatile Nanomagnetic Logic," Patent Application, 2013.

[BEK+14] S. Breitkreutz *et al.*, "1-bit full adder in perpendicular nanomagnetic logic using a novel 5-input majority gate," in *EPJ Web of Conferences*, vol. 75. EDP Sciences, 2014, p. 05001.

[BEZ+14] S. Breitkreutz, I. Eichwald, G. Ziemys, D. Schmitt-Landsiedel, and M. Becherer, "Influence of the Domain Wall Nucleation Time on the Reliability of Perpendicular Nanomagnetic Logic," in *Proceedings of the 14th IEEE International Conference on Nanotechnology (IEEE-NANO)*, 2014, pp. 104–107.

[BFK+15] S. Breitkreutz, A. Fischer, S. Kaffah, S. Weigl, I. Eichwald, G. Ziemys, D. Schmitt-Landsiedel, and M. Becherer, "Time-dependent domain wall nucleation probability in field-coupled nanomagnets with perpendicular anisotropy," *Journal of Applied Physics*, vol. 117, no. 17, p. 17B503, 2015.

[BKB+12] M. Becherer, J. Kiermaier, S. Breitkreutz, I. Eichwald, G. Csaba, and D. Schmitt-Landsiedel, "A non-volatile low-power zero-leakage nanomagnetic computing system," in *Frontiers in Electronic Materials: Correlation Effects, Spintronics, and Memristive Phenomena*

- *Fundamentals and Applications*, J. Heber, D. Schlom, Y. Tokura, R. Waser, and M. Wuttig, Eds. Wiley-VCH, 2012, pp. 194–195.

[BKB+13] M. Becherer, J. Kiermaier, S. Breitkreutz, I. Eichwald, and D. Schmitt-Landsiedel, "3D Integrated Circuits and Systems in Nanomagnetic Logic," Patent Application, 2013.

[BKB+14] M. Becherer, J. Kiermaier, S. Breitkreutz, I. Eichwald, G. Žiemys, G. Csaba, and D. Schmitt-Landsiedel, "Towards on-chip clocking of perpendicular nanomagnetic logic," *Solid-State Electronics*, vol. 102, pp. 46–51, 2014.

[BKE+12] S. Breitkreutz, J. Kiermaier, I. Eichwald, X. Ju, G. Csaba, D. Schmitt-Landsiedel, and M. Becherer, "Majority gate for nanomagnetic logic with perpendicular magnetic anisotropy," *IEEE Transactions on Magnetics*, vol. 43, pp. 4336–4339, 2012.

[BKE+13] S. Breitkreutz, J. Kiermaier, I. Eichwald, C. Hildbrand, G. Csaba, D. Schmitt-Landsiedel, and M. Becherer, "Experimental Demonstration of a 1-bit Full Adder in Perpendicular Nanomagnetic Logic," *IEEE Transactions on Magnetics*, vol. 49, no. 7, pp. 4464–4467, July 2013.

[EBK+12] I. Eichwald, A. Bartel, J. Kiermaier, S. Breitkreutz, G. Csaba, D. Schmitt-Landsiedel, and M. Becherer, "Nanomagnetic Logic: Error-Free, Directed Signal Transmission by an Inverter Chain," *IEEE Transactions on Magnetics*, vol. 48, no. 11, pp. 4332–4335, Nov 2012.

[EBK+14] I. Eichwald, S. Breitkreutz, J. Kiermaier, G. Csaba, D. Schmitt-Landsiedel, and M. Becherer, "Signal crossing in perpendicular nanomagnetic logic," *Journal of Applied Physics*, vol. 115, no. 17, p. 17E510, 2014.

[EBvGK+15] I. Eichwald, S. Breitkreutz-v. Gamm, F. Kunik, G. Ziemys, M. Becherer, and D. Schmitt-Landsiedel, "Towards integrated magnetoresistance sensors for electrical read-out in perpendicular Nanomagnetic Logic systems," in *20th International Conference on Magnetism (ICM)*, 2015.

[EBvGZ+15] I. Eichwald, S. Breitkreutz-v. Gamm, G. Ziemys, G. Csaba, and M. Becherer, "Demonstration of monolithically fabricated 3D Magnetic Computing Devices in perpendicular Nanomagnetic Logic," in *BIT's 4th Annual World Congress of Advanced Materials*, 2015.

[EBZ+14] I. Eichwald, S. Breitkreutz, G. Ziemys, G. Csaba, W. Porod, and M. Becherer, "Majority logic gate for 3D magnetic computing," *Nanotechnology*, vol. 25, no. 33, p. 335202, 2014.

[EKB+13] I. Eichwald, J. Kiermaier, S. Breitkreutz, J. Wu, G. Csaba, D. Schmitt-Landsiedel, and M. Becherer, "Towards a Signal Crossing in Double-Layer Nanomagnetic Logic," *IEEE Transactions on Magnetics*, vol. 49, no. 7, pp. 4468–4471, July 2013.

[KBE+13a] J. Kiermaier, S. Breitkreutz, I. Eichwald, M. Engelstädter, X. Ju, G. Csaba, D. Schmitt-Landsiedel, and M. Becherer, "Information transport in field-coupled nanomagnetic logic devices," *Journal of Applied Physics*, vol. 113, no. 17, p. 17B902, 2013.

[KBE+13b] J. Kiermaier, S. Breitkreutz, I. Eichwald, X. Ju, G. Csaba, D. Schmitt-Landsiedel, and M. Becherer, "Programmable Input for Nanomagnetic Logic Devices," *EPJ Web of Conferences*, vol. 40, p. 16007, 2013.

[PNC+14] A. Papp *et al.*, "Threshold gate based circuits from Nanomagnetic Logic," *IEEE Transactions on Nanotechnology*, vol. 13, pp. 990–996, 2014, to be published.

References

[1] G. E. Moore, "Cramming more components onto integrated circuits," *Electronics*, vol. 38, no. 8, pp. 114–117, April 1965.

[2] M. Ieong, K. Guarini, V. Chan, K. Bernstein, R. Joshi, J. Kedzierski, and W. Haensch, "Three dimensional CMOS devices and integrated circuits," in *Custom Integrated Circuits Conference, 2003. Proceedings of the IEEE 2003*, Sept 2003, pp. 207–213.

[3] (2012) The International Technology Roadmap for Semiconductors (ITRS): Update 2012. http://www.itrs.net. [Online]. Available: http://www.itrs.net/Links/2012ITRS/2012Chapters/2012Overview.pdf

[4] *The International Technology Roadmap for Semiconductors (ITRS): Emerging Research Devices (ERD)*, 2009. [Online]. Available: http://www.itrs.net/Links/2009ITRS/2009Chapters_2009Tables/2009_ERD.pdf

[5] *The International Technology Roadmap for Semiconductors (ITRS): Emerging Research Devices (ERD)*, 2013. [Online]. Available: http://www.itrs.net/Links/2013ITRS/2013Chapters/2013ERD.pdf

[6] *The International Technology Roadmap for Semiconductors*, 2007. [Online]. Available: http://www.itrs.net/links/2007_ITRS_CD/ExecSum2007.pdf

[7] T. R. Anthony, "Forming electrical interconnections through semiconductor wafers," *Journal of Applied Physics*, vol. 52, pp. 5340–5349, 1981.

[8] Y. Akasaka, "Three-Dimensional IC trends," *Proceedings of the IEEE*, vol. 74, pp. 1703–1714, 1986.

[9] E. Beyne, "3D system integration technologies," in *VLSI Technology, Systems, and Applications, 2006 International Symposium on.* IEEE, 2006, pp. 1–9.

[10] M. Shapiro, "3D Silicon Technology: Applications and Requirements." in *5th Annual 3D Architectures for Semiconductor Integration and Packaging Conference.*, 2008.

[11] R. Waser, *Nanoelectronics and Information Technology*, R. Waser, Ed. WILEY-VCH GmbH & Co. KGaA, Weinheim, 2005.

[12] T. Aign *et al.*, "Magnetization reversal in arrays of perpendicularly magnetized ultrathin dots coupled by dipolar interaction," *Physical Review Letters*, vol. 81, pp. 5656–5659, 1998.

[13] P. J. K. G. H. O. Daalderop and F. J. A. den Broeder, "Prediction and confirmation of perpendicular magnetic anisotropy in Co/Ni multilayers," *Phys. Rev. Lett.*, vol. 68, pp. 682–685, 1992.

[14] S. Breitkreutz, J. Kiermaier, S. V. Karthik, G. Csaba, D. Schmitt-Landsiedel, and M. Becherer, "Controlled reversal of Co/Pt dots for nanomagnetic logic applications," *Journal of Applied Physics*, vol. 111, no. 7, p. 07A715, 2012.

[15] M. Becherer *et al.*, "On-chip Extraordinary Hall-effect sensors for characterization of nanomagnetic logic devices," *Solid-State Electronics*, vol. 54, no. 9, pp. 1027–1032, 2010.

[16] J. Kiermaier, S. Breitkreutz, X. Ju, G. Csaba, D. Schmitt-Landsiedel, and M. Becherer, "Ultra-low volume ferromagnetic nanodots for field-coupled computing devices," in *IEEE Proceedings of the 40th European Solid-State Device Research Conference ESSDERC*, Sep. 2010, pp. 214–217.

[17] J. Kiermaier, S. Breitkreutz, G. Csaba, D. Schmitt-Landsiedel, and M. Becherer, "Electrical Input Structures for Nanomagnetic Logic Devices," *Journal of Applied Physics*, vol. 111, no. 7, p. E341, 2012.

[18] S. Breitkreutz, J. Kiermaier, X. Ju, G. Csaba, D. Schmitt-Landsiedel, and M. Becherer, "Nanomagnetic Logic: Demonstration of Directed Signal Flow for Field-coupled Computing Devices," in *IEEE Proceedings of the 41st European Solid-State Device Research Conference ESSDERC*, 2011, pp. 323–326.

[19] (2011) The International Technology Roadmap for Semiconductors (ITRS): Emerging Research Devices (ERD). http://www.itrs.net. [Online]. Available: http://www.itrs.net/Links/2011ITRS/2011Chapters/2011ERD.pdf

[20] V. L. Newhouse, "Magnetic core circuits," May 28 1957, US Patent 2,794,130.

[21] D. Bennion, H. Crane, and D. Nitzan, "Digital Magnetic Logic (Book on digital magnetic logic, considering digital magnetic core circuits consisting of magnetic components and interconnecting conductors)," 1969.

[22] S. Lee and H. Chang, "Magnetic bubble logic," *Magnetics, IEEE Transactions on*, vol. 10, no. 4, pp. 1059–1066, 1974.

[23] T. C. Chen and H. Chang, "Magnetic bubble memory and logic," *Advances in Computers*, vol. 17, pp. 223–282, 1978.

[24] D. A. Allwood, G. Xiong, M. D. Cooke, C. C. Faulkner, D. Atkinson, N. Vernier, and R. P. Cowburn, "Submicrometer ferromagnetic NOT gate and shift register," *Science*, vol. 296, pp. 2003–2006, 2002.

[25] M. Becherer, *Nanomagnetic Logic in Focused Ion Beam Engineered Co/Pt Multilayer Films*, ser. Selected Topics of Electronics and Micromechatronics, G. Wachutka and D. Schmitt-Landsiedel, Eds. Shaker Verlag, 2011, vol. 38.

[26] J. Kiermaier, *Integrated Nanomagnetic Logic System in Perpendicular Magnetic Media*, ser. Selected Topics of Electronics and Micromechatronics, G. Wachutka and D. Schmitt-Landsiedel, Eds. Shaker Verlag, 2014, vol. 45.

[27] K. Goser, P. Glösekötter, and J. Dienstuhl, *Nanoelectronics and nanosystems: from transistors to molecular and quantum devices*. Springer, 2004.

[28] A. O. Orlov, I. Amlani, G. H. Bernstein, C. S. Lent, and G. L. Snider, "Realization of a functional cell for quantum-dot cellular automata," *Science*, vol. 277, pp. 928–930, 1997.

[29] I. Amlani, A. O. Orlov, G. Toth, G. H. Bernstein, C. S. Lent, and G. L. Snider, "Digital Logic Gate Using Quantum-Dot Cellular Automata," *Science*, vol. 284, pp. 289–291, 1999.

[30] G. L. Snider, A. O. Orlov, I. Amlani, G. H. Bernstein, C. S. Lent, J. L. Merz, and W. Porod, "Quantum-Dot Cellular Automata: Line and Majority Logic Gate," *Japanese Journal of Applied Physics*, vol. 38, no. 12B, pp. 7227–7229, December 1999.

[31] R. P. Cowburn and M. E. Welland, "Room temperature magnetic quantum cellular automata," *Science*, vol. 287, pp. 1466–1468, 2000.

[32] G. Csaba, A. Imre, G. H. Bernstein, W. Porod, and V. Metlushko, "Nanocomputing by field-coupled nanomagnets," *IEEE Transactions on Nanotechnology*, vol. 1, no. 4, pp. 209–213, 2002.

[33] G. Csaba and W. Porod, "Simulation of field coupled computing architectures based on magnetic dot arrays," *Journal of Computational Electronics*, vol. 1, pp. 87–91, 2002.

[34] M. C. B. Parish and M. Forshaw, "Physical constraints on magnetic quantum cellular automata," *Applied Physics Letters*, vol. 83, no. 10, pp. 2046–2049, 2003.

[35] A. Imre, G. Csaba, G. Bernstein, W. Porod, and V. Metlushko, "Investigation of shape-dependent switching of coupled nanomagnets," *Superlattices and Microstructures*, vol. 43, pp. 513–518, 2003.

[36] A. Imre, L. Ji, G. Csaba, A. Orlov, G. H. Bernstein, and W. Porod, "Magnetic logic devices based on field-coupled nanomagnets," in *IEEE Semiconductor Device Research Symposium*, 2005, pp. 25–25.

[37] A. Imre, G. Csaba, L. Ji, A. Orlov, G. Bernstein, and W. Porod, "Majority logic gate for magnetic quantum-dot cellular automata," *Science*, vol. 311, pp. 205–208, January 2006.

[38] E. Varga, A. Orlov, M. T. Niemier, X. S. Hu, G. H. Bernstein, and W. Porod, "Experimental Demonstration of Fanout for Nanomagnetic Logic," *IEEE Transactions on Nanotechnology*, vol. 9, no. 6, pp. 668–670, 2010.

[39] E. Varga, G. Csaba, G. H. Bernstein, and W. Porod, "Implementation of a Nanomagnetic Full Adder Circuit," in *Proceedings of the 11th IEEE International Conference on Nanotechnology*, 2011, pp. 1244–1247.

[40] E. Varga, M. T. Niemier, G. Csaba, G. H. Bernstein, and W. Porod, "Experimental Realization of a Nanomagnet Full Adder Using Slanted-Edge Input Magnets," *IEEE Transactions on Magnetics*, vol. 49, no. 7, July 2013.

[41] P. Carcia, A. Meinhaldt, and A. Suna, "Perpendicular magnetic anisotropy in Pd/Co thin film layered structures," *Applied Physics Letters*, vol. 47, no. 2, pp. 178–180, 1985.

[42] F. Den Broeder, D. Kuiper, A. Van de Mosselaer, and W. Hoving, "Perpendicular magnetic anisotropy of Co-Au multilayers induced by interface sharpening," *Physical review letters*, vol. 60, no. 26, p. 2769, 1988.

[43] S.-i. Iwasaki and K. Ouchi, "Co-Cr recording films with perpendicular magnetic anisotropy," *Magnetics, IEEE Transactions on*, vol. 14, no. 5, pp. 849–851, 1978.

[44] M. Becherer, G. Csaba, R. Emling, L. Ji, W. Porod, P. Lugli, and D. Schmitt-Landsiedel, "Focused ion beam structured Co/Pt multilayers for field-coupled magnetic computing," in *Mater. Res. Soc. Symp. Proc. Volume 998E*, D. Pappas, Ed., no. 0998-J06-07, Warrendale, PA, 2007.

[45] C. Chappert *et al.*, "Planar patterned magnetic media obtained by ion irradiation," *Science*, vol. 280, pp. 1919–1922, 1998.

[46] G. Csaba, P. Lugli, M. Becherer, D. Schmitt-Landsiedel, and W. Porod, "Field-coupled computing in magnetic multilayers," *Journal of Computational Electronics*, vol. 7, no. 3, pp. 454–457, 2008.

[47] J. H. Franken, M. Hoeijmakers, R. Lavrijsen, J. T. Kohlhepp, H. J. M. Swagten, B. Koopmans, E. van Veldhoven, and D. J. Maas, "Precise control of domain wall injection and pinning using helium and gallium focused ion beams," *Journal of Applied Physics*, vol. 109, no. 7, pp. –, 2011. [Online]. Available: http://scitation.aip.org/content/aip/journal/jap/109/7/10.1063/1.3549589

[48] D. B. Carlton, N. C. Emley, E. Tuchfeld, and J. Bokor, "Simulation studies of nanomagnet-based logic architecture," *Nano Letters*, vol. 8, no. 12, pp. 4173–4178, 2008.

[49] M. Becherer, G. Csaba, W. Porod, R. Emling, P. Lugli, and D. Schmitt-Landsiedel, "Magnetic ordering of focused-ion-beam structured Cobalt-Platinum dots for field-coupled computing," *IEEE Transactions on Nanotechnology*, vol. 7, no. 3, pp. 316–320, 2008.

[50] M. Becherer, G. Csaba, R. Emling, W. Porod, P. Lugli, and D. Schmitt-Landsiedel, "Field-coupled nanomagnets for interconnect-free nonvolatile computing," in *Digest Technical Papers IEEE International Solid-State Circuits Conference, ISSCC*, Feb. 2009, pp. 474–475.

[51] M. Becherer, G. Csaba, R. Emling, P. Osswald, W. Porod, P. Lugli, and D. Schmitt-Landsiedel, "Extraordinary Hall-effect sensor in split-current design for readout of magnetic field-coupled logic devices," in *2nd IEEE International Nanoelectronics Conference, INEC08*, Shanghai, Mar. 2008.

[52] M. Becherer, J. Kiermaier, G. Csaba, J. Rezgani, C. Yilmaz, P. Osswald, P. Lugli, and D. Schmitt-Landsiedel, "Characterizing magnetic field-coupled computing devices by the Extraordinary Hall-Effect," in *IEEE Proceedings of the 39th European Solid-State Device Research Conference ESSDERC*, Athens, Sep. 2009, pp. 105–108.

[53] M. Becherer *et al.*, "On-chip Extraordinary Hall-effect sensors for characterization of nanomagnetic logic devices," *Solid-State Electronics, Selected papers of ESSDERC 2009*, vol. 54, pp. 1027–1032, 2010.

[54] M. Yasumoto, H. Hayama, and T. Enomoto, "Promissing new fabrication process developed for stacked LSI's," in *Electron Devices Meeting, 1984 International*, vol. 30, 1984, pp. 816–819.

[55] S. Malhi *et al.*, "Characteristics and Three-Dimensional Integration of MOSFET's in Small-Grain LPCVD Polycrystalline Silicon," *Solid-State Circuits, IEEE Journal of*, vol. 20, no. 1, pp. 178–201, Feb 1985.

[56] S. Takahashi, Y. Hayashi, T. Kunio, and N. Endo, "Characteristics of thin-film devices for a stack-type MCM," in *Multi-Chip Module Conference, 1992. MCMC-92, Proceedings 1992 IEEE*, Mar 1992, pp. 159–162.

[57] C. B. P. Garrou and P. Ramm, *Handbook of 3D Integration: Volume1 - Technology and Applications of 3D Integrated Circuits*, C. B. P. Garrou and P. Ramm, Eds. WILEY-VCH GmbH & Co. KGaA, 2008.

[58] M. K. P. Garrou and P. Ramm, *Handbook of 3D Integration: 3D Process Technology - Volume 3*, M. K. P. Garrou and P. Ramm, Eds. WILEY-VCH GmbH & Co. KGaA, 2014.

[59] S. Wong, A. El-Gamal, P. Griffin, Y. Nishi, F. Pease, and J. Plummer, "Monolithic 3D Integrated Circuits," in *VLSI Technology, Systems and Applications, 2007 International Symposium on*, April 2007, pp. 1–4.

[60] L. Solymar and D. Walsh, *Electrical properties of Materials.* Oxford University Press, 2003.

[61] H. Henke, *Elektromagnetische Felder - Theorie und Anwendung.* Springer, 2003.

[62] W. von Münch, *Elektrische und magnetische Eigenschaften der Materie.* Herausgeber: B.G. Teubner Stuttgart, 1987, vol. I, no. 3.

[63] B. Hillebrands and S. Blügel, *Lehrbuch der Experimentalphysik*, 2nd ed., R. Kassing, Ed. Walter de Gruyter, 2005, vol. 6 Festkï¿½rper.

[64] J. Miltat, G. Albuquerque, and A. Thiaville, "An introduction to micromagnetics in the dynamic regime," in *Spin Dynamics in Confined Magnetic Structures I.* Springer, 2002, pp. 1–33.

[65] J. E. Miltat and M. J. Donahue, "Numerical micromagnetics: Finite difference methods," *Handbook of magnetism and advanced magnetic materials*, 2007.

[66] T. L. Gilbert, "A phenomenological theory of damping in ferromagnetic materials," *IEEE Transactions on Magnetics*, vol. 40, no. 6, pp. 3443–3449, 2004.

[67] D. M.J. and P. D.G., "OOMMF User's Guide, Version 1.0," National Institute of Standards and Technology, Interagency Report NISTIR 6376, September 1999.

[68] W. Zeper, F. Greidanus, P. Carcia, and C. Fincher, "Perpendicular magnetic anisotropy and magneto-optical Kerr effect of vapor-deposited Co/Pt-layered structures," *Journal of Applied Physics*, vol. 65, no. 12, pp. 4971–4975, 1989.

[69] D. Allwood, G. Xiong, M. Cooke, and R. Cowburn, "Magneto-optical Kerr effect analysis of magnetic nanostructures," *Journal of Physics D: Applied Physics*, vol. 36, no. 18, p. 2175, 2003.

[70] S. Oliver, C. DiMarzio, S. Lindberg, S. McKnight, and A. Kale, "Measurement of magnetic fields using the magneto-optic Kerr effect," *Applied Physics Letters*, vol. 63, no. 3, pp. 415–417, 1993.

[71] D. Atkinson, D. Eastwood, and L. Bogart, "Controlling domain wall pinning in planar nanowires by selecting domain wall type and its application in a memory concept," *Applied Physics Letters*, vol. 92, no. 2, p. 022510, 2008.

[72] J. Kerr, "XLIII. On rotation of the plane of polarization by reflection from the pole of a magnet," *The London, Edinburgh, and Dublin Philosophical Magazine and Journal of Science*, vol. 3, no. 19, pp. 321–343, 1877.

[73] D. Rugar, H. Mamin, P. Guethner, S. Lambert, J. Stern, I. McFadyen, and T. Yogi, "Magnetic force microscopy: General principles and application to longitudinal recording media," *Journal of Applied Physics*, vol. 68, no. 3, pp. 1169–1183, 1990.

[74] S. Porthun, L. Abelmann, and C. Lodder, "Magnetic force microscopy of thin film media for high density magnetic recording," *Journal of Magnetism and Magnetic Materials*, vol. 182, no. 1, pp. 238–273, 1998.

[75] C. A. Ross, "Patterned magnetic recording media," *Annual Review of Materials Research*, vol. 31, no. 1, pp. 203–235, 2001.

[76] S. Liou, S. Malhotra, J. Moreland, and P. Hopkins, "High resolution imaging of thin-film recording heads by superparamagnetic magnetic force microscopy tips," *Applied Physics Letters*, vol. 70, no. 1, pp. 135–137, 1997.

[77] R. Proksch, P. Neilson, S. Austvold, and J. Schmidt, "Measuring the gigahertz response of recording heads with the magnetic force microscope," *Applied Physics Letters*, vol. 74, no. 9, pp. 1308–1310, 1999.

[78] D. Nyamjav, J. M. Kinsella, and A. Ivanisevic, "Magnetic wires with DNA cores: A magnetic force microscopy study," *Applied Physics Letters*, vol. 86, no. 9, pp. 093 107–093 107, 2005.

[79] H.-C. Wu, T.-W. Wang, J.-S. Sun, W.-H. Wang, and F.-H. Lin, "A novel biomagnetic nanoparticle based on hydroxyapatite," *Nanotechnology*, vol. 18, no. 16, p. 165601, 2007.

[80] J. Dunn, M. Fuller, J. Zoeger, J. Dobson, F. Heller, J. Hammann, E. Caine, and B. M. Moskowitz, "Magnetic material in the human hippocampus," *Brain Research Bulletin*, vol. 36, no. 2, pp. 149–153, 1995.

[81] C. Schönenberger and S. Alvarado, "Understanding magnetic force microscopy," *Zeitschrift für Physik B Condensed Matter*, vol. 80, no. 3, pp. 373–383, 1990.

[82] K. Babcock, M. Dugas, S. Manalis, and V. Elings, "Magnetic force microscopy: recent advances and applications," in *MRS Proceedings*, vol. 355. Cambridge Univ Press, 1994, p. 311.

[83] Y. Martin and H. K. Wickramasinghe, "Magnetic imaging by "force microscopy" with 1000 å resolution," *Applied Physics Letters*, vol. 50, no. 20, pp. 1455–1457, 1987.

[84] D. Rugar, H. Mamin, R. Erlandsson, J. Stern, and B. Terris, "Force microscope using a fiber-optic displacement sensor," *Review of Scientific Instruments*, vol. 59, no. 11, pp. 2337–2340, 1988.

[85] T. Göddenhenrich, H. Lemke, U. Hartmann, and C. Heiden, "Force microscope with capacitive displacement detection," *Journal of Vacuum Science & Technology A*, vol. 8, no. 1, pp. 383–387, 1990.

[86] T. Albrecht, P. Grütter, D. Horne, and D. Rugar, "Frequency modulation detection using high-Q cantilevers for enhanced force microscope sensitivity," *Journal of Applied Physics*, vol. 69, no. 2, pp. 668–673, 1991.

[87] H. Hug, P. Kappenberger, S. Martin, P. Reimann, R. Hoffmann, J. Rychen, W. Lu, and H.-J. Guntherodt, "High resolution quantitative magnetic force microscopy," in *Magnetics Conference, 2002. INTERMAG Europe 2002. Digest of Technical Papers. 2002 IEEE International*, p. EB5.

[88] J. Kiermaier, B. Neumeier, S. Breitkreutz, D. Schmitt-Landsiedel, and M. Becherer, "Variable and fast response 3D magnetic field module for magnetic force microscopy," in *International Scanning Probe Microcopy Conference (ISPM)*, Garching, Munich, June 2011.

[89] L. A. Giannuzzi and F. A. Stevie, *Introduction to focused ion beams: instrumentation, theory, techniques and practice.* Springer Science & Business Media, 2005.

[90] R. Watkins, P. Rockett, S. Thoms, R. Clampitt, and R. Syms, "Focused ion beam milling," *Vacuum*, vol. 36, no. 11, pp. 961–967, 1986.

[91] G. Carter, "The physics and applications of ion beam erosion," *Journal of Physics D: Applied Physics*, vol. 34, no. 3, p. R1, 2001.

[92] S. Parkin, X. Jiang, C. Kaiser, A. Panchula, K. Roche, and M. Samant, "Magnetically engineered spintronic sensors and memory," *Proceedings of the IEEE*, vol. 91, no. 5, pp. 661–680, 2003.

[93] J. Daughton, "GMR applications," *Journal of Magnetism and Magnetic Materials*, vol. 192, no. 2, pp. 334–342, 1999.

[94] J. Smyth, S. Schultz, D. Kern, H. Schmid, and D. Yee, "Hysteresis of submicron permalloy particulate arrays," *Journal of Applied Physics*, vol. 63, no. 8, pp. 4237–4239, 1988.

[95] R. New, R. Pease, and R. White, "Submicron patterning of thin cobalt films for magnetic storage," *Journal of Vacuum Science & Technology B*, vol. 12, no. 6, pp. 3196–3201, 1994.

[96] H. Morimoto, Y. Sasaki, K. Saitoh, Y. Watakabe, and T. Kato, "Focused ion beam lithography and its application to submicron devices," *Microelectronic engineering*, vol. 4, no. 3, pp. 163–179, 1986.

[97] T. Nagase, T. Kubota, and S. Mashiko, "Fabrication of nano-gap electrodes for measuring electrical properties of organic molecules using a focused ion beam," *Thin Solid Films*, vol. 438, pp. 374–377, 2003.

[98] J. Martın, J. Nogues, K. Liu, J. Vicent, and I. K. Schuller, "Ordered magnetic nanostructures: fabrication and properties," *Journal of Magnetism and Magnetic Materials*, vol. 256, no. 1, pp. 449–501, 2003.

[99] J. Ferré *et al.*, "Irradiation induced effects on magnetic properties of Pt/Co/Pt ultrathin films," *Journal of Magnetism and Magnetic Materials*, vol. 198, pp. 191–193, 1999.

[100] T. Devolder, "Light ion irradiation of Co/Pt systems: structural origin of the decrease in magnetic anisotropy," *Physical Review B*, vol. 62, no. 9, p. 5794, 2000.

[101] S. Breitkreutz, J. Kiermaier, S. V. Karthik, G. Csaba, D. Schmitt-Landsiedel, and M. Becherer, "Controlled reversal of Co/Pt Dots for nanomagnetic logic applications," *Journal of Applied Physics*, vol. 111, no. 7, p. 07A715, 2012.

[102] C. Maddalon, K. Barla, E. Denis, E. Lous, E. Perrin, S. Lis, C. Lair, and E. Dehan, "Planarization properties of hydrogen silsesquioxane (HSQ) influence on CMP," *Microelectronic engineering*, vol. 50, no. 1, pp. 33–40, 2000.

[103] P. Liu *et al.*, "The effects of plasma treatment for low dielectric constant hydrogen silsesquioxane (HSQ)," *Thin Solid Films*, vol. 332, no. 1, pp. 345–350, 1998.

[104] (2015) The Stopping and Range of Ions in Matter (SRIM): Update 2015. http://www.srim.org.

[105] M. Blois Jr, "Preparation of thin magnetic films and their properties," *Journal of Applied Physics*, vol. 26, no. 8, pp. 975–980, 1955.

[106] F. Den Broeder, W. Hoving, and P. Bloemen, "Magnetic anisotropy of multilayers," *Journal of Magnetism and Magnetic Materials*, vol. 93, pp. 562–570, 1991.

[107] H. Yamane, Y. Maeno, and M. Kobayashi, "Annealing effects on multilayered Co/Pt and Co/Pd sputtering films," *Applied Physics Letters*, vol. 62, no. 13, pp. 1562–1564, 1993.

[108] M. Speckmann, H. Oepen, and H. Ibach, "Magnetic domain structures in ultrathin Co/Au (111): on the influence of film morphology," *Physical Review Letters*, vol. 75, no. 10, p. 2035, 1995.

[109] Y. Huang, Y. Zhang, G. Hadjipanayis, A. Simopoulos, and D. Weller, "Hysteresis behavior of CoPt nanoparticles," *IEEE Transactions on Magnetics*, vol. 38, no. 5, pp. 2604–2606, 2002.

[110] J. Engelen, M. Delalande, A. Le Febre, T. Bolhuis, T. Shimatsu, N. Kikuchi, L. Abelmann, and J. Lodder, "Thermally induced switching field distribution of a single CoPt dot in a large array," *Nanotechnology*, vol. 21, no. 3, p. 035703, 2010.

[111] T. Thomson, G. Hu, and B. Terris, "Intrinsic distribution of magnetic anisotropy in thin films probed by patterned nanostructures," *Physical Review Letters*, vol. 96, no. 25, p. 257204, 2006.

[112] G. Csaba and W. Porod, "Behavior of nanomagnet logic in the presence of thermal noise," in *2010 14th International Workshop on Computational Electronics*, 2010.

[113] C. Lent and P. Tougaw, "A device architecture for computing with quantum dots," *Proceedings of the IEEE*, vol. 85, no. 4, pp. 541–557, Apr 1997.

[114] S. Bhanja, M. Ottavi, F. Lombardi, and S. Pontarelli, "QCA circuits for robust coplanar crossing," *Journal of Electronic Testing*, vol. 23, no. 2-3, pp. 193–210, 2007.

[115] K. Walus, G. Schulhof, and G. Jullien, "High level exploration of quantum-dot cellular automata." Proceedings Asilomar Conference Signals, Systems and Computers, 2004.

[116] M. T. Niemier, X. S. Hu, M. Alam, G. Bernstein, W. Porod, M. Putney, and J. DeAngelis, "Clocking structures and power analysis for nanomagnet-based logic devices," in *ACM/IEEE International Symposium on Low Power Electronics and Design (ISLPED), 2007.* IEEE, pp. 26–31.

[117] M. Niemier *et al.*, "Nanomagnet logic: progress toward system-level integration," *Journal of Physics: Condensed Matter*, vol. 23, no. 49, p. 493202, 2011.

[118] M. Albert, M. Franchin, T. Fischbacher, G. Meier, and H. Fangohr, "Domain wall motion in perpendicular anisotropy nanowires with edge roughness," *Journal of Physics: Condensed Matter*, vol. 24, no. 2, p. 024219, 2012.

[119] K.-J. Kim *et al.*, "Depinning field at notches of ferromagnetic nanowires with perpendicular magnetic anisotropy," *IEEE Transactions on Magnetics*, vol. 45, no. 10, pp. 4056–4058, 2009.

[120] S. Hashimoto, Y. Ochiai, and K. Aso, "Perpendicular magnetic anisotropy and magnetostriction of sputtered Co/Pd and Co/Pt multilayered films," *Journal of Applied Physics*, vol. 66, no. 10, pp. 4909–4916, 1989.

[121] [Online]. Available: http://www.mathworks.de/de/help/curvefit/cftool.html

[122] B. W. Lennart Rade, *Springers Mathematische Formeln - Dritte, durchgesehene Auflage.* Springer, 2000.

[123] N. F. Mott, "Electrons in transition metals," *Advances in Physics*, vol. 13, no. 51, pp. 325–422, 1964.

[124] J. W. F.Dorleijn, "Electrical conduction in ferromagnetic metals," *Philips Res. Rep.*, vol. 31, pp. 287–408, 1976.

[125] A. Fert, "Nobel lecture: Origin, development, and future of spintronics," *Reviews of Modern Physics*, vol. 80, no. 4, p. 1517, 2008.

[126] S. M. Thompson, "The discovery, development and future of GMR: The Nobel Prize 2007," *Journal of Physics D: Applied Physics*, vol. 41, no. 9, p. 093001, 2008.

[127] The Discovery of Giant Magnetoresistance - Scientific Background on the Nobel Prize in Physics 2007. The Class for Physics of the Royal Swedish Academy of Schiences.

[128] J. A. Thornton, "Influence of apparatus geometry and deposition conditions on the structure and topography of thick sputtered coatings," *Journal of Vacuum Science & Technology*, vol. 11, no. 4, pp. 666–670, 1974.

[129] T. Hikosaka, T. Komai, and Y. Tanaka, "Oxygen effect on the microstructure and magnetic properties of binary CoPt thin films for perpendicular recording," *IEEE Transactions on Magnetics*, vol. 30, no. 6, pp. 4026–4028, 1994.

[130] W. H. Meiklejohn and C. P. Bean, "New magnetic anisotropy," *Physical Review*, vol. 102, no. 5, p. 1413, 1956.

[131] D. E. Heim and S. S. Parkin, "Magnetoresistive spin valve sensor with improved pinned ferromagnetic layer and magnetic recording system using the sensor," Nov. 7 1995, US Patent 5,465,185.

[132] W. Egelhoff Jr, P. Chen, C. Powell, M. Stiles, R. McMichael, J. Judy, K. Takano, and A. Berkowitz, "Oxygen as a surfactant in the growth of giant magnetoresistance spin valves," *Journal of Applied Physics*, vol. 82, no. 12, pp. 6142–6151, 1997.

[133] C. Christides, S. Stavroyiannis, N. Boukos, A. Travlos, and D. Niarchos, "Microstructural modification in Co/Cu giant-magnetoresistance multilayers," *Journal of Applied Physics*, vol. 83, no. 7, pp. 3724–3730, 1998.

[134] D. J. Smith, A. Modak, T. Rabedeau, and S. Parkin, "Growth and structural characterization of highly oriented sputter-deposited (111),(110), and (100) Co/Cu superlattices," *Applied Physics Letters*, vol. 71, no. 11, 1997.

[135] T. Thomson, P. Riedi, and B. Hickey, "59Co nuclear magnetic resonance studies of the effect of annealing molecular beam epitaxy grown Co/Cu (111) multilayers," *Journal of Applied Physics*, vol. 79, no. 8, pp. 5119–5121, 1996.

[136] M. Hecker, D. Tietjen, D. Elefant, C. Schneider, A. Qiu, N. Cramer, R. Camley, and Z. Celinski, "Thermally activated deterioration processes in Co/Cu GMR multilayers," *Journal of Applied Physics*, vol. 89, no. 11, pp. 7113–7115, 2001.

[137] S. Mangin, D. Ravelosona, J. Katine, M. Carey, B. Terris, and E. E. Fullerton, "Current-induced magnetization reversal in nanopillars with perpendicular anisotropy," *Nature Materials*, vol. 5, no. 3, pp. 210–215, 2006.

[138] M. Julliere, "Tunneling between ferromagnetic films," *Physics letters A*, vol. 54, no. 3, pp. 225–226, 1975.

[139] J. S. Moodera, L. R. Kinder, T. M. Wong, and R. Meservey, "Large magnetoresistance at room temperature in ferromagnetic thin film tunnel junctions," *Physical Review Letters*, vol. 74, no. 16, p. 3273, 1995.

[140] H. Kurt, M. Venkatesan, and J. Coey, "Enhanced perpendicular magnetic anisotropy in Co/Ni multilayers with a thin seed layer," *Journal of Applied Physics*, vol. 108, no. 7, p. 073916, 2010.

[141] F. Den Broeder, E. Janssen, W. Hoving, and W. Zeper, "Perpendicular magnetic anisotropy and coercivity of Co/Ni multilayers," *IEEE Transactions on Magnetics*, vol. 28, no. 5, pp. 2760–2765, 1992.

[142] M. Johnson, P. Bloemen, F. Den Broeder, and J. De Vries, "Magnetic anisotropy in metallic multilayers," *Reports on Progress in Physics*, vol. 59, no. 11, p. 1409, 1996.

[143] S. Liu, G. Csaba, X. S. Hu, E. Varga, M. T. Niemier, G. H. Bernstein, and W. Porod, "Minimum-energy state guided physical design for nanomagnet logic," in *Proceedings of the 50th Annual Design Automation Conference*. ACM, 2013, p. 106.

Related Theses

[Bre09] Stephan Breitkreutz. Aufbau eines magneto-optischen Messplatzes zur Charakterisierung von Co/Pt-Mehrlagenschichten. Diplomarbeit, Technische Universität München, 2009.

[Efi14] Yanic Efinger. Herstellung und Charakterisierung von out-of-plane GMR-Sensoren auf Basis von Cobalt/Platin/Kupfer-Schichtstapeln. Master's thesis, Technische Universität München, 2014.

[Eic11] Irina Eichwald. Investigations on the magnetic properties of Cobalt-Nickel multilayers and nano-structures. Diplomarbeit, Technische Universität München, 2011.

[Kun14a] Frederik Kunik. Investigation of GMR-effect in CoNi/Cu multilayer by CPP-measurements for NML read-out sensor application. Bachelorarbeit, Technische Universität München, 2014.

[Kun14b] Frederik Kunik. Materialuntersuchung Co/Ni/Cu zur Erzielung senkrechter magnetischer Anisotropie in nanomagnetischen Strukturen. Ingenieurspraxis, Technische Universität München, 2014.

[Lec12] Benedikt Lechner. Herstellung und Charakterisierung eines GMR-Schichtsystems mit senkrechter Anisotropie. Bachelorarbeit, Technische Universität München, 2012.

[Neu09] Benedikt Neumeier. Konstruktion und Aufbau eines X-Y-Rastertisches zur Charakterisierung magnetischer Schichten an einem optischen Messplatz. Studienarbeit, Technische Universität München, 2009.

[Ruf12] Friederike Ruf. Charakterisierung von CoNi Mehrlagenschichten und Nanostrukturen unter Verwendung eines TaPt seedlayers. Bachelorarbeit, Technische Universität München, 2012.

[Wu12] Jie Wu. Unabhängige Signalübertragung in gekreuzten Co/Pt Leitungen separiert durch ein dünnes Dielektrikum. Diplomarbeit, Technische Universität München, 2012.

[Zie13] Grazvydas Ziemys. Influence of sub 100ns current pulses on the domain wall motion in magnetic nanowires. Master's thesis, Technische Universität München, 2013.

Danksagung

Die vorliegende Arbeit entstand während meiner Tätigkeit als wissenschaftliche Mitarbeiterin am Lehrstuhl für Technische Elektronik der Technischen Universität München. Ganz herzlich danken möchte ich Prof. Dr. Doris Schmitt-Landsiedel, die das Projekt "Nanomagnetische Logik in senkrechten Medien" ins Leben gerufen hat und damit die Basis für diese Arbeit geschaffen hat. Des weiteren möchte ich mich dafür bedanken, mir die Möglichkeit gegeben zu haben in der bestehenden Forschergruppe mitzuarbeiten, für Rat und Unterstützung bei allen Fragen und Problemen.

Ganz besonderer Dank gilt auch Herrn Prof. Dr. György Csaba für seine inspirierende Idee, Magnete mit senkrechter magnetischer Anisotropie zur Realisierung digitaler Logik-Schaltkreise zu verwenden. Ohne diese Idee würde es diese Arbeit nicht geben. Kritisches Hinterfragen und konstruktive Anmerkungen in vielen wertvollen Diskussionen mit ihm halfen mir die Thematik besser zu verstehen und dadurch die gewünschten Ergebnisse zu erzielen.

Der Weg zum Lehrstuhl führte mich über die bereits davor dort abgelegte Diplomarbeit im Bereich der Magnetik. Das Forscherteam bestehend aus Markus Becherer, Josef Kiermaier und Stephan Breitkreutz-von Gamm weckte damals meine Begeisterung für die Magnetik und inspirierte mich dazu auf diesem Gebiet weiter zu forschen. Allen voran gilt mein ganz besonderer Dank Markus Becherer, der es immer wieder schafft und geschafft hat, meine Begeisterung für die Magnetik weiter leben zu lassen. Lieber Markus, danke auch für die Weitergabe deines enormen und sehr wertvollen Technologie-, Magnetik- und Praxiswissens an mich.
Bei Josef Kiermaier möchte ich mich besonders für die anfängliche Unterstützung beim "Einleben" am LTE bedanken. Ein besonderer Dank gilt auch für die zahlreichen, ergiebigen, wissenschaftlichen Diskussionen und die Weitergabe persönlicher Erfahrung!
Stephan Breitkreutz-von Gamm gilt mein besonderer Dank für sein immer offenes Ohr. Egal ob bei wissenschaftlichen, organisatorischen oder persönlichen Fragen, es wurde immer eine Lösung gefunden. Danke dafür, dass du nie deinen Optimismus verlierst!
Grazvydas Ziemys danke ich besonders für seinen unermüdlichen Einsatz für die Magnetik, seine übergroße Hilfsbereitschaft und für seine ansteckende Begeisterung für Neues.

Grundvoraussetzung für das Gelingen der Arbeit war ein intakter Reinraum. Für ihren unermüdlichen Einsatz zur Instandhaltung des Reinraumes möchte ich mich bei Dr. Werner Kraus, Rainer Emling, Christoph Klösters, Wolfgang Pielock, Karl Demmel und Norbert Ley ganz herzlich bedanken. Ganz besonderer Dank gebührt Silke Boche für die außerordentliche Unterstützung bei technologischen Fragen. Liebe Silke, ich möchte dir des weiteren für deine sehr herzliche Persönlichkeit danken, die mir in manch' schwerer Stunde immer weitergeholfen hat. Bei Hans Mulatz möchte ich mich für das Bonden der Proben bedanken. Ohne seine sehr akkurate Arbeit wäre die Vermessung der Proben nicht möglich gewesen.

Des weiteren möchte ich mich recht herzlich bei meinen Kollegen aus dem Themengebiet der Schaltungstechnik bedanken: Cenk Yilmaz (für seine immer gute Laune und die Fähigkeit auch mal über andere Dinge als Arbeit zu diskutieren), Leonhard Heiß (für die reibungslose Organisation von Prüfungen und Prüfungseinsichten), Simon Stark (für die reibungslose Übernahme und seinen Einsatz bei der Bauelemente Zentralübung) und Martin Wirnshofer (für die Einführung in die Bauelemente Zentralübung).

Danke an die zahlreichen Studenten aus Praktika, Abschlussarbeiten und Zentralübung. Danke für die enorme und für mich sehr wertvolle Lehrerfahrung!

Abschließend möchte ich mich bei meinen Eltern, meinem Bruder und meinem Freund bedanken. DANKE, meine Lieben! Danke, dass ihr immer an mich glaubt und mich dazu ermutigt einen Schritt weiter zu gehen und niemals aufzugeben. Danke, dass ihr immer für mich da seid. Lieber Alexander, danke für das immer kritische Korrekturlesen meiner Arbeit(en). Erst dadurch ergibt sie ein "rundes Ganzes" für mich. ;-)